Directional Hearing at the Micro-Scale:

Bio-inspired Sound Localization

Andrew Reid

A thesis presented for the degree of
Doctor of Philosophy

Department of Electronic and Electrical Engineering
University of Strathclyde
20 September 2017

Declaration of Authenticity & Author's rights

This thesis is the result of the author's original research. It has been composed by the author and has not been previously submitted for examination which has led to the award of a degree.

The copyright of this thesis belongs to the author under the terms of the United Kingdom Copyright Acts as qualified by University of Strathclyde Regulation 3.50. Due acknowledgement must always be made of the use of any material contained in, or derived from, this thesis.

Signed:

Date:

Acknowledgements

Whatever is in any way good has its source of goodness in itself, and is complete in itself, praise forms no part in it. But praise doesn't seem to do it any harm so... Thank you to Dr. James Windmill, who was left with no choice but to take me on as a project student after I gamed the system by making him both my first and second choice for project supervisor and then magnanimously kept me on as a PhD Student and then post-doc despite clearly having better options than a fellow who showed up blearily to the lab with a baby strapped to his back. In return I have attempted to keep the schadenfreude to a minimum over the last year as the roles have been reversed and sleep-deprivation has taken its toll on him. James has been generous with his time, attention and support for many years now, and I have no doubt I would not be here without him. Thank you to Professor Michael Greenfield both for his patience in explaining basic biology to a fellow who didn't so much as do a standard grade biology and so thought that radial cleavage was a form of décolletage, and for his care and warm welcome when I stayed in Tours. For a man who hadn't stepped on a plane before the beginning of this PhD and was truly terrified at the prospect of staying in France to now feel so comfortable there is testament to his generosity. Thank you also to Professor Deepak Uttamchandani for his time and support on the MEMS side of the thesis, and for not giving me too much grief when the first microphone I designed actually performed worse as a microphone than one of his micro-mirrors. From my friends in the Centre for Ultrasonic Engineering, who have grown too numerous for me to do them justice here, I have to select a few names to mention in particular. A great thanks to David Mackie, who not only showed my around and got me started in my PhD but then helpfully disappeared off to Belgium leaving his post vacant right when I was looking for a job. Thank you to Yansheng Zhang and Ralf Bauer for doing the electrical engineering work necessary for my project, leaving me free to do an electrical engineering PhD which consisted entirely of mechanical engineering and biology. Thank you to Jeremy Gibson, for his support with the biological work in Glasgow, and for his understanding of my frustrations and providing the universal solution of dance. Thanks also to Flavia Barbossa, Alicia Jarrige and Darren Rebar in Tours, for tolerating my mangling of the French language and of their specimens. Thanks to Gordon Brown for his work in wire bonding and electron microscopy and for showing me around the clean room facilities. The research leading to these results has received funding from the DSTL-DGA UK France PhD programme and thank you to Peter Biggins and James Wilson for their support throughout this PhD. Finally, this is dedicated, as always, to Arthur and Alyssa. Although frankly they were no help at all.

Abstract

Miniaturization of sound localization sensors arrays is heavily constrained by the limited directional cues in intensity difference and phase difference available at the microscale. Micro-Electro Mechanical System (MEMS) sound localization sensors inspired by the auditory system of *Ormia ochracea* offer a potential solution to this problem by the apparent amplification of the available intensity and phase difference between the measurement points. An inherent limitation of these systems is that significant amplification of these cues is only available on or near one of the resonant frequencies of the device, severely limiting it application as a directional microphone. A lower amplification of directional cues can be achieved across a wide frequency range, forcing designers to compromise the goal of high amplification of directional cues to operate across the audio range. Here we present an alternative approach, namely a system optimized for the maximum amplification of directional cues across a narrow bandwidth operating purely as a sound-localization sensor for wide-band noise. In the devices presented in chapter four we present sound-localization sensors where the directional sensitivity is enhanced by increasing the coupling strength beyond the 'dual optimization' point, which represents the collocation of a local maximum in directional sensitivity and a local minimum in non-linearity, compensating for the loss of the desirable linearity of the system by restricting the angular range of operation. Intensity gain achieved is 16.3 dB at 10° sound source azimuth with a linear directional sensitivity of 1.6 dB per degree, while linear directional sensitivity in phase difference gain shows a seven fold increase over the 'dual optimization' point of 8 degrees per degree. In addition, during the course of this work it was discovered that the methods used to calculate the amplified intensity difference between the measurement points introduce unwelcome Cauchy noise which is difficult to reduce. Later iterations of the device demonstrate the process of optimization of a sound localization sensor for the maximum amplification of directional cues across a narrow bandwidth can be used to overcome that error, as well as describing mathematically what appears to have been a commonly encountered but unpublished problem with *Ormia* inspired directional sensors. In the second part of the thesis, beginning in Chapter 5 the sound localization strategies of another acoustic insect, the lesser wax moth *Achroia grisella*, is examined. Moths differ somewhat because their ears generally function as simple bat detectors with relatively little directional ability. Those moths that use sound signals for mating communication represent a yet more special case, as these species can localize sound sources but singing and the ability to localize conspecific song evolved well after the origin of hearing. The analyses revealed a novel localization mechanism wherein the geometry and structure of the tympanal membrane of each ear afford sharp sensitivity to sound arriving from a distinct angle. Females can thereby track singing males, but they only do so by following an indirect, curvilinear trajectory regularly interrupted by wide deviations.

List of publications arising from this thesis

The work in Chapters 3, 4 and 5 of this thesis has been presented at the following conferences:

- Eurosensors 2015, Freiburg, Germany - oral presentation
- IEEE Sensors 2015, Busan, South Korea - poster presentation

For the latter presentation a conference paper was published here: A. Reid, D. Uttamchandani, and J. F. C. Windmill, "Optimization of a bio-inspired sound localization sensor for high directional sensitivity," in 2015 IEEE SENSORS, 2015, pp. 1-4.

In addition a paper based on the over-coupling work in Chapter 4 was published in *Proceedia Engineering*: A. Reid, J. F. C. Windmill, and D. Uttamchandani, "Bio-inspired Sound Localization Sensor with High Directional Sensitivity," Procedia Engineering, vol. 120, pp. 289-293, Jan. 2015.

The work in Chapter 5 of this thesis has been published in the Proceedings of the National Academy of Sciences: A. Reid, T. Marin-Cudraz, J.F.C. Windmill, M.D. Greenfield, "Evolution of directional hearing in moths via conversion of bat detection devices to asymmetric pressure gradient receivers". Proceedings of the National Academy of Sciences. 2016 Nov 29;113(48):E7740-8.

Contents

List of Figures

List of Tables

List of Symbols

Sound and fluid dynamics

A - Wave amplitude (m)
f - Wave frequency (Hz)
ω - Angular velocity $(rads^{-1})$
ϕ - Wave phase (m)
v_p - Phase velocity (ms^{-1})
k - Wavenumber (m^{-1})
γ - Adiabatic index (unit)
p - Pressure (Pa)
ρ - Density (kgm^{-3})
K_S - Bulk modulus (isentropic) (Pa)
$\boldsymbol{x}$ - Displacement vector, with derivites wrt time $\dot{\boldsymbol{x}}, \ddot{\boldsymbol{x}}$ $\boldsymbol{r}$ - Position vector in spherical co-ordinates
r - Magnitude of vector $\boldsymbol{r}$ (m)
θ - Azimuth angle of vector $\boldsymbol{r}$ (rad)
ψ - Pitch agnle of vector $\boldsymbol{r}$ (rad)
Φ - Velocity potential
a_0 - Source radius (m)
v_N - Normal velocity (Superscript S indicated evaluated at surface) (ms^{-1})
d - Separation between sources or listening points (m)
M_g - Molar mass of gas $(g\ mol^{-1})$
M_c - Mach number (units)
M_θ - Mach angle (rad)
α - Attenuation factor
t - time (s)

Solid mechanics

E - Young's modulus (Pa)
w_b, w_m - Width of beam or membrane (m)
l_b, l_m - Length of beam or membrane (m)
t_b, t_m - Thickness of beam or membrane (m)

κ - Surface curvature (m^{-1})
Δz - Displacement is z-axis (Material frame) (m)
M_τ - Moment of force ($N \cdot m$)
I - Second moment of area (m^4)
$\boldsymbol{e}$ = strain vector (unit)
$\boldsymbol{S}$ = Compliance matrix (Pa^{-1})
z_n = Position of netural axis (of a beam) (m)
k - Stiffness (of spring) ($N\ m^{-1}$)
G - Torsional stiffness
W - Work (J)

Electrostatics and Piezoelectrics

Q = Charge (C)
V = Electric potential (V)
C = Capactiance (F)
ϵ = Permittivity (Fm^{-1})
$\boldsymbol{E_v}$ = Electric field vector (V)
$\boldsymbol{k_p z}$ = Piezoelectric coupling factor
$\boldsymbol{d}$ = Piezoelectric coupling coefficient matrix (Units)
$\boldsymbol{D}$ = Piezoelectric displacement vector (m)
$\boldsymbol{\eta}$ = Electric permittivity matrix

Statistical Analysis

AP - Auto power spectrum
CP - Cross power spectrum
χ_V - Vibrometer measurement spectrum
χ_R - Reference signal measurement spectrum
FRF - Frequency response function
N - Noise spectrum
COH - Magnitude of coherence
P_D - Probability distribution
μ_x, μ_y - Sample means (of datasets X and Y)

σ_x, σ_y - Sample standard deviations
Φ_x - Cumulative distribution
ρ - Correlation between samples

Symbols specific to Ormia inspired microphones

ω_r - rocking mode resonance frequency ($rads^{-1}$)
ω_t - translational mode resonance frequency ($rads^{-1}$)
Ω - Normalised frequency ω/ω_r
η - Ratio of resonance frequencies ω_r/ω_t
$mIID$ - mechanical Interaural Intensity Difference (dB)
$mIPD$ - mechanical Interaural Phase Difference (rad)
ADS - Average directional sensitivity (dB/° or °/°)
NL - Non-linearity of measurement

Chapter 1

Introduction

Microelectromechanical systems (MEMS) use integrated circuit batch processing techniques to combine mechanical and electrical components on a single microchip. MEMS devices are commonly used as transducers in commercial products where they are able to offer the advantages of miniaturization, reduced power consumption and a great reduction in costs due to batch fabrication. The functional components of MEMS sensors or actuators are defined at the microscale, with micro-scale motors [5], accelerometers [6], and microphones [7] already in wide commercial use [8]. In this work the focus is on the use of MEMS in directional microphone and sound localization systems, the first of which is already a well-established industry with an estimated market value of \$800 million in 2015 [9] and applications in mobile phones [10], hearing aids [11] and voice-activated technology [12]. Dedicated sound localization systems are of particular interest in military research, which forms the impetus behind the research detailed in this thesis as will be described in Chapter 3, but also have potential applications in policing [13], navigation [14] and teleconferencing systems [15]. The potential benefits from MEMS sensors are concomitant with particular challenges in working at the microscale. Forces such as electrostatic, atomic and capillary can be significant in microscale systems while material properties and fluid transport physics are highly size-dependent. For directional microphones and sound localization systems the problems of scale are particularly acute, with accurate localization relying on wave properties which change on a scale orders of magnitude larger than the measurement device (see Section 1.5). Guidance towards a solution to this problem may be found in phonotaxis in insects, since the auditory systems of many hearing insects are of the same scale as MEMS microphones and yet the capability to localize sound sources where the acoustic wavelength is many times the length of the insect's body can frequently be found (Section 1.2). Directional microphones based on the auditory system of *Ormia ochracea* are well researched (Chapter 3). This thesis presents new designs improving the directional sensitivity and linearity of directional measurement (Chapter 4). In addition an investigation into the phonotactic capabilities of another hearing insect, the Lesser Wax Moth *Achroia grisella*, is presented in Chapter 5, where the basis for sound localization has not previously been described. The thesis, and this introductory chapter, is therefore split between investigations of MEMS devices and biological systems with the intention of presenting novelty in a well-established bio-inspired technology as well as a nascent potential path for future bio-inspired research. This introductory chapter will cover brief overviews of the components of hearing systems in insects, the base equations for sound sources and measurements used in sound localization, MEMS technology, with a focus on MEMS microphones, and finally some discussion of the analysis of damping, capacitive comb transduction and piezoelectric transduction systems which later microphone designs will rely on. Chapter 2 will outline the methods and technologies used in this research: laser Doppler vibrometry, X-Ray micro-scale computer aided tomography (μCT) and finite element modelling using COMSOL. In Chapter 3 the physical principles behind the sound localization capabilities of *Ormia ochracea* are to be explored and a review of existing designs that have taken that system as inspiration is completed. This then leads to the potential application of *Ormia* inspired designs to gunshot localization in counter-sniper systems. In Chapter 4 the analytical models of Chapter 3 are applied to an *Ormia* inspired MEMS sound localization devices, with two further iterations of sensors fabricated in single layer Silicon-on-Insulator (SOI) presented in Chapter 5 and their sound localization properties investigated. Chapter 6 switches the focus of the thesis to biological systems, and an overview of *Achroia grisella*'s phonotaxis is presented, followed by behavioural, laser vibrometry and X-Ray μCT studies which reveal a novel method of sound localization in insects. Finally in Chapter 7 the findings on the thesis are summarised and the potential for future work addressed.

1.1 Hearing in insects

Hearing in insects is known to have evolved independently between 15-20 times [16] and the methods of detection are consequently varied. Sound detection falls into one of two categories: pressure detection systems and particle velocity detection systems. Particle velocity detection systems are design for use in the near-field of an acoustic source at low frequencies. They are typically small, light structures or hair-like mechano-receptors, such as the mosquito antenna which is used to detect the flight disturbance from a nearby mate [17]. Pressure receivers are exclusively tympanal systems, operating in the far field and capable of detecting sound into the far ultrasound range [18].

1.1.1 Structure of tympanal systems

Tympanal systems in insects comprise a membrane backed by an air filled sac and a chordotonal sensillum, whose function is the transduction of the mechanical movement of the tympanal membrane into neural impulses in the auditory nerve [19]. The membrane and sac are formed from the tracheal system, a branching network of tubes that carry oxygen to every part of the insect's body. The presence of air filled cavities close to the surface of the exoskeleton allows parts of the insect body to vibrate in response to acoustic energy, even without any clearly developed tympanic hearing [20]. The membrane is a thinned portion of the cuticular exoskeleton, usually isolated from the motion of the body by a thickened rim [16]. The chordotonal sensilla are stretch receptors, responding to displacement or acceleration. They are commonly found at the base of appendages or at the interface between body segments where they can be proprioceptive, forming part of the insect's kinaesthetic sense, or vibroreceptive, detecting external signals through the air or substrate [21]. The key components of the tympanic ear are common throughout the insect body, so it is not surprising to find that there is significant diversity in the location of hearing. In bushcrickets ears are commonly found on the tibia, in locusts and moths on the abdomen, and in butterflies at the base of the wing. Not all components are universally found, for example the bladder grasshopper *Bullacris memracioides* is atympanate, but detects sound via six pairs of abdominal sacs [22], while the green lacewing lacks an air cavity, instead being backed by a fluid cell on the radial vein of the wing [23, 24].

1.1.2 The tympanal membrane

The tympanal membrane is the mechano-acoustic interface of the tympanal system converting the difference in sound pressure between the two faces into a transverse vibration. The membrane is fixed around the periphery and typically ovoid, inviting a comparison with the familiar 'drum modes' of elastic membranes. Insect tympana are highly anisotropic, however, with the thickness and structure of the cuticle varying across the membrane and frequently have additional structures attached; such as the sclerotized oval plate on the outer membrane of the New Zealand tree weta [25], Muller's organ on the locust [26], or the scolopale rod of the chordotonal sensillum itself which can act as a point mass or a spring on the membrane.

1.1.3 Chordotonal sensillum

In tympanic systems the sensilla are formed from a scolopale rod, which at its cap is attached to the tympanic membranes surrounding a potassium rich space and cilium [27]. At the base of the scoloparium rests at least one sensory neuron, the auditory receptor cells connecting to the tympanic nerve (Figure 1.1).

The method of transduction from mechanical energy to nerve impulses is not currently known, although recent genetic studies of Drosophila have suggested that the dendrite contains a solution rich in potassium ions, which can create an electric potential when micro-channels in the cilium are opened by the stretching of the scolopale rods [28]. For the purposes of this thesis we can take a more naÃ¯ve phenomological approach, looking only at the resulting nerve signal. Movement of the tympanum is coded in the nerve as an electrical pulse train, with a higher frequency of pulses corresponding to a larger movement of the tympana (Figure 1.2).

1.2 Directional hearing in insects

The localization of sound sourced by small animals is a fundamental problem in bioacoustics [29]. Where body size is diminutive and inter-ear distance is short, as is generally the case in acoustic insects and anurans, an animal cannot rely on comparison between the intensity or time delay of signals received at either ear. These inter-aural intensity differences (IID) or inter-aural time differences (ITD) are used to resolve the azimuth angle towards the source, requiring a small bodied animal

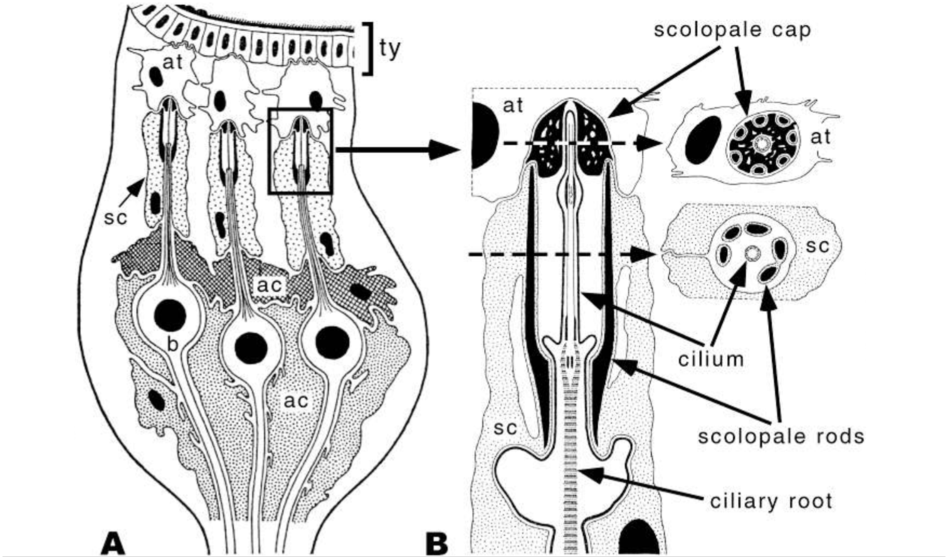

Figure 1.1: Cross section of a chordotonal organ taken from [16], where ac=accessory cells, b= bipolar sensory cells, at=attachment cells, sc=scolopale cell and ty=tympanum. a) Shows a sensory cell containing multiple scolopale rods, while b) shows an individual rod.

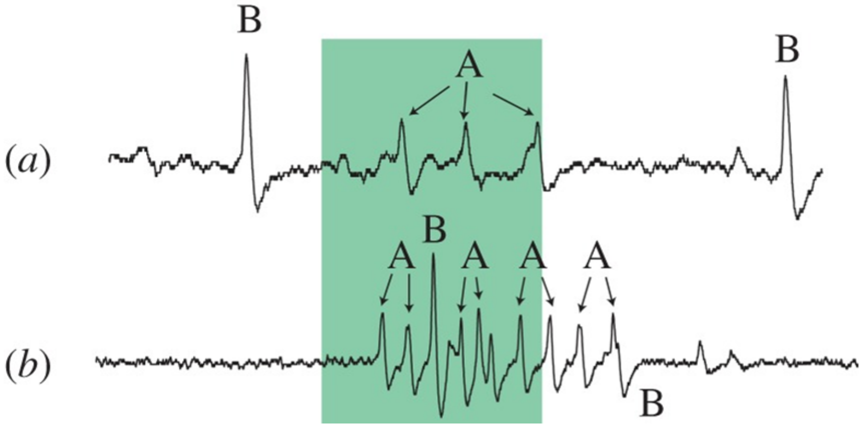

Figure 1.2: Example of electrophysiological recordings from a noctuid moth taken from [18]. The diagram represents the output from four different receptor cells (marked A) and a second, non-auditory cell (marked B). The top trace (a) is the nerve response to a sound pulse at 60 dB SPL while (b) is to a sound pulse at 90 dB SPL. The duration of the sound pulse is marked by a green strip.

to adopt an alternative strategy [30]. Some acoustic insects and anurans overcome their size constraints by means of multiple pathways along which sound arrives at both the external and internal surfaces of the tympanal membranes [31, 32]: because the separate pathways leading to the two surfaces of the tympanal membrane differ in length when the sound source is ipsilateral a phase difference between the external and internal sound waves can arise for specific sound frequencies and yield vibration of the membrane. The inter-aural difference between these external-internal phase differences, by generating a disparity in vibration between the two ears, may then serve as a reliable indicator of the azimuth angle toward the sound source. Certain small acoustic insects that do not possess the anatomical features permitting an inter-aural phase difference (IPD) mechanism are nonetheless quite efficient at sound source localization. In the tachinid fly *Ormia ochracea*, a parasitoid of singing male crickets, the two ears are separated by 500 μm and sound waves arrive only at the external surfaces of the tympanal membranes but a specialised rocker-arm apparatus connecting the ears magnifies both the IID and IPD [33] (a more complete description of *O. Ochracea*'s direction hearing is given in Chapter 3). These enhanced inter-aural differences, combined with pooling the responses of many individual receptor neurons, allow female *O. Ochracea* to localize their hosts with a high degree of directional precision [34]. Other small acoustic insects exhibit comparable localization ability without having access to either an inter-aural bridge or an IPD mechanism. Understanding their directional hearing would be valuable in an evolutionary context, as well as in the development of bio-inspired technology for sound localization.

1.3 Fundamentals of sound propagation

Sound is a propagating mechanical wave characterized by oscillations of pressure and displacement in a longitudinal wave and of displacement in a transverse wave. Longitudinal waves travel in the same axis as the displacement of the medium and can be supported by gases, liquids, solids and plasmas. Transverse waves may only be supported by solid media as the restoring force for the oscillation, the shear force, is not present in liquid media. At any point in space the properties of an acoustic wave can be described by the local pressure deviation, particle velocity and displacement. The harmonic oscillation of these properties allows the description of the wave in terms of the maximum pressure variation (the wave amplitude, A), the frequency of the oscillations (f) and the fraction of the wave cycle that has elapsed relative to the starting conditions (the wave phase, ϕ).

1.3.1 Speed of sound

The speed of wave propagation is determined by the density and pressure of the medium at equilibrium as given by the Newton-Laplace equation:

$$v_p = \sqrt{\frac{K_S}{\rho}} \tag{1.1}$$

where K_S is the compressibility of the medium (the elastic bulk modulus), ρ the density of the medium and v_p indicates the phase velocity of the wave, the speed at which any given phase of the wave appears to travel through space [35]. For an ideal gas the elastic bulk modulus is the gas pressure multiplied by the adiabatic index, γ. In air the attenuation of the sound wave can be considered minimal and the propagation of the wave essentially isentropic. For an isentropic process the speed of sound can be given directly in terms of the gas pressure p:

$$v_p^2 = \left(\frac{\partial p}{\partial \rho}\right)_S . \tag{1.2}$$

The phase velocity can also be described in terms of the frequency, f and wavelength λ, the distance which a wave will travel over a complete cycle:

$$v_p = f\lambda. \tag{1.3}$$

We may also describe the phase velocity in terms of the angular velocity of particle motion, defined simply as the number of complete oscillations of 2π radians per second. The phase velocity and angular velocity are then related through the wavenumber, $k = 2\pi f / v_p$, which represents the change in phase over a given distance: $v_p = 2\pi f / k$.

1.3.2 The wave equation

There is no transportation of mass in the propagation of an acoustic wave and the body forces acting on the medium can be considered negligible. The conservation of mass principle can be expressed in terms of the local density of the medium as:

$$\frac{\partial p}{\partial t} + \rho \nabla \dot{\boldsymbol{x}}(\boldsymbol{r}, t) = 0 \tag{1.4}$$

where $\dot{\boldsymbol{x}}(\boldsymbol{r},t)$ is the particle velocity at position given by the vector $\boldsymbol{r}(r,\theta,\psi)$ in spherical co-ordinates (Figure reffig:sphericalcoordinates) and ∇ is the gradient of the velocity scalar field, also given in spherical co-ordinates as:

$$\nabla\dot{\boldsymbol{x}} = \frac{\partial x}{\partial r}\hat{\boldsymbol{r}} + \frac{1}{r}\frac{\partial x}{\partial \theta}\hat{\boldsymbol{\theta}} + \frac{1}{r\sin\theta}\frac{\partial x}{\partial \Phi}\hat{\boldsymbol{\psi}} \tag{1.5}$$

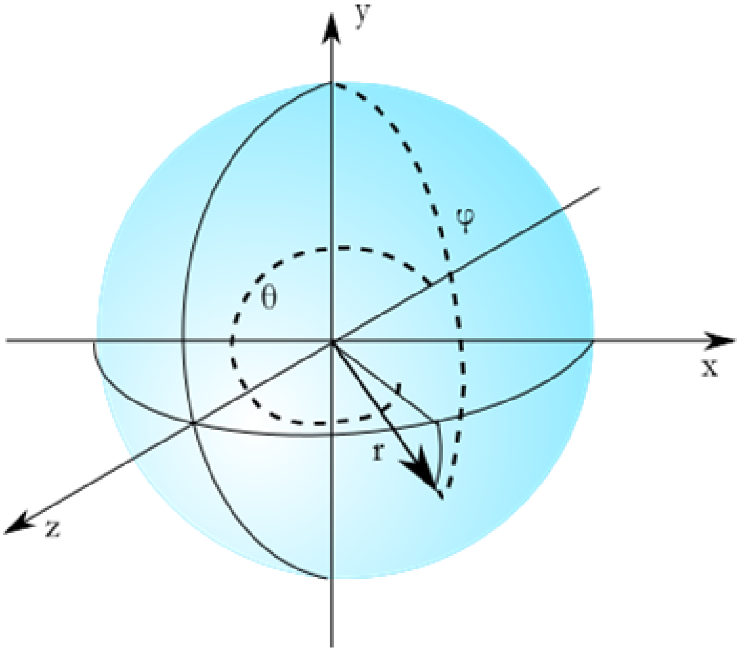

Figure 1.3: Co-ordinate system used throughout this work. Position in spherical co-ordinates given by the azimuth angle θ, the pitch angle ψ and the radius, r.

where $\hat{\boldsymbol{r}}, \hat{\boldsymbol{\theta}}, \hat{\boldsymbol{\psi}}$ are the unit directional vectors for distance, azimuth angle and pitch angle respectively. Combining equations 1.4 and 1.2 eliminates the rate of change of density from the equation:

$$-\frac{\partial p(\boldsymbol{r},t)}{\partial t} = \rho_0 v_p^2 \dot{\boldsymbol{x}}(\boldsymbol{r},t) \tag{1.6}$$

where ρ_0 represents the density of the material at equilibrium. Newton's second law can be expressed in terms of an infinitesimal volume of the medium as:

$$\rho_0 \frac{\partial \dot{\boldsymbol{x}}(\boldsymbol{r},t)}{\partial t} = \nabla p(\boldsymbol{r},t). \tag{1.7}$$

Eliminating the expression for particle velocity by combining equations 1.6 and 1.7

yields the homogeneous acoustic wave equation:

$$\nabla^2 p(\boldsymbol{r},t) - \frac{1}{v_p^2}\frac{\partial^2}{\partial t^2}p(\boldsymbol{r},t) = 0 \tag{1.8}$$

where the Laplace operator, ∇^2, is the divergence of the gradient of the pressure field:

$$\nabla^2 p = \frac{1}{r^2}\frac{\partial}{\partial r}\left(r^2\frac{\partial p}{\partial r}\right) + \frac{1}{r^2\sin\theta}\frac{\partial}{\partial\theta}\left(\sin\theta\frac{\partial p}{\partial\theta}\right) + \frac{1}{r^2\sin^2\theta}\frac{\partial^2 p}{\partial\psi^2}. \tag{1.9}$$

The wave equation can be simplified by writing it in terms of the velocity potential, Φ, defined so that:

$$\dot{\boldsymbol{x}} = \nabla\Phi. \tag{1.10}$$

The wave equation then becomes:

$$(\nabla^2 + k^2)\Phi = 0. \tag{1.11}$$

1.3.3 Sound pressure levels

Sound pressure in air is commonly expressed as the logarithmic ratio of the pressure disturbance to a reference value. The standard reference sound pressure in air is 20 μPa:

$$SPL = 20\log_1 0\frac{p}{p_r ef} \tag{1.12}$$

with the result is expressed in decibels (dB). As inter-aural intensity differences (as described in Section 1.2) are equivalent to a ratio of pressures it is often useful to express them in dB as well:

$$IID = 20\log_1 0\frac{p_i psi}{p_c ontra} \tag{1.13}$$

with $p_i psi$ and $p_c ontra$ indicated the measured pressure at the ipsilateral and contralateral ear respectively.

1.4 Sound sources

The homogeneous wave equation describes the propagation of an acoustic wave in a free field, absent any interaction with boundaries or sound sources. At the most basic level an acoustic source represents the transduction of energy into acoustic energy and its radiation away from the source. The source is typically modelled as a vibrating solid body in contact with the medium. Sound sources are modelled as monopoles, dipoles and quadropoles although all can be considered linear superpositions of multiple monopole sources in the far field (Figure 1.4).

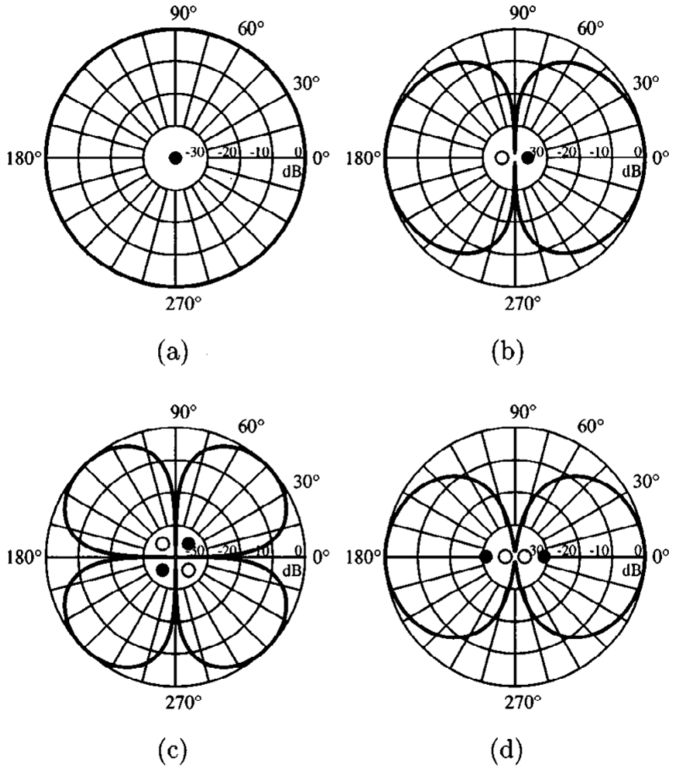

Figure 1.4: Directivity patterns for the far-field sound pressure levels for a monopole (a), dipole (here shown as the superposition of two closely spaced monopoles) (b), and two variations of quadropole (c) and (d) again presented as linear superpositions of monopole sources [36]

1.4.1 Monopole sources

The simplest form of solution to the wave equation is for an acoustic monopole, in which sound is radiated equally in all directions. In terms of the solution to the wave equation we can write:

$$\frac{\partial \Phi}{\partial \theta} = 0; \frac{\partial \Phi}{\partial \psi} = 0 \tag{1.14}$$

indicating that the velocity field changes only with distance from the source. An acoustic monopole can be thought of as a pulsating sphere, exerting a force on the surrounding medium as it expands and contracts. At the interface between the source and the medium the displacement and velocity of the medium must match that of the source. A standard solution to the wave equation would be given solely in terms of the distance from the sphere wall [36]:

$$\Phi(r,t) = \frac{1}{1+\imath k a_0}\frac{Q_m}{4\pi r}e^{\imath(\omega t - k(r-a_0))} \tag{1.15}$$

The radius of the sphere at equilibrium is a_0, $\imath$ is the imaginary operator and Q_m is the source strength; representing the rate of volume of fluid displaced by the sphere. For a pulsating sphere this is simply the product of the surface area and the velocity at the boundary between the sphere and the medium:

$$Q_m = 4\pi a_0^2 v_n^S \tag{1.16}$$

where v_n^S is the normal velocity of the sphere wall. If we make the assumption that the sphere is much smaller than the wavelength of sound produced then $ka_0 << 1$ and $r - a_0 \approxeq r$ simplifying equation 1.15 to:

$$\Phi(r,t) = \frac{a_0^2 v_n^S}{r^2}e^{\imath\omega t - kr}. \tag{1.17}$$

The particle velocity in the sound field is then:

$$\dot{x}(r,t) = \frac{a_0^2 v_n^S}{r^2}(1 - \imath kr)e^{\imath\omega t - kr}. \tag{1.18}$$

The pressure is related to the velocity potential through the Bernoulli equation for steady, irrotational flow:

$$p = -\rho\frac{\partial\Phi}{\partial t} = \frac{\imath\omega\rho a_0 v_N^S}{r}e^{\imath\omega t - kr} \tag{1.19}$$

The velocity field has both a real and imaginary component. The real component describes the near field, which decays with $1/r^2$ and is out of phase with the pressure. The imaginary component is the far field term, which decays as $1/r$ and is in phase with the pressure. As r increases $kr >> 1$ and the equation can be simplified to the far field approximation:

$$\dot{x}(r,t) = \frac{\imath k a_0^2 v_n^S}{r} e^{\imath\omega t - kr}. \tag{1.20}$$

The pressure and velocity are related through the specific acoustic impedance z, defined as:

$$z = \frac{p}{\dot{x}} = v_p \rho \tag{1.21}$$

1.4.2 Dipoles

An acoustic dipole can be thought of as two monopoles of equal source strength separated by a distance smaller than the wavelength of the sound being radiated (i.e. $kd << 1$ where d is the separation between the monopoles). The monopoles vibrate out of phase, with fluid flow in the near field primarily being passed back and forth between the sources. The near acoustic field is not entirely radial, and its expression is beyond the scope of this thesis, however the far field can be expressed as a simple linear combination of two monopole sources using the far field approximation. Taking the origin as the midpoint between two monopole sources and placing the acoustic monopoles $d/2$ on either side we can say:

$$p(r,\theta,t) = -\frac{\imath\omega\rho a_0^2 v_N^S}{r} kd \cos\theta e^{\imath\omega t - kr}. \tag{1.22}$$

1.5 Sound localization

Sound localization requires measurement to be made of at least two points in the sound field. Measurements can be based on either the time delay of arrival (TDOA) or the inter-aural intensity difference (IID). When using the TDOA method only the distance between the listening point and the speed of sound in the medium needs to be known. The arrival time at each listening point can be calculated from a particular point in the phase of the sound wave, the wavefront, in the case of a simple sinusoidal wave or estimated from the cross correlation function in the case of more complex wave patterns. The calculation of sound source angle is analogous to the dipole field estimate of pressure. The distance from each of the microphones

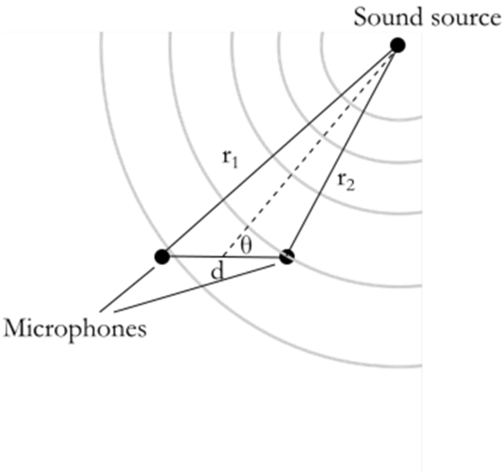

Figure 1.5: Sound source localization by time difference of arrival with two microphones. Sound localization is in a single 2D plane.

to the source is calculated from the law of cosines (Figure 1.5):

$$\sin\theta = \frac{r_1 - r_2}{d} = \frac{\sqrt{r^2 + \frac{d^2}{4} + rd\sin\theta} - \sqrt{r^2 + \frac{d^2}{4} - rd\sin\theta}}{d}. \tag{1.23}$$

If the distance to the source is much larger than the separation between the microphones (far field approximation) the r^2 term dominates and the solution can be approximated to:

$$\sin\theta = \frac{r}{d} = \frac{\Delta t v_p}{d} \tag{1.24}$$

Here Δt is the time difference of arrival between the listening points. This is analogous to considering the wavefronts to be planar at the measurement point. The solutions here are for sound localization in the azimuth only, if the pitch angle is non-zero the solutions exist on a paraboloid curve, with a definitive localization not possible without a second microphone pair (Figure 1.6). The pressure gradient between the listening points may also be used to localize the sound source. The calculation of angle either requires the source strength to be known, in which case the distances r_1 and r_2 can be calculated and the source triangulated, or the expected difference in the path length must be less than a wavelength, allowing the

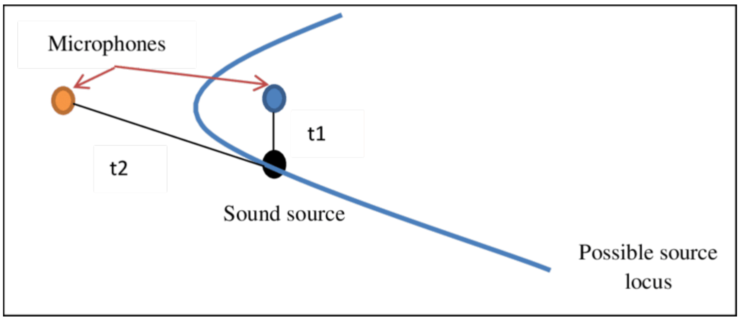

Figure 1.6: Using only a single microphone pair sound localization in two dimensions produces a range of solutions on a paraboloid curve.

pressure difference to be compared to the expected phase difference:

$$\phi_1 - \phi_2 = \frac{2\pi d}{\lambda} \sin\theta \tag{1.25}$$

$$\frac{p_1}{p_2} = \frac{r_2}{r_1} e^{\imath(kr_2 - kr_1)}. \tag{1.26}$$

If the separation between the listening points is small the ratio $r_2/r_1 \approxeq 1$ and the pressure difference will give the phase difference for a known frequency:

$$\imath \sin\theta \approxeq \frac{\lambda}{2\pi d} \ln \frac{p_1}{p_2}. \tag{1.27}$$

The phase difference may also be measured directly from the TDOA of the wavefronts if the separation is sufficiently small, giving the inter-aural phase difference (IPD) and the angle calculated according to equation 1.25.

1.6 MEMS design

The sub-micron tolerances required during fabrication are achieved through either surface micro-machining or bulk micro-machining [37]. In surface micromachining thin films are deposited on the surface of a substrate which are then patterned through the application of photoresists and photolithography. Structures which require to be released from the substrate are achieved through the use of sacrificial layers, with the result that the cavity is only as deep as the deposited sacrificial layer, typically a few micrometres. In contrast bulk micromachining uses the substrate as a mechanical part of the device, with patterning still done via photolithography but with the addition of a deep reactive ion etch to release the structure on the surface of the device. Given the reliance of MEMS technology on integrated circuit design most MEMS are silicon based, with surface micromachining typically exploiting the properties of poly-silicon [38] and single crystal silicon used for bulk micromachining. It is the latter process, and specifically MEMSCAP's commercial multi-user Silicon on Insulator (SOI) fabrication service (SOIMUMPS), which is used throughout this thesis.

1.6.1 System overview

In the following sections the individual components of an *Ormia* inspired directional microphone will be introduced. Given the disparate nature of the fields of study a brief system overview is presented here, based on previous *Ormia* inspired designs described in Chapter 3 of this thesis and forming the basis for the work in Chapter 4. In a näive description of the system, the directional microphone consists of two membranes coupled by a bridge with the displacement of each membrane exerting force on the other which will constructively or destructively interfere (Figure 1.7). When the coupling strength is correctly tailored the membrane closest to the sound source will experience constructive interference strengthening its response which the membrane furthest away will suffer destructive interference.

The tailoring of this system to achieve this result will be the subject of the majority of this work, however at this time it suffices to say that the stiffness of this coupling bridge is the key variable which must be matched to the precise damping conditions experienced by the membranes. The relative motion of the membranes must then be assessed by an appropriate transduction method which can then be used to obtain an azimuthal angular heading to the sound source. Considerations in estimating and modelling the stiffness of the bridge in the chosen medium (single crystal silicon) are discussed in sections 1.6.2 and existing techniques and requirements of microphones in that medium discussed in section 1.7. Estimation and modelling of damping is then discussed in section 1.8 and finally transduction methods and strategies are discussed in section 1.9. The two principle strategies that are relevant to this work are piezoelectric sensing, in which a thin Aluminium Nitride film is deposited on the cantilever requiring the modelling of a composite beam with the piezo-active layer considerably displaced from the neutral axis and a capacitive comb measurement scheme in which the a interdigitated combs are places

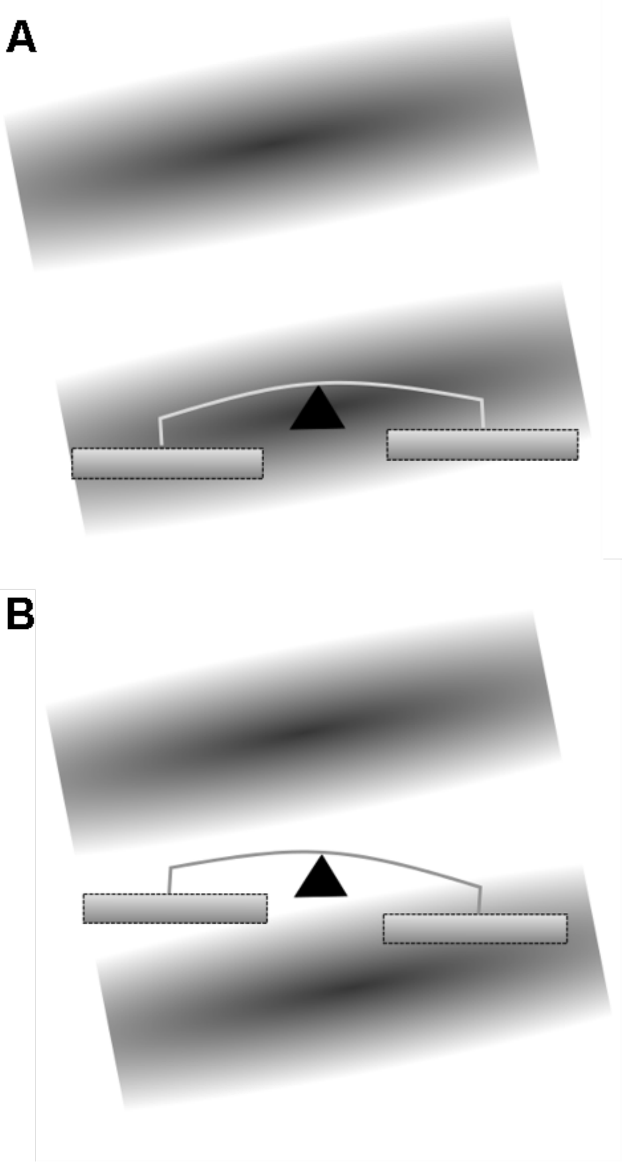

Figure 1.7: The Ormia ear mechanism. The ear's two membranes are connected by an intertympanal bridge. The bridge motion has two natural modes of vibration: 1) A rocking mode about the bridge center point (triangle); 2) A translational mode with both membranes moving in-phase while the bridge bends at the center. A sound wave, depicted by shading causes the system to move, with the difference in pressure between the membranes stimulating the rocking mode and the sum of the pressure on the membranes stimulating the translational mode. (A) At one quarter cycle the force from the total pressure is at a maximum while there is no pressure gradient between the membranes, reinforcing the movement of the ipsilateral membrane while repressing the movement of the contralateral membrane. (B) The forces from the pressure gradient and total pressure on the membrane are 90 degrees out of phase. At three-quarters cycle the pressure gradient is at a maximum while the total pressure is reduced to zero by the angle of the membrane to the sound wave origin.

at the membrane edges and the rate of change of capacitance with the motion of the membrane used to measure displacement.

1.6.2 SOIMUMPS fabrication process

The process consists of a SOI wafer with a fixed 400μm handle wafer, a 1μm buried oxide layer and either a 10μm or 25μm single crystal silicon device layer [39]. A single photolithography step is applied to the device layer and to the substrate, which is then etched with deep reactive ion etching. The buried oxide is then removed by a vapour hydrogen fluoride (HF) process. This step, as well as releasing structures which lie over areas where the handle wafer has been etched (the trench layer), also undercuts structures on the SOI layer by between 1.5μm and 1.8μm allowing for sufficiently thin structures to be undercut without etching the substrate. Single crystal silicon is anisotropic, meaning that the material properties will depend on the orientation with respect to the crystallographic axes. The Young's modulus varies from 130 GPa to 188 GPa between the $< 100 >$ and $< 111 >$ axes [40]. In the MEMSCAP process the x and y axis of the lithography step are both along the $< 110 >$ crystallographic axis with the device face being the plane of the $< 001 >$ axis [41]. Care must therefore be taken when performing finite element analysis to ensure that the orientation of the model's axes coincide with the crystallographic axes (Figure 1.8). A second, well known issue with the SOI layer is the through-thickness stress gradient which results from the deposition and doping stages in fabrication, specifically the use of phosphorous to increase the conductivity of the device layer which is not uniform. The stress gradient will cause patterned areas in the device layer to deform when released, removing the stress and resulting in an out of plane curvature [41]. With the assumption that the stress is distributed linearly though the layer thickness the average stress in the mid-plane of a released cantilever can be calculated from the surface curvature:

$$\bar{\sigma} = -\frac{E\kappa t_b}{2} \tag{1.28}$$

$$\kappa = \frac{2\Delta z}{\Delta z^2 + l_b^2} \tag{1.29}$$

where E is the Young's modulus, κ is the curvature, t_b is the beam thickness, l_b is the beam length and Δz is the deflection at the tip. The stress gradient can be calculated in terms of the moment:

$$M_\tau = \Delta\sigma I \tag{1.30}$$

where I is the second moment of area of the beam. Thus using the relationship for the curvature of a cantilever $\kappa = M/EI$ we can express the stress gradient as:

$$\bar{\sigma} = E\kappa \tag{1.31}$$

The value used in this report for the stress gradient in 10μm thick device layers was taken as $2.4MPa/\mu m$ [42].

The SOIMUMPS process then begins with the doped n-type silicon on insulator wafers. The silicon is patterned lithographically with the device layer mask and the unwanted material removed with a deep reactive ion etching (DRIE) step. The 400 μm handle wafer is then patterned with the silicon device layer covered

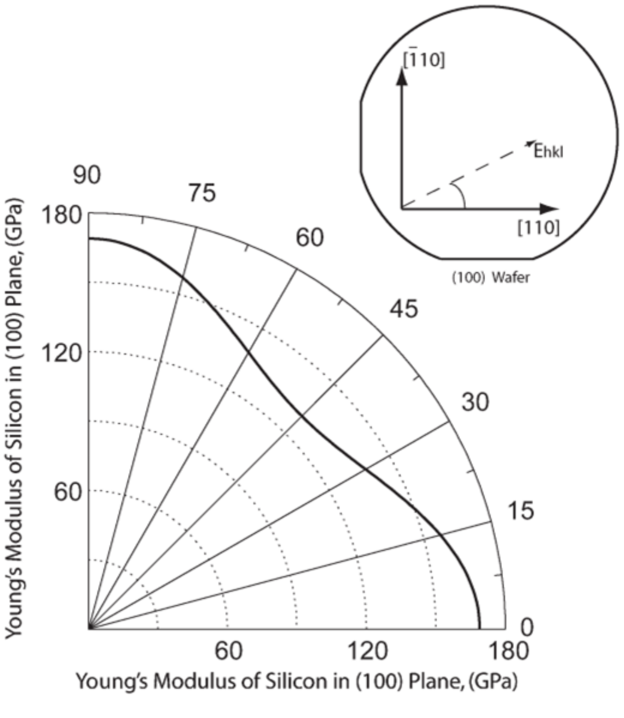

Figure 1.8: Value of Young's Modulus and Poisson's ratio against orientation in single crystal silicon. Values are for the $< 100 >$ plane [40].

by a protective mask, giving the trench layer step [39]. The thin oxide layer is then removed in the areas etched in the trench layer using a vapour hydrogen fluoride, releasing the structures on the device layer that are located over holes in the trench layer. Finally a pad metal layer consisting of 500 nm of gold on top of 20 nm of chrome is deposited and patterned using a shadow masking technique, wherein a stand-off mask is temporarily bonded to the front side of the device and the unwanted metal layer evaporated with an electron beam (These process steps are shown in Figure 1.9). In addition to the stress gradient caused by the doping process in the silicon there is an additional stress gradient created by the deposition of the metal layer (Figure 1.10) [43]. In the SOIMUMPS designs described above this situation does not arise, however in later iterations when the use of piezoelectric material is integrated into the design the stress gradient through the material becomes an important consideration for managing the electrical connections on the device. Later device iterations take advantage of a novel process which became available from MEMSCAP in 2013, the PIEZOMUMPS process. Functionally the stages and materials in the PIEZOMUMPs process are identical to SOIMUMPs, but with the addition of a piezo-active 500 nm thick Aluminium Nitride (AlN) layer and a further oxide layer which can be placed underneath the AlN layer to maintain electrical isolation from the SOI device layer. In the PIEZOMUMPS process the 2000 Angstrom thick oxide layer, the 500 nm Aluminium Nitride layer and the Gold/Chrome metal layer are grown and patterned before the patterning of the silicon device layer and trench layer, which otherwise proceed as with the SOIMUMPS process. The Aluminium Nitride is a polar compound with a piezoelectric strain coefficient, d_33, of between 3.4-6.5 pC/N [44].

In all processes the final product is diced using a laser, with the delivered chips consisting of a 9 mm x 9 mm device area surrounded by a 2 mm handle region (which may not be patterned). In the second and third run of devices, these were further sub-diced into four 4.5 mm x 4.5 mm chips with a single device on each chip to maximise the use of available space.

1.7 MEMS microphones

The micrometre range tolerances available in MEMS devices, as well as the potentially lower costs available from batch manufacturing of chips and the potential integration with signal processing systems, make MEMS microphones a particularly

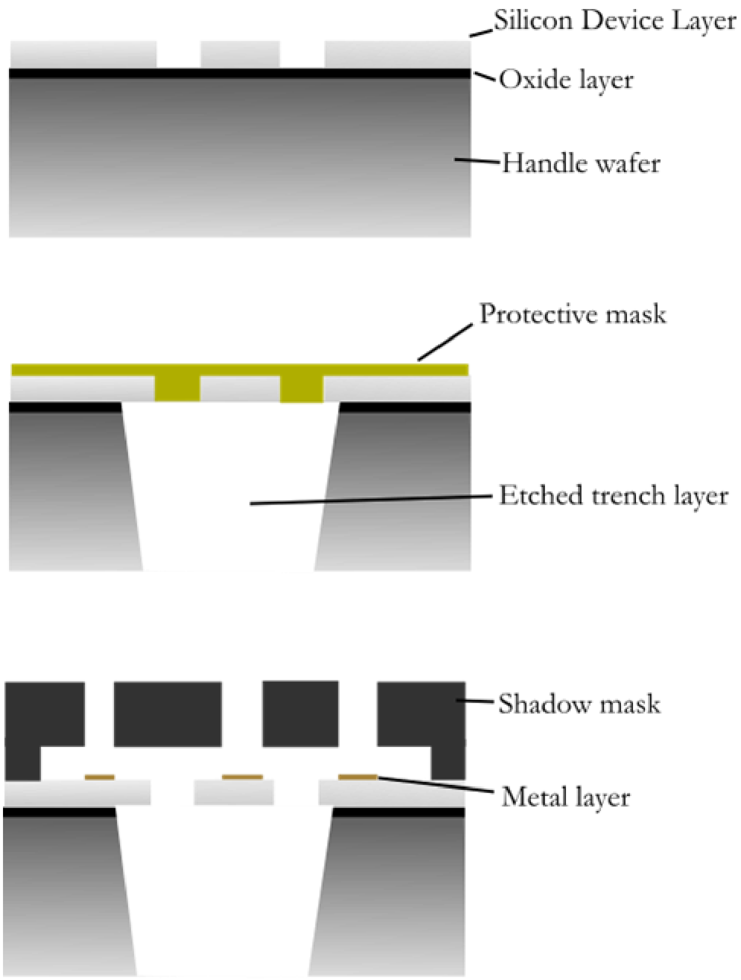

Figure 1.9: (Top) The lithographic patterning step consists of coating the device layer with a UV-sensitive photoresist and then developing it. The unwanted material is removed with a deep reactive ion etch (DRIE). (Middle) The device layer is coated with a protective mask and the wafer etched with a similar lithographic process, this time in two stages with a reactive ion etch and a deep reactive ion etch. Any remaining oxide is then removed with vapour Hydrogen Fluoride. (Bottom) The metal conductive layers are deposited using a shadow mask which is temporarily bonded to the device layer. After the process is completed the shadow mask is removed.

interesting application. One common method for MEMS microphone manufacture involves the bonding together of two MEMS wafers, with the top wafer etched from the back side to the silicon device layer to produce a flexible diaphragm and the bottom wafer etched to produce a small, submillimetre deep cavity where the de-

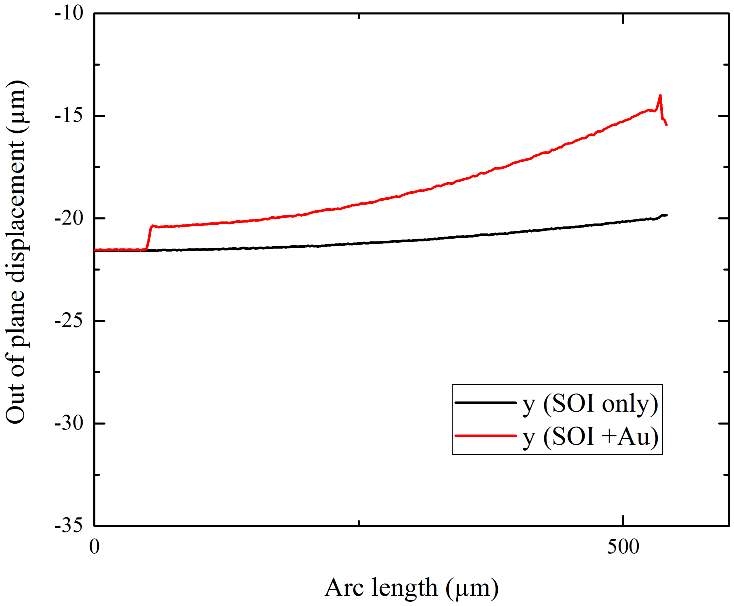

Figure 1.10: Optical profiles of two cantilevers, both 50μm wide and one with 30 μm wide deposition of gold/chrome. The deposition of the metal layer adds a significant stress gradient to the material, causing it to curve further out of plane than the SOI alone.

vice layer acts as the capacitive back-plate for the microphone [45] (Figure 1.11). Microphones can be designed using a surface micromachining process, however the gap between the diaphragm plate and the back-plate is then limited by the thickness of the sacrificial layers (typically 1-2 μm) with the result that the microphone performance is inhibited by extremely high thin film damping (See section 1.8.4).

1.7.1 General operation of condenser microphones

Condenser microphones consist of a closed cavity with one boundary being formed of a flexible membrane and the opposite boundary a fixed back-plate which is used to measure the change in capacitance as the membrane deflects (Figure 1.12) [47]. The microphone is designed so that the membrane resonance frequency is considerably higher than the operating range of the microphone, giving a frequency response far below this range which can be considered flat. In order to achieve a linear relationship between membrane displacement and the change in capacitance, a high bias voltage and a relatively large air-cavity is used, necessary since with the high bias voltage between the membrane and back-plate a significant 'pull-in' force is generated which may cause the diaphragm to collapse onto the back-plate if the membrane deformation is sufficiently large. If we can assume a constant charge on the back-plate (typically achieved by placing a bias voltage across a large resistance, however in electret style microphones the change is embedded in a polymer attached to the back-plate) then the standard relations between charge and capacitance hold:

$$Q = CV \tag{1.32}$$

$$C = \frac{\epsilon s_p}{g} \tag{1.33}$$

$$\Delta V = \frac{Q}{\Delta C} = \frac{Q \Delta z}{\epsilon s_p} \tag{1.34}$$

Where s_p is the area of the back-plate, ϵ is the absolute permittivity of the medium in the gap (typically air in which case $\epsilon \approxeq \epsilon_0$, the vacuum permittivity) and g is the gap between the membrane and the back-plate. The back-plate slots are intended to relieve some of the reaction pressure in the air-gap between the membrane and the back-plate, and therefore lessen the effect of thin-film damping on the membrane. In a condenser microphone the thin-film damping is the dominant damping effect [48] , and therefore also the dominant source of mechanical noise via the Johnson-Nyquist relation:

$$N_P = \sqrt{4 k_b T R_f} \tag{1.35}$$

Where N_P is the noise in the pressure measurement, k is the Boltzmann's constant, $1.38 \times 10^{-23} Ws/K$, T is the temperature and R_f is the flow resistance. In MEMS microphones the small length scale makes many other forms of damping important [49].

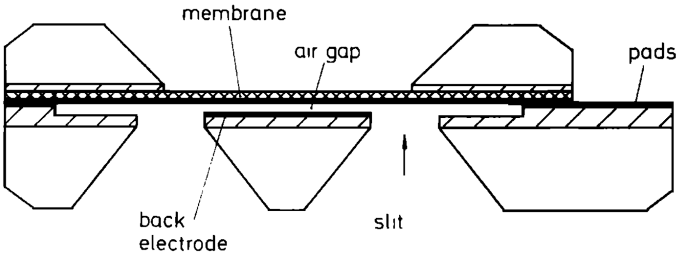

Figure 1.11: Miniature silicon nitride condenser microphone made from the bonding of two wafers. The image is from Hohm and Hess' design in 1989 [46].

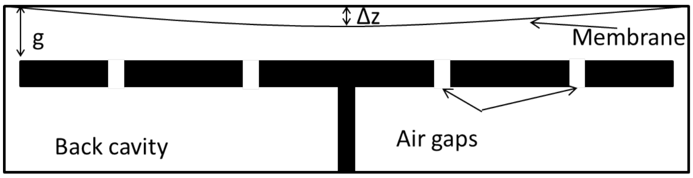

Figure 1.12: Cross section of condenser microphone operation

1.8 Damping

The main sources of damping are expected to be internal (structural) damping, drag force damping on the plate, viscous damping from Couette flow between any capacitive combs and between the plate and surrounding wafer and thin-film damping. As mentioned above, in microphones with a back plate the dominant source will be thin-film damping, however in this thesis we predominantly consider other transduction methods (see Section 1.9). Each of the forms of damping considered below have a frequency dependence, becoming the dominant noise source at some point in the frequency range of operation.

1.8.1 Structural damping

The most frequently considered mechanism in structural damping is thermo-elastic loss, which occurs when heat is transferred between the area of the plate under compression and that under tension. The dissipation of energy from this oscillating heat transfer has been shown to be the dominant form of structural damping in microstructures [50]. Analysis by Zener [51] and Lifshitz and Roukes [52] has been successfully used to model the structural damping in micro-beams, however their usefulness when applied to plates is less certain. Given the complexity in solving the equations for thermo-elastic damping a simplification proposed by Photiadis et al. [53] is used where the damping is assumed to be equivalent to the loss rate associated with the flexural mode. This allows us to approximate the thermo-elastic damping using:

$$\xi_{TE} = \frac{E\alpha_V T}{c_p}\left(\frac{\omega\tau_R}{1+\omega^2\tau_R^2}\right) \tag{1.36}$$

where E is the Young's modulus, α_V is the coefficient of thermal expansion, c_p is the specific heat, T the temperature and τ_R the thermal relaxation time given by:

$$\tau_R = \frac{t_b^2 c_p}{\pi^2 \alpha_V} \tag{1.37}$$

where t_b is the beam thickness and the ratio α_V/c_p is the thermal diffusion constant.

1.8.2 Drag force damping

Fluid mechanical damping of the diaphragm can be described by the incompressible Navier-Stokes equations:

$$\rho\left(\frac{\partial \dot{\boldsymbol{x}}}{\partial t} + (\dot{\boldsymbol{x}} \cdot \nabla)\dot{\boldsymbol{x}}\right) = \nabla \boldsymbol{p} + \upsilon \delta \dot{\boldsymbol{x}} \tag{1.38}$$

$$\nabla \cdot \dot{\boldsymbol{x}} = 0 \tag{1.39}$$

$$\dot{\boldsymbol{x}}^S = \boldsymbol{v}_{\boldsymbol{N}}^{\boldsymbol{S}} \tag{1.40}$$

where $\boldsymbol{p}$ is the pressure field, $\dot{\boldsymbol{x}}$ is the particle velocity field and υ the dynamic viscosity. The superscript 'S' in equation 1.40 indicates the field evaluated on the surface of the structure, and represents the continuity between the fluid and the structure itself. Drag damping is obtained by integrating the Navier-Stokes equations over pressure [54]:

$$\boldsymbol{F_d} = \frac{\boldsymbol{v_N}}{|\boldsymbol{v_N}} c_d \rho |\boldsymbol{v_n}^2| \left(\frac{s_d}{2}\right) \tag{1.41}$$

where s_d is the base area of the diaphragm and c_d is the drag coefficient which can be determined empirically. For a flat plate this value is approximated as 1.17. As the drag force is proportional to the velocity squared the damping coefficient will be proportional to the velocity:

$$\xi_d = \frac{c_d \rho |\boldsymbol{v_n}| s_d}{4 \omega m} \tag{1.42}$$

where m is the mass of the membrane.

1.8.3 Couette flow and viscous damping

Fluid mechanical interaction with the comb structure has been shown to be the dominant source of damping for micro mirrors [55]. Micro mirrors rely on banks of inter-digitated comb fingers to actuate the mirror membrane through electrostatic force, a method of actuation which will be investigated as a method of transduction in section 1.9. Here we are condsidering the general case of fluid flow around the boundaries of the moving body and the effect of shear damping on the motion of the body when the size of the air gap is small relative to the scale of displacement of the moving object. The problem is similar to pipe folow, however the nature of the fluid flow through the combs and around the membrane itself changes depending on whether the combs are engaged or disengaged and if the membrane is in plane with the surrounding substrate or not, however the amplitudes in the devices under test are unlikely to exceed the plate thickness so only the engaged state is considered here. In this regime the flow through the combs can be considered as Couette flow, which has a linear velocity profile between the rotor and the stator combs. Here the damping is given by [56]:

$$F_c = \frac{\upsilon_e s_b}{g} \tag{1.43}$$

where s_b is the surface area of the comb sides or membrane sides and g is the size of the air channel between combs or between membrane and substrate. The effective dynamic viscosity, υ_e is given as a function of the Knudsen number:

$$\upsilon_e = 0.1474\frac{\upsilon}{0.1474 + \frac{Kn(Kn+2.507)}{Kn+3.095}} \tag{1.44}$$

In this thesis, drag force damping and viscous damping are estimated in finite element modelling by integrating the viscous stresses over the surface area of the diaphragm (and combs) (See Chapter 4).

1.8.4 Thin-film damping

For the majority of the designs the thin film damping should be insignificant as the air cavity behind the device is 400 microns deep. The most approachable way to model thin film damping is to consider the membrane as a simple beam and then the coefficient of damping force for a thin beam is given as:

$$\xi_{TF} = \frac{\upsilon l_b w_b^3}{2g^3 m\omega} \tag{1.45}$$

where xi_{TF} is the damping coefficient of thin film damping, l_b and w_b are the width of the beam or membrane and g is the size of the air gap between membrane and back plate. m and $omega$ are the mass and angular frequency of the resonant membrane. This straightforward approach may not yield accurate results as it assumes that the fluid at the boundary of the beam is at ambient pressure, however in a more practical device the flow escaping from around the plate might contribute to the damping force. This is modelled by Bao et al. [48] as a change to the effective width of the beam, which for a comb drive with a small gap between the plates might be more practically modelled as a solid plate.

1.8.5 Resonant frequency shift

This note concerns a caution that must be applied to designing micro-scale systems at a specific resonance frequency: as will be described in Chapter 4 in the devices designed resonance frequency and damping must be closely matched. At these small length scales the change in the resonance frequency due to the effective mass of the membrane must be taken into consideration. This accounts for the change in momentum imparted to the fluid surrounding the device when it vibrates. An analytical expression for the change in resonance frequency of vibrating plates in water was developed by Lindholm [57] and adjusted for gas by Sandberg et al. [58].

$$f_{n,gas} = f_{n,vac}\left(1 + \frac{\pi M_g p w_b}{4R_f T \rho t_b}\right)^{-1/2} \tag{1.46}$$

Here M_g is the molar mass of the gas (28.967 g/mol for air), p is the air pressure and its density ρ, width w_b and thickness t_b are the properties of the cantilever. For the 2 mm x 1mm diaphragms described in this report at room temperature (293Â° K) the resonant frequency shift should be approximately 98% of the resonance frequency calculated from Euler-Bernoulli beam theory or from simple solid mechanics only finite element simulations.

1.9 Transduction methods

One of the most serious limiting factors in designing an *Ormia* inspired MEMS microphone is the small displacement of the diaphragms, typically of the order of 10's of nanometres. From Yu [59] the directional sensitivity of the *Ormia* ear is approximately 0.4dB per degree change in incident sound angle at 5kHz and 1 degree phase difference per degree change in incident sound angle both of which require displacement measurements to be made in the sub-Angstrom range (see Chapter 3). Established capacitive, piezo-resistive and piezoelectric techniques have minimum resolutions about the order of 1nm [60] which are likely to limit the minimum resolvable sound source angle. Optical techniques, using diffraction gratings [61, 62, 63, 64] and Fabry-Pérot [65, 66] interferometers promise much finer resolution but require expensive laser equipment and multiple device layers. The most promising available transduction methods for a see-saw device on silicon on insulator technology are comb finger capacitive or aluminium nitride piezoelectric sensing.

1.9.1 Comb finger capacitors

The use of inter-digitated comb fingers for electrostatic actuation and control and for optical transduction have been a common feature for *O. ochracea* inspired microphone design, however using these combs as a capacitive sensor was usually a secondary feature [63, 61]. Cui, Miles and Homentcovsci [67] present a device in which capacitive comb sensing is the primary transduction method. Displacement is measured by change in capacitance as the membranes displace out of the plane of the device (Figure 1.13). If the capacitive combs are modelled as a series of simple parallel plate capacitors then the change in capacitance is given by:

$$\frac{dC}{dz} = \frac{d}{dz}\left(\frac{2n\epsilon s_c}{g}\right) \tag{1.47}$$

where n is the number of capacitance comb unit cells (the unit cell is shown in Figure 1.14), ϵ is the absolute permittivity of air, g is the gap between comb fingers and s_c is the overlapping surface area of the sidewalls of the comb finger. The change in capacitance would therefore be modelled as the rate of change of surface area with displacement (The electric fields for engaged and disengaged combs are shown in Figure 1.15).

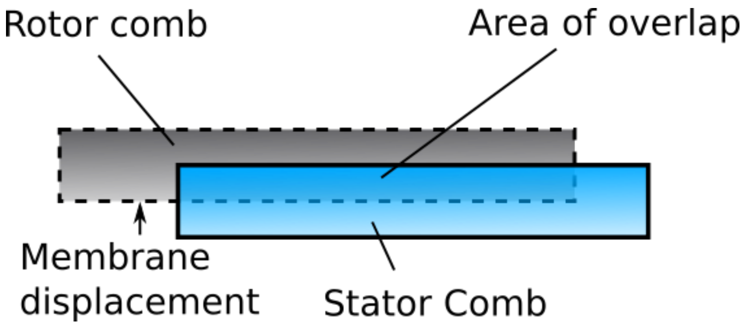

Figure 1.13: Overview schematic of comb sense system. A set of combs attached to the membrane displaces with the membrane (the rotor set) causing a change in overlapping surface area with the interdigitated stator set attached to the substrate and a corresponding change in capacitance.

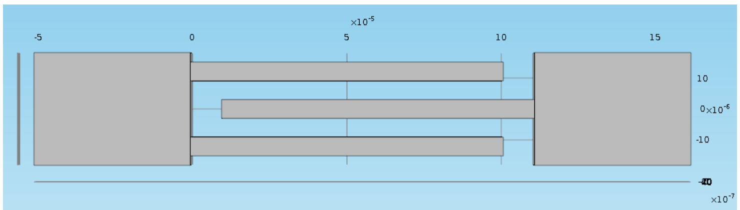

Figure 1.14: Unit cell of capacitive comb displacement transducer

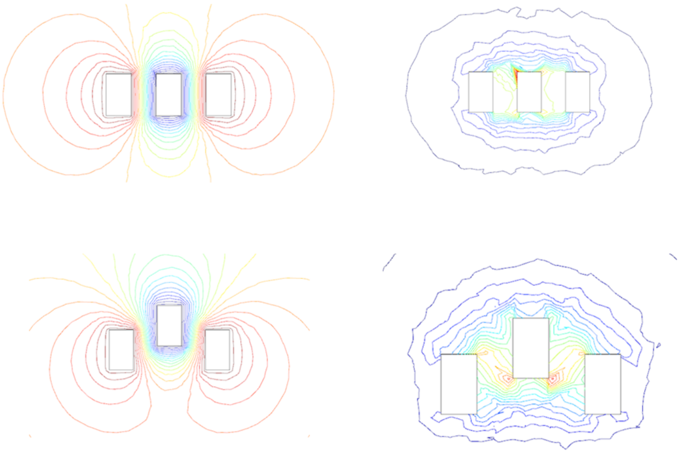

Figure 1.15: COMSOL models of Electric potential (left) and electric field normals (right) for unit cell of comb fingers fully engaged and displaced by 6μm.

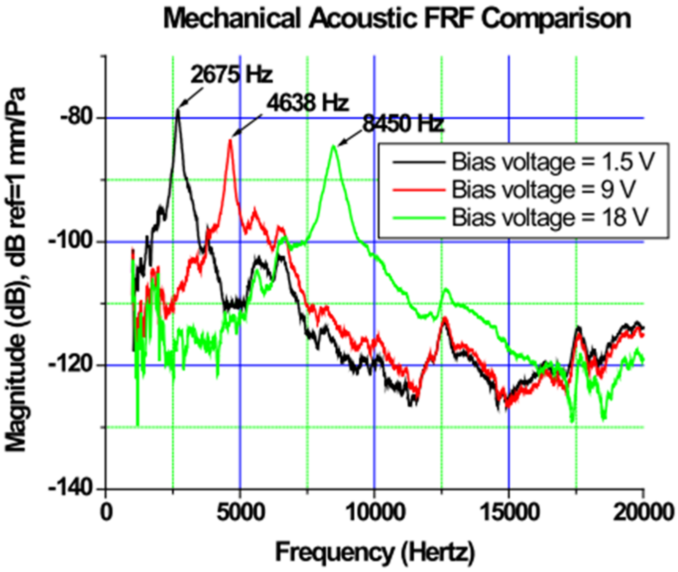

Figure 1.16: Change in resonance frequency with comb bias voltage [67].

This simple treatment is unlikely to give a useful prediction of sensitivity as it neglects the fringe fields of the comb fingers and the motion of the combs is unlikely to be piston-like as it will be driven by the curvature of the diaphragm. In addition there will be a curvature of the diaphragm at rest due to curling caused by the stress gradient at manufacture. Applying a DC bias to each of the static comb fingers produces a positive, linear spring for small deflections - effectively increasing the stiffness of the system and increasing the resonant frequency (Figure 1.16). A clear problem with comb sense capacitance is the ambiguity between membrane displacement above and below the stator arms. Clearly the maximum capacitance occurs when the membrane is at neutral position with the capacitance decreasing equally with motion to either side. An ideal solution would be for the membrane's neutral position to be displaced to one side, allowing a linear and unambiguous reading of displacement.

1.9.2 Piezoelectric transduction

The use of piezoelectric materials in MEMS is restricted by access to deposition techniques which produce consistent results. The most common piezoelectric used in macroscale transducers, lead zirconate titanate (PZT), poses considerable challenges in processing and, although some of those problems have now been solved

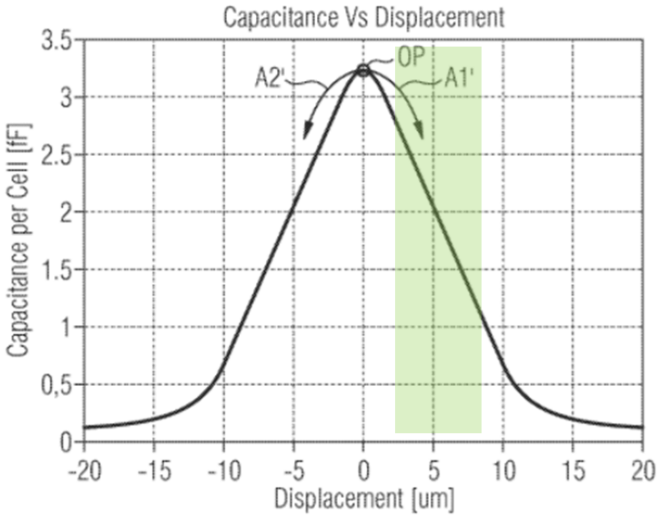

Figure 1.17: Capacitance is at maximum when displacement is zero in the comb sense transduction scheme and the reading is equivalent for displacements above and below. An ideal solution would be for the range of motion to be constrained on one side of the maximum (green shaded area) where there is a linear relationship between capacitance and displacement with no ambiguity for up/down displacement [68].

[69], access to the technology is still limited. Aluminium Nitride piezoelectric deposited by physical vapour deposition techniques have seen considerable activity in recent years, notably in ultrasonic transducers [70, 71, 72], microphones [73, 74] and strain sensors [49]. Aluminium Nitride deposition also has the advantage that it is easily commercially available through MEMSCAP's PIEZOMUMPs service, which is similar to the SOIMUMPs process save for the inclusion of the Aluminium Nitride piezoelectric layer and the loss of a secondary mask metal layer [75]. The principle figures of merit for piezoelectric sensors are the piezoelectric voltage constant $\boldsymbol{g_P z = E_v/\sigma}$, where E_v is the induced electric field and σ the applied stress and $g_P z$ the piezoelectric coupling factor:

$$g_P z = \sqrt{\frac{StoredEnergy}{InputEnergy}}. \tag{1.48}$$

Using the PIEZOMUMPs process allows us to place a thin film of aluminium nitride on the surface of a single crystal silicon device layer with electrodes at the top and bottom surface. The polarization of the AlN layer is normal to the large surfaces at top and bottom and the position of the electrodes allows an electric field to be generated in parallel or anti-parallel to the polarization direction. The tensor form of the piezoelectric equations are given in terms of the strain vector ($\boldsymbol{e}$), the compliance matrix ($\boldsymbol{S}$), the piezoelectric coupling coefficient matrix ($\boldsymbol{d}$), the electric field vector ($\boldsymbol{E_v}$), the electric displacement vector ($\boldsymbol{D}$) and the electric permittivity matrix ($\boldsymbol{\eta_{Pz}}$) [76]:

$$\boldsymbol{e} = \boldsymbol{S\sigma} + \boldsymbol{d^T E_v} \tag{1.49}$$

$$\boldsymbol{D} = \boldsymbol{d\sigma} + \boldsymbol{\eta_{Pz} E_v} \tag{1.50}$$

Assuming the electric field is negligible parallel to the direction of polarization ($E_1 = E_2 = 0$) and the majority of the stress field is in the direction perpendicular to the electric field ($\sigma_1 1$) we can reduce this to:

$$e_1 = S_{11}\boldsymbol{\sigma_1} - d_{31}\boldsymbol{E_{v3}} \tag{1.51}$$

$$-\boldsymbol{D_3} = d_{31}\boldsymbol{\sigma_1} - \eta_{33}\boldsymbol{E_{v3}} \tag{1.52}$$

The combination of the piezoelectric on the silicon forms a bimorph with the silicon element resisting the deformation of the piezoelectric. If the beams are narrow we may assume that the radius of curvature is the same for both beams[77]:

$$e_1 = \frac{z_N - z}{\kappa} \tag{1.53}$$

Where z_N is the neutral axis and κ is the radius of curvature. The stress, assuming constant temperature, is then:

$$\boldsymbol{\sigma_1} = \frac{1}{S_{11}}(\boldsymbol{e_1} - d_{31}\boldsymbol{E_{v3}}). \tag{1.54}$$

For a given cross sectional area A the force is therefore:

$$\boldsymbol{F_1} = \int_A \frac{1}{S_{11}}\left(\frac{z_N - z}{\kappa} - d_{31}\boldsymbol{E_{v3}}\right) dA \tag{1.55}$$

$$\boldsymbol{F_1} = \frac{z_N A - zA}{\kappa S_{11}} + \frac{zAd_{31}\boldsymbol{E_{v3}}}{S_{11}}. \tag{1.56}$$

The moment must be balanced by the internal stresses:

$$M_\tau = \frac{I + Az^2 - z_n z A}{\kappa S_{11}} + \frac{zAd_{31}\boldsymbol{E_{v3}}}{S_{11}} \tag{1.57}$$

The force on the silicon foundation of the bimorph would be:

$$F_{1,si} = \sigma_{1,si} A = \frac{Ae_{1,si}}{S_{11,si}} \tag{1.58}$$

$$M_{\tau,si} = z\sigma_{1,si} A = \frac{ze_1 A}{S_{11,si}} \tag{1.59}$$

which allows the description of the radius of curvature in terms of unit torque:

$$\kappa = \frac{I_{si} + A_{si}(z_N - z)^2}{S_{11,si}} + \frac{I_{pz} + A_{pz}(z_{pz} - z_N)^2}{S_{11,pz}}. \tag{1.60}$$

This can be used to describe the electric field between the terminals of the piezoelectric:

$$\boldsymbol{E_{v3}} = \frac{D_3 - \frac{d_{31}(z_N - z)M}{S_{11}\kappa}}{\eta_{pz,33}} \tag{1.61}$$

which simplifies upon the assumption that both terminals are grounded to provide an expression for the charge:

$$Dt_b = \frac{d_{31}E_v M_\tau}{\kappa} \int_{z-t_b/2}^{z+t_b/2} z_N - z dz. \tag{1.62}$$

Given that:

$$Q = Dw_b l_b \tag{1.63}$$

the charge on the plate is therefore:

$$Q = \frac{d_3 1 M_\tau}{\kappa}(z_N - z)s_p. \tag{1.64}$$

1.10 Directional microphones

A completely closed back cavity in a microphone will produce an omnidirectional sensitivity, however most commercial microphones require a pressure outlet that allows for changes in barometric pressure. As air pressure at sea level is several orders of magnitude larger than the amplitude of an acoustic signal a relatively small change in atmospheric pressure can result in the collapse or destruction of the membrane if the pressure on both sides of the membrane cannot be stabilized. Introducing this pressure vent creates a second acoustic path to the underside of the membrane with an accordant phase difference dependent on the travel path which creates a directional response in the microphone as well as lowering its sensitivity. This can be compensated for by designing a long, thin vent which acts as a low pass passive acoustic filter, limiting the sensitivity losses to the sub-kilohertz range. In many applications it may be desirable to increase the directional response, and so a second path to the microphone is deliberately designed to induce a pressure difference between the front and back of the membrane. At the length scale of MEMS microphones, however, the path difference is likely to be extremely small compared to the wavelengths of the frequency range of interest, resulting in a small phase difference and little directional response. An alternative approach to directionality is to use arrays of closely spaced omnidirectional microphones, using the pressure differentials in the acoustic field (as described in section 1.3). The accuracy with which this array of microphones will approach the true acoustic field depends on the number of microphones (the order of the array) and the spacing between them. For the purposes of simplification, if we assume a linear array of microphones the only parameter of interest is the pressure field along a single dimension along the top surface of the membranes. We can then write the time varying acoustic pressure field as:

$$p(r,\theta) = Ae^{\imath(\omega t - kr\cos\theta_w)} \tag{1.65}$$

Where k is the wave number, r is the distance from the origin, A is the pressure amplitude and θ_w represents the incident angle of the incoming sound wave (or more generally the angle between the wave vector and the position vector). We can separate and ignore the time dependence to calculate only the spatial properties of the wave along a line, then the nth derivative along the position vector is:

$$\frac{d^n}{dr^n}p(d,\theta) = A(-\imath k\cos\theta)^n e^{\imath kd\cos\theta} \tag{1.66}$$

The nth order differential has directivity with the shape of a cosine to the power of n, and also acts as a high pass filter with a slope of (6n) dB/octave. The directional sensitivity is determined by the spacing between the microphones, which will be proportional to $(k\Delta d)^n$, with Δd being the distance between microphones (73). Clearly in MEMS systems, where the spacing is likely to be small in comparison to the wavelength, the directional sensitivity will be extremely low.

Chapter 2

Methods

Scanning laser vibrometry offers non-contact measurement of the oscillation of a surface. Two Scanning Laser Doppler Vibrometers (LDV) were used during the experiments described in this thesis: a Polytec PSV-300-F scanning laser vibrometer and OFV056 scanning head fitted with a close up attachment and a 3D scanning laser vibrometer (Polytec MSA-100-3D). Both systems measure the velocity of a vibrating surface through the Doppler effect on back-scattered light from the surface being measured [78]. In the simpler 2D scanning LDV a class II helium neon laser beam (wavelength 633 nm) is projected onto the surface to be measured [79]. The beam is split through two beam splitters, giving a reference beam, which is passed through an acousto-optic modulator (Bragg cell) which uses sound waves to frequency shift the light from the reference beam allowing the creation of two heterodynes of the two frequency signals (the reference beam and the reflected beam) [80]. The measurement beam is passed through a second beam-splitter and the reflected light redirected to the photodetector unit (Figure 2.1). At the photodetector the signal received will be a combination of the measurement beam, frequency shifted by the movement of the surface, and the reference beam, frequency shifted by the Bragg cell. The measurement beam's Doppler shift is given by:

$$\Delta f = \frac{2\dot{x}(t)\cos\theta_b}{\lambda} \tag{2.1}$$

where Δf is the change in the beam frequency, λ is the wavelength of the HeNe laser, θ_b is the beam angle, which in a 2D system will be perpendicular to the device under test and $\dot{x}(t)$ is the velocity of the device under test. The result at the photodetector

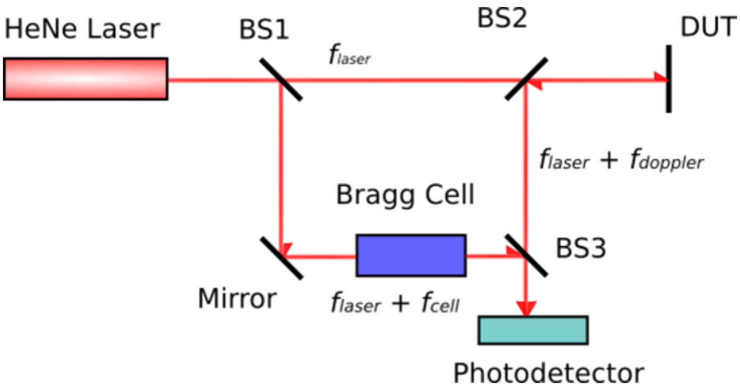

Figure 2.1: Principles of operation of Laser Doppler Vibrometer

is a beat frequency caused by the interference of the two beams, with the Bragg cell shift representing the carrier frequency and the Doppler shift modulating it. The velocity decoder outputs a voltage proportional to the frequency shift due to the Doppler Effect (and therefore the velocity of the object under test). The output voltage has a range of 0-10 V, with the sensitivity, which ranges from 1 mms^{-1}/V to $1ms^{-1}/V$ set via the software allowing the range and resolution to be tailored to the expected movement of the device. The scanning function allows automated sequential measurement of the vibration at a number of predefined points. The spot diameter is between 3 - 5 μm, depending on the focal length of the beam. In the experiments conducted here the sample was placed approximately 5 cm from the close up lens due to the small scanning area of less than 2 mm x 1 mm. The angular precision is less than 0.002 deg which at five centimetres corresponds to an error of not more than 17 μm. Positioning of the laser beam is performed manually by observing the spot on a video feed of the object under test. In the 3D laser vibrometer there are three linearly independent interferometer paths. Backscatter from the laser on the measurement point is received by three interferometers: the on-axis interferometer which is co-located with the laser beam and catches the reflected signal through a beam-splitter, and two off-axis directions. The result is a matrix of velocity readings: an x, y and z velocity for each of the reflected laser signals received at the two orthogonal detection points in the case of the x and y velocities and at the detection point co-located with the stimulating laser in the case of the z velocity (Figure 2.2). The unit vectors for vibration are then

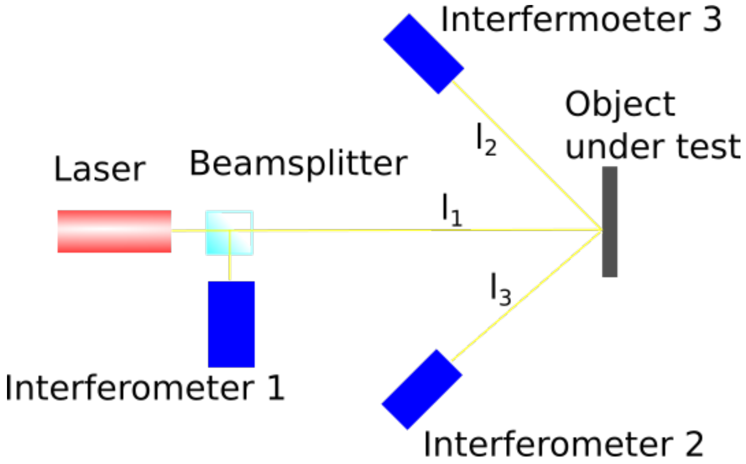

Figure 2.2: Principles of 3D laser vibrometry. The source contains an associated photodetector, which detects the on-axis backscatter from the object under test, while two separate interferometers detect the off-axis backscatter.

calculated using the transformation matrix given in equation 2.2.

$$\begin{Bmatrix} v_x \\ v_y \\ v_z \end{Bmatrix} = \begin{Bmatrix} l_{1x} & l_{1y} & l_{1z} \\ l_{2x} & l_{2y} & l_{2z} \\ l_{3x} & l_{3y} & l_{3z} \end{Bmatrix}^{-1} \cdot \begin{Bmatrix} v_1 \\ v_2 \\ v_3 \end{Bmatrix} \tag{2.2}$$

In order to complete the transformation into the object under test's co-ordinate system the geometry of the system must be known. In the case of the experiments described in this thesis alignment of all three backscattered beams was required to be completed manually, effectively restricting their use to single measurement points or small clusters of measurement points before the alignment process became prohibitively time intensive. Additionally as the system requires a significant amount of the backscattered light to reach the photodiodes in the x and y axes, surfaces which are particularly smooth (as would be expected from the MEMS devices) and therefore reflect most of the energy back towards the stimulating laser are not suitable for 3D vibrometry measurement.

2.0.1 Calculation of power and noise estimates

The output of the laser vibrometer system is a Fourier series, splitting the time domain recorded signal into a sum of vibrations at different frequencies. In order to determine the response to a given stimulus - in this case an acoustic pressure wave - a reference signal is also recorded by the vibrometer. In the experiments detailed here the sound stimulus was measured using a Bruel & Kjaer 4138 1/8" microphone. The frequency response function (FRF) is then generated from the auto power (AP) and cross power (CP) spectrum, themselves calculated from the complex vibrometer velocity measurement spectrum (χ_V) and reference microphone pressure spectrum (χ_R):

$$AP_{VV} = \chi_V^* \chi_V \tag{2.3}$$

$$AP_{RR} = \chi_R^* \chi_R \tag{2.4}$$

$$CP_{VR} = \chi_V^* \chi_R \tag{2.5}$$

where the subscripts 'V' and 'R' represent the vibrometer and the reference measurements, so AP_VV is the auto-power of the vibrometer measurement and CP_VR is the cross power of the reference and vibrometer measurements respectively and χ_R and χ_V represent the complex measured values of the reference and vibrometer with the superscript * denoting the complex conjugate of the measurement. When the signal is not averaged the frequency response function is simply the ratio of the cross power between the reference and vibrometer signal divided by the auto power of the reference:

$$FRF = \frac{CP_{RV}}{AP_{RR}} = \frac{\chi_V}{\chi_R^*} \tag{2.6}$$

however it is more common to use some averaging on the vibrometer signal to exclude some noise. In this case two transfer functions are calculated, termed H1 and H2 by Polytec, which estimate the FRF of the surface under test:

$$H1_{VR} = \frac{C\bar{P_R}V}{A\bar{P}_{RR}} \tag{2.7}$$

$$H2_{VR} = \frac{A\bar{P}_{VV}}{CP_{VR}} \tag{2.8}$$

where the barred CP and AP represent averaged values. The accuracy of these estimates depends on the unknown noise in the reference channel and the vibrometer signal. If the signal to noise ratio of the reference channel is very high, that is if $N_R^2 << AP_{RR}$ where N_R is the noise attributable to the reference microphone then the function H1's relation to the 'true' frequency response function can be approximated as:

$$H1 = FRF\left(1 - \frac{N_R^2}{A\bar{P}_{RR}}\right). \tag{2.9}$$

Similarly if the noise attributable to the vibrometer measurement is very low ($N_V << AP_{VV}$) H2 can be appoximated as:

$$H2 = FRF\left(1 + \frac{N_V^2}{A\bar{P}_{VV}}\right). \tag{2.10}$$

The magnitude squared coherence between the vibrometer signal and the reference signal (COH_{VR}) is defined as:

$$COH_{VR} = \frac{|C\bar{P}_{VR}|^2}{A\bar{P}_{VV}A\bar{P}_{RR}} = \frac{H1}{H2} \tag{2.11}$$

For signals where there is good coherence, and therefore a good signal-to-noise ratio, we can use the approximations for H1 and H2 to give an estimate of the noise power:

$$COH_{VR} = \frac{1 - \frac{N_R^2}{AP_{RR}}}{1 + \frac{N_V^2}{AP_{VV}}}. \tag{2.12}$$

. For the case where $N_R^2 << AP_{RR}$ and $N_V^2 << AP_{VV}$ we can simplify the expression further:

$$COH_{VR} \approx \left(1 + \frac{N_P^2}{A\bar{P}_{VV}}\right)\left(1 + \frac{N_R^2}{A\bar{P}_{RR}}\right). \tag{2.13}$$

For readings with high coherence we can approximate the noise power from both input noise and output (vibrometer) noise. The signal to noise ratio of the reading can be described combined as:

$$SNR = 10\log_{10} 1 - COH_{VR}. \tag{2.14}$$

Alternatively an individual noise power can be calculated as:

$$N_V^2 = \frac{A\bar{P}_{VV}(H1 - COH_{VR}H2)}{H2 - H1}. \tag{2.15}$$

2.1 X-Ray micro computer aided tomography

The X-Ray μCT takes a series of shadow images of an object while rotating in fixed steps over 180deg or 360deg. The shadow images are collected with a high resolution photodetector and are saved as a TIFF file, with the result being a series of standard 2D X-Ray projections of the object under test. A pixel which shows some X-Ray absorption will represent an object whose position in the x and z axes well defined, but with a distance from the source that is unknown. If we think of the potential position of the object as a line perpendicular to the photodetector, then by rotating around the object we can create similar, overlapping lines of X-Ray absorption (fig 2.3). The object location is not triangulated; instead an array of absorption levels is created by superimposing each of the absorption lines. This array of superimposed lines is used to create a reconstructed slice in the plane normal to the z-axis for each row of pixels in the photodetector ultimately generating a 3D array of voxels each with a relative absorption value. These absorption arrays are not yet true images. In reconstruction it is necessary to transform this array into an image with the absorption values in the array being converted into an 8-bit greyscale value. This is done by selecting the minimum and maximum values in the reconstruction software, with the goal of the user being to select a minimum value that gives clear resolution of the object without losing any data and a maximum level that allows sufficient contrast between different materials within the object. The volumetric reconstruction is stored as a series of 8-bit bitmap images of each of these virtual slices.

2.1.1 Sample preparation

The images produced by the μCT are based on the level of attenuation through the sample, which is dependent on the thickness of the material and its absorption coefficient. The absorption coefficient is linearly proportional to the density of the material [81]. When scanning insect bodies there are therefore two major obstacles; the sub-micron thickness of the structures of interest (e.g. the tympanal membranes) and the relatively uniform attenuation coefficient and density of the insect's soft body, which makes contrast between structures within the body difficult. Preparation of the insect can help alleviate some of these problems. Initial scans were performed fresh post mortem; however the results were significantly improved when the samples were dried. Critical point drying was used for the *Galleria*

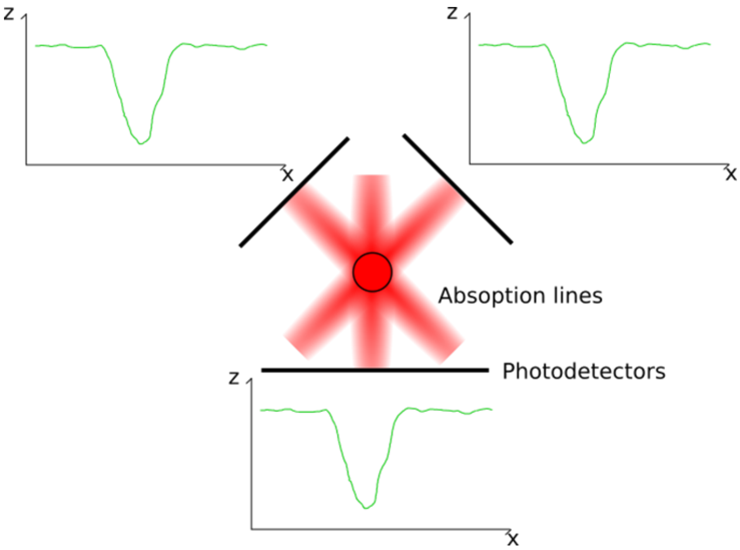

Figure 2.3: Schematic view of three different positions of the source and the corresponding triangulation from the absorption lines.

mellonella, a technique in common use for electron microscopy imaging of insects [82, 83], however access to critical point drying facilities was limited so most drying was accomplished by soaking the insect in 70% ethanol and then air drying for at least eight hours. Higher concentrations of ethanol, for example Ethanol 96, are more effective as drying agents but tend to make the specimens highly inflexible resulting in frequent damage during the scanning process. Insects can also be stained prior to scanning in order to lend greater contrast to the image [84], however trials with Iodine and Tungsten stains found that the muscle fibres and soft body took up the stain far more than the cuticular structures in which the primary interest lay, often producing an image of the insect's flight muscles surrounded by a ghostly exoskeleton.

2.1.2 Considerations for low density contrast

The insect body is highly translucent to X-Rays, with little difference in density or absorption coefficient between the cuticle and the soft body. The X-Ray source is polychromatic (Figure 2.4), meaning that the attenuation of the X-Rays through the object under investigation is not linear, but rather an apparent attenuation as higher energy photons will pass more readily through the material. The effect of this for low density / low attenuation coefficient samples is to skew the mea-

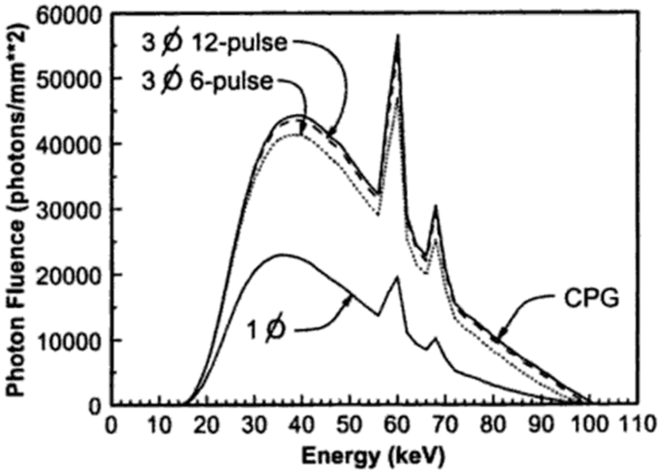

Figure 2.4: X-Ray spectra generated from a 100kV source. The curves illustrate the energy density of photon fluence for 3 phase systems (marked 3Φ) and single phase systems (marked 1Φ), although the shape of the distribution remains similar for both systems, with the majority of photons at the lower end of the energy spectrum ([85]).

sured attenuations downwards as a significant proportion of the X-Ray energy is simply not affected by the material. The inverse effect, where high density, high attenuation coefficient samples are scanned resulting in near total attenuation of the signal is mitigated by 'beam hardening' - placing a metal filter in front of the X-Ray source which stops the majority of the low energy photons, effectively preventing blank areas of the X-Ray image from being saturated by the low energy photons and allowing a tighter range of relative attenuation to be considered. Here of most interest is 'softening' the X-Ray source - disregarding X-Rays at higher energy levels which are unlikely to be attenuated by the soft body of the insect and again tightening the range of attenuations. This is most easily achieved by lowering the energy of the X-Ray source. In most cases a voltage of around 50-60kV with a current between 80-100 μA gives satisfactory results, allowing the cuticle to be penetrated while still giving some distinction in the soft body of the insect. Scans as low as 30kV were attempted which is particularly useful for obtaining clear scans of the exoskeleton when modelling the sound field around the insect (described in Chapter 5), however at these low energies the entire insect body appears opaque giving what is essentially a 3D silhouette of the insect. Given the low density of the object a full 360deg scan is unnecessary, and processing time can be minimised by selecting rotation steps no larger than 0.2deg with minimal averaging (between 2-4). Increasing beyond these values gives little improvement in the quality of the scan while greatly increasing processing time and the size of the data produced.

2.1.3 Post processing

The output from the scanning stage is a series of high resolution .tif X-Ray images which need to be converted into a series of reconstructed transversal sections in order to generate a volumetric image (as discussed in section 2.1). Reconstruction of these slices is governed by four major parameters: misalignment compensation, ring artefact reduction, smoothing and beam hardening compensation. The last of these refers to the range of relative attenuations we will consider. The orientation of the sample may also be adjusted at this stage and a region of interest selected to remove any extraneous material (usually any holder / surrounding tube can be safely removed at this point). As insect scans are more likely to use 'soft', low-energy X-Rays beam hardening corrections are not necessary. Similarly ring artefacts are often a result of high density material, allowing the use of this feature to be minimised as well. Smoothing was also found to be counter-productive and was switched off. Misalignment compensation is estimated by comparing the attenuation the image for a given rotation step along a profile line normal to the z-axis - by default at the centre of the z-axis of the scan. For two adjacent steps, the curves should be closely aligned, with the peaks and valleys of the attenuation profile roughly coincident. Poor correlation between the attenuation profiles results in discontinuities in the reconstructed transversal slices - most noticeable in circular objects where the upper and lower hemispheres of the object do not appear to connect (Figure 2.5). Selecting the relative attenuation range is similarly done by eye, with the user generating a preview single transversal section and selecting the range manually. A histogram of the attenuation is provided alongside the preview reconstructed section which will usually have a single dominant peak. This would be expected to represent no obstruction, the most common array element in most scans, and the lower bound should be placed at the apex of this peak. The upper bound can be selected to encompass the remaining extent of the histogram or can be used to exclude higher attenuations to provide more contrast to an object of interest. In the insect scans this may be used to exclude or reduce the cuticular exoskeleton in order to examine the soft body of the insect in greater detail.

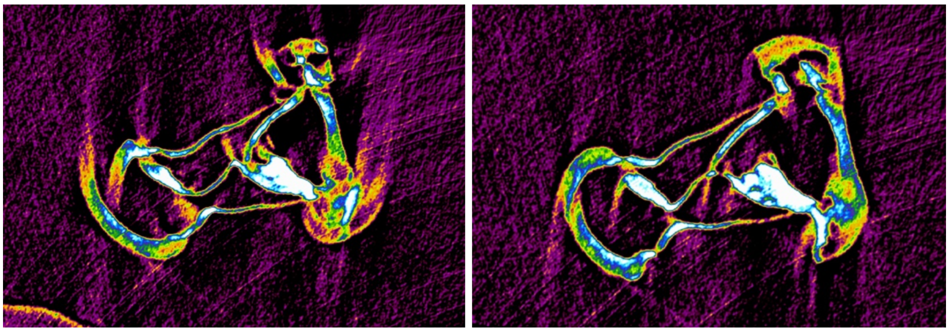

Figure 2.5: Image of an insect tibia with strong misalignment manifesting in disconnected lines between the front and rear of the object scanned (left) and a well aligned reconstruction (right)

2.2 Finite element analysis

The Finite Element Method (FEM) was developed in 1909 as a practical method of deriving approximate solutions to the deformation of solids under stress [86]. Later iterations developed the technique by breaking down the problem domain into triangular regions, applying a series of linear functions to the node points and solving, for a given set of boundary conditions, the unknown coefficients [87]. Although the method was developed for structural dynamics, which remains the base module of many commercial finite element analysis programs today, it can be applied to the solution of other types of general field problems, such as heat conduction, fluid dynamics and electrical and magnetic fields. Finite element analysis starts with the definition of a domain, Ω, with a boundary Γ that describes a closed polygonal curve. The boundary can take one of two forms, depending on the nature of the problem to be solved. It can be a Dirichlet boundary, where the values of the solution are specified giving a fixed boundary condition (e.g. the fixed end of a cantilever, or a no-slip boundary in fluid dynamics). Alternatively it can be a Neumann boundary, where the derivative of the solution is specified: for example the rate of flux across the boundary, or the stress on a beam component. Whichever boundary conditions are chosen, an approximate solution to some unknown scalar valued function defined on the domain Ω is sought such that:

$$-\Delta u + cu = f \tag{2.16}$$

where u is the unknown scalar value, c is a constant and f is a function on Ω, in principle the strong form of the field equation that is to be solved which can be considered the surface density of the forces across Ω. Solving these problems makes use of Green's First Formula:

$$\int_{\Omega} (\Delta u)v + \int_{\Omega} \Delta u \cdot \Delta v = \int_{\Gamma} (\partial_n u)v \tag{2.17}$$

where ∂_n indicates a normal derivative, which when integrated over the boundary Γ which is the boundary condition given on a Neumann boundary. The term v is a test function, used with the intention that the solutions across the domain will be averaged with a weighting specified by v. Combining (2.16) and (2.17), and imposing the Dirichlet or Neumann boundary conditions on the right hand side gives:

$$\int_{\Omega} \Delta u \cdot \Delta v + c\int_{\Omega} uv = \int_{\Omega} fv + \int_{\Gamma} (\partial_n u)v + \int_{\Gamma} gv \tag{2.18}$$

The boundary integral has now been split into two on the right hand side: the Neumann boundary as before and the fixed boundary with the solution g. Solutions are then sought for this equation that fit the boundary conditions, beginning with the assumption that the test function v will be approaching zero. In this sense, the test function is similar to the principle of virtual work or virtual displacement. The finite element method discretizes the domain into series of triangles or quadrilateral elements and solving for u at the nodes of these elements for which there is a Dirichlet boundary condition. The result is a linear system of equations with as many equations as unknowns, with the unknowns being the values of u at the nodes on the non-Dirichlet boundaries [88].

2.2.1 COMSOL Multiphysics

The finite element modelling package used throughout this thesis was COMSOL Multiphysics (version 5.3a, COMSOL, Inc. Burlington, MA, USA), with the overwhelming focus being on Acoustic-Structure interaction models - a template multiphysics model provided by COMSOL which solves the Helmholtz equation in the fluid domain and uses this as a boundary condition on a structural mechanics domain and vice-versa. A full description of the solution of this two way interaction can be found in [89]. In the fluid domain there are then two boundary conditions: one on the outer perimeter of the domain which specifies an incident plane wave and provides a perfectly matched layer for the outgoing spherical wave from the solid domain, and the acoustic structure boundary. On the solid domain there are also two boundary conditions: the aforementioned acoustic-structure boundary and a fixed constraint, representing a connection on the membrane which we wish to consider rigid. Due to the small feature size of the diaphragms the solid domain is treated as a shell domain, a specialized interface in COMSOL designed for the modelling of thin or slender structures. The interface is used to prevent prohibitively large numbers of elements being generated when a mesh is created through the 10μm thickness of the sensor, but by necessity this will eliminate any through-thickness effects in the membrane. In the case of the MEMS simulations the principle losses are the thermal-elastic damping in the structure and the stress-gradient, which have to be applied manually to the domain through the 'intrinsic loss factor' and 'pre-stress and strain' elements in the shell interface. In practise the thermal-elastic loss is found to be negligible compared to the fluid damping and the stress gradient does not impact the mechanical motion of the device, and is easily applied in the simulations of capacitance and piezoelectric effect. The air domain presents some more challenges in setting up. A good simulation will require several elements over the space of one wavelength, which is rarely a problem even at the higher frequencies, but will also require an air domain which is sufficiently large to account for all diffraction effects around the object under investigation. Here a guideline from COMSOL's documentation that the diameter of the air domain should be 10 times the size of the largest feature on the object under investigation was used [90], resulting in a 10 mm radius air domain. Several methods were attempted to provide the correct modelling of the diffraction around the handle wafer: the creation of a baffle between the upper and lower hemispheres of the air domain, removal of the lower hemisphere of the air domain and replacing it with a second air domain with the volume of the back cavity, or simply modelling the handle wafer as a solid body within the air domain. Of these the second was the more computationally efficient, and was frequently used when rapid iterations of the design were desirable, however given the impact of the boundary layers in the trench layer of the MEMS device the accuracy of this method was questionable. Modelling the entire solid domain, combined with shell connections requires not only a third multi-physics element, and additional interactions between the elements of the model, but also greatly complicates the meshing of the model to the extent that more intricate designs required access to the university High Power Computing cluster to complete successfully. Final model designs were most frequently run using a 4.5 mm × 4.5 mm baffle in the centre of the air domain which provided a good representation of the handle wafer's impact without being prohibitively memory intensive. The external boundaries of the air domain were designated radiation boundaries, with an input acoustic wave generated by the 'Spherical wave radiation' module, with the option 'Incoming plane wave'. The orientation of this wave is determined by a vector triad, the values of which were determined by setting two angular variables, 'theta' and 'phi' (Romanised variables in program) as global parameters and using these to set three further variables k1, k2, and k3 which were the directional vector coefficients in the x, y and z axes respectively:

$$k1 = \sin(theta)\cos(phi) \tag{2.19}$$

$$k2 = \sin(theta)\sin(phi) \tag{2.20}$$

$$k3 = cos(theta) \tag{2.21}$$

Finally the solver configurations can be set to sweep the parameters of the simulation. The primary parameter for this simulation type is naturally the frequency; however an additional parametric sweep can be set by specifying the global variable which we wish to change with the two sweeps existing in a nested loop. In most cases this will be the elevation angle 'theta', which is swept over one hemisphere (from $-\pi/2$ to $\pi/2$). The step size of both the frequency sweep and the sound angle can also be varied to change the granularity of the sweep, with the obvious caveat that finer step sizes will increase the solution time significantly.

2.2.2 Meshing considerations

In theory, as the mesh size decreases towards zero the approximation to the solution provided by the FEM solver will become exact, however in practise a compromise is necessary for a more time-efficient solution. The balance between minimizing the error and ensuring the solution compiles in a timely fashion can be parametrically measured by using a mesh refinement analysis, in which the convergence of the desired criteria is measured over a sweep of progressively finer meshes (see, for example, COMSOL's own guidance on meshing in a loudspeaker problem [91]). In the structure described in this thesis, and as discussed in the previous section, the mesh element size should be smaller than the minimum feature size in the model (or more strictly, element vertices should not cross between Dirichlet and non-Dirichlet boundary conditions) which inevitably constrains the range of options to the finest mesh the processor and memory of the computer can handle. COMSOL offers mathematically generated meshes in the form of free tetrahedrons for 3D geometry (and free triangular or free quadrilateral for 2D geometries) with predefined size parameters, only the finest of which (labelled 'Extremely fine' by the software) offers minimum element sizes of 2 μm - a frequent minimum feature size of the models in this thesis. Meshing at this size results in very dense meshes which are often not required outside the immediate vicinity of the sensor device. Customising the meshing parameters allows the reduction of the number of mesh elements while still retaining control of the fine detail regions. COMSOL Multiphysics offers five parameters for meshing control: maximum element size, minimum element size, growth rate, curvature factor and resolution of narrow regions. Increasing the values of the maximum element size and curvature factor from the extremely fine pre-set values allows a significant reduction of elements in the air domain; however care must be taken regarding the element quality. COMSOL will generate meshing statistics which provide details of the minimum element quality and a histogram of element quality across the mesh (Element quality is naturally a relative term, the results provided by COMSOL measure the correlation of the local parametric co-ordinate system associated with the mesh element to the parameters in the domain co-ordinate system). As a guide, a minimum element quality of 0.1 is sought, while reducing as far as possible the number of degrees of freedom of the system. One further technique that may be used is the setting of symmetries. Here the model is split in half, with symmetry planes set in the physics setting (for all physics types) along the cut boundary. While this reduces the number of mesh elements in half, it also restricts the model to solutions where the incoming plane wave is symmetrical about this plane. While this technique would extremely useful for MEMS simulations it was unworkable for the biological simulations.

2.2.3 Post processing

In contrast to the post-processing options in the μCT system, finite element post processing will not significantly alter the data and is primarily important for visualisation and for calculating derived values from the data set; such as local maxima and minima, integrals and point evaluations of displacement. Data sets, when working in the frequency domain, are 3D representations of a frozen moment in the cycle defaulting to COMSOL's own virtual trigger $\phi = 0$ (here ϕ refers to the phase from a frequency domain simulation, as opposed to the romanised 'phi' used in simulation to calculate the wave vector as in equation 2.19). Since the simulations often deal with phase differences between the acoustic and mechanical response this frequently will give a misleading picture of the motion of the device. Of particular interest to the investigations here are the point evaluations of phase and displacement, taken at the outside corners of the MEMS devices, which provide the amplitude of displacement in the z-axis and the phase of displacement in the z-axis. These results are compiled into tables which can be exported to other visualisation software such as Origin Pro or Excel.

2.3 Considerations for live insects

In additions to the testing and characterisation of MEMS microphones, two species of Pyralidae moths were scanned; the lesser wax moth (*Achroia grisella*) and the Greater wax moth (*Galleria mellonella*). The lesser wax moths came from a long established laboratory colony in the Institut de la recherce sur la Biologie d'Insects in Tours, France originally collected in Florida in 2003 and raised on a diet of honey, beeswax, flour, glycerol and brewer's yeast [92] and kept in an environmental chamber maintained at 25Â° Celsius and with a 12h:12h light:dark photoperiod. The Greater wax moths were ordered from Blades biological supplies as waxworms and reared in the laboratory at Strathclyde on a similar diet of beeswax, glycerol, honey and flour. The waxworm larvae were kept in simple Tupperware containers and separated out into individual containers when the pupae formed. As adult *Achroia grisella* and *Galleria mellonella* do not eat during their five day lifespan they required no further food or water. The separation was performed to ensure that only virgin females were used in the behavioural tests, since females that have mated become unresponsive to the male mating call, and to facilitate the sexing of the animals for the laser vibrometry experiments. Sexing of both species of moth was primarily done by size: female *A. grisella* and *G. mellonella* are both notably larger than the males. Additionally smell was also a useful indicator of sex, as the males of both species emit a powerful and distinctive pheromone which is absent in the females. Final confirmation can be performed with the insect under the microscope where the insect's genitalia can be seen on the final segment of the abdomen, with the females' protruding ovipositor being easily recognisable. As the tympana are located on the first segment of the abdomen and are almost entirely hidden behind the hind legs and the thorax the insects required to be pinned down for laser vibrometry experiments. Insects were prepared by freezing for five minutes after which their legs were removed and they were pinned to a wax block through the thorax, holding the lower segments of the thorax above the tympana. Care needed to be taken not to damage the tympana during this procedure, and to avoid killing the animal since in an animal so small drying occurs rapidly post mortem significantly altering the material properties of the tympana (c.f. Michelsen on the locust tympana [26]). As the mating call of *Achroia grisella* is at 100 kHz, beyond the usable range of most super-tweeters, a custom built ultrasonic transducer was used. The ultrasonic transducer was previously used in investigations of bat sonar and is capable of producing a flat acoustic response between 50 kHz and 1 MHz [93]. The transducer requires a high bias voltage of 200 V (generated by a Brandenburg high voltage source) which is combined through a bias de-coupler with the function generator signal.

Chapter 3

Directional hearing inspired by *Ormia ochracea*

The parasitoid fly *Ormia ochracea* (Figure 3.1) is an obligate parasitoid at the larval stage, forcing gravid females to deposit their larvae on a host *Gryllus integer* or *Gryllus rubens* [94]. The female *O. Ochracea* locates a potential host through phonotaxis to the cricket's mating call [95], where it will deposit a clutch of 1-6 larvae on or near the host [96]. The parasitic lifecycle imposes a significant evolutionary constraint on the flies: their body size is limited by that of their hosts. Consequently the auditory organs of *Ormia ochracea* can only be separated by a short interaural distance, making sound localization challenging due to the vanishingly small time difference of arrival between the tympana. Similarly there is little scope for generating path differences through diffraction of the sound field, as with *Ormia ochracea*'s sometime host *Gryllus bimaculatus*, as the mating call which is to be tracked has a relatively pure frequency between 4.5 kHz and 5.2 kHz and a wavelength at approximately 66 mm - 73 mm, over ten times the body length of *Ormia ochracea* [97]. In order to overcome this limitation *Ormia ochracea* appears to have evolved *de novo* a unique coupled tympanal system which simultaneously measures the total pressure on the tympana and the pressure difference between them. The resulting vibration of the coupled tympana is a function of the modal force ratio between the total pressure and pressure difference, which is proportional to the phase difference of the stimulating acoustic wave but greatly amplified.

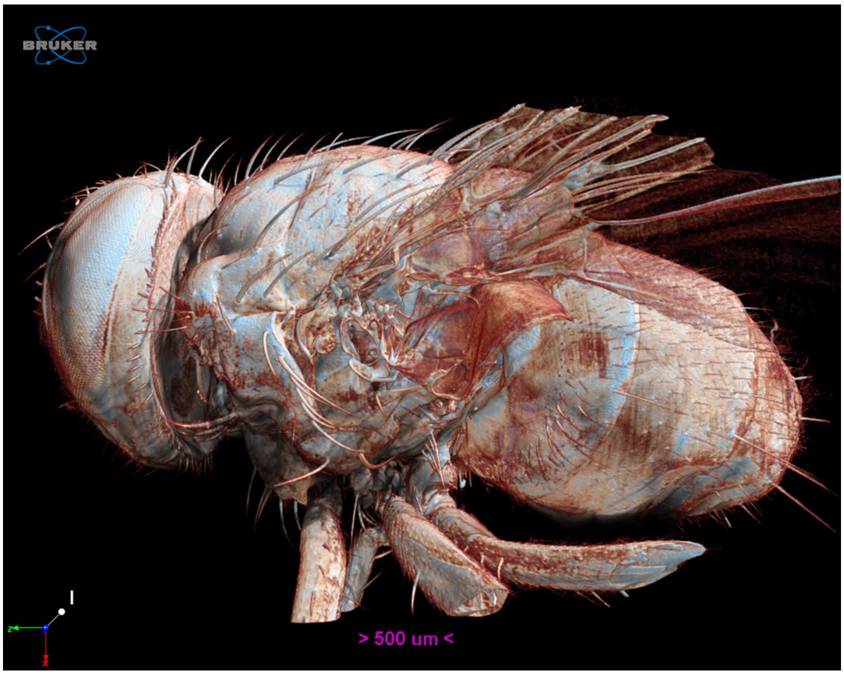

Figure 3.1: X-Ray μCT image of Ormia ochracea, side view.

3.1 Morphology of tympanal system

The tympanal membranes of *Ormia ochracea* are located on the prothorax, largely occluded by the insect's head. Uniquely in tympanal hearing systems both tympanal membranes are backed by a single, undivided tympanal pit. The tympanal pit is a loose, bladder-like feature on the base of the prosternum open to the air via two mesothoracic spiracles (Figure 3.2). The tympanal membranes sit on the anterior side of this chamber (Figure 3.3) and display significant sexual dimorphism. In the female the tympanic membrane show radial corrugations, with the membranes spanning the width of the thorax (1.68±0.19 mm) while the males are notably smaller (1.05 ± 0.04mm) [98] (Figure 3.4). The tympana are separated by a small segment of thick cuticle with each being connected to the base of the tympanal pit by the auditory apodeme, upon which the bulba acoustica rests connecting the system to the auditory nerve [99]. The apodeme is a stiff cuticular rod which transfers the vibration of the membrane into deformation of the bulba acoustica. The acoustic sensors are therefore separated by only 520 μm [100]. Externally the tympanic membranes are mechanically coupled by a raised cuticular bridge, fixed at a pivot point centrally between the membranes and to each of the membranes

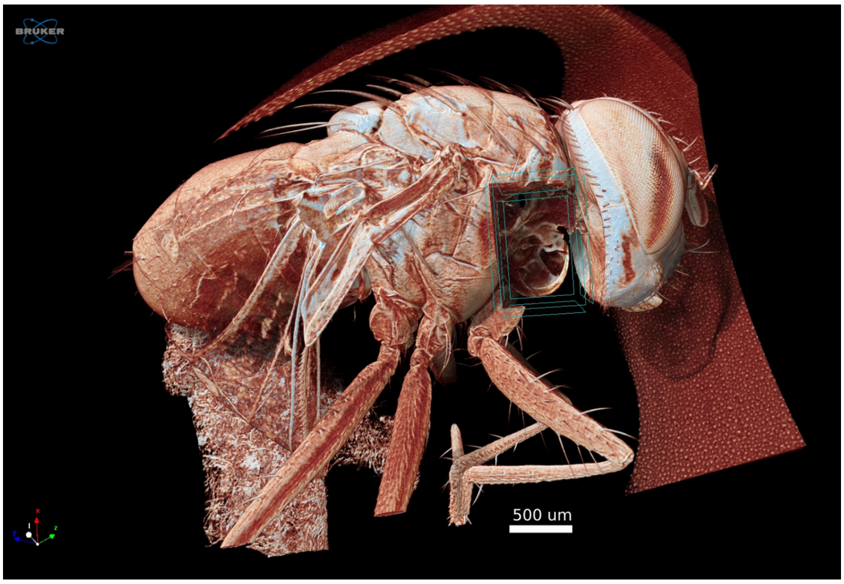

Figure 3.2: Ormia ochracea XRay μCT cut away at prothorax (blue bounding box). A single, undivided air chamber holds the tympanal membranes.

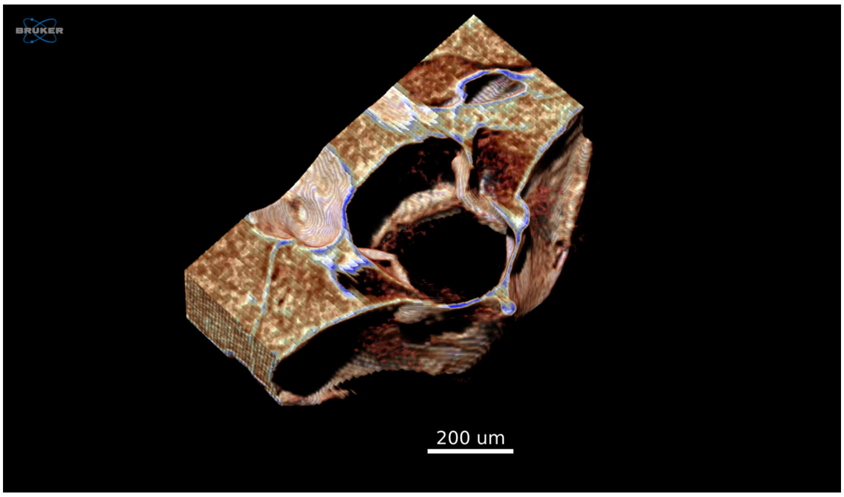

Figure 3.3: Cut away of the air chamber. The membranes and pivot of the intertympanal bridge can be seen on the bottom right, while inside the air chamber can be seen the bulba acoustica and connecting apodeme.

Figure 3.4: The tympanal membranes front view. The membranes are connected by a cuticular bridge and central pivot.

themselves [101]. This structure is known as the intertympanal bridge, and plays a key role in *Ormia ochracea*'s sound localization capability. Although tympanal hearing systems are overwhelmingly comprised of bilaterally symmetrical pairs of tympanal membranes, the combination of the external anatomical linkage between the membranes and the single, undivided air chamber behind the membranes allows the hearing organ of *Ormia ochracea* to be thought of as a single system with two primary vibrational modes: a translational mode in which both tympana oscillate in phase and a rocking mode around the pivot point of the intertympanal bridge in which the tympana oscillate out of phase. The *bulba acoustica* contains the scoloparium of this insect, of which there are an atypically large number: between 65 and 74 in the female and 75 to 76 in the male [98]. The scoloparium are monodynal, with a single sensory cell. The number of sensors is extremely large relative to other tympanal hearing systems on the same scale, such as the noctuid moths *Argotis exlamationis, Noctua pronuba* and *Xestia triangulum*, which possess only three sensory neurons per tympanum [102]. Individual auditory receptors respond with a single spike to a pulse of sound, with increases in sound intensity coded by a decrease in response latency which is highly consistent with the intensity across all the receptors [103]. The large number of neurons and the consistence of the latency to stimulus intensity suggests that directionality is based on the time code of the spikes at the receptor level, with the large number of neurons permitting pooling to compensate for the time code jitter (the standard deviation of latency) which is estimated at 70 μs [103].

3.1.1 Phonotaxis in *Ormia ochracea*

The phonotaxis of a gravid female *Ormia ochracea* to a cricket's mating call occurs in two stages: free flight towards the stimulus followed by landing and walking to close the distance for larviposition [104]. *O. Ochracea* displays a remarkably acute phonotactic ability, being able to localize sound sources to within 2° azimuth [103]. With a separation between measurement points of the order of 500 μm the time difference of arrival at the maximum azimuth of 90° would be 1.45 μs and only 52 ns at 2° azimuth - far below the ability of the central auditory nervous system's ability to time code or process. The intensity difference between the tympana is immeasurably low [100] leaving only the phase difference in instantaneous pressure as a possible directional measurement mechanism. Despite the small directional cues available the vibrational response of the tympanal membranes shows large differences in both amplitude and phase. With a 5 kHz sound source at 45° the amplitude of vibration of the ipsilateral tympanum is 13.6 dB higher than that of the contralateral tympanum, with a time difference of 58 μs representing a 100° phase shift over the stimulating acoustic wave [100].

3.2 Lumped parameter model of *Ormiine* ear

The auditory system of *Ormia ochracea* can be modelled as a mass, spring damper system with each of the membranes represented by a simple mass, m, with an associated membrane stiffness, k_1 and k_2, and damping ratio c_1 and c_2. The two masses are linked by the intertympanal bridge with stiffness k_3 and damping c_3 (Figure 3.5). If the instantaneous sound pressure on each tympana is p_{ipsi} and p_{contra} then each tympanum is subject to a sinusoidal point force with a phase difference between them of:

$$\phi = \frac{2\pi f d}{v_p} \sin\theta \tag{3.1}$$

where θ is the angle of incidence of the incident sound wave, f is the frequency of the wave, v_p the velocity of sound in air and d the separation between the two membranes. The motion of each mass can be given by the following coupled

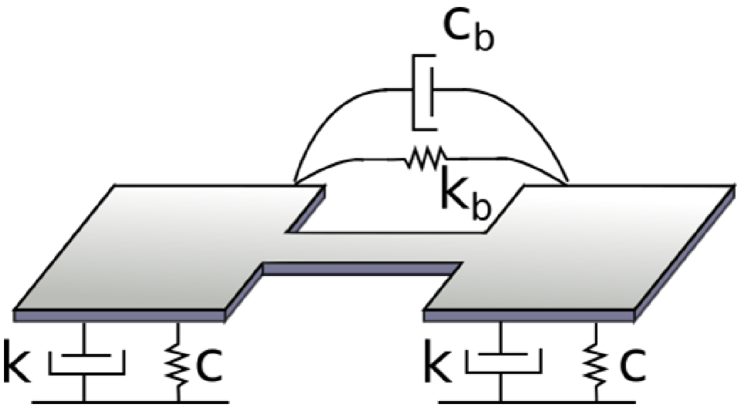

Figure 3.5: The Ormiine ear is modelled as two linked diaphragms, becoming a series of mass - spring - dashpot elements. The masses and stiffness of each of the diaphragms (k and c) is assumed to be the same and exist in parallel to the stiffness and damping of the linking bridge (k_b and c_b).

equations where x_1 and x_2 are the displacement of the masses:

$$m_1\ddot{x_1} + (c_1 + c_3)\dot{x_1} + c_3\dot{x_2} + (k_1 + k_3)x_1 + k_3x_2 = F_1 \tag{3.2}$$

$$m_2\ddot{x_2} + (c_2 + c_3)\dot{x_2} + c_3\dot{x_1} + (k_2 + k_3)x_2 + k_3x_1 = F_2. \tag{3.3}$$

The displacements of each of the membranes are denoted by x_1 and x_2 and the forces incident on each of the membranes by F_1 and F_2. Assuming the masses m_1 and m_2 are equal as well as the associated stiffnesses ($k_1 = k_2 = k$) and damping ($c_1 = c_2 = c$) we can simplify the above equation and put in matrix form:

$$\begin{bmatrix} m & 0 \\ 0 & m \end{bmatrix} \begin{bmatrix} \ddot{x_1} \\ \ddot{x_2} \end{bmatrix} + \begin{bmatrix} c + c_3 & c_3 \\ c_3 & c + c_3 \end{bmatrix} \begin{bmatrix} \dot{x_1} \\ \dot{x_2} \end{bmatrix} + \begin{bmatrix} k + k_3 & k_3 \\ k_3 & k + k_3 \end{bmatrix} \begin{bmatrix} x_1 \\ x_2 \end{bmatrix} = \begin{bmatrix} F_1 \\ F_2 \end{bmatrix} \tag{3.4}$$

The resonance frequencies may be obtained by taking the Fourier transform of each side and calculating the determinant:

$$\begin{bmatrix} -\omega^2 m + k + k_3 & c_3 + k_3 \\ c_3 + k_3 & -\omega^2 m + k + k_3 \end{bmatrix} \boldsymbol{X(\omega)} = \boldsymbol{F(\omega)} \tag{3.5}$$

$$\begin{vmatrix} -\omega^2 m + k + k_3 & c_3 + k_3 \\ c_3 + k_3 & -\omega^2 m + k + k_3 \end{vmatrix} = 0 \tag{3.6}$$

$$(-\omega^2 m + k + k_3)^2 + k_3^2 = 0 \tag{3.7}$$

$$\omega^2 = \frac{k + k_3 \pm \sqrt{k_3^2}}{m}. \tag{3.8}$$

The resonance frequencies are then:

$$\omega_r = \sqrt{\frac{k}{m}} \tag{3.9}$$

$$\omega_t = \sqrt{\frac{k + 2k_3}{m}} \tag{3.10}$$

where ω_r is the rocking mode resonance and ω_t the translational mode resonance. The next stage in this analysis involves decomposing the equations into the contributions of these individual mode shapes, viewing the complete motion of the system as the linear superposition of the rocking mode and translational mode. This slightly unusual step is taken as the amplification of directional cues can be viewed as constructive interference of these modes on the ipsilateral side and the destructive interference on the contralateral side, allowing a simple expression to be created which relies solely on a simple resonance equation. The method used is post-multiplying by the modal matrix and pre-multiplying by the transpose of the modal matrix [105]. The modal matrix can be seen intuitively as equal motion in phase and out of phase, or calculated by substituting the values of ω_r and ω_t into equation 3.5:

$$X = \begin{bmatrix} 1 & 1 \\ 1 & -1 \end{bmatrix} \tag{3.11}$$

$$[X]^T[m][X]\ddot{\boldsymbol{q}} + [X]^T[c][X]\dot{\boldsymbol{q}} + [X]^T[k][X]\boldsymbol{q} = [X]^T\boldsymbol{f} \tag{3.12}$$

were $[m]$,$[k]$ and $[c]$ are the coefficient matrices for mass, stiffness and damping respectively which are now associated with the generalised parameter $\boldsymbol{q} = q1, q2^T$. Multiplying out yields the diagonalised form:

$$\begin{bmatrix} 2m & 0 \\ 0 & 2m \end{bmatrix} \ddot{\boldsymbol{q}} + \begin{bmatrix} 2c + 2c_3 & 0 \\ 0 & 2c \end{bmatrix} \dot{\boldsymbol{q}} + \begin{bmatrix} 2k + 4k_3 & 0 \\ 0 & 2k \end{bmatrix} \boldsymbol{q} = \begin{bmatrix} F_1 + F_2 \\ F_1 - F_2 \end{bmatrix} \tag{3.13}$$

where each of the equations represents one of the mode shapes of the system. By taking the Fourier transform of each of these the transfer function can be derived:

$$H_{t(F,x)} = \frac{\frac{F_1(\omega)+F_2(\omega)}{2m}}{-\omega^2 + \frac{\imath\omega(c+2c_3)}{m} + \frac{k+2k_3}{m}} \tag{3.14}$$

$$H_{r(F,x)} = \frac{\frac{F_1(\omega)-F_2(\omega)}{2m}}{-\omega^2 + \frac{\imath\omega c}{m} + \frac{k}{m}} \tag{3.15}$$

which can then be simplified by noting the imaginary term is the velocity dependent damping term and declaring:

$$\xi_t = \frac{c+2c_3}{m} \tag{3.16}$$

$$\xi_r = \frac{c}{m} \tag{3.17}$$

where ξ_t and ξ_r are the damping coefficients for the translational and rocking modes respectively. The transfer functions then become:

$$H_{t(F,x)} = \frac{\frac{F_1(\omega)+F_2(\omega)}{2m}}{\omega_t^2 - \omega^2 + \imath\omega\xi_t} \tag{3.18}$$

$$H_{r(F,x)} = \frac{\frac{F_1(\omega)-F_2(\omega)}{2m}}{\omega_r^2 - \omega^2 + \imath\omega\xi_r} \tag{3.19}$$

noting that the final terms on the denominator were the rocking and translational mode resonance frequencies in equations 3.9 and 3.10. The motion of each mass will be the linear superposition of the rocking and translational modes:

$$x_1 = A_t \sin(\omega_t t + \phi_t) + A_r \sin(\omega_r t + \phi_r) \tag{3.20}$$

$$x_1 = A_t \sin(\omega_t t + \phi_t) - A_r \sin(\omega_r t + \phi_r) \tag{3.21}$$

where A_t, A_r, ϕ_t and ϕ_r are the amplitudes and phases of the rocking and translational mode oscillations respectively. The forces F_1 and F_2 result from the incident sound pressure which, if the sound is assumed to be a harmonically oscillating planar wave and the diaphragms are symmetrical can be given in terms of the displacement from the pressure at the midpoint between the two diaphragms:

$$F_1 = se^{\imath\omega\tau} \tag{3.22}$$

$$F_2 = se^{-\imath\omega\tau} \tag{3.23}$$

where the diaphragm area is s and τ is the time difference between the measurement points given by:

$$\tau = \frac{\lambda}{d}\sin\theta. \tag{3.24}$$

Combining equations 3.18-3.23 yields an expression for the displacement of the masses x_1 and x_2 in terms of the mode shapes:

$$x_1(\omega) = \frac{\frac{s\imath\sin(\frac{\omega\tau}{2})}{m}}{\omega_r^2 - \omega^2 + \imath\omega\xi_r} + \frac{\frac{s\cos(\frac{\omega\tau}{2})}{m}}{\omega_t^2 - \omega^2 + \imath\omega\xi_t} \tag{3.25}$$

$$x_2(\omega) = \frac{\frac{s\cos(\frac{\omega\tau}{2})}{m}}{\omega_t^2 - \omega^2 + \imath\omega\xi_t} - \frac{\frac{s\imath\sin(\frac{\omega\tau}{2})}{m}}{\omega_r^2 - \omega^2 + \imath\omega\xi_r}. \tag{3.26}$$

Expressing the frequencies in terms of the normalized ratio $\Omega = \omega/\omega_r$ and $\eta = \omega_t/\omega_r$ simplifies the expression for the displacement to:

$$x_1(\omega) = \frac{sp_0}{k}\frac{\cos(\frac{\omega\tau}{2})}{1-\Omega^2+2\imath\Omega\xi_r}(\Lambda + \imath\tan(\frac{\omega\tau}{2})) \tag{3.27}$$

$$x_2(\omega) = \frac{sp_0}{k}\frac{\cos(\frac{\omega\tau}{2})}{1-\Omega^2+2\imath\Omega\xi_r}(\Lambda - \imath\tan(\frac{\omega\tau}{2})) \tag{3.28}$$

where:

$$\Lambda = \frac{1-\Omega^2+2\imath\Omega\xi_r}{\eta^2-\Omega^2+2\imath\Omega\eta\xi_t}. \tag{3.29}$$

This form of the equations, used by Miao Yu [59], provides two main benefits. First it illustrates that the displacement of each of the diaphragms is only dependent on the ratio of the two resonant modes, the ratio of the incident wave frequency to the rocking mode, the damping ratios and the time difference between the diaphragms. Secondly it provides a simple method of calculating two figures of merit for any *O. Ochracea* inspired microphone device: the mechanical interaural intensity difference (mIID) and the mechanical interaural phase difference (mIPD) which can be compared to the phase and intensity difference of the incident pressure wave to give the gain of the system. The mechanical intensity difference is the difference in the power spectral distribution at a single frequency:

$$mIID = 20\log_{10}\frac{|x_1|}{|x_2|} = 20\log_{10}\left|\frac{\Lambda + \imath\tan(\frac{\omega\tau}{2})}{\Lambda - \imath\tan(\frac{\omega\tau}{2})}\right| \tag{3.30}$$

$$mIPD = \angle\left|\frac{\Lambda + \imath\tan(\frac{\omega\tau}{2})}{\Lambda - \imath\tan(\frac{\omega\tau}{2})}\right|. \tag{3.31}$$

3.3 Directional sensitivity and coupling strength

Accurate measurement of a sound source angle will depend on the sensitivity of the measures of mIID and mIPD to the change in azimuthal angle; that is the rate of change of mIID and mIPD with theta:

$$DS_{mIID} = \frac{\partial}{\partial\theta} mIID \tag{3.32}$$

$$DS_{mIPD} = \frac{\partial}{\partial\theta} mIPD. \tag{3.33}$$

The directional sensitivity around the mid-line is directly influenced by the coupling strength between the membranes, i.e. the stiffness of the intertympanal bridge. It is possible to consider the amplification of directional cues in terms of destructive interference: either in terms of the individual diaphragms' movement, where the motion of the ipsilateral diaphragm retards the motion of the contralateral, or in terms of the mode shapes where the translational mode constructively interferes with the rocking mode on the ipsilateral side and destructively interferes on the contralateral side. In either presentation, optimum amplification of directional cues requires the forces to be of comparable strength. The coupling strength can be given in terms of the ratio of resonance frequencies:

$$\eta = \sqrt{1 + \frac{2k_3}{k}} \tag{3.34}$$

illustrating the strength of the modal decomposition of the equations of motion performed in the previous chapter: the key parameters of the equations of motion and the size of the mIID and mIPD measures are now calculated in terms of resonance frequencies. If the coupling strength is weak the motion of each diaphragm has little influence on the other leading to a very slight amplification of directional information. This situation approaches that of two independent membranes, with the directional sensitivity showing a similar sine dependency on the angle of the incoming sound wave as would be shown by two omnidirectional microphones the same distance apart. Here the translational mode is of far greater strength. If the coupling strength is high the dominant force on each membrane comes from the

Parameter name	Value
ω_r	6.99 kHz
ω_t	30.10 kHz
m	2.88×10^{-10} kg
k	0.576 Nm^{-1}
c	$1.15 \times 10^{-5} Nsm^{-1}$
k_3	$5.15 Nm^{-1}$
c_3	$2.88 \times 10^{-5} Nsm^{-1}$
s	0.288×$10^{-6} m^2$

Table 3.1: Parameter values corresponding to auditory system of O. ochracea

motion of the other membrane, making the rocking mode dominant. Directional sensitivity is consequently high around the midline, but quickly saturates within a few degrees change in azimuth rendering the system impractical for measurement of sound source angle (Fig 3.6). In addition, and particularly noticeable in the mIPD measure, is the increase in non-linearity with a null appearing around the midline where directional sensitivity drops. The coupling strength required is dependent on the damping of the system and the distance between the membranes. Systems with lower damping will become 'over-coupled' more easily, providing optimum amplification of the directional cues with the resonance frequencies far closer together. Higher damping also requires a higher coupling strength if the system is not to act like two independent membranes.

3.4 Application of lumped parameter model to *Ormia ochracea*

Miles et al. [101] give estimated numerical values for a lumped parameter model of the *O. Ochracea* auditory system (shown in table 3.1). The weight and area of the auditory system are measured results whereas the spring and dashpot constants have been generated to provide the best fit to measured data. This gives damping coefficients for each of the modes of $\xi_r = 0.89$ and $\xi_t = 1.23$. Using these figures to calculate the mIPD and mIID across a range of incident sound angles gives us a picture of the directional sensitivity to phase of the Ormiine ear. At 5 kHz a region of linear directional sensitivity in the mIPD measure can be identified around the midline of sound source angles, with frequencies below 5 kHz showing much lower directional sensitivity and a mIPD that more closely resembles the sine dependence

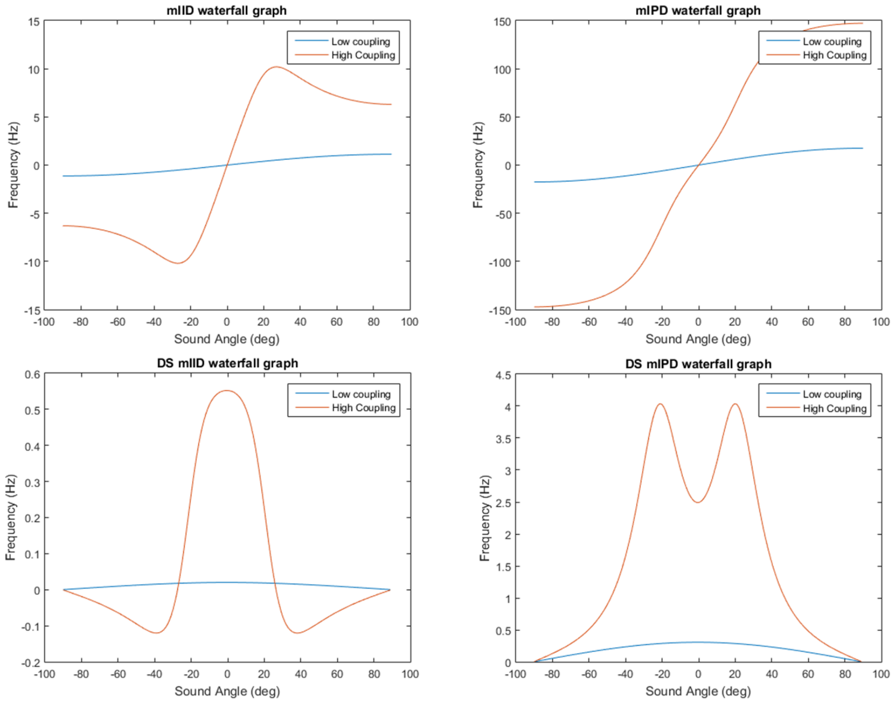

Figure 3.6: If the coupling strength is weak the motion of each diaphragm has little influence on the other leading to a very slight amplification of directional information. This situation approaches that of two independent membranes, with the directional sensitivity showing a similar sine dependency on the angle of the incoming sound wave as would be shown by two omnidirectional microphones the same distance apart. Here the translational mode is of far greater strength. If the coupling strength is high the dominant force on each membrane comes from the motion of the other membrane, making the rocking mode dominant. Directional sensitivity is consequently high around the midline, but quickly saturates within a few degrees change in azimuth rendering the system impractical for measurement of sound source angle. In addition, and particularly noticeable in the mIPD measure, is the increase in non-linearity with a null appearing around the midline where directional sensitivity drops.

of the stimulating sound wave, and those above 5 kHz displaying a much higher directional sensitivity but with a 'null' region of low or zero directional sensitivity around the midline (Figure 3.7). The region of linear sensitivity in the mIPD measure correlates both with the frequency of the mating call of the host cricket and with the fly's behaviour: *O. Ochracea* will turn towards a stimulus sound source but only be capable of making an accurate measurement if it is able to complete the turn towards the sound source, i.e. the signal continues until the sound source is within ±30° of the insect's midline [34]. A similar region of directional sensitivity exists in the mIID measure, although it occurs at over 8 kHz, between the resonance frequencies for the rocking mode and translational mode of the *Ormiine* ear. The presence of this region of linear sensitivity around the calling frequency of *Gryllus rubens* and *Gryllus integer*, and the correlation with the turning behaviour of the fly suggests that it is the phase difference that is being measured by *Ormia ochracea.* However the directional sensitivity is still only a 0.95° change in phase difference per degree change in azimuthal angle, giving an estimated phase difference of 1.9° for an azimuth angle change of 2°, the smallest change Ormia ochracea has been measured as capable of distinguishing [103]. The time difference between the ipsilateral and contralateral ears which *O. Ochracea* must therefore be able to encode is only 1 μs which, although an amplification of 20 times the time difference of arrival of the stimulating sound field, is still well below the measured 70 μs jitter in the pulse response of an individual scoloparium (ibid). The large number of scoloparium contained in the *bulba acoustica* may simply be for the purpose of pooling the response times, effectively averaging out the jitter of individual neurons. However, given the large intensity differences available to the insect and the relative ease with which such intensity differences can be measured by ears with few neuronal attachments the question is raised why the *Ormiine* ear was not adapted to take advantage of this directional cue.

3.4.1 Average directional sensitivity and non-linearity

An ideal directional measurement system would show a linear change in mIID or mIPD with changes in sound source angle, with a directional sensitivity which is as large as possible. From inspection it is clear that the change in mIPD and mIID is only approximately linear around the midline, and there is a limited frequency range. Here we introduce two further measures, the average directional sensitivity

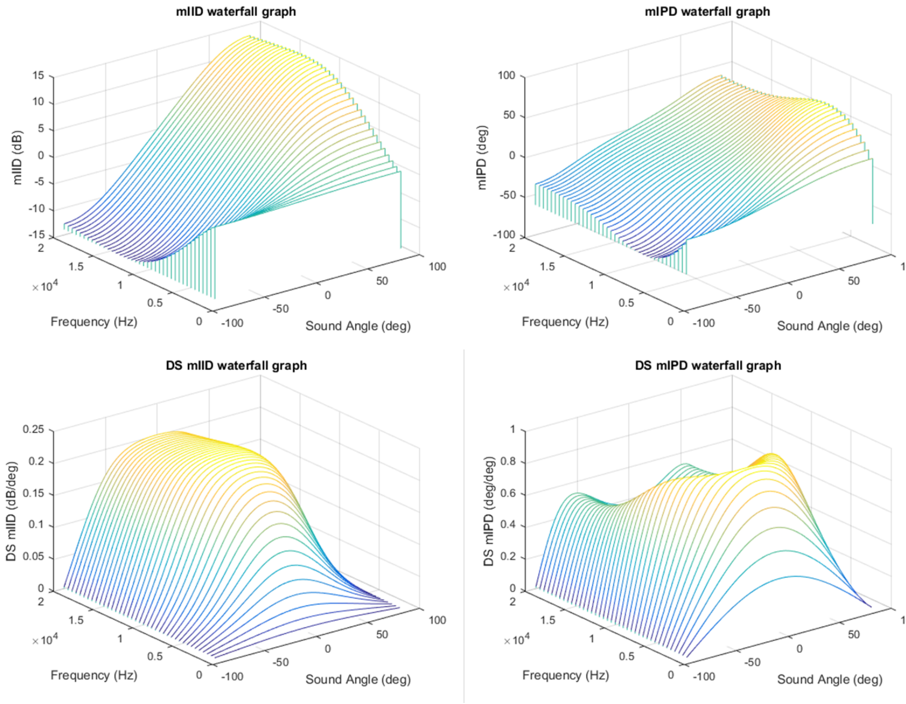

Figure 3.7: (Top left) Waterfall graph of mIID for lumped parameter system using Ormia ochracea parameters. The largest change in directional sensitivity occurs at 8kHz. (Top right) Waterfall graph of mIPD in system using O. Ochracea parameters. In the phase difference the peak directional sensitivity is more pronounced at 5 kHz and the frequency range smaller. This is the frequency range of the mating call of the host Gryllus. (Bottom left) Directional sensitivity of mIID measure in top left panel. A region of linear directional sensitivity can be seen beginning at approximately 8 kHz. (Bottom right) Directional sensitivity of mIPD measure in top right panel. The region of linear directional sensitivity occurs at 5 kHz only, with frequencies beyond that range showing a significant drop in directional sensitivity around the midline.

(ADS) and the non-linearity (NL) of the response. The ADS is measured in a given angular range around the midline ($-\Theta < \theta < \Theta$) and is based on linear least squares:

$$mIPD(\theta) = mIPD_{\theta=0} + ADS \cdot \theta \tag{3.35}$$

where $mIPD_{\theta=0}$, the phase difference when $\theta = 0$, would be expected to be zero for any symmetric system, leaving the estimated mIPD as the product of the ADS and the angle. Here we calculate the average directional sensitivity around the midline numerically:

$$\lim_{h\to 0} ADS_{mIID} = 20\log_{10}\frac{1}{h}\left(\left|\frac{\Gamma + \imath\tan(2\pi f d\sin(\theta+h))}{\Gamma - \imath\tan(2\pi f d\sin(\theta+h))}\right| - \left|\frac{\Gamma + \imath\tan(2\pi f d\sin(\theta))}{\Gamma - \imath\tan(2\pi f d\sin(\theta))}\right|\right) \tag{3.36}$$

$$\lim_{h\to 0} ADS_{mIID} = \angle\frac{1}{h}\left(\left|\frac{\Gamma + \imath\tan(2\pi f d\sin(\theta+h))}{\Gamma - \imath\tan(2\pi f d\sin(\theta+h))}\right| - \left|\frac{\Gamma + \imath\tan(2\pi f d\sin(\theta))}{\Gamma - \imath\tan(2\pi f d\sin(\theta))}\right|\right) \tag{3.37}$$

The non-linearity is then the measure of the error in the estimate mIID or mIPD from the ADS:

$$NL = \frac{1}{|ADS|}\sqrt{\frac{1}{2\Theta}\int_{-\Theta}^{\Theta}(mIPD_{ADS}(\theta) - mIPD(\theta))} \tag{3.38}$$

Applying these measures to *Ormia ochracea* shows that in the mIPD measure the maximum ADS and the minimum non-linearity occur at the same frequency (Figure 3.8). This point, referred to as the 'dual optimization' point, can be obtained in engineered systems by the tailoring of the intertympanal bridge stiffness to the damping conditions of the device [106].

3.5 Summary of *Ormia ochracea* inspired hearing

The connected ears of *Ormia ochracea* are a unique solution to the problem of directional hearing at the micro-scale. The linked diaphragms are capable of simultaneous measurement of the total acoustic pressure and the pressure gradient between them through the stimulation of the translational and rocking modes respectively. When these modes are of comparable strength they will destructively interfere on the contralateral membrane and constructively interfere on the ipsilateral. As the sound source moves away from the midline the pressure gradient increases while the total pressure decreases, increasing the effect of the interference.

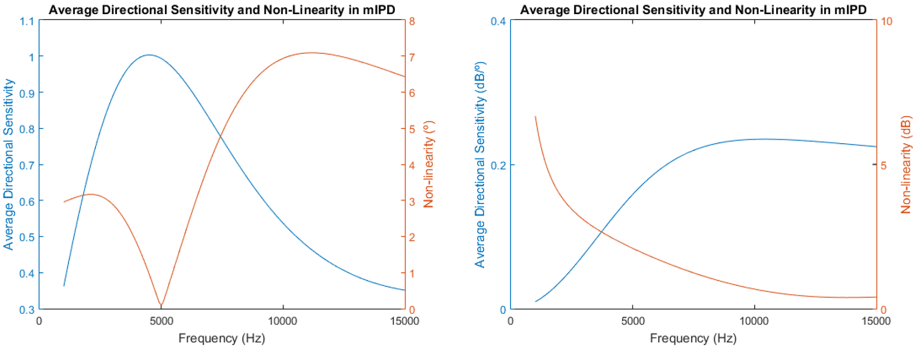

Figure 3.8: (Left) The average directional sensitivity and non-linearity measures for the phase difference in the Ormiine ear. There is a clear correlation between the peak in directional sensitivity and the minima in non-linearity at the biologically relevant frequency of 5 kHz. (Right) Average directional sensitivity and non-linearity for intensity difference. Here the peak in directional sensitivity and minima in non-linearity are not well aligned, illustrating a key problem with 'dual-optimization' systems - a system may only be optimized for one of the two measures of mIID or mIPD but not both.

Effectively the measurement is of the ratio of the modal forces generated by the pressure gradient and the total pressure. Given the reliance on a carefully balanced ratio of resonance frequencies (or coupling strength) the amplification effect is necessarily band limited. Wide band operation therefore comes at the cost of reduced amplification of directional cues, while optimization for maximum directional sensitivity restricts use to a single frequency.

3.6 Previous work on *Ormia ochracea* inspired microphones

Miniature directional microphones have applications ranging from hearing aid systems [107] to military systems for locating the position of snipers [108, 109, 110]. A variety of systems based on the hearing system of *Ormia ochracea* have already been proposed, both at the micro and macro scale. As was shown in previous sections of this chapter the amplification of directional cues in such a system is dependent on the modes being of comparable strength, which is primarily dependent on the coupling strength between the membranes and the damping experienced by the system [111]. Two main strategies for dealing with this problem can be recognised

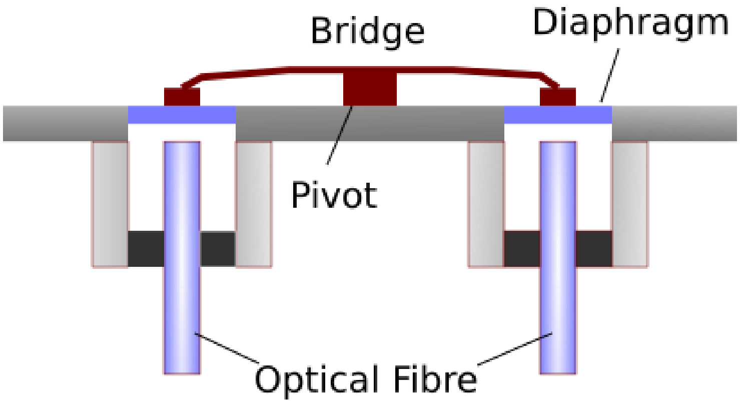

Figure 3.9: Diagram of Ormia inspired microphone using fixed periphery membranes, a raised bridge and pivot with optical fibre transduction.

in the literature: compromising the amplification of directional cues to achieve a wide-band amplification of directionality, and operating at a single frequency with the maximum directional sensitivity. The former approach frequently looks for a flat gain in directional cues across the audio range for use as a microphone, for example in hearing aids. In the latter approach, the majority of signal information is lost and the system ceases to be a microphone and becomes a simple sound localization device for single frequencies or wide-band noise that nevertheless has reliable energy content at the device's designed optimal frequency. This system is primarily useful for tracking signals which have a known frequency content, for example Unmanned Aerial Vehicles (UAVs) [112] or for localising the muzzle blast or supersonic compression wave from projectile fire [113, 114, 115].

3.6.1 Fixed periphery devices

Systems directly imitating the structure of the intertympanal bridge and pivot provided a proof of concept for *Ormia ochracea* inspired directional hearing. In these systems the two diaphragms are connected to a raised bridge at the centre of each diaphragm, with a raised pivot point at the midpoint between them (Figure 3.9). Structures directly imitating the form of *Ormia ochracea* are difficult to realise at the micro-scale, as they require large offsets between components in the z-axis (which is to say that these are true 3D structures). As the release of structures in MEMS devices is usually achieved via the use of sacrificial layers, which are typically only a few microns deep [116], these devices have been constructed on a larger scale. For example, the device presented in Figure 3.9 consists of two Mylar plates with radius of 3.5 mm each connected by a steel beam 25.4 mm by 1.9 mm for a total device footprint of 32.4 mm x 7 mm [65, 117]. This device is fabricated using traditional machining and assembly tools. Given the scale of the device the resonance frequencies are consequently low: the translational mode occurs at 2 kHz and the rocking mode at 1.2 kHz. Despite this change of scale the device showed amplification comparable to *Ormia ochracea* at a frequency of 1.1 kHz, slightly below the measured rocking mode frequency. At this frequency a gain in phase difference of 4.4x the stimulating sound wave was recorded at 90° azimuth, with a linear directional sensitivity of 6.5 μs/deg within the range of ±30° [65]. Progressing towards the micro-scale, but retaining the same design, a further fixed periphery device was fabricated by micromachining [118]. Using a 500 nm thick sputtered polysilicon layer as the membrane layer, a silicon-on-insulator (SOI) wafer serves as the base for the design. The wafer is then patterned with a photoresist sacrificial layer, with the intertympanal bridge and pivot consisting of alternating layers of silicon dioxide and silicon nitride [119]. Again, the device is designed for single-frequency operation, albeit at a higher base frequency given the reduced scale of the device. Here the rocking mode was found at 14.1 kHz and a translational mode approximately at 32 kHz. This device produces an amplified time delay of 0.54 μs per degree at the rocking mode frequency (compared to the time delay in the acoustic wave of 63 ns per degree). The ratio of resonance frequencies gives a value of η of 2.13, which when fitting the measured phase difference of the sensor to the lumped parameter model, suggests that the modal damping ratios are in the region of 0.1 - 0.16. The device is therefore far from the optimized maximum amplification of directional cues (which would suggest a ratio closer to 1.6 for maximum amplification while retaining linearity around the midline). This is explained by the authors to be the result of some unexpected hardening of the beam during the baking process which resulted in a higher than predicted translational mode frequency. Both the designs here have maximum displacements at the nanoscale, necessitating a highly sensitive method of transduction. Capacitive back-plating is not considered for these microphone types as the resulting thin film damping will radically change the required stiffness of the intertympanal bridge as well as greatly reducing the mechanical sensitivity of the device (see Chapter 4 for a full discussion). Here, with a fixed periphery device, the solution was to use the diaphragm deflection in conjunction with an optical fibre inserted into the

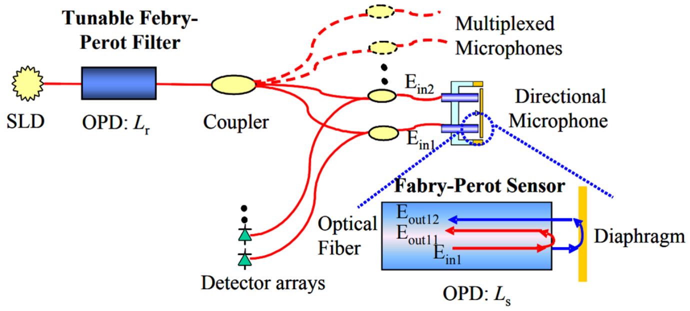

Figure 3.10: The Fabry-Perot interferometer sends broadband light from a light emitting diode through two optical couplers to be reflected from the diaphragms where it is redirected through the filters to two photo-detectors [110].

back cavity of the microphone as a Fabry-Perot interferometer (Figure 3.10). This fibre-optic interferometer measures the phase change between the transmitted and reflected light, which is proportional to the displacement of the diaphragm [120]. Although this measurement system provides extremely low noise, high sensitivity measurements the complex modulation scheme and cost of the broadband superluminescent light emitting diode greatly increase the footprint of the device and act as an obstacle to further miniaturisation of the system.

3.6.2 Rocking mode devices

The bulk of micro-machined sensors inspired by *Ormia ochracea* adopted a simpler, single layer method of coupling two sensors consisting of a stiffened plate with a central pivot (Figure 3.11). The rocking mode of this device is therefore determined by the torsional stiffness of the pivot and the membrane stiffness rather than that of any bridge between the membranes, while the translational mode is solely determined by the membrane stiffness. Notions of intertympanal bridge stiffness, which has previously been described as being the principle determinant of the amplification of directional cues, are therefore somewhat more abstract and the system can be more easily described in terms of the ratio of resonant modes, η. The principles of superposition of the rocking and translational modes developed in the lumped parameter model still hold for this class of device. The earliest iterations of these central pivot systems was proposed by Gibbons and Miles in 2000 [2] and represented a hybrid between a central pivot system and those using an intertympanal bridge. Here the device was fabricated from polysilicon, but utilised a solid stiff-

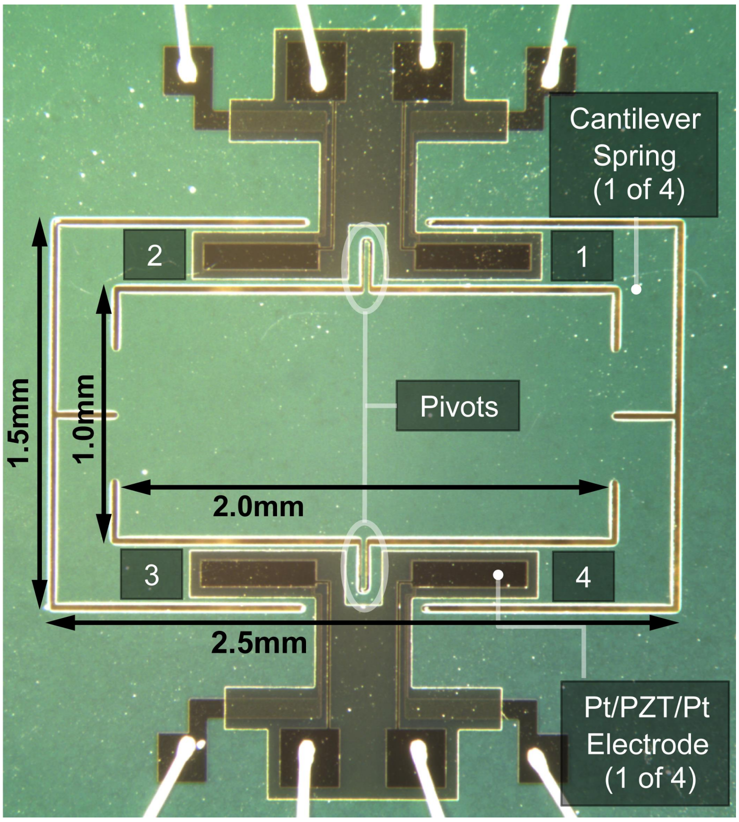

Figure 3.11: Basic single layer device (this image is taken from a relatively recent paper [1], rather than the original from Gibbons and Miles [2]). This device is connected to the wafer via two pivots on the central line. Lever arms connected to the ends of either membrane are intended as part of a piezoelectric sensing system, which most earlier designs omit these in favour of capacative or interferometric based transdcution systems.

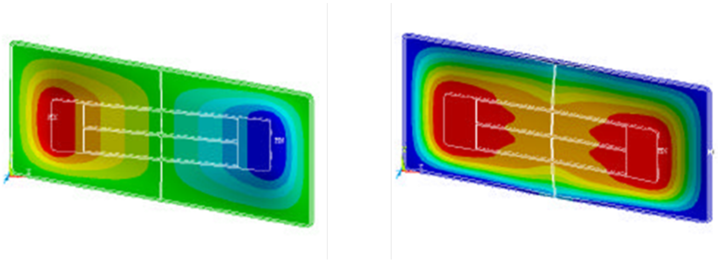

Figure 3.12: : Rocking and Translational eigenmodes of device presented in [2]

ener running centrally through the membrane to enhance the stiffness of the device [121]. The result was that despite the fact that the periphery of the membrane was free, the point of maximum deflection still occurred at the central point of each diaphragm (Figure 3.12). The device is 2 mm long x 1 mm wide and the polysilicon layer is 20 μm thick, dimensions which have become quite standardised over the past 20 years. This device is designed to work with a perforated capacitive back-plate with an air gap of 3 μm, giving an extremely over-damped translational mode (estimated at a damping ratio of 9.0) and an under-damped rocking mode (estimated at 0.1). The resonance frequencies were 1272 and 9349 Hz for the rocking and translational modes respectively giving a ratio η of 7.35. The high coupling strength is necessitated by the high damping on the translational mode, but also these designs are not intended to mimic the single frequency operation of *Ormia ochracea* and the fixed periphery designs described in the previous section, but to operate as true directional microphones over the audio frequency range. This has particular application to the development of directional hearing aids, where the rejection of sounds to the side of or behind the listener has been shown to greatly improve the intelligibility of speech [122, 123]. To this end the optimal amplification of directional cues is sacrificed to provide a low level of amplification over a broad frequency range: in this case a relatively flat amplification of directional cues of approximately 50% (as opposed to the gains of 20 times the original cues) over the range of 1500 to 5000 Hz. Later designs from the same team using polysilicon membranes and capacitive back-plates used perforated diaphragms as well as back-plates to control the extremely high damping, although the trade-off of reduced sensitivity to the incident force of the pressure wave was found to be prohibitive [124]. Later iterations abandoned the capacitive back-plate in favour of either optical sensing (using a diffraction grating imprinted on the membrane and an LED laser to provide diffraction patterns) [64], a capacitive comb readout [67], or in more recent devices through the use of a sputtered PZT layer measuring the stress of lever arms attached to the edges of the membrane [1, 125]. In the majority of these cases, while the transduction methods differ, the aim of stabilizing the gain over a wide frequency range remains. This can be illustrated in the case of two recent central pivot devices - one using a capacitive comb sensing scheme [3] and the other an optical diffraction grating [126] - which nevertheless show the same mechanical characteristics. The resonance frequencies for these devices places the lower, rocking mode at 735 Hz with the higher at 15427 Hz, for a very strongly coupled system with an η of 20.99. The estimated damping remains low, given the absence of a back-plate in either design, at 0.16 for the rocking mode and 0.25 for the translational mode. Using these figures in the lumped parameter model of the *Ormiine* ear shows the rationale behind the high coupling - a uniform directionality from 5 kHz - 10 kHz with approximately 3 dB difference between a sound source directly ahead and one at 90° to the membrane long axis. The directional sensitivity is extremely low, reaching only 0.0473 dB/° around the midline and a negligible 0.02 degrees phase change per degree azimuth in the mIPD measure (Figure 3.13). While these microphones have the benefit of extremely low noise [127], even allowing for the trade-off of limited amplification of directional cues their use still presents several problems. Most critically for their use in hearing aids the frequency range over which the gain is steady lies several kilohertz above the rocking mode frequency. The fundamental frequency of speech falls between the range of 85 Hz to 255 Hz [128], far below the rocking mode of this device. Lowering this first resonant peak further is unlikely, leaving devices operating in this scheme with very little directivity in the crucial region for speech intelligibility. Secondly both the directivity and the low noise performance of the device rely on the minimisation of damping which creates a sharp resonant peak. In this case at 735 Hz this peak will severely distort the incoming signal. Traditional solutions to this problem in omnidirectional microphones, such as moving the resonant peaks out-with the desired frequency range or introducing passive damping, would destroy the directional properties of the microphone as well as reducing the sensitivity of the device. While some correction of this may be possible, through the use of a compensation filter or by incorporating active feedback into the microphone [61] the design requirements for a microphone and those of an *Ormia* inspired directional sensor appear to be mutually contradictory.

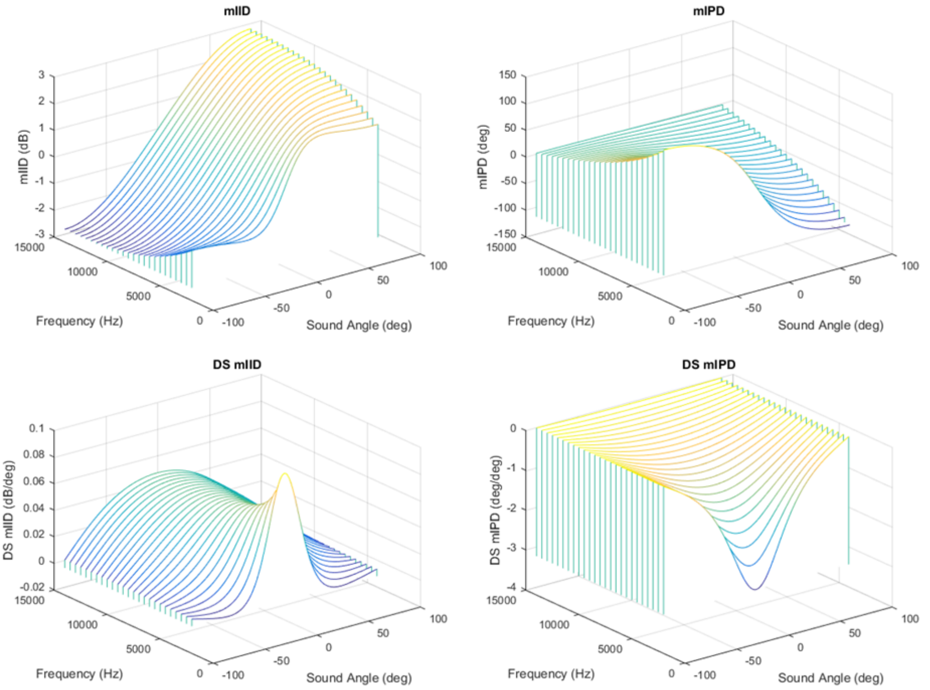

Figure 3.13: Waterfall graphs of mIID and mIPD calculated from parameters of directional microphone described in [3]. (Top left) mIID between 5kHz and 15kHz, showing consistent change in intensity across the range. (Top right) mIPD between 5kHz and 15kHz. Some directionality is evident at around 5kHz but quickly becomes negligible. (Bottom left) Directional sensitivity of mIID measure, showing distinct non-linearity and very low sensitivity. (Bottom right) Directional sensitivity of mIPD measure showing nearly zero sensitivity at higher frequencies.

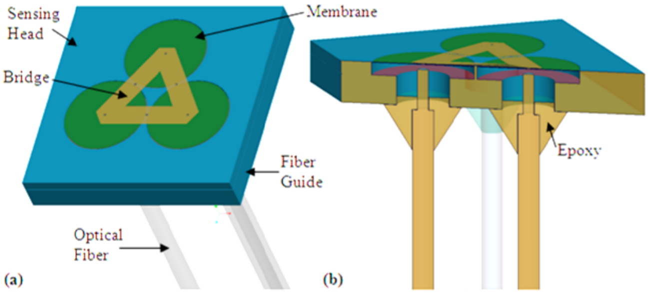

Figure 3.14: Sound localization in two dimensions using a triangular configuration of membranes. Overview is shown on left with cross section of design on right [111].

3.6.3 Directional sensing in two dimensions

The microphones presented here only permit the localization of sound on one axis, either the azimuth measured around the axis normal to the plane of the device, or the pitch, measured around the axis normal to the line between the two diaphragms. In any situation where either the azimuth or the pitch cannot be assumed to be zero there will be some ambiguity in the results, with the directional reading of the sensor describing an paraboloid surface in space. The problem could be potentially solved with an array of directional microphones; however several teams have attempted to create sensors which extend the principles of *Ormia* inspired hearing to three dimensions. The simplest of these consists of three mechanically linked diaphragms in a triangle formation around a central pivot (Figure 3.14) [111]. Using the lumped element model the system can again be reduced to a mass, spring and dashpot system for each of the membranes (Figure 3.15). Again the masses or each of the membranes is assumed to be constant, as well as the stiffnesses of each diaphragm and those of each of the three intertympanal bridges. Using the same method as presented in Section 3.2 the mass, damping and stiffness matrices are now:

$$M = \begin{bmatrix} m & 0 & 0 \\ 0 & m & 0 \\ 0 & 0 & m \end{bmatrix} \tag{3.39}$$

$$C = \begin{bmatrix} c + 2c_p & c_p & c_p \\ c_p & c + 2c_p & c_p \\ c_p & c_p & c + 2c_p \end{bmatrix} \tag{3.40}$$

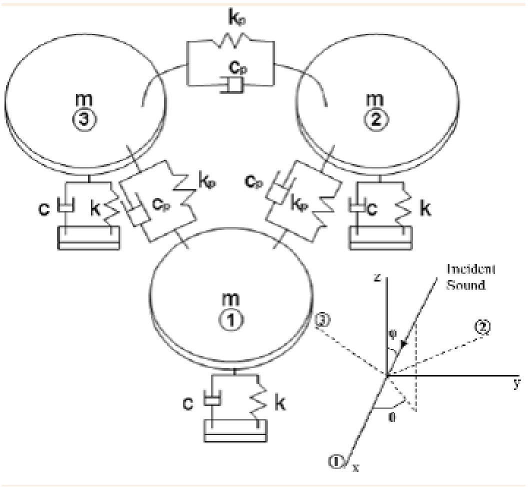

Figure 3.15: Lumped parameter model of triangular configuration of linked membranes.

$$
\begin{bmatrix}
k+2k_p & k_p & k_p \\
k_p & k+2k_p k_p & \\
k_p & k_p & k+2k_p ...
\end{bmatrix}
\tag{3.41}
$$

where k is the stiffness of each individual membrane and k_p is the coupling stiffness as shown in figure 3.15. Solving for the un-damped case:

$$(-\omega^2[M] + [K])\boldsymbol{x} = 0 \tag{3.42}$$

$$(\omega^2 m + k + 2k_p)^3 - 3k_p^2(-\omega^2 m + k + 2k_p) + 2k_p^3 = 0 \tag{3.43}$$

which can be solved as a third order polynomial by setting $\alpha = -\omega^2 m + k + 2k_p$:

$$\alpha^3 - 3k_p\alpha + 2k_p^3 = 0 \tag{3.44}$$

$$(\alpha - k_p)^2(\alpha + 2k_p) = 0 \tag{3.45}$$

$$\omega_1 = \omega_2 = \sqrt{\frac{k + k_p}{m}} \tag{3.46}$$

$$\omega_3 = \sqrt{\frac{k + 4k_p}{m}}. \tag{3.47}$$

The two repeated roots give us eigenvectors which are not orthogonal: -1,1,0 and -1,0,1. It is possible to generate a linearly independent set of eigenvectors by noting that:

$$\alpha \begin{bmatrix} -1 \\ 0 \\ 1 \end{bmatrix} + \beta \begin{bmatrix} -1 \\ 1 \\ 0 \end{bmatrix} \perp \begin{bmatrix} -1 \\ 1 \\ 0 \end{bmatrix} \tag{3.48}$$

which will be true when $\alpha = -2$ and $\beta = 1$ giving a set of orthogonal eigenvectors:

$$X = \begin{bmatrix} 1 & -1 & 1 \\ 1 & 1 & 1 \\ -2 & 0 & 1 \end{bmatrix}. \tag{3.49}$$

In the third natural frequency all membranes clearly oscillate in phase, however at other frequencies a combination of two modes corresponding to the two possible rocking modes will be observed: either the device rocks along the axis which bisects the third membrane, resulting in two membranes oscillating out of phase while the third remains stationary, or it rocks along the parallel axis which results in the first two membranes oscillating in phase while the third is 180° out of phase with twice the magnitude (Figure 3.16). Solving in terms of the transfer functions for each of the mode shapes gives:

$$\begin{aligned} &-\omega^2 \begin{bmatrix} 6m & 0 & 0 \\ 0 & 2m & 0 \\ 0 & 0 & 3m \end{bmatrix} + \imath\omega \begin{bmatrix} 6c+6c_p & 0 & 0 \\ 0 & 2c+2c_p & 0 \\ 0 & 0 & 3c+12c_p \end{bmatrix} \\ &+ \begin{bmatrix} 6k+6k_p & 0 & 0 \\ 0 & 2k+2k_p & 0 \\ 0 & 0 & 3k+12k_p \end{bmatrix} = \begin{bmatrix} F_1+F_2-2f_3 \\ F_2-F_1 \\ F_1+F_2+F_3 \end{bmatrix} \end{aligned} \tag{3.50}$$

$$H_{x1,f}(\omega) = \frac{\frac{F_1+F_2-2F_3}{6m}}{\omega_1^2 - \omega^2 + 2\imath\omega_1\omega\xi_1} \tag{3.51}$$

$$H_{x2,f}(\omega) = \frac{\frac{F_2-F_1}{2m}}{\omega_2^2 - \omega^2 + 2\imath\omega_2\omega\xi_2} \tag{3.52}$$

$$H_{x3,f}(\omega) = \frac{\frac{F_1+F_2+F_3}{3m}}{\omega_3^2 - \omega^2 + 2\imath\omega_3\omega\xi_3} \tag{3.53}$$

where $(x_1, x_2, x_3), (\omega_1, \omega_2, \omega_3)$ and (ξ_1, ξ_2, ξ_3) refer to the displacements of each of the membranes, and the natural resonance frequencies and damping ratios of each

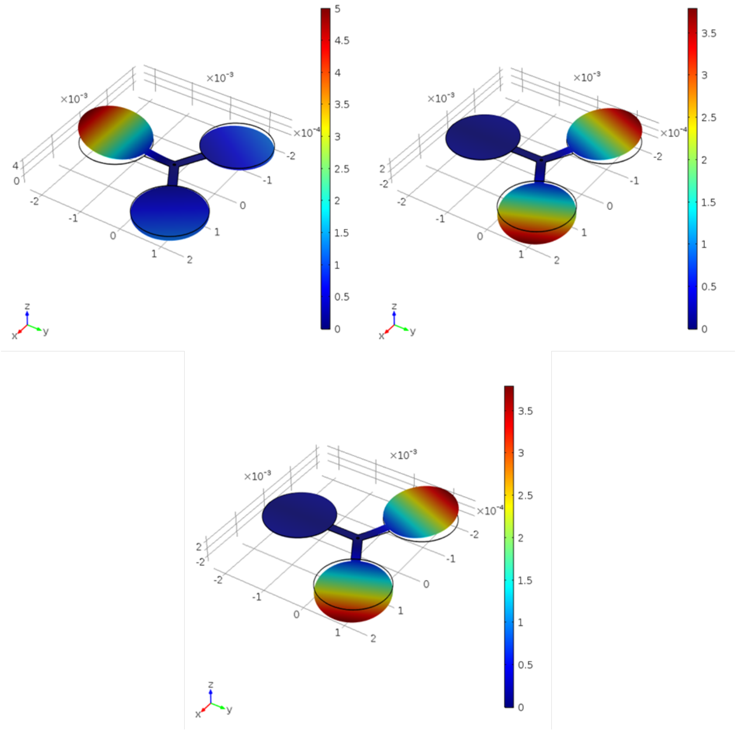

Figure 3.16: Eigenmodes of triangular array of linked membranes. This illustration of the mode shapes was generated in COMSOL using an eigenmode analysis of a 10 μm layer of polysilicon in the three membrane shape shown above supported by a central pivot 30 μm radius at the centre of the device.

of the three mode shapes. Comparing the phase difference between any two diaphragms will yield a set of azimuth and pitch angles, which can then be correlated to the set produced by another pair of diaphragms to localize the sound source [129]. Although this sensor is capable of resolving the ambiguity in pitch and azimuth angle it does so by triangulation and offers little improvement over a similarly spaced array of *Ormia* inspired microphones. Another approach is to mimic the structure of the fly ear as a centrally supported diaphragm, which offers three vibration modes: two orthogonal rocking modes about the central gimbal and a translational mode in which the periphery of the diaphragm oscillates in phase [130, 131]. This sensor was constructed from a 30 μm thick bronze foil supported by a 7 mm central gimbal. The diaphragm itself was 21.6 mm wide and backed by an array of four capacitive sensors. Again, given the macro scale of the device and the low resonance frequencies the amplification of the directional cues was slight. Recent iterations of this design have moved to the micro scale and provided stronger coupling, which should in theory provide a higher amplification of directional cues [132] however few experimental results for the directional sensitivity have been published.

3.6.4 Second order devices

Focusing on the use of *Ormia* inspired microphones for use as hearing aids a potential improvement in the rejection of off-axis noise was made through the use of second-order directional microphones. These consisted of two standard central pivot rectangular membranes which were themselves coupled with a flexible hinge [4]. The system can be modelled by first constructing the lumped element model of the two individual directional sensors and then adding the constraint of the central hinge, which holds the near sides of each diaphragm to the same displacement (Figure 3.17). The response model is calculated by assuming the diaphragm is comprised of two rigid plates that move about their hinges. The motion of the system is described in terms of a generalised rotational co-ordinate, $\boldsymbol{\phi}$:

$$2I\ddot{\boldsymbol{\phi}} + C\dot{\boldsymbol{\phi}} + 2G_t\boldsymbol{\phi} = \boldsymbol{Q} \tag{3.54}$$

Here I is the moment of inertia of the diaphragm, G_t the torsional stiffness and C the damping. To express $\boldsymbol{\phi}$ in terms of sound pressure we take the virtual work in

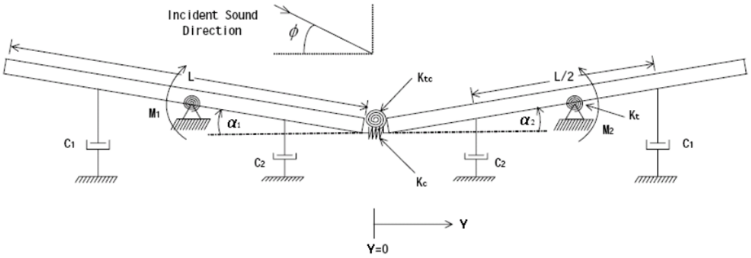

Figure 3.17: 2nd Order directional microphone from [4]. The diaphragms are each connected to the substrate through a central pivot point, and to each other at the near side. Each of the angular displacements ϕ of the diaphragm is then tied to the lateral displacement w.

the system $\partial W = Q\partial\phi$:

$$\partial W = \int_{-2d}^{2d} bp(x,t)\partial w(x,t)dx \tag{3.55}$$

where b is the width of the diaphragm, $w(x,t)$ is the deflection at the central hinge and $p(x,t)$ is the sound pressure. The sound pressure of the harmonic wave is $p(x,t) = Pe^{(}\imath\omega t - kx)$. As the plates are considered rigid the relation of displacement to angular displacement in the generalised co-ordinate system is:

$$w(x,t) = \pm(x+d)\phi \tag{3.56}$$

and the virtual work is therefore:

$$\begin{aligned}\partial W = bPe^{\imath\omega t}\left[-\int_{-2d}^{0} e^{-\imath kx}(x+d)\partial\phi\partial x + \int_{0}^{2d} e^{-\imath kx}(x-d)\partial\phi\partial x)\right] \\ = bPe^{\imath\omega t}2\imath\sin(kd)\left(\frac{2d\cos(kd)}{\imath k} + \frac{2\imath\sin(kd)}{k^2}\right)\end{aligned} \tag{3.57}$$

If the device is sufficiently small that we can assume kd is much smaller than one the relation can be approximated to:

$$Q \approx \frac{4\omega^2}{3c^2}\cos^2\theta d^4 bPe^{\imath\omega t}. \tag{3.58}$$

Solving for the rotation using only the rocking mode obtains:

$$\phi = \frac{2\omega^2}{3Ic^2}\cos^2\theta\frac{d^4bPe^{\imath\omega t}}{\omega_r^2-\omega^2+2\omega\omega_r\xi_r\imath} \tag{3.59}$$

The directivity pattern of the microphone should be proportional to the square of the cosine of the azimuthal angle. Assuming the resonant frequency of the structure as a whole is far below the operating range the angle of rotation of the structure is given by [133]:

$$\phi \approx \frac{2}{3Ic^2}\cos^2\theta d^4bPe^{\imath\omega t} \tag{3.60}$$

In theory, this gives the microphone a wide bandwidth of operation as the relative motion of the two diaphragms is not dependent on the frequency [134]. Again, the sensitivity of the microphone is low and the problem of effective transduction into an electrical signal for this design is particularly pronounced as the ideal measurement point for deflection would occur at the hinge between the two membranes which prohibits some of the simpler and more cost effective schemes of sensing such as capacitive combs. In addition the sensitivity of the second order microphone increases with the square of the surface area, rather than being directly proportional, leading to significant miniaturisation challenges [133].

3.7 Counter sniper detection systems

The firing of a gun produces two main acoustic signals: the first is generated by the muzzle blast and forms a spherical acoustic wave. The second is generated when the projectile travels at supersonic speeds producing a shockwave which emanates as a cone from the trajectory of the projectile [135]. The muzzle blast typically lasts for less than 3 milliseconds and propagates through the air at the speed of sound [136]. Localization based solely on the muzzle blast can be complicated by the sound primarily being directed in the direction of fire, meaning the primary pressure gradient is that of the (assumed unknown) directivity of the muzzle itself rather than the phase difference of the acoustic wave. Additionally reflections from the surrounding ground and buildings will cause secondary signals to be received, as well as distortions caused by temperature and pressure gradients in the air. The acoustic shock wave expands in a conic fashion behind the bullet with the wave front propagating at the speed of sound (Figure 3.18), however as it is formed by

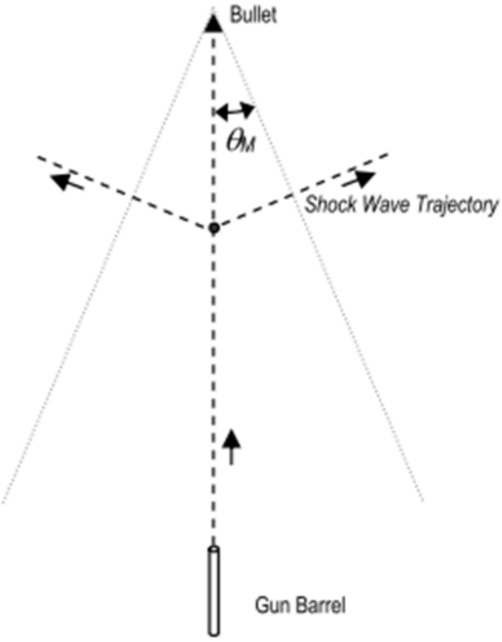

Figure 3.18: Illustration of supersonic shockwave and Mach angle.

a supersonic projectile it is typically the first to arrive at the sensor. The cone trailing the bullet has an inner angle related to the Mach number:

$$\theta_M = \arcsin\left(\frac{1}{M_c}\right) \tag{3.61}$$

where M_c is the Mach number and θ_M is termed the Mach angle [137]. The acoustic shock wave has a near vertical rise to overpressure followed by a more gradual descent to rarefaction and a rapid return to normal which forms a characteristic 'N' shape (Figure 3.19). The time interval of the 'N' wave is proportional to the size of the projectile with the relationship approximated as [138]:

$$\tau_N \approx 1.82\frac{r_b}{v_p}\left(\frac{M_c x}{l}\right)^{\frac{1}{4}} \tag{3.62}$$

where r_b is the projectile diameter, l is the length and d is the separation between bullet and listening point.

Existing localization systems have focused on detecting time of arrival differences of the shock wave in arrays of microphones which typically have a base of 0.5

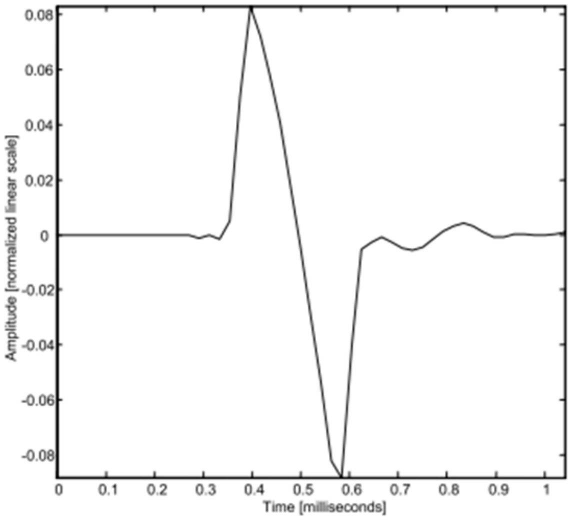

Figure 3.19: Characteristic 'N' shape of acoustic shock wave [136].

- 1 m [13], or measure the time difference of arrival between the muzzle blast and the shockwave [135, 108]. Miniaturisation of the first detection scheme is clearly problematic; however the TDOA between muzzle blast and shockwave also presents problems in terms of the dynamic range of the microphone. The pressure spike from 'N' type compression wave can reach 500 Pa, while the muzzle blast at source is likely to be of the order of 200 Pa and will attenuate rapidly through the air [139]. In addition, the secondary reflections of both the muzzle blast and shockwave from the ground will complicate measurement. In contrast, the short rise times and duration of both the shockwave and muzzle blast, while presenting problems for digital characterization of the signal and classification of the source, give the signal a broad power spectrum (Figure 3.20). The broad frequency spectrum alleviates one of the challenges of *Ormia* inspired microphones for directional sensing - the extremely narrow frequency range in which directional cues may be amplified. Here it is proposed that over such a narrow frequency range the power from either the muzzle blast or shock wave may be treated as essentially flat in the frequency domain. If the input signal is modelled as an ideal impulse the response of an *Ormia* inspired microphone will be the transfer function of that microphone. In practice the measures of mIID and mIPD should be zero or near zero at all frequencies other than that at which the amplification of directional cues occurs, where it will be proportional to the angle of incidence of either the muzzle blast or the shock

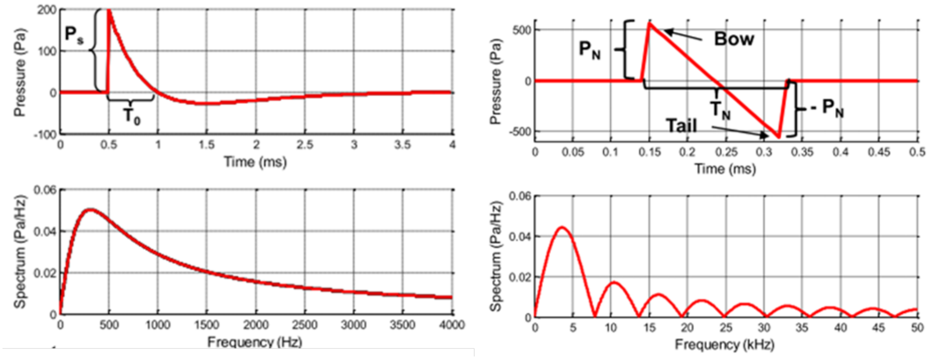

Figure 3.20: Frequency spectrum of muzzle blast from small arms fire [139].

wave. Either the spherical radiation of the muzzle blast or the attack angle of the shock wave may be measured, but localization using the shock wave will still require characterisation of the projectile and estimated Mach cone.

Chapter 4

Design of an *Ormia* inspired MEMS sound localization sensor

Micro-Electro Mechanical System (MEMS) microphones inspired by the auditory system of *Ormia ochracea* offer the promise of micro-scale directional microphones; however amplification of the directional cues available relies on careful tailoring of the system's stiffness and resonance frequencies to the expected damping conditions effectively restricting their use to narrow frequency bands. While some extension of the bandwidth has been shown in more highly damped devices their use is limited due to the catastrophic effect of damping on sensitivity and noise. Current iterations therefore use relatively high Q systems and optimize their operation for a limited amplification of intensity and phase difference that is stable across a wide frequency range [126, 127, 3]. Here the investigation focuses on an alternative approach, inspired by the problem of miniaturisation of counter sniper detection systems discussed in Section 3.7, of optimizing a device for the maximum amplification of directional cues across a narrow bandwidth. This approach is intended for wide band noise, or for the localization of acoustic sources where the spectral signature is already well known. This can have particular applications for counter-sniper detection systems, as well as drone or vehicle detection which, in their existing form, are large, vehicle-mounted or ground based systems [140, 141]. As directional information at any frequency other than the design frequency is now negligible, and the system performs poorly at the transduction of non-directional time domain signals, the device may reasonably be considered no longer to be a microphone but a single purpose sound localization sensor. For these applications the accuracy with which the azimuthal angle to the sound source can be measured is paramount, the critical determinant of which is the rate of change of mIID and mIPD to sound source angle, known as the directional sensitivity. For the purposes of this investigation it is assumed that there will be significant frequency content at around 5 - 8 kHz - a reasonable assumption for both muzzle blast and shock wave detection without focusing on the armaments themselves. More crucial to this thesis is a linear measurement scheme and a high directional sensitivity, both of which transpire to be linked in the hearing system of *Ormia ochracea* [120], and which we show to be achievable in a much more lightly damped MEMS system through careful iteration of the stiffnesses and resonance frequencies. Fabrication of the MEMS microphones was completed by MEMSCAP using their MUMPS process (see Section 1.6.2), with the single layer Silicon on Insulator (SOI) process being the starting point. Designs are therefore constrained to be single layer, although later iterations utilized MEMSCAPS newer PIEZOMUMPS process, which is an extension of the SOI capabilities to include the deposition of a 500 nm thick Aluminium Nitride layer for transduction of the mechanical signals.

4.1 Core ideas

The fundamental idea behind an *Ormia* inspired sound localization sensor is the removal, or vast reduction, of signal processing and filtering. In essence the concept is to use the membrane mechanics to 'process' the signal, resulting in a clear, unambiguous output. To that end we wish the relative power of the membranes motions at the frequency of operation to have a linear relationship with the sound source angle (Figure 4.1). In order to achieve this, and to achieve this at the point of maximum sensitivity and the closest fit to a linear y=mx+c approximation (frequently called here a 'linear' relationship, but not to be confused with the linear superposition of modes referred to in Chapter 3) we must make estimates of bridge stiffness and damping, compare these to the lumped element models of chapter 3 to obtain the 'dual optimization' point and then simulate the response in COMSOL, iteratively tuning the response to the damping and stiffness parameters until we reach a point of testing. The workflow assumed in the following two chapters is outlined in Figure 4.2. The system overview of the first iteration design is that of

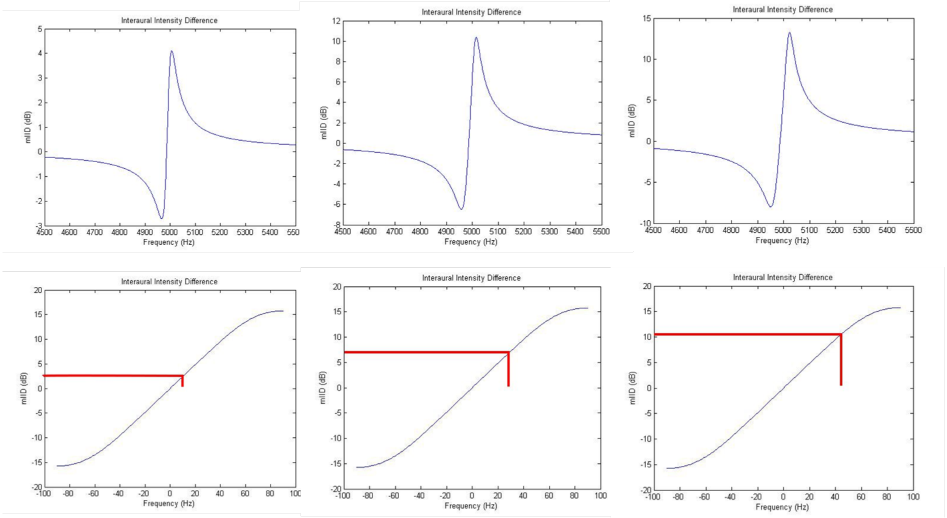

Figure 4.1: MATLAB simulations of a linear mIID response. The ratio of the two resonance frequencies should have a linear relationship with the sound incidence angle of the form y=mx+c where c is ideally zero. This allows a direct reading of sound source angle with no signal post processing.

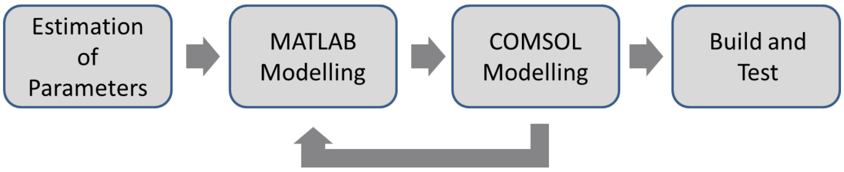

Figure 4.2: Workflow overview for iterative design of coupling bridge stiffness. Initial estimation of damping parameters is fed into lumped element model to obtain idealised resonance frequencies (coupling bridge stiffness). COMSOL simulation of designed system results in updated damping parameters and stiffnesses which are then recalculated in lumped element model to produce next COMSOL model. As the models converge the design is sent to MEMSCAP for manufacture and returned for testing.

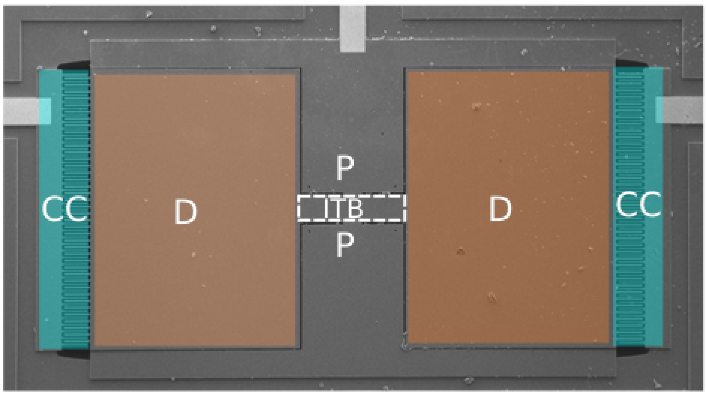

Figure 4.3: Overview of first design. Two diaphragms (D) are linked by an inter-tympanal bridge (ITB) anchored to the substrates by two pivots (P). Transduction is my means of interdigitated capactive combs (CC) at the outer edges of the membranes.

two square membranes with a linking bridge which is itself attached to the substrate by two pivot arms. Transduction is intended to be with capacitive combs located at the outer edges of each of these membranes which are interdigitated with stator combs attached to the anchor layer of the die.

4.2 First iteration - dual optimization

For any given damping conditions the location of the point of dual optimization must be found parametrically. The response of the ADS and NL to the frequency is plotted for a range of coupling strengths. The point of dual optimization can be identified by a local maxima in ADS collocated in the frequency domain with a local minima in NL (Figure 4.4).

4.2.1 Estimation of damping

With the goal of reaching the point of 'dual-optimization' a good estimate of the losses that would be experienced in the sensor would be required before any design could be considered. Since the devices are processed in single-layer silicon with

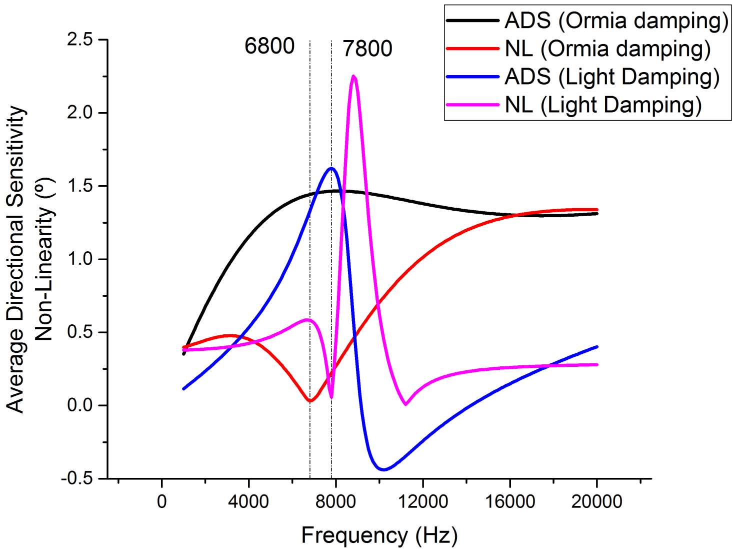

Figure 4.4: Average directional sensitivity and non-linearity for a lightly damped system ($\xi_t = 0.25, \xi_r = 0.16$*) (Blue and purple lines) compared to that of the near critically damped Ormia ochracea ear (*$\xi_t = 1.23, \xi_r = 0.89$*) (Black and red lines).*

a thickness of 10 μm any losses from structural damping or to the mounting is assumed to be negligible, or at least dwarfed by the fluid-mechanical damping. Atypically for microphones thin-film damping is also not significant due to the 400 μm deep back cavity in all the devices presented - a feature which allows claims of low-noise performance for those designs intended for use as hearing-aids [73]. The main sources considered are therefore the slide-film damping from Couette flow around the capacitive combs (when used) and the drag force damping of the membrane itself. Both of these are velocity, and therefore frequency, dependent meaning design of an optimized directional sensor must be an iterative process: beginning with a rough form and frequency range, estimation of damping and then refinement of the design and particularly the coupling strength between the membranes followed by recalculation of the damping and so on. With capacitive combs in place the viscous lateral damping would be expected to dominate [56, 142], however both the damping force from viscous damping and the drag force damping can be calculated as a whole by integrating the viscous stresses around the boundaries of the device in COMSOL's Fluid-Structure Interaction physics models. This is somewhat computationally expensive with the large aspect ratio and small element sizes, so some rough estimation is performed first. Beginning

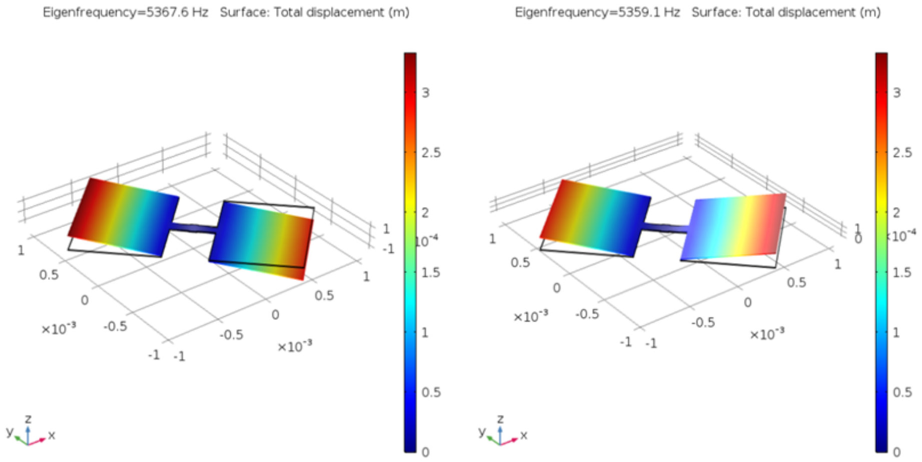

Figure 4.5: Resonance frequencies of 'bow-tie' design MEMS. The combs are not yet present in this design.

with the assumption that our device will work in the frequency range of 5 - 8 kHz - where the majority of the energy from a muzzle blast is concentrated - a simple pair of connected diaphragms is designed and the resonance frequencies simulated through COMSOL's structural mechanics module. The first design uses a 'bow-tie' configuration rather than the flat plates of Miles et al. as it is likely to prove necessary that the rocking mode and bending mode frequencies are relatively close together (Figure 4.5). In contrast, microphones intended as directional hearing sensors require a large coupling strength between the membranes, with the rocking mode below 1 kHz to capture as much as possible of the normal human speech range. The design considerations behind this will be expanded on in the section below. Using this simplified model of the MEMS resonator an initial estimate of the damping is obtained through COMSOL's thermo-viscous acoustics module and performing an Eigenfrequency analysis a second time. This interface includes the thermal and viscous damping in the air domain surrounding the device directly, solving the full continuity and energy equations in addition to the Navier-Stokes of the solo acoustics module. Similarly to the fluid-structure interaction model the thermos-viscous acoustics module is computationally expensive; however by limiting it to the solution of the two Eigenfrequencies of interest a good initial estimate of the damping may be obtained. The output is a complex Eigenfrequency (f_c) with the real component corresponding to the centre frequency of resonance and the imaginary part giving the attenuation factor, α:

$$\alpha = 2\pi \Im f_c \tag{4.1}$$

where $\Im f_c$ refers to the imaginary part of the complex Eigenfrequency. The damping coefficient is then:

$$\xi = \frac{\alpha}{\omega_0} = \frac{1}{2\pi} \frac{\Im f_c}{\Re f_c}. \tag{4.2}$$

For the initial run the estimated complex Eigenfrequencies for the rocking (f_{cr}) and translational (f_{ct}) modes are $5367.3+10.72\imath$ Hz and $5357.2+11.379\imath$ Hz respectively, giving damping ratios of $\xi_r = 0.00199$ and $\xi_t = 0.00212$.

4.2.2 MATLAB modelling of device

Now with a starting point for the resonance frequencies and damping ratios the process of optimizing the design can begin. Using the lumped element model described in Chapter 3 as the basis for a MATLAB program a series of parametric sweeps are run to determine the optimal coupling strength for the estimated damping. Full code is included in the Appendix A along with references to the equations in Chapter 3. First the design is modelled as is, giving rocking and translational frequencies of 5367.3 Hz and 5357.2 Hz respectively for a coupling strength, $\eta = 0.998$. Taking the damping ratios taken as above a frequency sweep of the lumped parameter model is performed with the sound incidence angle at 30°, which shows the extremely narrow band of amplification of sound cues clearly (Figure 4.6). The performance is extremely poor, as can be seen when the same device parameters are swept over the angle of sound incidence at 5360 Hz, the peak of the mIID measure (Figure 4.7). The point of 'dual-optimization' occurs when the directional sensitivity is at a maximum and that corresponds with a local minimum in non-linearity. To solve this problem it is necessary to add calculations for the directional sensitivity around the mid-line, which is taken as the limit:

$$DSmIID_{\theta=0} = \lim_{h \to 0} \frac{mIID(\theta+h) - mIID(\theta)}{h}. \tag{4.3}$$

The non-linearity measure is then simply the difference between the lumped parameter estimate of mIID when swept over the sound incidence angle and the estimated

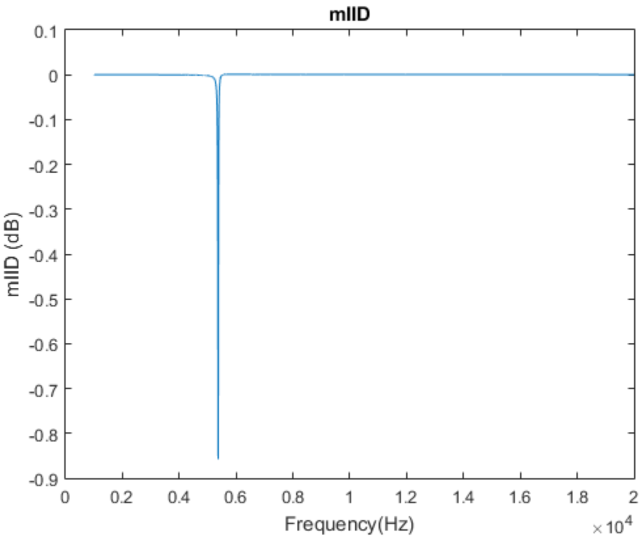

Figure 4.6: mIID for first iteration of design swept through frequencies of 1kHz to 20kHz. The peak occurs at 5360 Hz, very close to the rocking mode frequency.

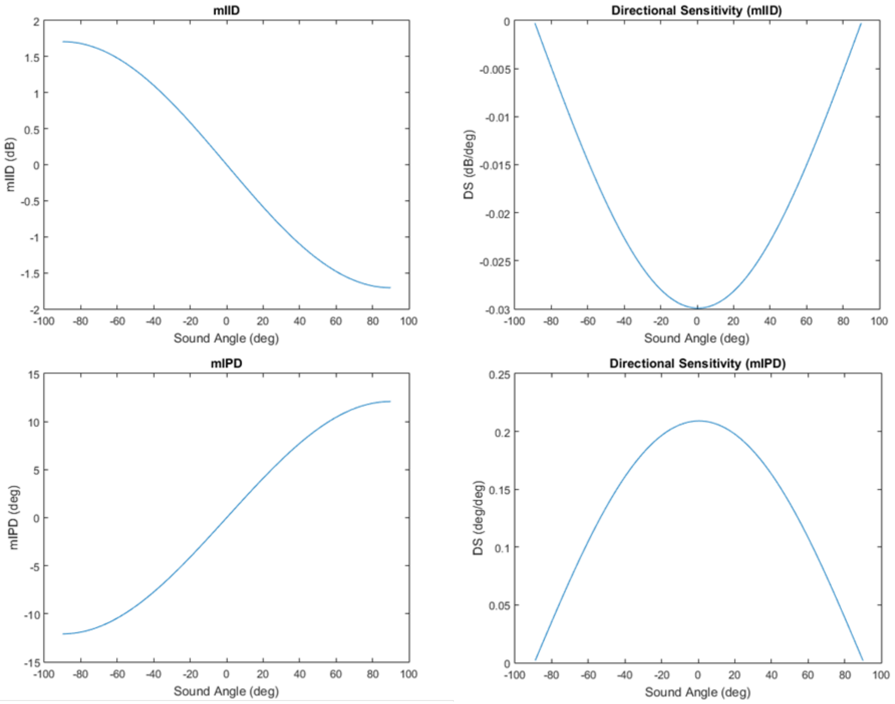

Figure 4.7: First design concept swept over angle of incidence of sound wave in the lumped parameter model. Amplification of directional cues is low and the linearity of the measurement is poor.

Parameter	Value
Plate Length	$2mm$
Rocking Frequency	5367.3 Hz
Damping coefficient in rocking mode	0.00199
Damping coefficient in translational mode	0.00212
Angular sweep area (Θ)	30°

Table 4.1: Estimated damping and rocking mode resonance for an Ormia inspired device.

mIID from equation 4.3:

$$NL = \frac{1}{DSmIID_{\theta=0}}\sqrt{\frac{1}{N}\sum_{n=1}N(DSmIID_{\theta=0}\theta_n - DSmIID(\theta_n))^2} \tag{4.4}$$

The total number of steps in this discretized version of the non-linearity equation in chapter 3 (Equation 3.36) depends on the angular range being considered. Here a range of ±30° is considered as a reasonable range for a linear measurement. The optimized amplification of directional cues is obtained by maintaining the parameters in Table 4.1, while iterating over the coupling strength η. The optimized stiffness for the mIID measure is considered first, and is found at η=1.014, giving a translational mode frequency of 5442.4 Hz (Figure 4.8). While this is the ideal case for mIID, at the same stiffness coefficient the mIPD measure is highly non-linear at the rocking mode frequency, instead appearing to have two local minima above and below the rocking mode frequency (Figure 4.9). A slight improvement in the mIPD measure is possible by strengthening the coupling coefficient; however this comes at the cost of some linearity over the range of ±30°. The coupling strength of η=1.014 is then taken as a good design choice for a device with rocking mode resonant frequency of 5367 Hz. A suitable design would therefore have a translational mode at 5442 Hz.

4.2.3 COMSOL modelling of device

The easiest method to change the relative stiffness of the intertympanal bridge (other than changing the thickness of the device) is to alter the length and width of the two pivots which anchor the device to the substrate. The model tested used a 100 μm × 400 μm bridge supported by pivots 6 μm × 70 μm, giving resonance frequencies at approximatly 4826 Hz and 4893 Hz for the rocking and translational

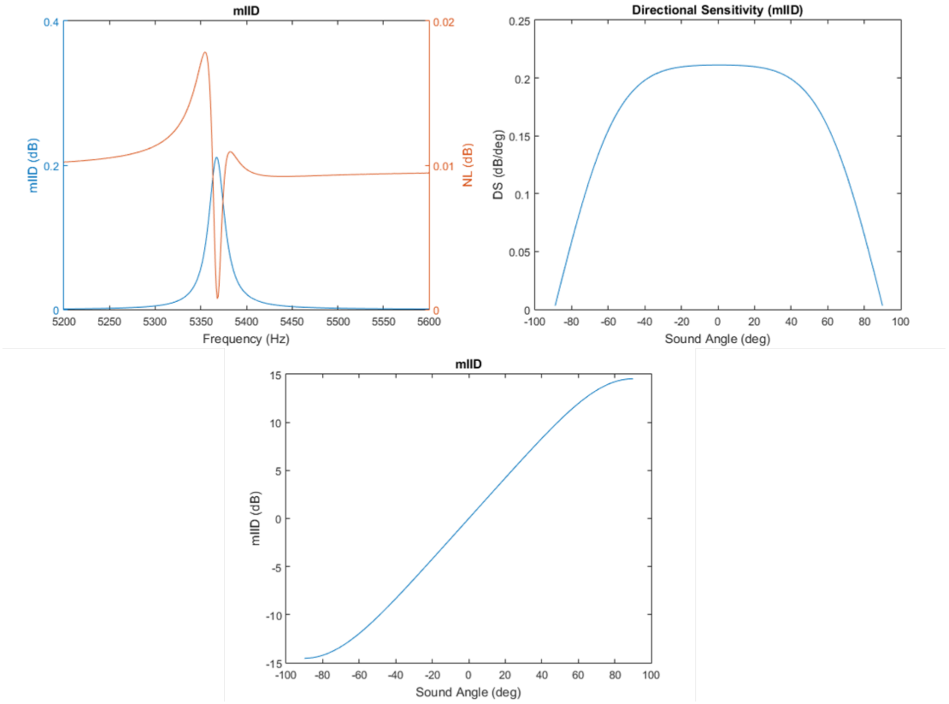

Figure 4.8: Optimized mIID over a range of 30° is found with coupling stiffness coefficient of 1.014. (Top Left) The maximum mIID at the midline is co-located with the minimum in non-linearity. At higher coupling strengths the mIID at the midline increases further but at the expense of linearity. (Top Right) The directional sensitivity at 5367 Hz shows a constant sensitivity at 0.2 dB/° between -30° and 30°. (Bottom) The mIID at 5367 Hz for the optimized system.

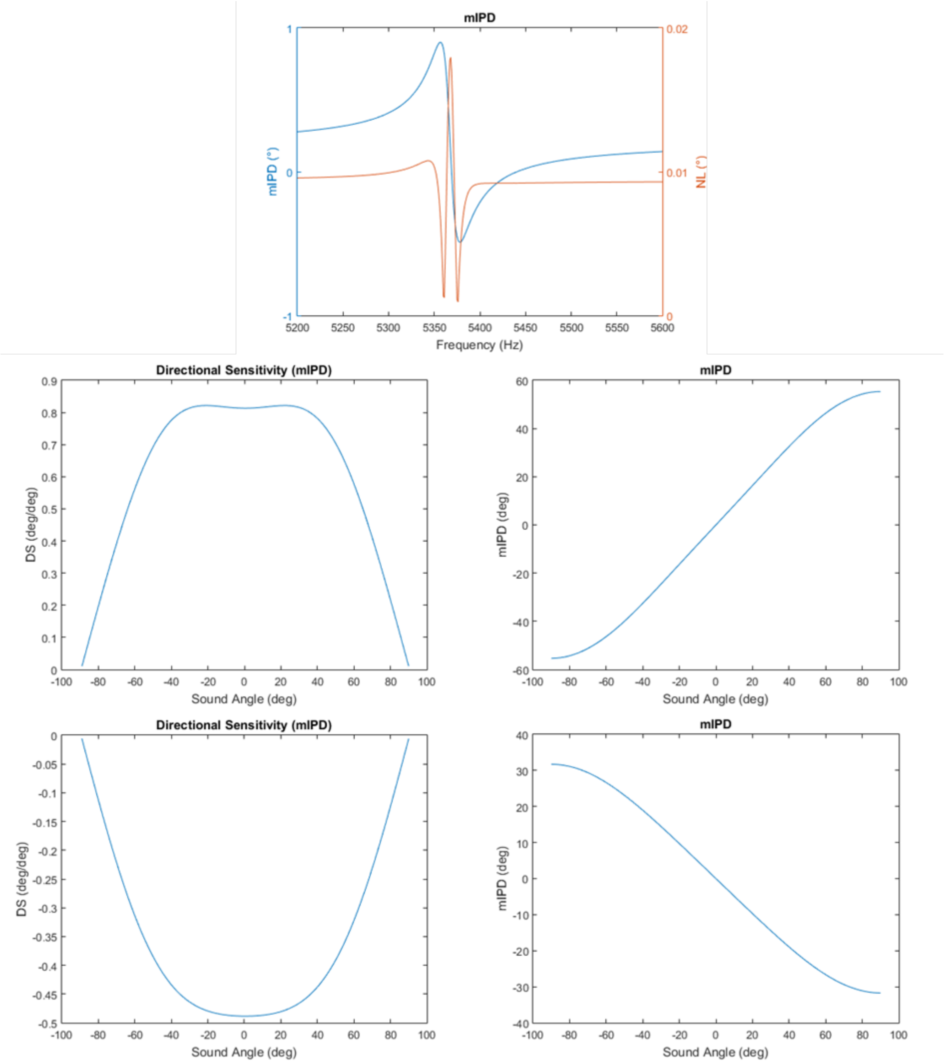

Figure 4.9: mIPD at the same stiffness coefficient as above. Two local minima appear by the local maximum above and below the rocking mode frequency (Top). (Centre Left) A directional sensitivity of 0.8°/° is seen at the lower minimum at 5361 Hz, but there appears to be some non-linearity in the signal. (Centre Right) The mIPD measure at 5361 Hz. (Bottom left) At 5377 Hz a lower directional sensitivity is shown and the range appears to be less. (Bottom right) The mIPD at 5377 Hz.

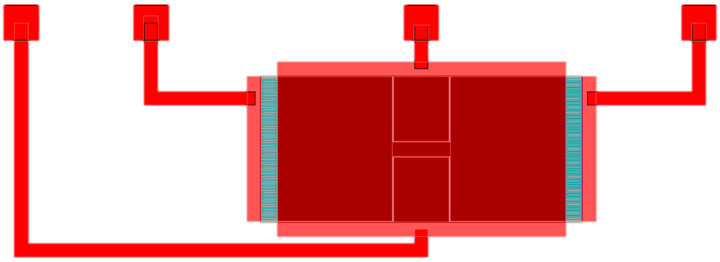

Figure 4.10: Layout of first iteration design with comb finger capacitance sensing. Each wing of the diaphragm is 800 μm × 1000 μm while the bridge is 400 μm × 100 μm supported by two 75 μm × 6 μm pivots. Each of the combs is 100 μm long by 6 μm wide with a gap of 6 μm between the stator and rotor combs. Electrical connections to wire bond pads extend from the left and right combs and a ground plane is attached to the membrane through the pivots.

modes respectively (Figure 4.10). Using the acoustic structure interaction simulation the frequency is first swept around the resonance frequency range with the sound incidence angle at 30° to the midline (the predicted limit of the linear region) to confirm both the resonance frequencies and the mIID gain. The point evaluation of the amplitude of displacement in the z-axis and the instantaneous phase are taken at the outer corners of each membrane (Figure 4.11). The simulation is then run again at the frequency showing the maximum mIID, this time holding frequency constant and sweeping the sound incidence angle between ±90° around the y-axis (the azimuthal angle). The results shown in Figure 4.12 are markedly different to the lumped parameter analysis, although both show significant amplification of directional cues around the midline. The lumped parameter model does not account for the sound diffraction around the device, which is simulated here as having the rear of the device closed. Since the device contains an air gap, sound also diffracts around the membrane and this diffraction is dependent on both the sound frequency and the angle of incidence. The standard models use the pressure at the midline of the device as a reference and calculate the pressure on each wing of the device as a function of the phase change over half the diaphragm length. Hence:

$$p_1 = A_0 e^{\frac{\imath\omega\tau}{2}} \tag{4.5}$$

This assumes that the pressure behind the membrane is unchanged, which is not the case for the see-saw devices. Homentcovschi et al. [143] presented a solution to the Helmholtz equations for a simplified system which showed the forces and

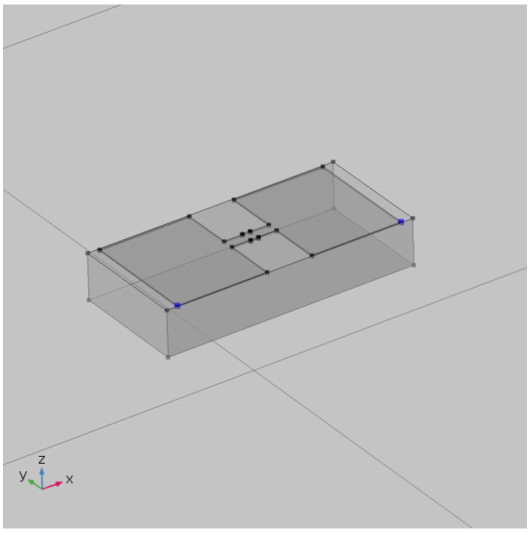

Figure 4.11: Point evaluation at tips of the membranes. The amplitude and phase of motion in the z-axis were recorded to obtain the results below.

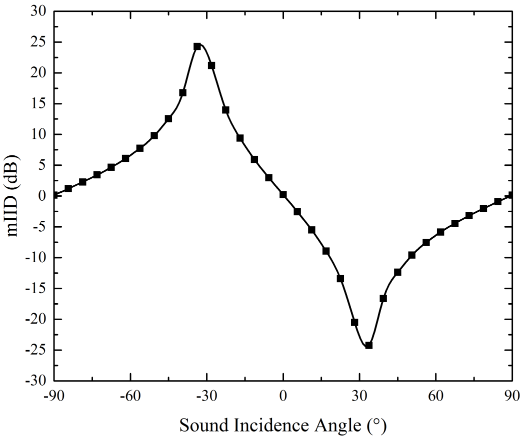

Figure 4.12: Simulated mIID swept over sound incidence angle at 4850Hz. Compared to the lumped parameter model this simulation shows a sharper peak and the mIID drops to zero at 90°.

moments on the diaphragm varied with the air gap around the device and the depth of the back chamber. Broadly, the problem is similar to that of diffraction around a thin disk: the diffraction of the sound field can be considered as the linear superposition of the incident plane wave and a diverging wave centred on the disc (which is assumed to be generated by the vibration of the disc). At low frequencies, where $kr << 1$ with k being the wavenumber and r the radius of the disc, there is a small intensification of the sound field in front of the disc and a very small reduction behind it, resulting in far less force being imparted on the disk [144]. At 5 kHz $kr \approx 0.1$ for 1 mm radius disc, resulting in a very limited pressure difference between the front and rear faces. Counterintuitively the net pressure on the sensor increases when the back side of the cavity is left open since there are now two paths to the back side of the membrane: diffraction around the membrane itself and diffraction around the membrane and wafer. The relative influence of each of these pressure paths with respect to the angle of incidence of the incoming wave can be shown using COMSOL (Figure 4.10). The integrated net pressure on each wing of the membrane is calculated for the same membrane with the rear of the handle wafer exposed and closed. The exposed simulations show over double the net pressure on both wings of the membrane (and in simulations, a far higher amplitude of displacement) than those with a closed back. The phase of this net pressure approaches anti-phase between the left and right membranes at 90° in the case of the open backed membrane, and 45° in the case of the closed backed membrane. The latter case coincides with the unexpected spike in mIID in the COMSOL simulation, which has the unfortunate effect of both reducing the range of the desired linearity as well as severely hampering the mechanical sensitivity of the membrane.

4.2.4 Results

The devices returned from MEMSCAP (the primary device tested here is shown in Figure 4.14) were characterised using the 2D scanning laser vibrometer (See section 2.1). The die under test is mounted on a 70 mm x 30 mm PCB base with a through hole drilled centrally. The die is then placed so that the device under test fit over this hole, and the board mounted vertically. Laser vibrometry measurements are taken from the rear of the die, through this drilled hole and stimulated with a Heil Air-Motion Transformer at a distance of 80cm from the

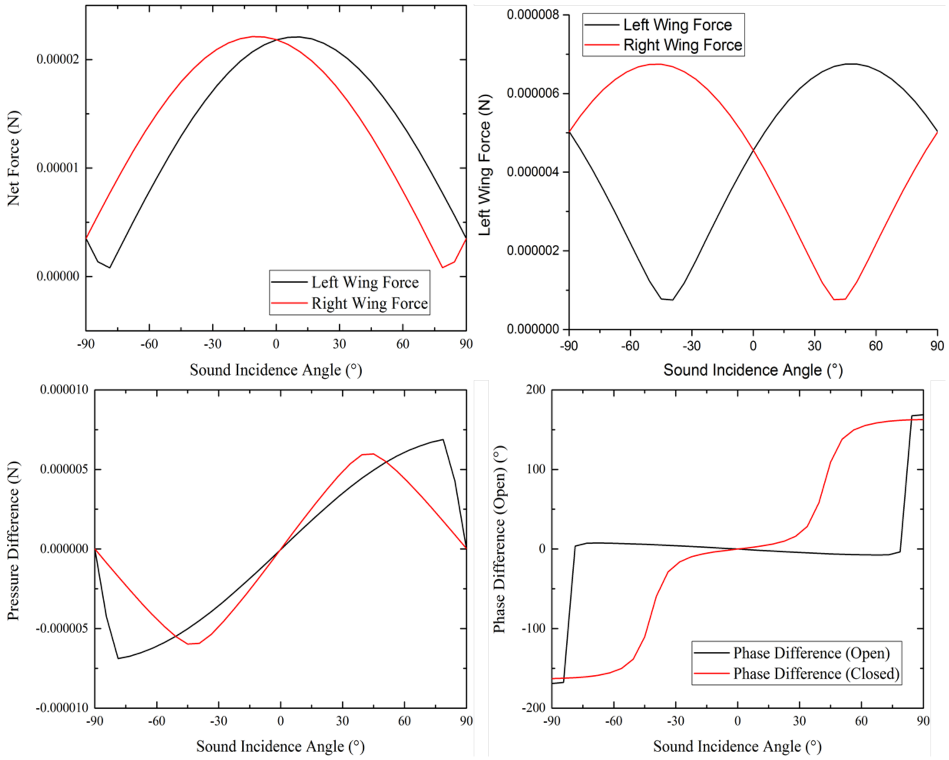

Figure 4.13: Finite element simulations of average net pressure on membrane with open back (top left), closed back (top right) and force difference between left and right membranes (bottom left) all at 5 kHz. The net force with the open back is 2.5x larger than that of the closed back, however the pressure difference between the membranes varies only in shape. On the bottom right is the phase difference between the forces on the left and right membrane, showing the forces sharply moving to antiphase in the open backed model as the sound incidence angle approaches 90°.

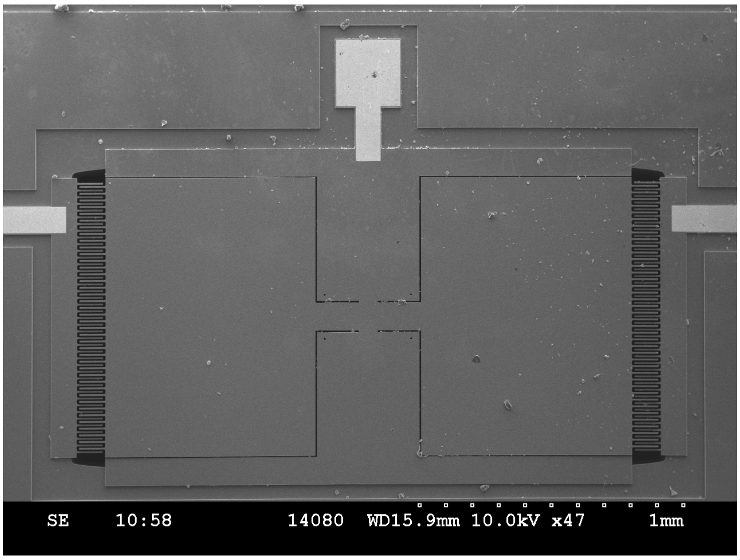

Figure 4.14: SEM Image of Fabricated device

device. The sound source is then moved in 5° increments around the device under test. Reference pressures are taken with a Bruel and Kjaer 4138 microphone placed 1 cm from the device under test. Resonance frequencies are found at 5130 Hz and 5150 Hz giving a bridge stiffness coefficient η of 1.004, significantly smaller than the 1.014 intended (The simulated resonance frequencies were 4826 Hz and 4893 Hz). In addition the damping measured from the half power bandwidth of the resonant peaks are estimated at 5.6×10^{-3} and 5.9×10^{-3} for the rocking and translational modes respectively rather than the estimated 0.00212 and 0.0019 from COMSOL's thermos-viscous Eigenfrequency simulation. As might then be expected the estimation of sound source angle from these devices was poor (Figure 4.15). It might have been anticipated that although the device was far from optimal a good measurement of sound source angle may have been obtained, at least with optical measurement. Previous literature on these devices has boasted of the extremely good signal to noise ratio possible as a result of eliminating the capacitive backplate and the thermal noise associated [126, 3], very much making a virtue of a necessity. Measured displacement in a silent soundproof chamber using the MSA-100-3D 3D laser vibrometer gave a signal due to noise across the spectrum below resonance of 10.76 pm while with a sound source at 5 mPa (45.29 dB ref 20 μPa) the signal power was 0.25 nm giving a signal to noise ratio of 27.2 dB, while around the rocking mode resonance the noise between 5125 Hz and 5135 Hz is 71.59 pm with a

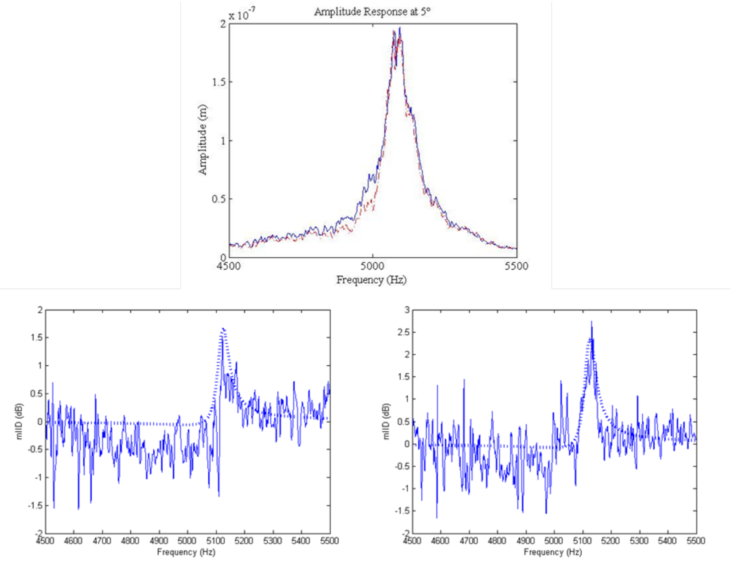

Figure 4.15: (Top) Amplitude response of ipsilateral (blue) and contralateral (red) membranes at 5°. The gain at 5 kHz appears to be a function of noise rather than a true amplification of directional cues. (Bottom panels) mIID measured from ratio of amplitudes at ipsilateral and contralateral membranes at 30° (left) and 45° (right) is shown as a solid line compared with lumped parameter model prediction corrected for measured damping (dashed line). The noise in the mIID measure is readily apparent.

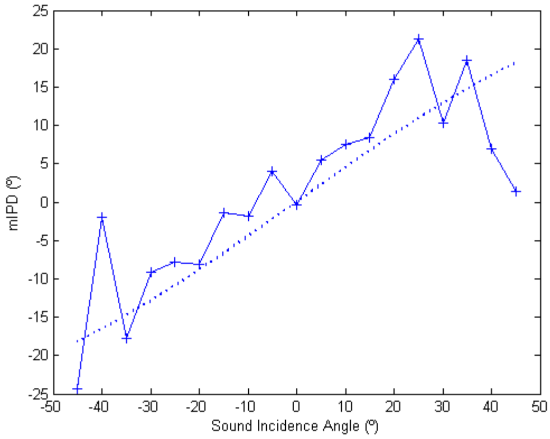

Figure 4.16: Measured mIPD against sound incidence angle at 5080 Hz, the best linear gain in phase for this device. The dashed line shows the estimated mIPD from the directional sensitivity at 0°. Again there is considerable error in the measurement.

signal of 15.588 nm for a SNR of 46.7 dB. At first inspection in the mIID measure the SNR is clearly much poorer. The immediate observation is that this measurement is obtained by taking the ratio of two noisy signals, which would lead to a Cauchy-like distribution in the mIID and mIPD signals. While the devices returned were far from optimal, measurements of sound source angle is far more hampered by this Cauchy noise than by the failure of the optimization of the device (Figure 4.16 and Figure 4.17). In the mIPD measure the estimated directional sensitivity at 5080 Hz is 0.425 degrees phase difference per degree change in azimuthal angle with a mean squared error of 1.69° (the predicted mIPD directional sensitivity was 0.8 degrees phase per degree azimuth). In the mIID measure the best estimate of directional sensitivity was 0.05 dB per degree change in azimuthal angle (against the designed for 0.2 dB/°) with a mean squared error of 0.125 dB. The out of plane displacement of the device due to the residual stress gradient was measured using a white light interferometer (Wyko NT1100 Optical profiler). Of primary interest is the engagement of the stator and rotor capacitive combs, crucial to obtaining an electrical signal from the device. The comb offset is measured at approximately 6 μm, with the comb thickness of 10 μm the combs are therefore largely disengaged at rest (Figure 4.18 and Figure 4.19). Attempts to obtain an electrical signal from this device were inconclusive, given the already small anticipated capacitance of

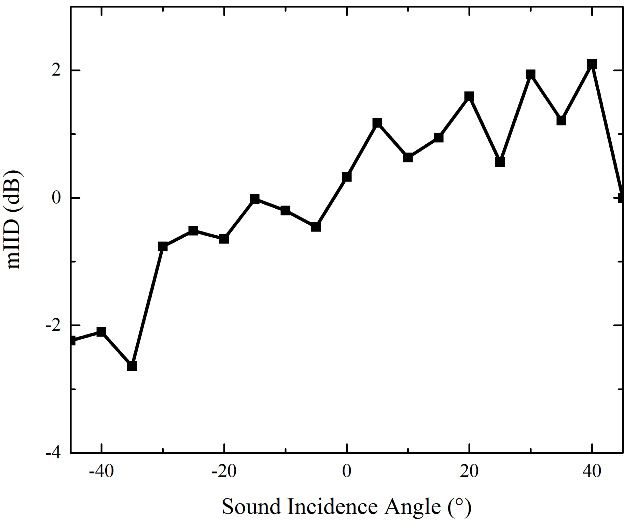

Figure 4.17: For the mIID measure against sound incidence angle at the predicted 'best' gain at 5130 Hz the power difference compared to the noise is so low as to make any measurement of sound source angle here a failure.

the device and the large offset between the stator and rotor combs. In addition, even relatively small bias voltages (beyond 20V) were found to increase the pull in of the combs to the point of short circuit since the thin pivots and slender coupling bridge gave the device some rotational compliance around the z-axis.

4.3 Discussion

While the first run undoubtedly failed to meet any of the planned objectives, the problems which arose from this design suggested new design paths that could be pursued. The first, and most obviously solved problem, was the incorrect estimation of the damping parameters - given by the thermo-viscous acoustic-solid interaction simulation as twice the measured value. Measurements taken omitting the thermal and viscous effects in the boundary layers returned damping estimates of 7.55×10^{-5} and 1.7×10^{-5} for the rocking and translational modes respectively, results that were considered obviously wrong. Perhaps more worrying is that the damping was overestimated even given the omission of the comb drives from the 3D model (due to the difficulty in meshing such small features). An explanation for the poor modelling of thermo-viscous losses in this type of simulation has so far not been found. It had been speculated that the large differences in scale and

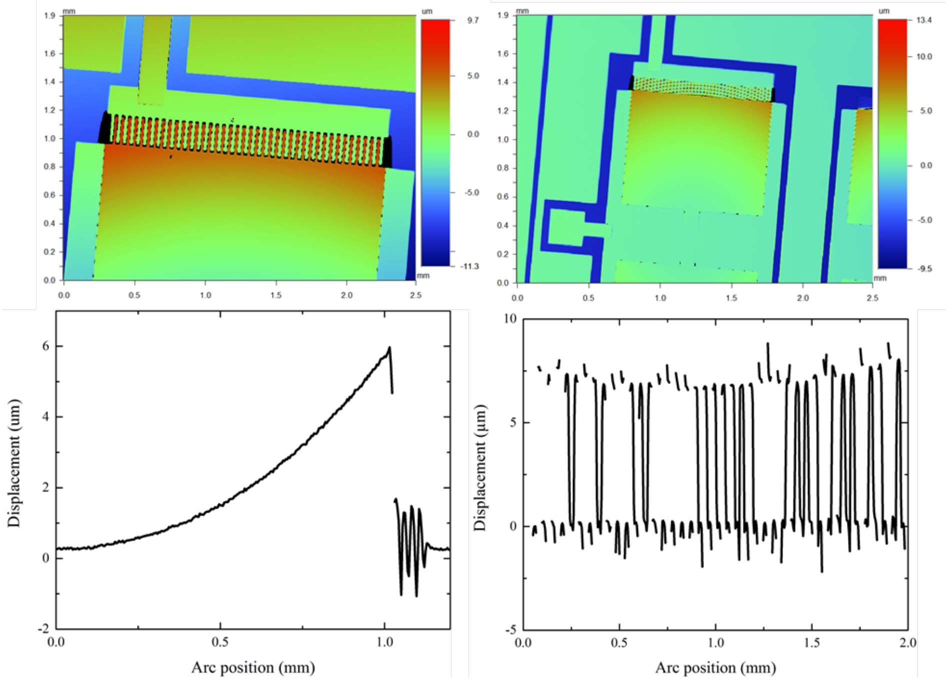

Figure 4.18: (Top left) Spectral plot of surface elevation for the fabricated device. (Top right) Close up plot of the capacitive comb sensors showing the large offset between the stator and rotor combs. (Bottom Left) Measured curvature of membrane along an arc on the midline of the device. The displacement at the edge of the device is approximely 6 μm. (Bottom Right) Surface profile along an arc across the width of the stator combs showing the 6 μm offset between stators and rotors.

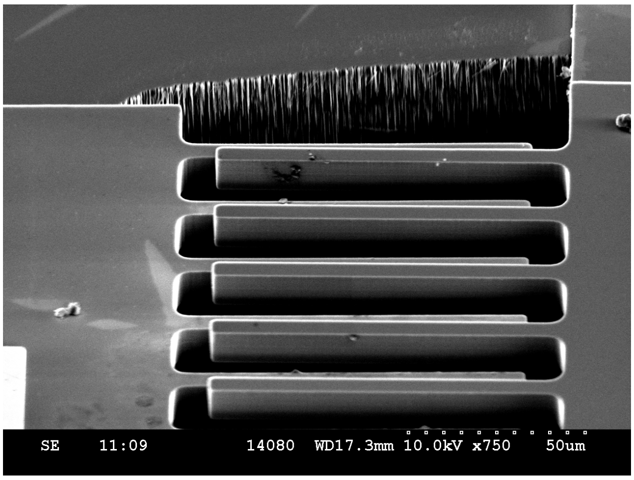

Figure 4.19: SEM image showing the disengagement of the combs due to the residual stress gradient in the material.

large aspect ratio have led to inappropriately coarse meshing in the boundary layers around the devices, however given minimum element sizes of 2 μm for the fine detailed regions and a predicted thermal boundary layer of 31 μm at 5 kHz the resolution of the boundary layers should be sufficient. An alternative strategy for estimating the damping is therefore required, and in the subsequent sections the use of a Fluid-Structure interaction simulation is investigated to obtain the shear force on the device. In addition, the measured damping parameters of the first iteration device can be used as a starting point and a sanity check. The second problem lies in the electrical transduction of the signal where, due to the unavoidable curvature of the membrane from the residual stress gradient, a capacitive comb sensing system is forced to compromise between mechanical sensitivity and electrical sensitivity. During the course of this research publications from other laboratories made comparisons of this trade-off, with the conclusion that prioritising the electrical signal, and the engagement of the combs, was the most beneficial arrangement and suggesting the use of 25 μm thick combs to reduce the effect of the stress gradient at the cost of device sensitivity [145]. However an alternative scheme also became available through MEMSCAP's PIEZOMUMPS service in 2013, which allowed a SOI MEMS wafer to be patterned with a 500 nm thick aluminium nitride layer, offering the potential to avoid this conflict. The final and far more insidious problem is that of the Cauchy-like noise, which, if truly Cauchy-like, will not respond to averaging and will see little benefit from improving the already reasonable SNR of the device. Correspondence with other research groups working on similar devices has revealed this to be a well-known, but rarely spoken of or published, problem with no obvious solution. The only practical method for obtaining more accurate directional measurements would therefore be to increase the directional sensitivity of the device - which given the intended design was theoretically optimized over the range of ±30° can only be done at the expense of the angular range in which the measurement would be linear.

4.3.1 Uncertainty from ratio of noise distributions

In the previous section it was stated that improving the SNR of the microphone would have limited impact on the error in the mIID measurement. In this section an attempt is made to understand and quantify the error in the mIID measurement. Working on the assumption that the amplitudes of each of the membranes in the device follow a Gaussian distribution with mean μ_x, μ_y and variance σ_x^2 , σ_y^2 we know that for the case where $\mu_x = \mu_y = 0$ the distribution of the ratios will be a Cauchy distribution. Since the distribution of $\boldsymbol{U} = \boldsymbol{X}/\boldsymbol{Y}$ is:

$$P(u) = \int_{-\infty}^{\infty} |y| f(\boldsymbol{u}, y, y) dy \tag{4.6}$$

$$= \frac{1}{2\pi\sigma_x\sigma_y} \int_{0}^{\infty} |y| e^{-\left|\frac{y^2}{2\sigma_y^2} + \frac{u^2y^2}{2\sigma_x^2}\right|} dy. \tag{4.7}$$

Since:

$$\int_0^{\infty} y e^{ay^2} dy = \frac{1}{2a} \tag{4.8}$$

the probability density function is then:

$$P(u) = \frac{1}{\pi\sigma_x\sigma_y} \frac{1}{2\left(\frac{1}{2\sigma_y^2} + \frac{u}{2\sigma_x^2}\right)} \tag{4.9}$$

$$= \frac{1}{\pi} \frac{\sigma_x\sigma_y}{u^2\sigma_y^2 + \sigma_x^2} \tag{4.10}$$

$$= \frac{1}{\pi} \frac{\frac{\sigma_x}{\sigma_y}}{u^2 + \left(\frac{\sigma_x}{\sigma_y}\right)^2} \tag{4.11}$$

This is a Cauchy distribution. Plotting a histogram of the mIID measurements at 0°, where the mIID is expected to be 0 dB it can be seen that the distribution has the distinctive fat tails of a Cauchy distribution (Figure 4.21). The interquartile from this example is 0.97 dB, while the median is slightly skewed from the expected 0 dB at 0.2 dB. In the case here the distributions of the amplitudes of vibration do not have zero mean, and so we employ Hinkley's formulation to obtain the distribution [146]:

$$P(u) = b(u) \cdot \frac{d(u)}{a^3(u)} \frac{1}{\sqrt{2\pi}\sigma_x\sigma_y} \left[\Phi \frac{b(u)}{\sqrt{1-\rho^2}a(u)} - \Phi \frac{-b(u)}{\sqrt{1-\rho^2}a(u)} \right] + \frac{\sqrt{1-\rho^2}}{a^2(u)\pi\sigma_x\sigma_y} e^{-\frac{c}{2\sqrt{1-\rho}}} \tag{4.12}$$

where:

$$a(u) = \sqrt{\frac{1}{\sigma_x}u^2 - \frac{2\rho u}{\sigma_x\sigma_y} + \frac{1}{\sigma_y}} \tag{4.13}$$

$$b(u) = \frac{\mu_x}{\sigma_x^2}u - \rho\frac{\mu_x + \mu_y u}{\sigma_x\sigma_y} + \frac{\mu_y}{\sigma_y^2} \tag{4.14}$$

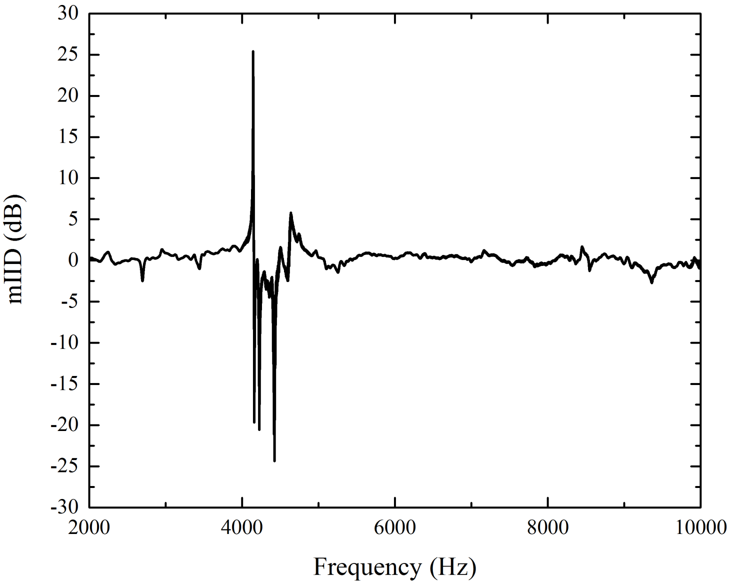

Figure 4.20: The distribution of mIID over the range of 2 kHz - 10 kHz. The expected reading at all frequencies is 0, however the measured values show spikes as high as 25 dB.

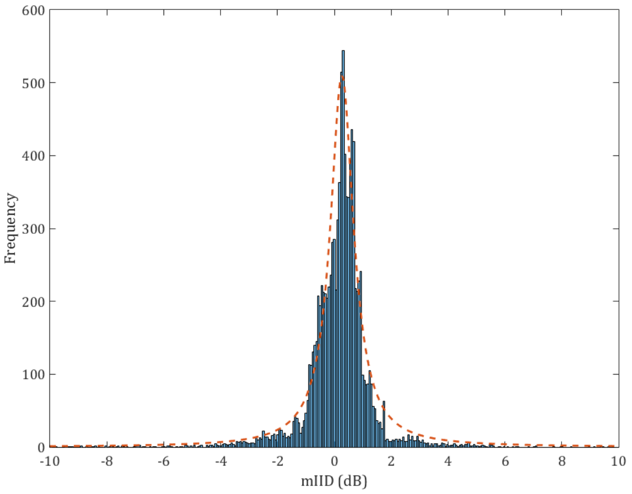

Figure 4.21: The distribution of the measured mIID has a median of 0.026 dB. The dashed line represents a Cauchy distribution with positive scale parameter of 0.5 and a location parameter of 0.

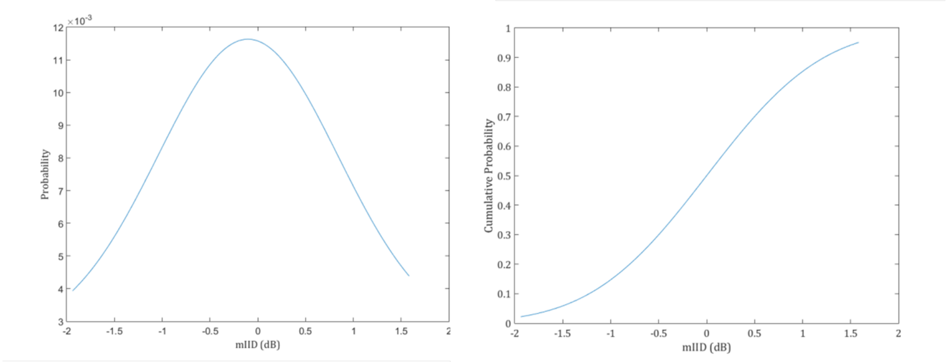

Figure 4.22: Probability distribution function (left) and cumulative distribution function (right) for Hinkley distribution with $\mu_x = \mu_y = 0.2nm$ *and* $\sigma_x = \sigma_y = 10pm$. *In this example, which follows the SNR below the resonant peaks, the interquartile range is 1.2 dB.*

$$c(u) = \frac{\mu_x}{\sigma)x^2} - \frac{2\rho\mu_x\mu_y}{\sigma_x\sigma_y} + \frac{\mu_y}{\sigma_y^2} \tag{4.15}$$

$$d(u) = exp\left[\frac{b^2(u) - ca^2(u)}{2(1-\rho^2)a^2(u)}\right] \tag{4.16}$$

and Φ is the cumulative distribution function of the normal distribution. For the case where X and Y are independent ($\rho = 0$) and $\mu_x = \mu_y >> \sigma_y$ the Hinkley distribution is centred on 0 dB (Figure 4.22). An alternative approach to ratio distributions is given in Cedilnik et al. (2004) [147], which describes the probability density function as a product of a Cauchy-like function and a 'deviant part', with the Cauchy part of the function dependent only on the correlation and the standard deviations of X and Y. With either method, the Cauchy-like distribution function is inevitable however an increased SNR, as would be found at the resonant peaks, will reduce the interquartile range of the distribution. At the highest SNR (near the translational mode resonant peak) the interquartile range is reduced to 0.12 dB, which given an ideal directional sensitivity of 0.2 dB per degree still represents a significant potential error. More detailed measurements of the effect of SNR on the measurement error are made in later iterations of the device and are described in section 4.2.4.

Chapter 5

Revision and optimization of MEMS sound localization sensors

The principle concern in the second iteration of the device was overcoming the noise due to the relatively large interquartile range from the ratio of two noisy signals. A brute force approach would be to increase the directional sensitivity, preferably beyond even that of the optimized sensitivity described in section 4.2.2. This approach is realisable by sacrificing the angular range in which a linear measurement can be made, i.e. instead of optimising for linearity over a range of ±30° we can optimize over ±10°. Secondly a more robust method for estimating the damping must be developed, and now with the advantage of a physical device to test any models against. A similar problem can be found in the study of the mechanical properties of comb actuated micro-mirrors, where the major source of damping is discovered to be the shear force damping between the stator and rotor combs [148, 54, 56, 142]. COMSOL simulations focusing on the 2D simulation of the fluid-structure interactions on the comb sensors were created and compared to the first generation device, and then used to predict damping in the next iteration. Finally with the advent of MEMSCAP's PIEZOMUMPS process, the use of Aluminium Nitride as a piezoelectric transducer is investigated.

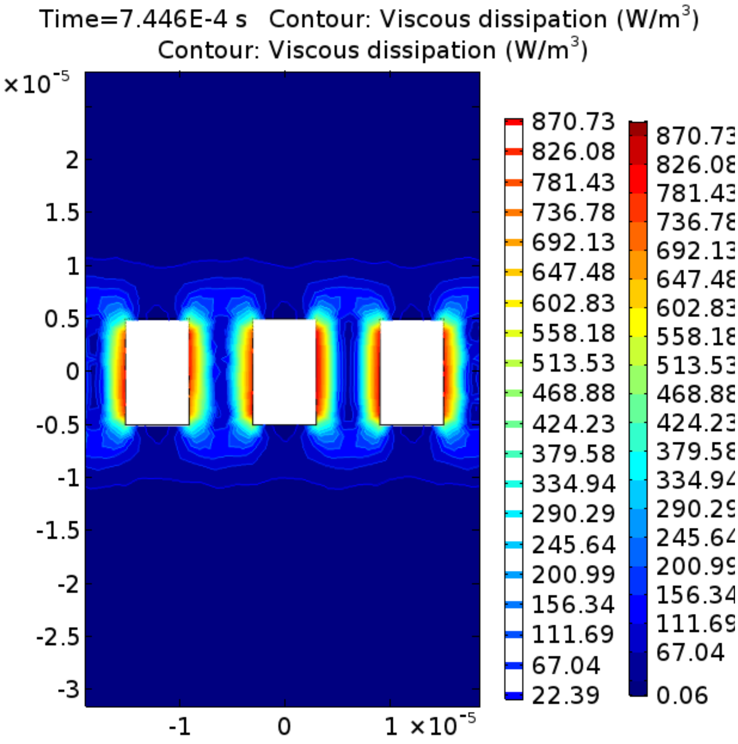

Figure 5.1: Viscous dissipation around the comb drives.

5.1 Revisited damping model

In order to correct the previous underestimation of damping the viscous damping around the capacitive combs are considered separately from the thermal and viscous boundary layers around the device itself. The first model considers the viscous stresses around the capacitive combs in a 2D time dependent fluid structure interaction model (Figure 5.1).

The model was simulated by creating a 2D cross section of the capacitive combs, and designating the combs alternately 'stators' and 'rotors'. The stators were fixed in place while the rotors were given a prescribed velocity in the y-direction of $2\pi f A \sin(2\pi f t)$, with A being the amplitude of displacement. Here a reasonable value of 1 μm was chosen. The viscous stress in the y-direction was then integrated around the boundaries of the rotor combs to provide the damping force (Figure 5.2). This approach gives a far more accurate estimate of the damping with a mean value of 0.0051 compared to the measured values of 0.0053 and 0.0058.

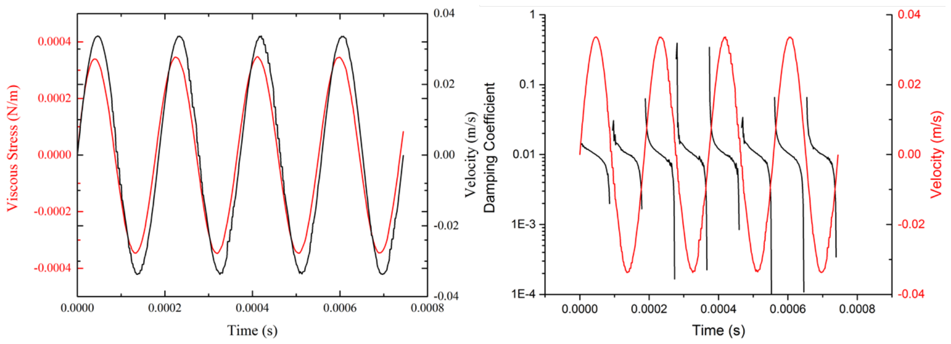

Figure 5.2: (Left) comparison of Viscous stresses and velocity around the capacitive combs. A slight phase lag is evident between the velocity and viscous stresses. The right panel shows the damping coefficient, which centres at 0.005.

5.2 MATLAB modelling

Using the same method as described in section 4.2.2. the average directional sensitivity (ADS) and (NL) for the lumped parameter model is calculated in MATLAB. 'Over-coupling' beyond the point of dual optimization shows a distinctive dual minima shape in the mIID measure of sensitivity (Figure 5.3). Increasing the coupling strength further shows the minima no-longer present when calculating the non-linearity over an angular range of ±30°; however they do still occur when calculating over an angular range of ±10°. Similarly in the mIPD measure over-coupling causes the minima in non-linearity no longer to coincide with the maximum ADS, however the ADS at the linear measurement place is still higher than that of the dual optimized case again accepting the loss of angular range (Figure 5.5).

5.3 Transduction via piezoelectric sensing

MEMSCAP's PIEZOMUMPS facility offers the ability to deposit a layer of 500 nm of Aluminium Nitride with a given d_{33} of 4 - 6 pC/N [75]. From the COMSOL simulations of the first iteration design the points of maximum stress, and therefore the most likely locations for piezoelectric sensing, occur in the coupling bridge. Unfortunately a significant portion of the stress is also found in the torsion of the pivots anchoring the bridge to the substrate (Figure 5.6). In order to prevent loss of information from missing the torsional stresses around the pivots an alternative design is adopted where the piezoelectric sensing is achieved by connecting four lever arms to the end of each membrane. This device design follows a strategy

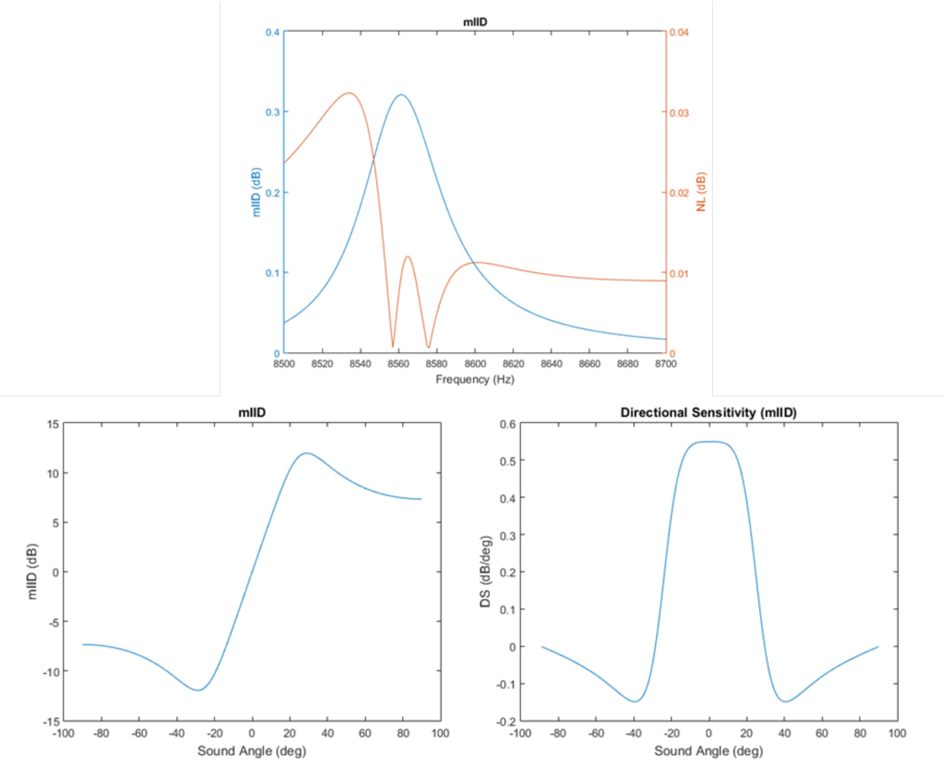

Figure 5.3: Theoretical example of an over-coupled device. (Top) Two minima in Non-Linearity are found above and below the maximum ADS. Although the minima no longer coincide with the maximum ADS, the ADS at those minima is larger than the 'dual-optimized' case in section 4.2.2. The angular range over which non-linearity is measured is still ±30°.(Bottom left) The compromise required can be seen in the mIID measure swept over sound incidence angle. The angular range of linear measurement has decreased. (Bottom right) Here an ADS over the midline of 0.5 dB per degree is predicted.

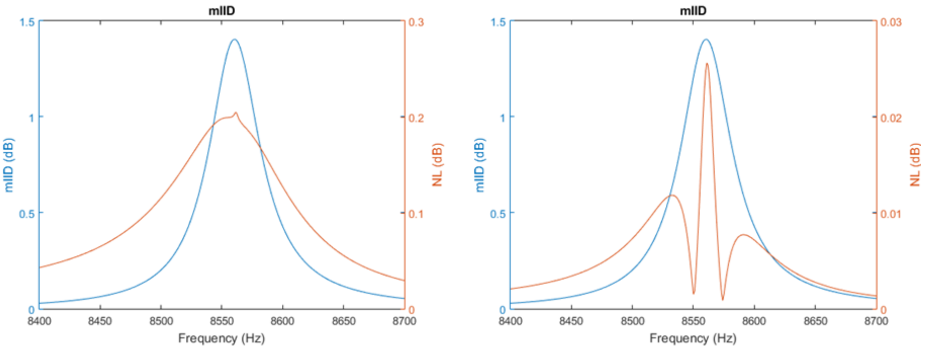

Figure 5.4: Comparison of ADS and Non-Linearity for coupling coefficient η=1.085 with damping coefficients $\xi_r = \xi_t = 0.005$ over a range of $\pm 30°$ (left) and over a range of $\pm 10°$ (right).

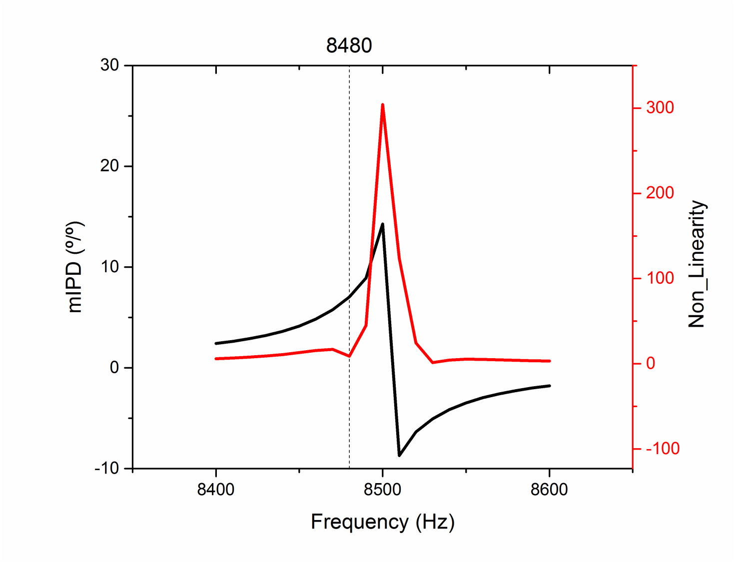

Figure 5.5: : Theoretical average directional sensitivity and non-linearity in an 'over-coupled' device. Here it is the maximum non-linearity which is aligned with the maximum directional sensitivity, as opposed to the 'dual optimized' case where the minima in non-linearity and the maximum directional sensitivity are co-located. The increase in directional sensitivity from over-coupling allows operation away from the maximum while still showing an improvement over the sensitivity of the dual optimized design with only a slight increase in non-linearity. The spike in non-linearity manifests as a null in directional sensitivity within 1° - 2° of the midline.

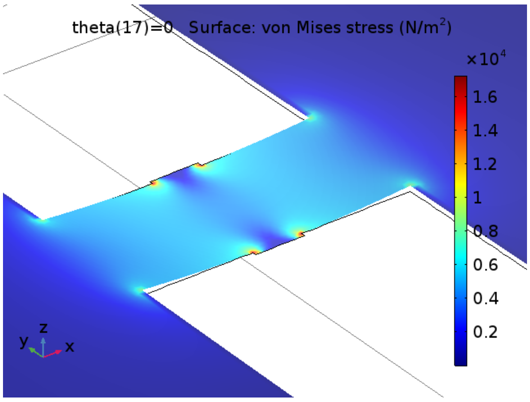

Figure 5.6: COMSOL simulation of Von Mises stresses in first iteration of device. Stresses are concentrated around the coupling bridge, with significant stresses around the pivots.

employed by Kuntzman et al. [1] where piezoelectric sensing was achieved with four lever arms sputtered with PZT (Figure 5.7 and Figure 5.8). COMSOL simulations of the expected output of the piezoelectric lever arms are employed to give the expected output (Figure 5.9). A single lever arm was simulated in a Piezoelectric-Solid model with fixed amplitude of oscillation of 1 μm at 5000 Hz, a reasonable expectation for the largest range of movement from such a device. The terminals of the AlN layer are treated as part of a simple circuit, with a resistance of 1 kΩ connected in series with a 5V DC Voltage source. The output current is read across the terminals of this resistor (Figure 5.10).

5.4 COMSOL modelling of full device

As the device contains no back plate or combs, the principle contributors to damping are expected to be the viscous and thermal losses in the boundary layer around the device. Two approaches are adopted in this section, the thermos-viscous Eigenfrequencies approach of Chapter 4 and the Fluid-Structure Interaction approach described in section 5.1. For the thermos-viscous Eigenfrequencies the depths of the boundary layers are given by:

$$\delta_v = \sqrt{\frac{2\mu}{\omega\rho_0}} \tag{5.1}$$

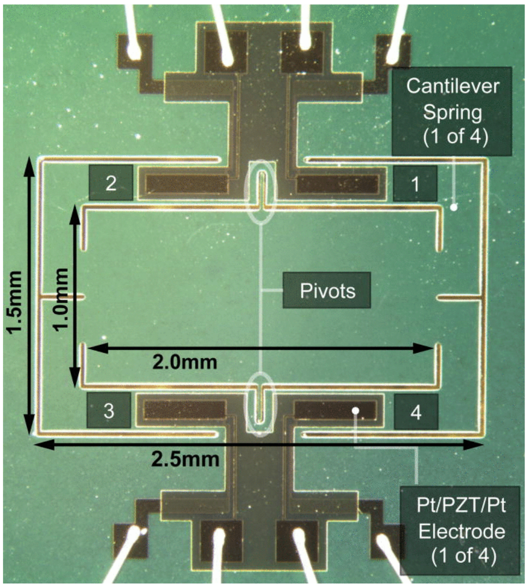

Figure 5.7: Piezoelectric sense Ormia inspired microphone designed by Kuntzman et al.[1]

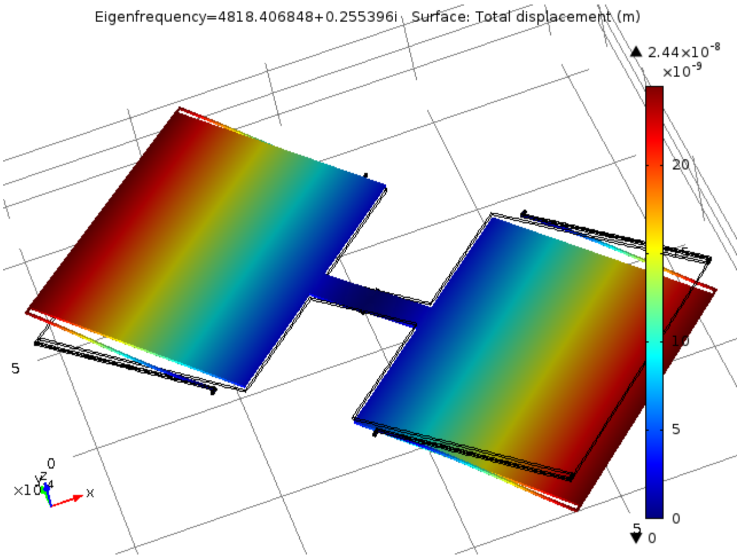

Figure 5.8: COMSOL simulation of second iteration of device, showing the four 700 µm x 40 µm lever arms connecting the diaphragms to the substrate. Each of those arms is coated for the first 500 µm with a 30 µm wide layer of Aluminium Nitride.

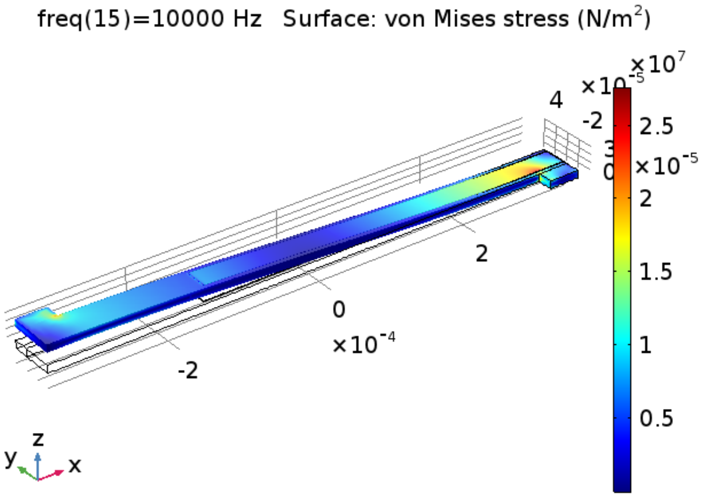

Figure 5.9: COMSOL simulation of single lever arm with 500 nm thick AlN layer covering the first 500 μm of the lever arm.

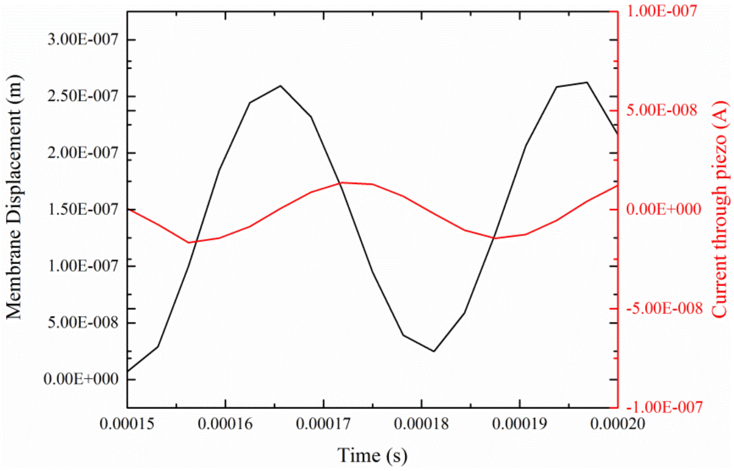

Figure 5.10: Lever arm displacement and simulated current through resistor with bias voltage of 5 V. The sensitivity is approximately 0.036 nA/nm.

	COMSOL simulated resonances and damping			
	Resonance Frequency (Hz)		Damping Coefficients	
Air Temp	Rocking	Translational	Rocking	Translational
0°	8224.5	8846	4.43×10^{-3}	5.52×10^{-3}
20°	8229	8851.4	5.25×10^{-3}	5.25×10^{-3}
20°	3165.8	3403.2	40.2×10^{-3}	41.3×10^{-3}

Table 5.1: Simulated resonance frequencies and damping

$$\delta_t = \sqrt{\frac{2k}{\omega\rho_0 C_p}} \tag{5.2}$$

where δ_v and δ_t are the depths of the thermal and viscous boundary layers, μ is the viscoscity of the fluid medium, ω the angular velocity of the solid's displacement, ρ the density of the material at equilibrium, k the heat conduction velocity and C_p the heat capacity at constant pressure. In order to obtain a single lumped damping coefficient for each of the mode shapes estimations of the total damping force are made via Finite Element Analysis using COMSOL Multiphysics' thermo-acoustic module. The model comprises three components: the diaphragm, modelled as a shell layer made of single crystal silicon, the air domain around the diaphragm, modelled using the thermo-acoustics interface, and an extended air domain, modelled using the simpler pressure acoustics interface (Figure 5.11). A plane sound wave with an amplitude of 1 Pa (94 dB ref 20 μPa), is simulated with the direction of propagation perpendicular to the face of the diaphragms. The resulting Eigenfrequencies and damping ratios are given in Table 5.1 and the simulated mIID in Figure 5.12. Secondly the fluid structure interaction approach is adapted for the membrane body, lever arms and surrounding substrate. The mean damping coefficient is found to be 0.0049, this time showing an error of only 8% over the thermo-viscous Eigenfrequency estimation, suggesting that poor simulation of the capacitive combs was responsible for the error in the estimate of damping in the first iteration. The final design chose the base resonance frequency of 8229 Hz with a translational mode frequency of 8851 Hz giving a coupling strength of η=1.076, falling neatly into the desired over-coupled range. The simulated mIID and mIPD of 0.5 dB/° and 3 ° phase / ° azimuth respectively (Figure 5.12) should allow measurements of sound source angle to be made to within half a degree if realisable.

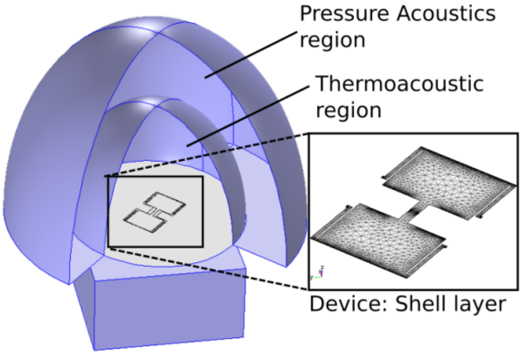

Figure 5.11: The COMSOL model air domain is split, with viscosity and thermal conductivity omitted in the outer layer (Pressure Acoustics domain) and the more computationally intensive thermos-acoustic equations solved in the smaller inner layer. The device is a shell layer 10 μm thick attached to the substrate at the pivots and the end of each of the spring arms, simulating the piezoelectric sensing device.

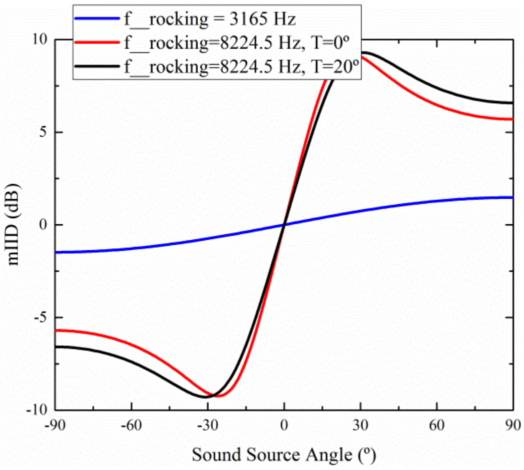

Figure 5.12: The effect of damping on the sensitivity of the device is pronounced. Each of the three cases above have the same coupling strength, however the lower resonance frequency device Q is much reduced giving a sensitivity around the midline of 0.025 dB / ° (and 0.2 degrees phase difference per degree change in sound source angle in the mIPD measure). In the same device the temperature change from 0° C - 20° C can result in a change of sensitivity from 0.52 dB/° to 0.45 dB /° around the midline (3.03° phase / ° azimuth to 2.516° phase / ° azimuth in the mIPD measure).

5.5 Results

The devices (shown in Figure5.13) were characterised using the same procedure as described in section 4.2.4. The measured resonance frequencies are found to be 8560 Hz for the rocking mode and 9281 Hz for the translational mode, with the peak mIID being found at 8572 Hz (Figure 5.14) and the peak mIPD at 8565 Hz. Damping coefficients are measured from the half power bandwidth of each of the resonance mode peaks at 0.005 for the translational mode and 0.0045 for the rocking mode; showing a vast improvement in the estimations of damping with an error of +6% and +18% respectively in the COMSOL simulations. The mIID and mIPD measurements are taken at 8540 Hz, which is found to produce the largest directional sensitivity without loss of linearity near 0° sound source angle (Figure 5.15). Peak values are attained at 10° for each with an average directional sensitivity of 1.6dB per degree in mIID and of 8° phase difference per degree sound source incidence angle in mIPD. Mean absolute error is 0.38 dB in mIID and 3.49° in mIPD for a sound source angle measurement error of 0.24° and 0.44° respectively. The scaling parameter of the Cauchy noise is estimated at 0.52 dB by taking half

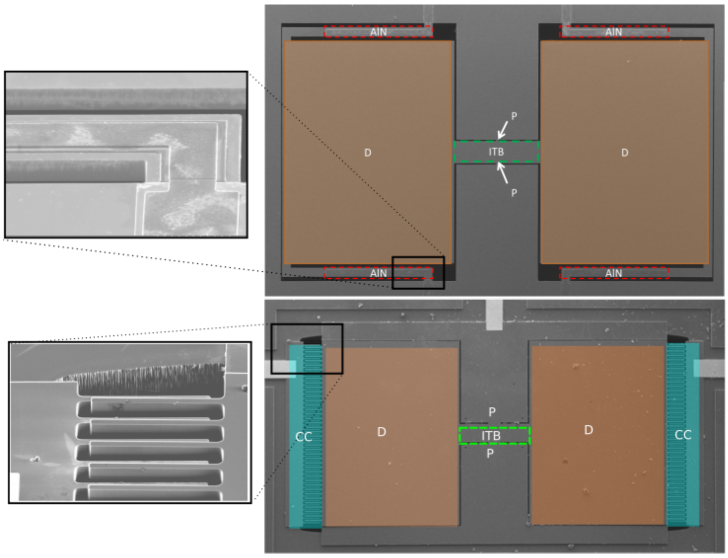

Figure 5.13: Comparison of first and second iterations of device. PiezoMUMPS device is shown at the top with the two diaphragms (D) connected by the intertympanal bridge (ITB) anchored to the substrate by pivots (P) with Aluminium Nitride sensing on the four lever arms (AlN). Close up view of the AlN layer is shown in inset. Below is shown the SOIMUMPS device with capacitive comb sensing (CC) and close up of the comb disengagement in inset.

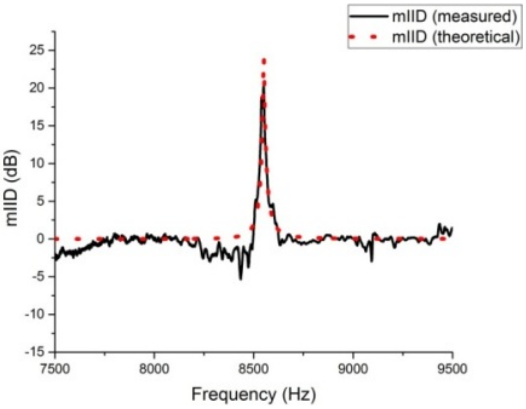

Figure 5.14: mIID swept over frequency range for fabricated device with comparison to lumped parameter estimates.

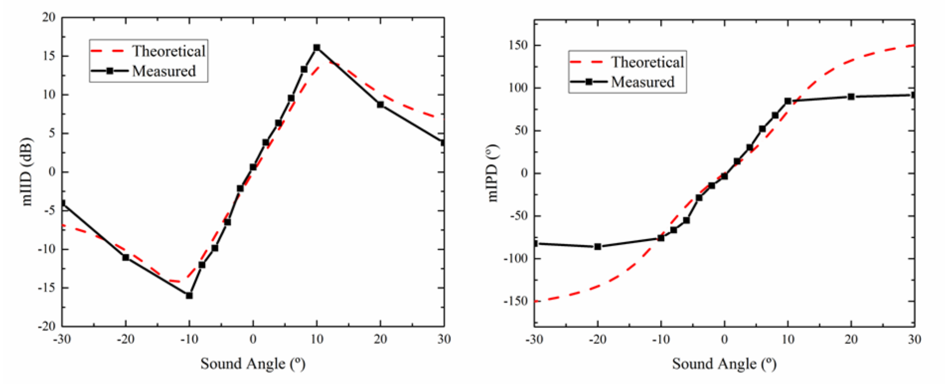

Figure 5.15: Comparison of lumped parameter model estimates for mIID and measured values in the Piezoelectric device based on the measured device frequencies of 8560 Hz and 9281Hz and the damping parameters of 0.005 in the translational mode and 0.0045 in the rocking mode. mIPD measurements of directional sensitivity agreed well with those modelled, however the measured signal was found to saturate before predicted.

the interquartile range from measurements made with the sound source at 0° (wave fronts parallel to the top layer of the device) at the rocking mode resonance (over 25 samples). The error of the device could therefore be far larger, but would be most likely to fall within 0.325° of the sound source angle, a considerable improvement on the first iteration of the device. Electrical transduction using the Aluminium Nitride layer was measured using a custom built transimpedance amplifier with an 80 dB gain, however given the small size of the piezoelectric layer the output signal was measured at 1.5 μV/Pa at the translational resonance frequency, and with 16 averages the noise floor was measured at 500 nV for a SNR of 6 dB. Readings at the rocking mode resonance frequency were indistinguishable from noise.

5.6 Discussion

The methods described here show the design process behind an *Ormia ochracea* inspired sound localization sensor with a directional sensitivity many times great than that of a 'dual optimized' design. In accepting the limitations on bandwidth and angular range of operation a single purpose sound localization sensor can be created. Limiting the angular range of measurement has some benefits outside the intended goal of increasing the directional sensitivity of the device. Phase shifts in the pressure difference from diffraction around the device and handle wafer are minimised, allowing more confidence in the assertion that the directivity of this device is attributable to the mechanical properties of the membrane and not to the diffraction of the sound field around the body. In addition this also removes (or minimises) the undesirable non-linearity in measurement that occurred as the sound source angle approached 45° in simulations of the first iteration of device, although this problem was not actually encountered in the first device due to the poor optimization. Successful electric transduction in a single layer device remains elusive. While the piezoelectric sensing was an improvement on the disengaged comb drives of the first iteration the dielectric constant of Aluminium Nitride is unfortunately low. Additionally the use of lever arms constrains the area which may be coated with the AlN as they create an additional stiffness on the diaphragms, increasing the resonance frequencies. As such an electrical reading could only be made at the translational mode resonance while the sensor was being driven at 94 dB SPL, and readings out-with resonance fell below the noise floor.

5.7 Third iteration - improving signal and stability of the system

The final design attempts to solve the problem of the transduction of the signal, using a tapered 'bow-tie' design instead of lever arms allowing the AlN layer to be placed on the lower third of the membrane itself. The design is intended to concentrate the stresses on the membrane, rather than the pivot arms and so increase the surface area covered with AlN while minimising the loss of information. The same resonance frequencies and estimates of damping as the second generation design are retained, and again fabrication is performed using the PIEZOMUMPS service from MEMSCAP. In addition to the piezoelectric sensing a capacitive comb sense scheme is included, although the additional stress gradient from the AlN would be expected to increase the curvature of the membrane and further disengage the rotor combs from the stator combs. With the piezoelectric sensors at the base of each membrane the bias voltage will curve the membrane downwards again, counteracting some of the effect of the stress gradient as well as altering the resonance frequencies of the design. In this way a combination of piezoelectric and capacitive sensing is hoped to allow fine-tuning of the stiffness of the coupling between membranes as well as improve the electrical sensitivity of the device. The primary goals for this iteration are to replicate the high, over-coupled directional sensitivity of the second iteration design in a new membrane while improving the electrical output of the device.

5.7.1 COMSOL Modelling

As the intention is to replicate the principles from the lumped parameter model of the second iteration design the ideal resonance frequencies should be similar, with the caveat that increased damping from the capacitive comb drive must be accounted for. Replicating the methods from the second iteration design, COMSOL models are created to determine the complex Eigenfrequency of the membrane - this time with the combs included - and a separate Fluid-Structure Interaction study to determine the viscous damping around the combs. The quality of the mesh elements around the combs, which had been a problem in the first iteration design, is improved by creating a 2.2 mm x 1.2 mm x 30 $^{\mu}$m bounding box around the membranes which is meshed separately with a much finer mesh with minimum element size 0.5 μm. The remainder of the air domain and substrate are then meshed using a far coarser, faster mesh giving a mesh element quality around the diaphragm and combs of between 0.8 and 1 (Figure 5.16). Although the minimum mesh element quality is 0.03 (COMSOL guidelines suggest a minimum mesh element quality of 0.1) the lowest element quality around the combs drives is 0.4. Unsurprisingly the simulations offer similar values to those measured from the first iteration design, with both rocking and translational mode damping around 0.005 (ξ_r = 0.0053,ξ_t = 0.0056). The maximum mIID and mIPD are anticipated to occur with a sound incidence angle of 10°. Using the same model and meshing techniques a frequency sweep is created with the incidence angle stepping at 10 Hz increments around the expected resonance frequency of 8200 Hz. The mIID measure is found to peak at 8080 Hz while the two peaks from the mIPD measure are found at 8000 Hz and 8020 Hz, with the maximum phase difference at this angle 132° and the maximum intensity difference 26.05 dB (Figure 5.17). The full frequency sweeps for mIPD and mIID are shown in Figure 4.36, as well as the sound incidence angle sweeps for mIPD and mIID. All sweeps are shown for 8080 Hz and give an estimated directional sensitivity of 12.6 degrees phase difference per degree change in sound incidence angle and 2.3 dB /° in the mIID measure. From these simulation results there is a good confidence that the high directional sensitivity measured in the second iteration of the device will be replicated here.

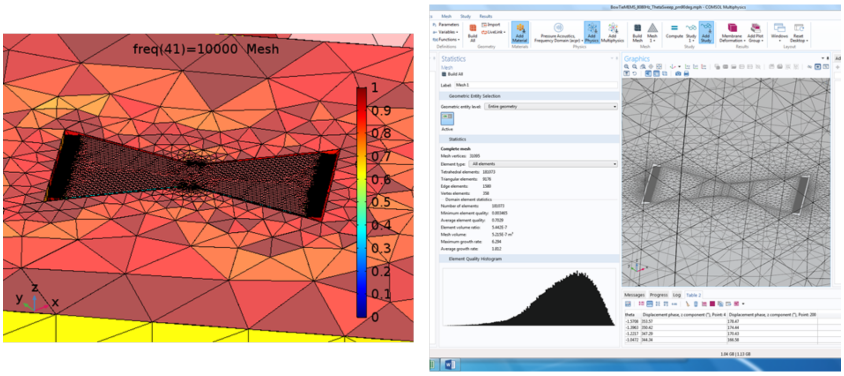

Figure 5.16: Bow Tie Model MEMS device. Caution needed to be taken with the meshing to correctly incorporate the damping from the combs. (Left) Mesh quality around the device and combs. (Right) Histogram of mesh element quality and meshing around the combs. The minimum element quality is 0.03, which is lower than the ideal minimum of 0.1 however the bulk of the mesh elements around the device and combs lie within the range of 0.8-1.

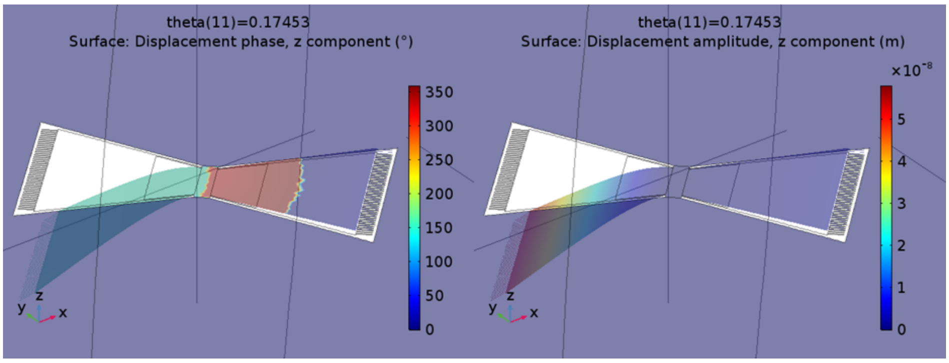

Figure 5.17: COMSOL simulation showing phase difference (left) and membrane deformation (right) at 10Â° from the normal position at 8080Hz.

Simulation of the effect of the piezoelectric sensing on the operation of the device focused on the anticipated membrane deformation from the bias voltage as well as looking at the expected measurement sensitivity. The deflection is measured in a stationary analysis (which finds the equilibrium point of a system) with a bias voltage swept from 0-40V across the aluminium nitride layer (Figure 5.19). At 40 V the deformation of the membrane is 2.3 μm, which may allow some improvement in the re-engagement of the capacitive combs.

5.7.2 Results

The devices returned from MEMSCAP (Figure 5.20 above) are mounted on PCBs with a through-hole drilled behind the device area and the resonance frequencies characterised with the 2D laser vibrometer as described in section 4.2.4. Resonance frequencies are measured at 8124 Hz and 8806 Hz giving a coupling bridge strength of η=1.084 with damping ratios of 0.0052 and 0.0055 in the rocking and translational modes respectively. Both the mIID and mIPD measures are taken at 8120 Hz using a single frequency pure tone with the results shown in Figure 5.21 below against the COMSOL simulations. Both measures show good agreement with the simulated results, although the mIID measure continues to show the effects of the Hinckley style noise from taking the ratio of two noisy signals. Scans around the midline are taken in 2° increments with 10° increments thereafter up to ±60°, giving an average directional sensitivity between ±10° of 17.09° phase difference per degree change in azimuth angle in the mIPD measure and 2.49 dB/° in the mIID measure. Average error from the average directional sensitivity results between ±10° was 2.1 dB in the mIID and 8.12° in the mIPD giving an average directional error of 0.84° sound incidence angle in the mIID measure and 0.48^circ sound incidence angle in the mIPD measure. While the directional measurement error from phase difference is comparable to the last iteration of the device (measured at 0.44° sound incidence angle error) the mIID measurement error was greatly increased (measured at 0.24° in the previous iteration of the device). The larger error in the latter measurement appears not simply to be as a result of noise, but some loss of linearity in the design as a result of the higher coupling bridge strength. Nevertheless, both measures give a reasonable estimate of sound source location to within ±1° and the mechanical operation of the device appears acceptable. Surface profile scans of the comb drives reveal the anticipated increase in the stress gradient on

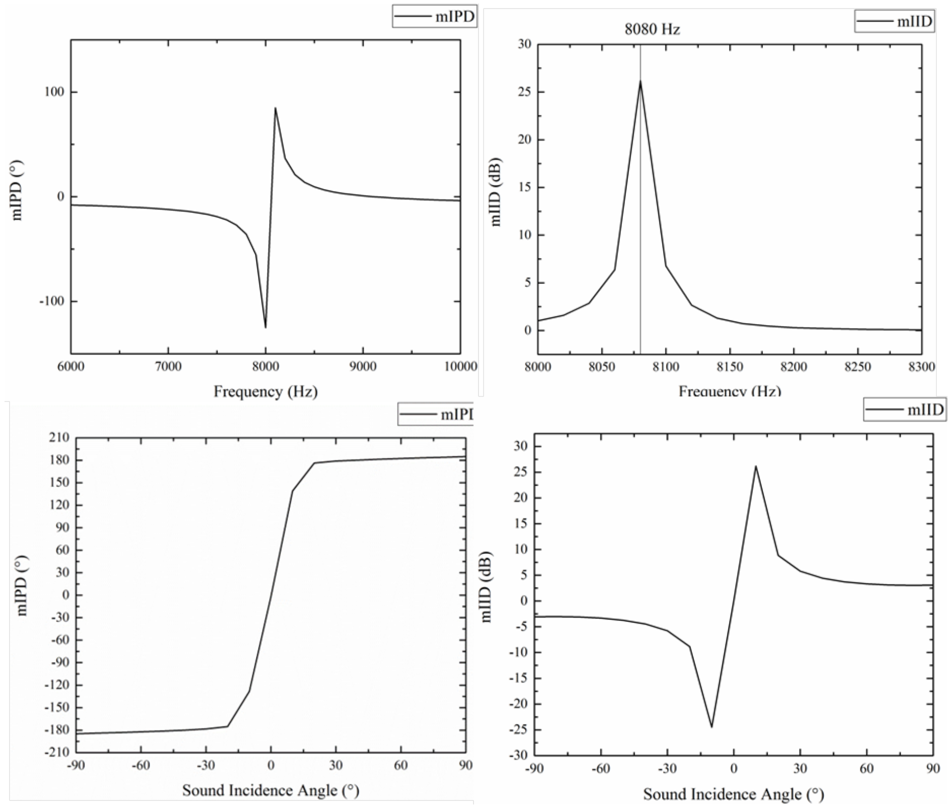

Figure 5.18: COMSOL simulation results for Bow-Tie MEMS model. (Top left) Frequency sweep of mIPD measure with sound incidence angle at 10° showing peaks at 8000 Hz and 8020 Hz. (Top right) Frequency sweep of mIID measure with sound incidence angle at 10Â° showing a single peak at 8080Hz. (Bottom left) Sound incidence angle sweep at 8080Hz of mIPD measure. Directional sensitivity around the midline is 12.8 degrees phase difference per degree change in sound incidence angle. (Bottom right) Sound incidence angle sweep of mIID measure at 8080 Hz showing a maximum mIID of 25 dB and a directional sensitivity of 1.9 dB/° around the midline.

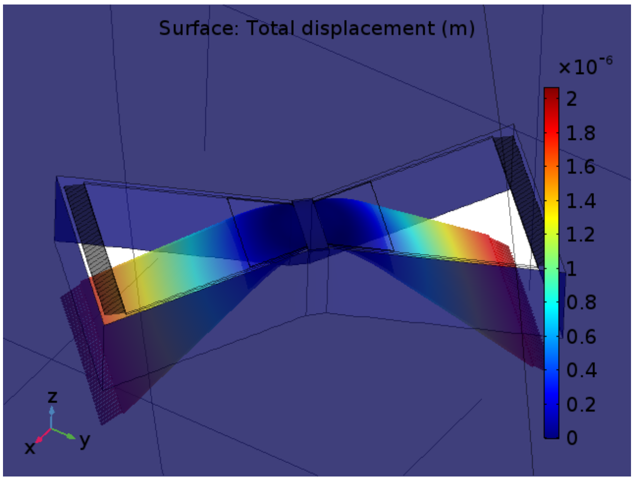

Figure 5.19: Deformation on membrane from bias voltage across the AlN piezoelectric layer at 40 V.

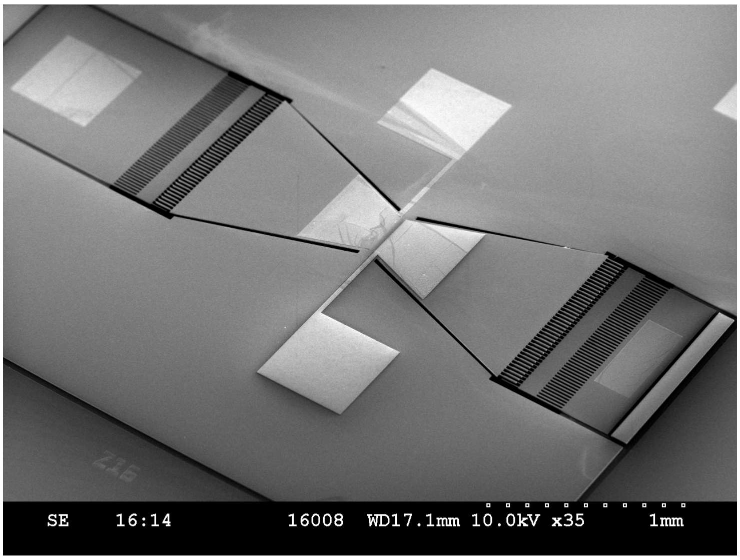

Figure 5.20: Scanning electron microscope image of bow-tie model device.

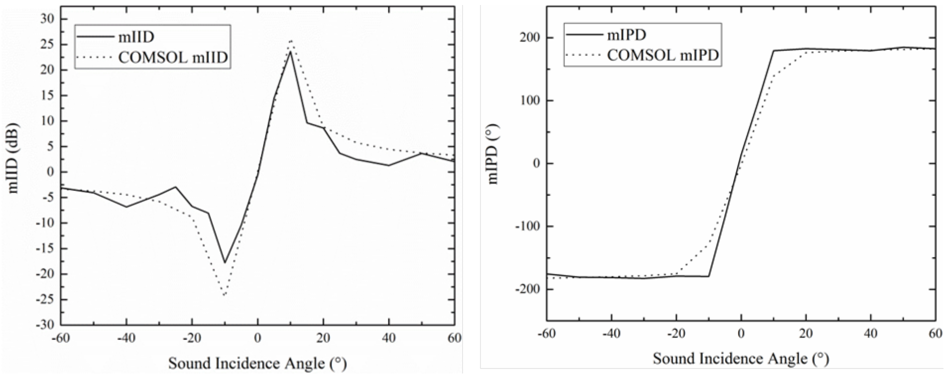

Figure 5.21: Measured mIID and mIPD plotted against the predicted results from COMSOL. (Left) mIID measurement is taken at 8120 Hz (COMSOL Measurement taken at 8080 Hz). The match with the predicted values appears reasonable, but there is a notable offset between measurements with the sound source to the left and right of the device. (Right) The mIPD measure shows a good linearity around the centre region but has saturated earlier than predicted. Both measures were taken at 2° intervals between ±10° and at 10° intervals thereafter.

the device (Figure 5.22). Disengagement of the combs ranges from 6.67 μm at the base of the rotor combs to 8.15 μm at the rotor comb tips, leaving the combs once again nearly fully disengaged. Electrical measurements are made via wire bonds to the PCB holders that have been used throughout these trials. Measurements from both the piezoelectric sensors and the capacitive comb sensors are performed using a custom built instrumentation amplifier with a gain of approximately 45 dB and two 4th order Bessel filters creating a pass band from 100Hz - 15 kHz. The output waveforms are saved as .csv files via a Tektronix TBS1032B Digital Oscilloscope and the input waveforms generated by a Tektronix AFG3012 Dual Channel Arbitrary Function Generator and broadcast via the Heil Air-Motion Transformer. The device is mounted vertically on a small manual rotational stage 50 cm from the Heil Air-Motion Transformer and readings taken simultaneously from the left and right piezoelectric or capacitive sensors with the device rotated at 2° intervals from -10° to 10° in response to a pure tone at 8200 Hz and to a frequency sweep from 1 kHz - 15 kHz over a period of 1 second. Signals are successfully recorded from both the piezoelectric and capacitive sensors with pure tone signals; however there was some notable cross talk in both sets of experiments despite careful grounding which introduced an additional error to the measurements. Despite this the directionality of the microphone could be observed in the pure tone readings from the

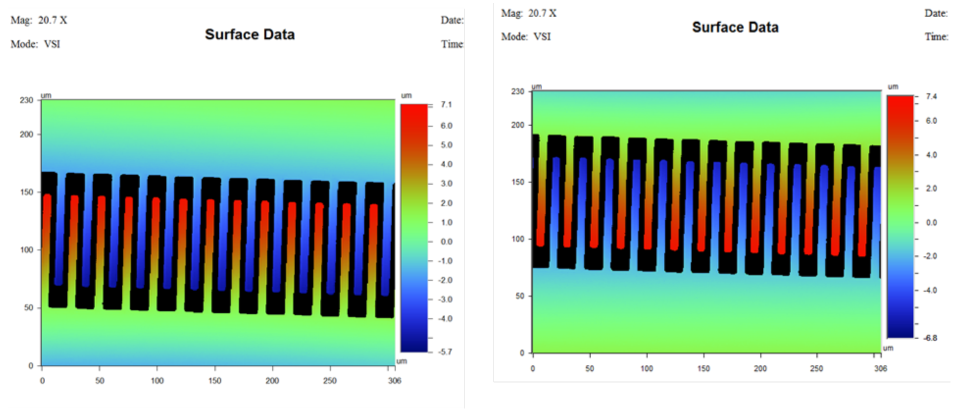

Figure 5.22: Surface profile of third iteration of device near the comb tips (Magnification x20.7). The radius of curvature is markedly different between the two membranes, with a displacement of 12.8 μm on the upper membrane and 14.2 μm on the lower.

piezoelectric sensing (Figure 5.23 and Figure 5.24) In the capacitive sense, a signal is obtained however results were corrupted by the occurrence of an in-plane rotational mode at around 2 kHz. The mode, which occurred in COMSOL simulations of Eigenfrequency but was not thought to be strongly stimulated, allowed a rotation around the z-axis closing the distance between the capacitive combs and causing a far greater change in capacitance than the out of plane motions that were hoped to be recorded. This results in a spike in the electrical signal at 2 kHz and a relatively small signal at the frequency of interest which is again barely distinguishable from the noise floor (Figure 5.25).

Directional measurements from the mIID are compromised by the electromagnetic interference. All readings are biased by the extraneous signal; however some directionality could still be seen. Far clearer are the readings from the mIPD measure where an average directional sensitivity of 9.243° phase difference per degree change in azimuthal angle is recorded. Within the range of ±10° an average error to the estimated ADS of 17.3° is recorded, giving a directional measurement error of 1.87° (Figure 5.26).

5.7.3 Discussion

The primary goal for this iteration was to recreate the high directional sensitivity from the second iteration design while improving the electrical sensitivity of the

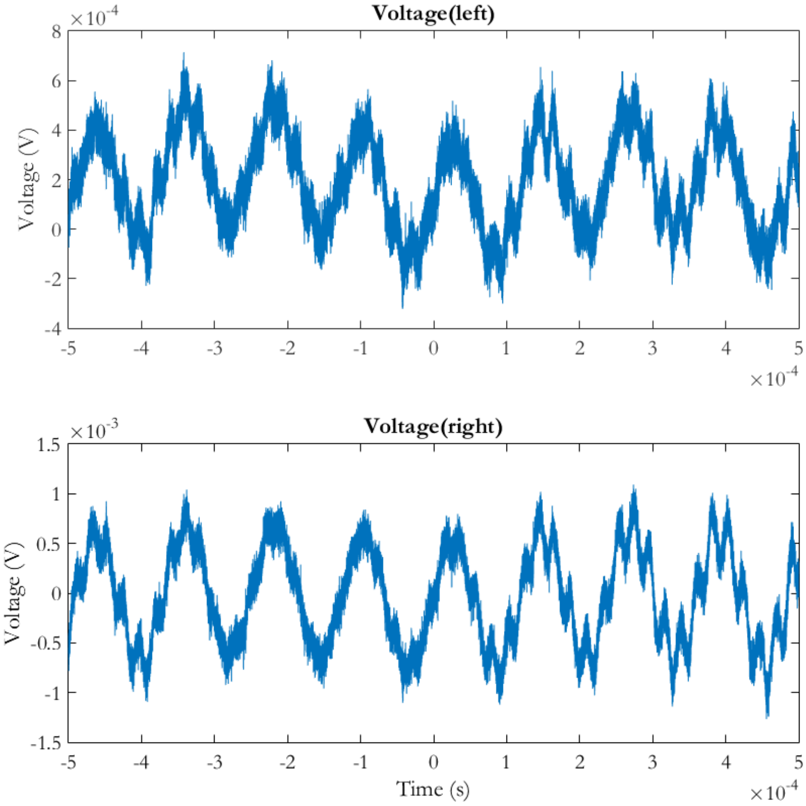

Figure 5.23: Waveform recorded from piezoelectric sensing with device at -10° to sound source. This trace used 32 averages to obtain a SNR of 29.5 dB.

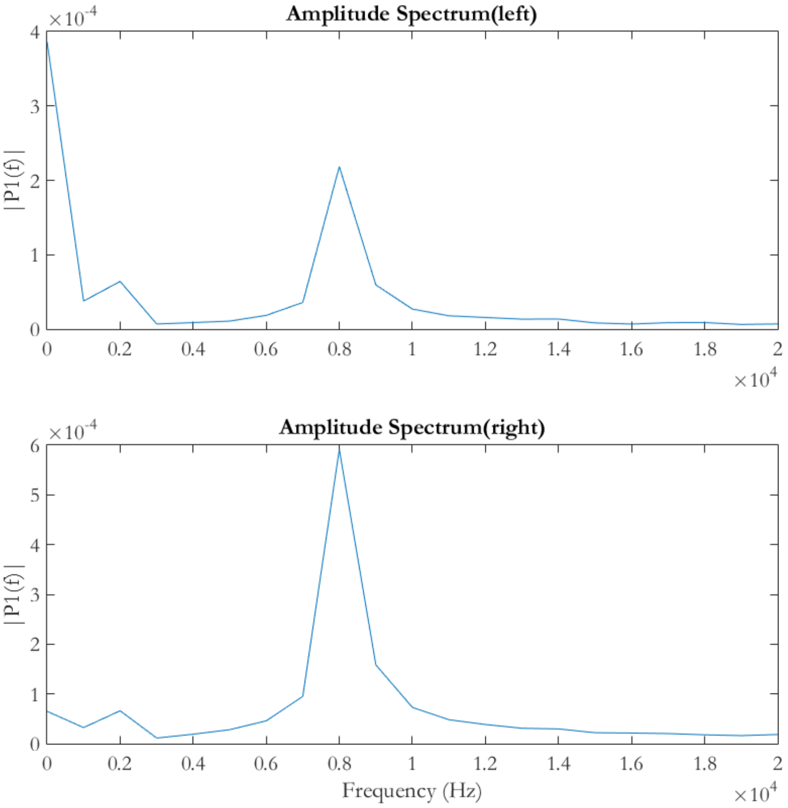

Figure 5.24: Single sided amplitude spectrum from trace in Figure 5.23. The mIID measurement is -9.12 dB at -10°, however a large component of the signal on the top (contralateral) trace is likely to be from electromagnetic interference.

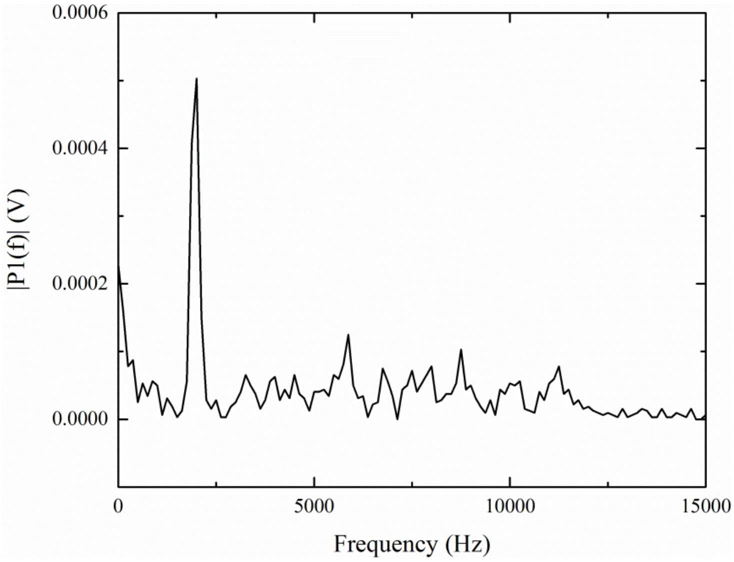

Figure 5.25: Electrical response of capacitive comb sense to frequency sweep. The large spike at 2 kHz appears to be from an unwanted in-plane rotational mode to which the comb sense is far more sensitive.

device. The measured mIID and mIPD from the laser vibrometry experiments matched well with the predicted directional sensitivity, linearity and range and compared favourably to those from the second iteration design (17.09° phase difference per degree change in azimuth angle in the mIPD measure and 2.49 dB/° in the mIID measure for the third iteration compared to 8° phase difference per degree sound source incidence angle in mIPD and 1.6dB per degree in mIID from the second iteration). From the point of view of the acousto-mechanical operation of the sensor, the methodology for correctly predicting the resonance frequencies and damping of the finished device has shown itself to be reliable. For the first time the major goal of obtaining an electrical signal from the device was achieved, with an (unamplified) sensitivity of 0.3 mV/Pa. Unfortunately this signal strength was still too low to obtain a reasonable measure of mIID as the device readings were contaminated by the electromagnetic interference from the loudspeaker but a good reading of mIPD was made at 8200 Hz giving a directional sensitivity of 9.24 degrees phase difference per degree change is azimuthal angle; again a good match for COMSOL simulations at this frequency (which is away from the predicted maximum directional sensitivity at 8120Hz). The offset and lower sensitivity is likely explained by the windowing and sampling frequency, resulting in 100 Hz bins for the electrical

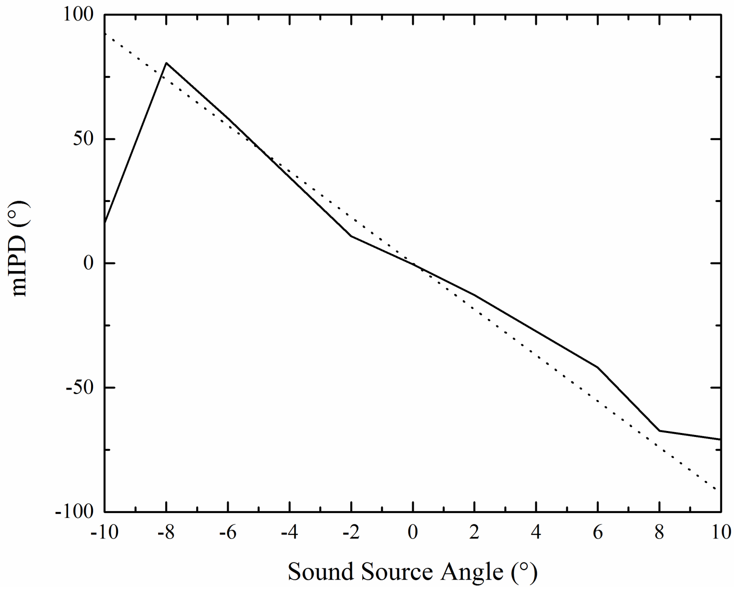

Figure 5.26: mIPD measurement from phase difference of recorded signal from piezo sensors. The bias from the electromagnetic interference has far less of an effect on this reading and a good linear measurement of sound source angle from phase difference is possible. Here an average directional sensitivity of 9.24Â° phase difference per degree change in azimuthal angle is estimated (dotted line, with the actual measurements shown as a solid line) with an average error of 17.3Â° for a directional measurement error of 1.87Â°.

Signal to Noise Ratio	Interquartile Range	Measured Signal Error
20 dB	1.66 dB	1.297 dB
30 dB	1.02 dB	0.85 dB
45 dB	0.72 dB	0.82 dB
60 dB	0.51 dB	0.49 dB
85 dB	0.23 dB	0.52 dB

Table 5.2: Average signal error between ±10° as measured by the LDV compared to estimates made from Hinckley distribution for increasing SNR. The predicted half-interquartile range from the Hinckley distribution shows a reasonable match for the measured average error between 30 dB SNR and 60 dB SNR, but the anticipated improvement when a SNR of 85 dB is used does not manifest. Large increases in SNR are required in order to obtain a small improvement in the average signal error.

measurement. The mIID measurements were repeated with progressively higher signal to noise ratios to confirm the effect of the Hinckley distribution on the likely error. The results over the range of ±10° are given in 5.2. All the measurements below were obtained with the Laser Doppler Vibrometer, where the principle source of noise would be expected to be the thermal-mechanical noise of the membrane itself. The results show that the Hinckley distribution has a good predictive value of the average signal error given the signal to noise ratio, although the predicted improvement at 85 dB is not apparent, the measured signal error bottoming out at approximately 0.5 dB. The electrical measurements with 32 averages had an SNR of 18.6 dB, which would have introduced a significant measurement error if experimental error had been overcome. Given the likely application of determining the source of a sound extensive signal averaging is likely to be too time costly, and an un-averaged signal from this system would be anticipated to be close to 0 dB SNR. The half interquartile range from the Hinckley distribution is this event would be 12 dB, again reducing the system to the point where even distinction between left and right is ambiguous. The capacitive comb measurements were made possible via the use of extensive filtering, high gain instrumentation amplifiers and averaging despite suffering from a higher offset than those of the first iteration device. Unfortunately with the thin coupling bridge in the first iteration and even with the bow-tie design there is a tendency for the device to move in the x and y axes (in the plane of the device), to which the capacitive comb sense is naturally more sensitive. It had been hoped that placing a bias voltage across the piezo device would allow some tuning of the resonance frequencies as well as re-engaging the combs for a greater electrical sensitivity. Unfortunately even a relatively low bias voltage of 10 V caused the 500 nm AlN layer to collapse, shorting and burning the device before any significant deformation of the membrane could occur.

5.8 Conclusions

The ultimate goal of obtaining a measurement of azimuthal angle to a sound source from an *Ormia* inspired device was achieved with the final iteration of the sound localization sensor, albeit with a level of signal enhancement that would prove prohibitive in any commercially realisable system. The goal of sound localization using an *Ormia* inspired device presents a very different set of challenges to those of conventional microphone design, but perhaps the most unexpected was the role that noise would play. Much has been made in the literature about the strong noise performance of *Ormia* inspired microphones (see for example [149, 126, 3]) based on the low mechanical damping of a back-plate free microphone design and the advantages of optical sensing. The low noise performance design also creates problems with the mechanical sensitivity of the system, since any design not closed around the periphery will create a minimal sound shadow where $ka > 1$ (where k is the wavenumber of the acoustic field and a is the smallest relevant dimension of the device). In practise this means that there is a significant loss of mechanical sensitivity anywhere in the acoustic range, and consequently a disappointingly low SNR. The problem is then compounded by the effect of the Hinckley distribution on the mIID measurement, causing a far larger 'noise' signal in the sound incidence angle measurement. The final result produced an average sound incidence angle measurement error in the mIPD measure of 1.87°. The intended, brute-force solution to the measurement error of increasing the directional sensitivity around the midline was successful in overcoming the noise problem, but comes with a high cost of angular range. A practical system to localize sound using such devices would have to consist of an array, not only to distinguish the ambiguity in azimuthal angle and pitch angle, but to cover the complete angular range of measurements.

Chapter 6

Directional hearing in *Achroia grisella*

The lesser wax moth (*Achroia grisella*, Pyralidae: Galleriinae) inhabit diseased colonies of honeybee (*Apis mellifera*), depositing their larvae on the detritus of the hive [150]. The adults leave the hive directly after eclosion, with the females remaining closely in the region of the hive while the males immediately begin searching for a mate [151]. *A. Grisella*'s mating strategy is unusual as although the male will emit a powerful pheromone from a pair of glands located at the base of the forewing which can stimulate sexual behaviour at close range, the primary method of localizing a mate is through an ultrasonic advertisement call which the female will follow [152].

The ultrasonic mating call is produced by a pair of tymbals on the metathorax, located near the base of the lesser wing pair [153]. The motion of the wing drives the tymbal via a tegular wing coupling producing a short ultrasonic click during both the downstroke and upstroke [154]. Males will begin the wing fanning behaviour from the moment of eclosion and call continuously, producing a train of damped pulses of ultrasound of between 70 - 130 kHz at 80 to 100 pulses per second with a pulse length of 100 to 150 μs [155]. Receptive females will run towards a singing male, with many behavioural studies conduction on *A. Grisella* showing that such localization is often direct and accomplished within 10-15 seconds [153, 156, 155, 157].

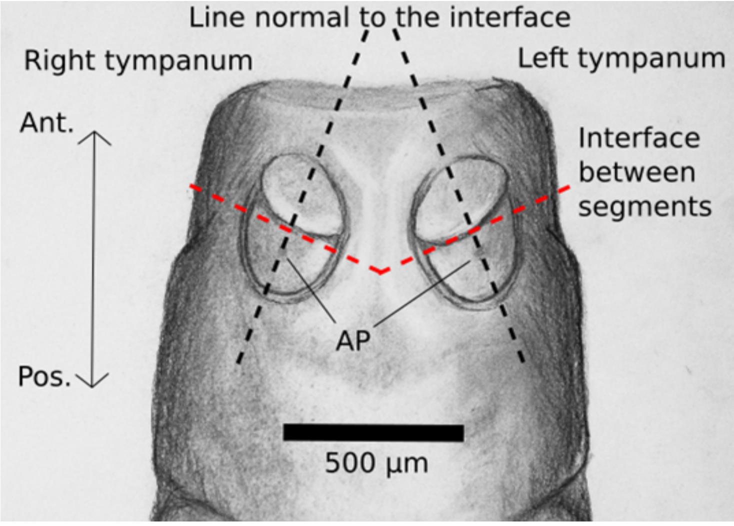

Figure 6.1: Illustration of ventral side of the first abdominal segment of A. Grisella showing the general shape and position of the two tympana. Each tympanum is divided into a relatively thick anterior segment, the conjunctivum (Cj) or counter-tympanum, and a membranous posterior segment (M) where the peripheral neurons, collectively forming the scoloparium, are attached (AP). The line normal to the interface between the anterior and posterior sections that passes through the attachment point is marked.

6.1 Auditory system of *Achroia grisella*

Adult body length of male and female *Achroia grisella* average 8.5 mm and 11.5 mm respectively, with the tympana located ventrally on the first abdominal segment. The tympana are largely occluded from view by the hind legs and the thorax, occupying a cleft in the body between the abdomen and the thorax. The tympana themselves are oval shaped, with a longitudinal axis of between 500 μm and 550 μm in the females and 400 μm and 420 μm in the male [158]. Each tympanum is divided into a white, opaque anterior section, the conjunctivum (Cj.) and a transparent posterior section [159] (Figure 6.1). The single scoloparium attachment point is located at the centre of the posterior section and is enervated by three peripheral neurons [160]. The tympana are angled slightly inwards with a separation of less than 600 μm between the attachment points. As the tympana are adjacent on the abdomen with no significant baffle between them no sound diffraction is expected to occur. The time difference of arrival is also extremely small, with a maximum difference of 1.75 μs for a sound source arriving at 90° to the insect midline. Unlike

Ormia ochracea no mechanical connection has been found between the tympana of *Achroia grisella*. This supposition is confirmed with the aid of X-Ray μCT scans of the tympana in the following section.

6.2 X-Ray micro Computer Aided Tomography

To eliminate the possibility that some of the moth's localization of a sound source could be attributed to a pressure difference mechanism or to a mechanical connection between the two ears X-ray micro Computer Tomography (μCT) scans were conducted of the auditory system. The μCT scans were performed using the Bruker Skyscan 1172 (see Chapter 2: Methods).

A moth was mounted on a block of dental wax with the dorsal side up and encased in a 5 mm diameter plastic tube. The tube was placed vertically, with the moth's head upwards, in the imaging chamber of the scanner. The scans were conducted at a voltage of 80 kV, with the scanning head positioned 85.79 mm from the centre of rotation of the subject. No filter was applied to the X-Ray source, and images were generated with 2664 x 4000 pixels at a resolution of 3.58 μm per pixel. A total of 2400 images were taken in 0.3° increments around one hemisphere of the moth with an average of four frames taken at each rotation increment. The images were collected and volumetric reconstruction of the moth body was generated by Bruker's proprietary CTVol software. The threshold for the attenuation signal was adjusted manually in order to reveal only sclerotized structures and ignore the soft tissue of the moth. Three moths were scanned in this way, two of which were prepared by saturation in ethanol for 8 hours followed by drying for 8 hours. The scans were then performed the following day. The remaining moth was scanned immediately post mortem with no additional preparation. The μCT scans revealed no indication that a trachea leads to the air cavities behind the tympanal membrane, which each appeared isolated by a thin layer of sclerotized material from the tracheal system. Similarly they revealed no indication of an internal sclerotized connection between the ears that could magnify the IID or ITD (Figure 6.2). While it remains possible that one of the linking structures above could exist below the detection resolution of 3.58 μm it is unlikely that any structure at that scale could affect significant energy transfer between the membranes. Although this resolution is too large to show the membranes in volumetric reconstruction, a clear picture of the isolation of the membranes and separation of the tympanal pits in *A. Grisella* is

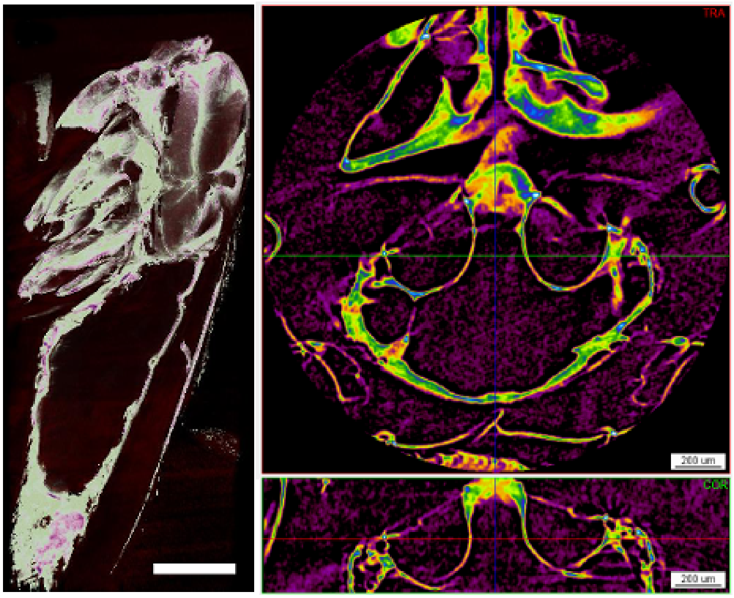

Figure 6.2: μCT scans of a female moth focusing on the region between the two tympana. a) Sagittal scan of the entire body. TRA indicates transverse plane through the tympana on the first abdominal segment. Scale bar is 1 mm. b) Transverse scan of plane indicated by TRA in scan a. Yellow line indicates a sclerotized region. Tympanal cavities are clearly shown (TY) and appear closed with no connection between the cavities. COR indicates coronal plane through the tympana. Scale bar is 200 μm. c) Coronal scan of plane indicated by COR in scan b. Again, no connection is evident between the tympana. Scale bar is 200 μm.

given by adjusting the image thresholds to show only the cuticle (Figure 6.3).

6.3 Sound source localization tests

Achroia grisella used in the experiments came from a laboratory colony established from moths collected in Florida in 2003. The moths were raised on a standard diet of honey, beeswax, flour, glycerol and brewer's yeast [92] and kept in an environmental chamber maintained at 25° Celsius and with a 12h:12h light:dark photoperiod. Because *Acroia grisella* females normally become unreceptive to stimulus following a single mating only virgin females were used in the tests. Adult females were prepared for the experiments by removing pupae from the colony and placing them in 30 ml cups, ensuring the insects isolation from potential mates from the moment of its eclosion. All females were between 1-3 days old at the time of their tests, which were conducted during the first four hours of the photoperiodic night.

Sound localization was measured by analysing phonotactic responses of females to a synthetic male song stimulus while running on a locomotion compensation sphere (Syntech LC3000). The stimulus was a song recorded from a single male individual in the laboratory colony who exhibited acoustic features that were average for the population. The stimulus was broadcast from a high-frequency loudspeaker (Avisoft Scanspeak, driven by an Avisoft Ultrasound Gate Player 216M digital to analogue converter and amplifier) attached to a movable arm. The apparatus allowed the positioning of the loudspeaker at the same elevation as the test females' situation on the top of the sphere while orienting it directly at her but from a variable location behind the sphere. In each trial the stimulus was adjusted to 80 dB SPL (ref 20 μPa) at the female's location, 50 cm distant from the loudspeaker. Stimulus amplitude was re-calibrated at the beginning of each test day. Although female *Achroia grisella* will commonly approach a mate by walking [151], the wings were removed prior to the experiments to facilitate the positioning. Preparation involved first cooling the insect for 45 seconds and then removing their wings to allow for greater control of the insect. The moths were given a day to recover after the process. The operation of the locomotion compensation sphere retained the test females at the top of the sphere throughout the trial. The servosphere functioned as a spherical treadmill, with the trajectory of the insect being recorded by the error signal from the movement of the sphere at 100 ms intervals. Three behavioural experiments were conducted on the locomotion compensation sphere:

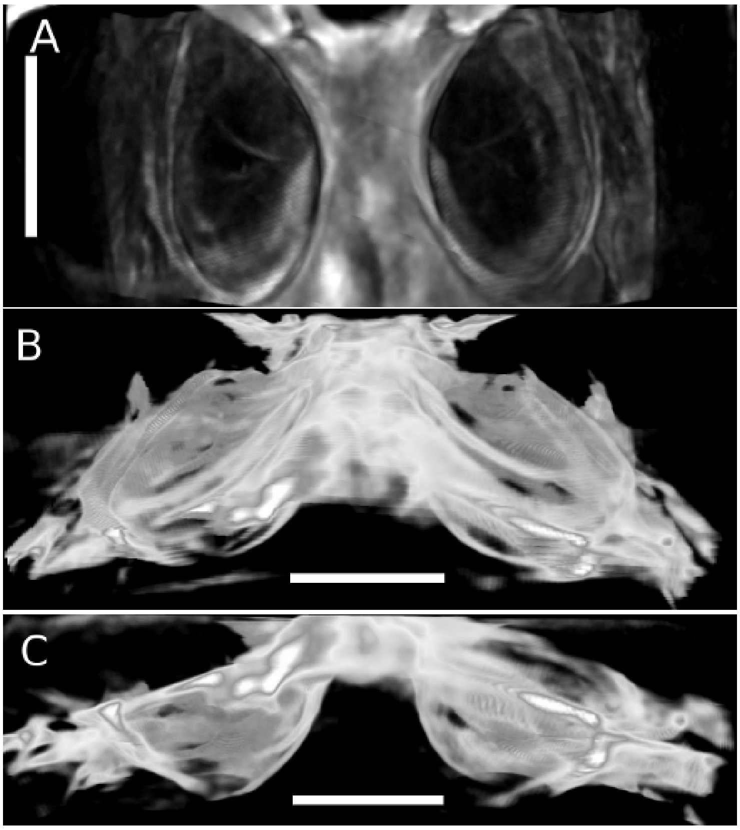

Figure 6.3: Volumetric reconstruction of auditory system of Achroia grisella. (A) View of the ventral surface of the abdomen in which the outline of the tympanal pits and orientation can be seen. (B) Moving down through the body of the insect the tympanal cavities can be seen. The soft body of the insect has been filtered from this image. (C) View through the body of the insect toward the anterior. The tympanal pits can clearly be seen to be isolated from the body and from each other.

a constant broadcast stimulus of 30 seconds duration (n=25), an 8 second stimulus followed by 3 seconds of silence and then a further 8 seconds stimulus (n=26), and an 8 second stimulus broadcast from a location at 0° azimuth relative to the frame followed by an 8 second stimulus broadcast from 135° azimuth (n=26). In all trials the recordings were bracketed by 3 seconds of silence before the first stimulus was broadcast and another 3 seconds of silence at the end of the trial. The female's trajectory was reconstructed by the Syntech TrackSphere software as a series of x,y co-ordinates in virtual space. This data was used to determine the insect path, as well as the running average of the insect's azimuth heading relative to the stimulus taken over the previous 1 second, 5 seconds and 10 seconds and an instantaneous azimuth heading taken over the previous 100 ms. The average velocity of the insect over the last 100 ms and last 1 second was also calculated from the data.

6.3.1 30 second constant stimulus trials

74% of A. grisella females tested on the locomotion compensation sphere ran toward the virtual source of synthetic song stimulus for at least 15 seconds (for example Figure 6.4). Absolute angular deviation of travel headings with respect to the stimulus, whose heading was defined as 0°, taken over the previous 1 second of movement ranged from 21° - 38° for the initial 10 seconds of phonotaxis (average values of 17 females taken at 1 second intervals beginning at 1 second). Travel headings were evenly divided between the right and left sides of the 0° heading (sign test, p¿0.25) and had standard deviation ranging from 15° - 25°. Whereas the highest absolute angular deviation (38°) occurred at 1 second following the onset of phonotaxis, deviation did not decline significantly over the following 9 seconds (repeated measured ANOVA, p = 0.07; for 1 second intervals beginning at 2 s, p = 0.30). At 15 seconds the absolute angular deviation was still 27° (±24° S.D.). Six moths began their movement with an 'instantaneous heading', measurement taken over the last 100 ms, over 90° with respect to the stimulus but in five of these six insects the travel heading measured over the previous 1 second was already less than 45° at 1 second. Running speed remained high throughout the trials (5.7 ± 1.6 cm·s^{-1}, mean ± S.D.), equivalent to 5-6 body lengths per second as measured along the trajectory (Figure 6.5). 90% of the females tested made at least one circling movement of small radius (¡ 3 cm), as well as angular deviation exceeding 90° during their trials. Females spend the majority of the 30 seconds phonotaxis

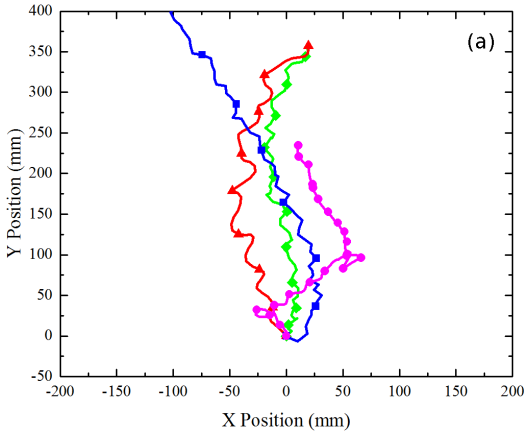

Figure 6.4: Trajectories of a sample of four of 25 females tested for orientation to male song stimulus while running on a locomotion compensation sphere. Each trajectory shows the females x,y co-ordinates in a virtual plane over the course of her trial. The starting point is 0,0 and the sound source is located along the vector normal to the x-axis. Symbols along each of the trajectories indicate the females position at successive 1 second intervals. The females heading relative to the sound source over a given interval t seconds in length would be determined by the angle between the vertical and the line connecting the most recent symbol with t symbols previous.

oriented at an absolute error of mean 25°. There appears to be no significant favour to either the left or the right side with females commonly switching mid-trajectory (Figure 6.6).

6.3.2 Interrupted stimulus trials

Females tested with a song stimulus that included a 3 second silent pause beginning at 8 seconds usually made angular deviations wider than 90° (for example Figure 6.7) , and even circled completely, at the beginning of the silent pause, movement that had been observed less frequently during the last 3 seconds of the stimulus prior to the pause (sign test, p¡0.01, Table 6.1). By the end of the pause many females had ceased movement (13 of 25 insects), but they usually began reorienting and moving toward the stimulus when the sound continued and again made wide angular deviations during the initial 3 seconds, activity performed less frequently during the succeeding 3 second interval (sign test, p¡0.01).

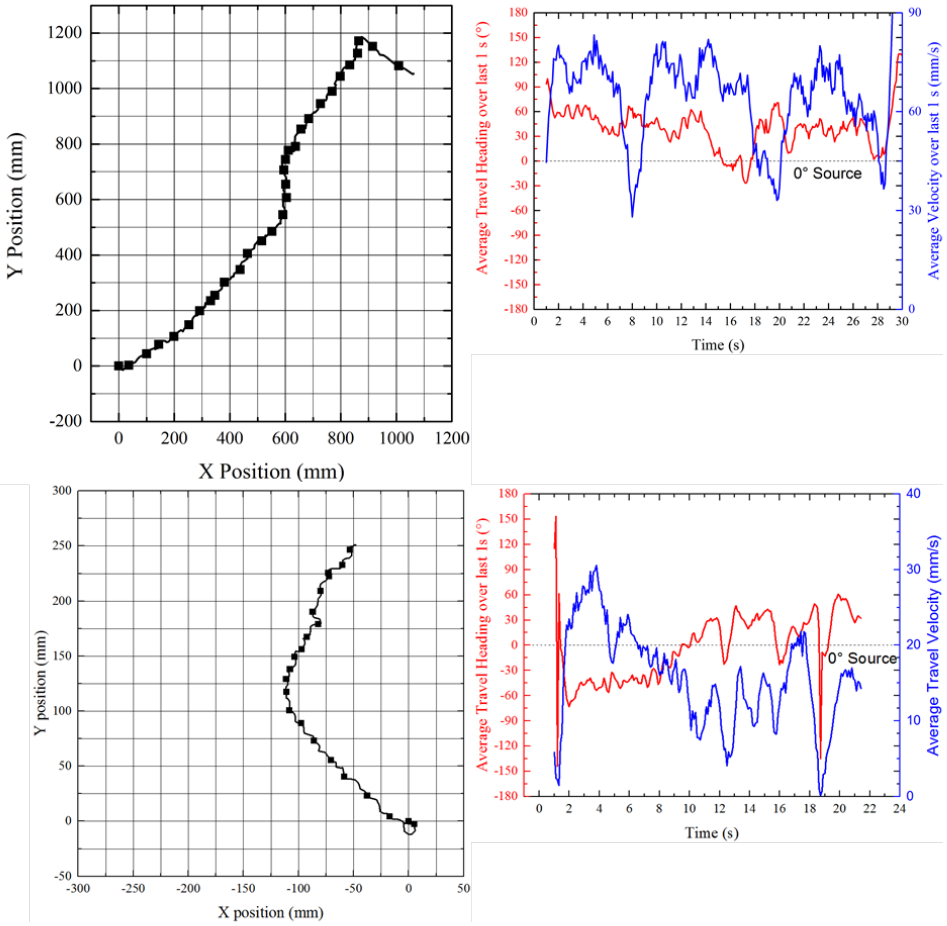

Figure 6.5: Trajectories and average velocities of two representative A. Grisella females tested for orientation to a 30 second male song stimulus while running on a locomotion compensation sphere. The panels on the top left and bottom left show the females x,y co-ordinates in a virtual plane over the course of her trial. The panels on the top right and bottom right show the females average heading relative to the sound source over the preceding 1 second interval as measured every 100 ms (red line) and her velocity over the same preceding 1 second interval (blue line). The females depicted in the top two panels retains a heading from 30° to 50° throughout the trials, whereas the females depicted in the bottom two panels follows a heading approximately +45° for the first 10 seconds and then switches to a heading approximately -30°.

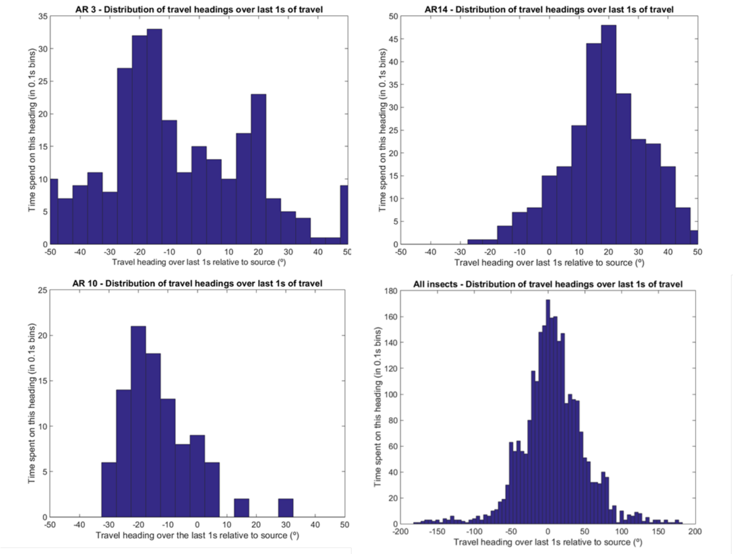

Figure 6.6: Distribution of travel heading in bins of 5° with travel heading taken over last 1 second of travel in intervals of 100 ms. (Top left) Distribution of travel headings from an insect favouring the left ear. The majority of the travel time is spent with a heading error of between -25° and -15° relative to the source stimulus. (Top right) Similar distribution of travel heading from an insect favouring the right ear. Again the majority of travel time is spent at an absolute error of 15° to 25° from the source. (Bottom left) Bimodal distribution from a single insect where phonotaxis switched from a trajectory to the left of the source to one with a similar absolute error to the right of the source. (Bottom right) Distribution of travel headings across all insect paths. Although travel headings would be expected to show a bimodal distribution here the distribution appears unimodal with a mean at 0°. Given the standard deviation of insect paths is comparable to the expected difference between the two means of distribution the unimodal appearance of the distribution is a reasonable expectation.

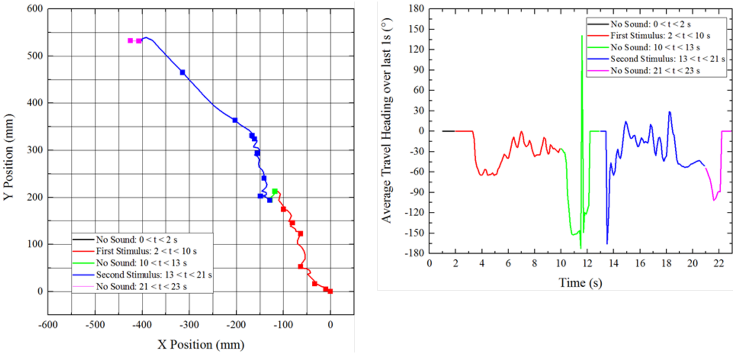

Figure 6.7: Trajectory of a representative females tested for orientation to a 19 second stimulus consisting of 8 second of song 3 seconds of silence followed by a further 8 seconds of song. The left panel shows the insect path and the right shows the average heading over the preceding 1 second. The females follows a heading approximately -30Â° during the first 8 seconds of song, circles during the 3 second silent pause and then stops before resuming a heading from -20Â° to -40Â° during the second 8 seconds of song.

Female	1st Stim	Move 1	3s Silence	Move 2	Stop?	2nd Stim (0-2s)	Move 3	2nd Stim (2-4s)
FL18	0		+	Reversals	Y	+		0
FL21	0		+	Reversals	N	0		0
FL22	0		+		Y	+		
FL23	0		+	Reversals	N	+		
FL26	0		+	Reversals	N	0		
FL27	+	reversals	+	Reversals	N		No Movement	
FL28	0		+	Reversals	Y	+		0
FL200	0		+		Y	+		
FL206	0		0		N	0		
FL208	+		+		N	0		0
FL209		No Movement	+		N			0
FL210	0		+	Reversals	N	0		0
FL211	0		+	Reversals	N	+	Reversals	0
FL212	+	Reversals	0		N	+		0
FL214	0		+	Reversals	N			0
FL221	0		0		N	0		0
FL222	0		+	Reversals	Y	0		0
FL223	+		+	Reversals	Y	+	Reversals	0
FL225	0		+		Y	+		0
FL228	0		+	Reversals	Y	+		0
FL229	0		+	Reversals	Y	+		0
FL230	0		+	Reversals	Y	+		0
FL231	0		+		Y	+		0
FL232	0		+	Reversals	Y	+		0
FL233	0		+	Reversals	Y	+		0
FL234	0		+	Reversals	Y	+		0

Table 6.1: Summary of insect behaviour during trials presenting 8 second song stimulus, 3 seconds of silence and then a further 8 second song stimulus. Coding '+' represents an average travel heading over the last 1 second of over 90° while '0' represents a travel heading which never exceeds 90°. 'Reversals' indicates a reversal in travel direction. Headings which deviate strongly from the direction of the source stimulus are far more common during the 3 second silence and the initial 2 seconds of the 2nd stimulus compared to the 1st stimulus and the latter parts of the 2nd stimulus, while circling or 'reversals' occur during the silent period in 16 of the 25 insects tested.

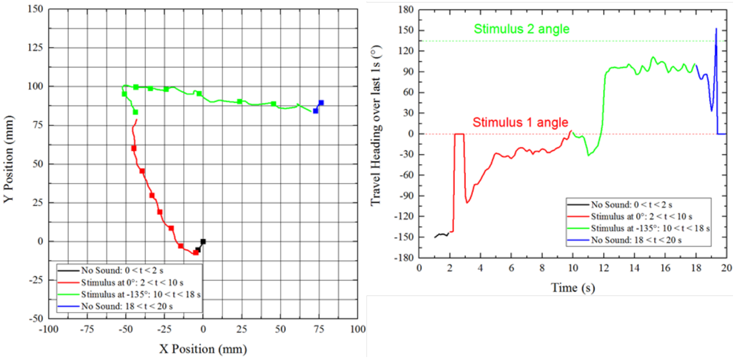

Figure 6.8: Trajectory of a representative female tested for orientation to a 16 second stimulus consisting of 8 seconds of song from a speaker at 0Â° followed by 8 seconds of song from a speaker at 135Â°. The left panel shows the trajectory while the right panel shows the average heading over the preceding 1 second interval. The average heading is shown relative to 0Â° for both parts of the trial. The female follows a heading approximately -30Â° with respect to the first speaker and then turns clockwise and follows a heading approximately 100Â°, equivalent to -35Â° with respect to the second speaker.

6.3.3 Two speaker trials

Females tested with a stimulus broadcast from two sound sources, the first 8 seconds from a speaker at 0° and the second for a speaker at 135° mostly turned clockwise (16 of 21 females), as opposed to counter-clockwise, during the initial 2 seconds of the broadcast from the second speaker before reorienting and moving toward it (Table 6.2). The reorientations were generally gradual and finished with a travel heading within 45° of the heading of the second speaker (For example Figure 6.8).

Female	0° speaker		Turn	135° speaker		Adjustment time
FL29	15	-60	clockwise	80		2s
FL30	0	75	clockwise	150	165	2s
FL32	-90	30	clockwise	135	165	2s
FL40	-50		clockwise	120	110	2s
FL65	0	40	clockwise	120	145	2s
FL67	0	-50	Counter clockwise	100		2s
FL70	50	0	Counter clockwise	150		2s
FL71	0	-50	clockwise	110		2s
FL72	50	-50	Counter clockwise	110		5s
FL73	50	-30	clockwise	160	80	3s
FL86	0	-55	clockwise	100		2s
FL89	-20	-50	clockwise	80	110	1.5s
FL90	0	50	clockwise	140	155	2s
FL92	50	0	clockwise	110	160	2s
FL95	-10	-50	Counter clockwise	150	120	2s
FL97	-30	-20	clockwise	100		2s
FL98	0	30	clockwise	100		2s
FL99	-100	-70	Counter clockwise	110	60	1s
FL100	40	10	clockwise	70	90	1.5s
FL103	0	-20	clockwise	110	130	1.5s
FL104	20	40	clockwise	140	150	1s

Table 6.2: Summary of insect behaviour during trials presenting 8 second song stimulus from a speaker oriented at 0° azimuth relative to the frame and then switching to a second speaker orientated at 135° azimuth for a further 8 seconds. The majority of insects turned clockwise towards the second source, and those which turned counter clockwise followed a trajectory that had deviated far to the left of the initial source.

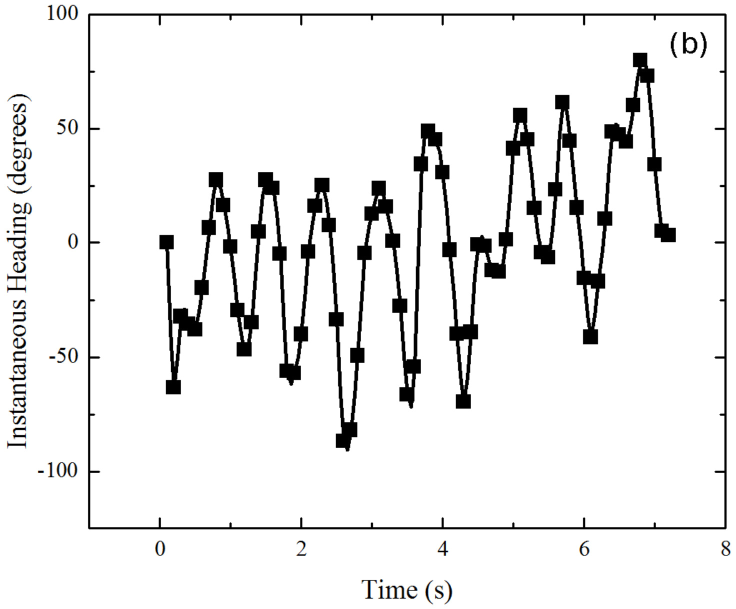

Figure 6.9: Individual insect's instantaneous heading to a sound source at 0°.

6.3.4 Counterturning behaviour

The instantaneous heading of the moths was also recorded by taking the angle of the moth's vector at 0.1s intervals. On this timescale the moths could be observed turning rapidly from left to right while following the sound source, with oscillations around the main heading of 30° or more (Figure 6.9). This movement showed noticeable periodicity with a complete oscillation occurring every 0.74 seconds (+/- 0.24 seconds SD, measured over the first eight oscillations of 10 insects) during walking. The rate of oscillation appeared to show no correlation with walking speed or the accuracy of the insect.

6.4 Laser Vibrometry experiments

Two sets of laser vibrometry experiments were carried out: the first, scanning both tympana simultaneously, was conducted with the Polytec PSV-300-F scanning laser vibrometer using an OFV056 scanning head fitted with close-up attachment (See Methods). The second set of measurements was conducted with the Polytec MSA-100-3D micro-system analyser and scanned only a single tympanum. Measurement was complicated by the location of the tympana on the ventral surface of the first abdominal segment, largely occluding them from view by the hind legs and the last segment of the thorax. In order to access the membranes the insects were anesthetised by cooling for 5 minutes then pinned to a mixture of resin and beeswax through the thorax, lifting it away from the abdomen in the process, and their legs removed. The insects could be observed moving throughout the scans which lasted 2-3 hours. All data presented here is from scans taken from living insects.

6.4.1 Vibrational modes of the tympana

Previous laser vibrometry measurement of the tympanal membranes have shown that the tympana vibrate in an anti-symmetric mode (or rocking mode), with the opaque, anterior section (conjunctivum) oscillating in anti-phase to the transparent posterior section [161]. This mode was found to dominate across the frequency range from 20 - 100 kHz, although the response amplitude drops off significantly below 40 kHz. However these measurements were taken with the wave fronts parallel to the ventral surface of the insect. The first set of laser vibrometry experiments showed that the previously reported anti-phase motion of the conjunctivum and posterior segment of the membrane only occurred when there was no acoustic phase difference across the membrane, i.e. when the wave fronts were parallel to the membrane surface as in the experiments conducted by Rodriguez et al. or when the wave fronts were parallel to the interface between the two sections of the membrane (Figure 6.10). At all other angles of incidence the phase difference between the upper and lower sections of the membrane varied very little, with a typical phase difference of between 18° and 22° (Figure 6.11). At a frequency of 100 kHz this phase difference corresponds to a phase difference in an acoustic wave between two points 170 μm and 200 μm apart (by $\delta\phi = 2\pi f d \sin(\theta)/v_p$, where d is the distance between the measurement points, ϕ is the phase difference in radians, v_p is the speed of sound, and θ is the angle of incidence of the sound wave). At 60° the phase difference jumps to 74.98° (±12.11° S.D.). At this position the phase difference across the membrane should be approaching zero as the wave fronts will be perpendicular to the interface between the two sections of the tympana - a situation which will also occur when the wave fronts are parallel to the ventral surface of the tympana as in the experiments conducted by Rodriguez et al. The large phase difference appears to be the consequence of the asymmetric nature of the membrane which gives a greater modal weight to the anti-phase oscillation of the lower section and

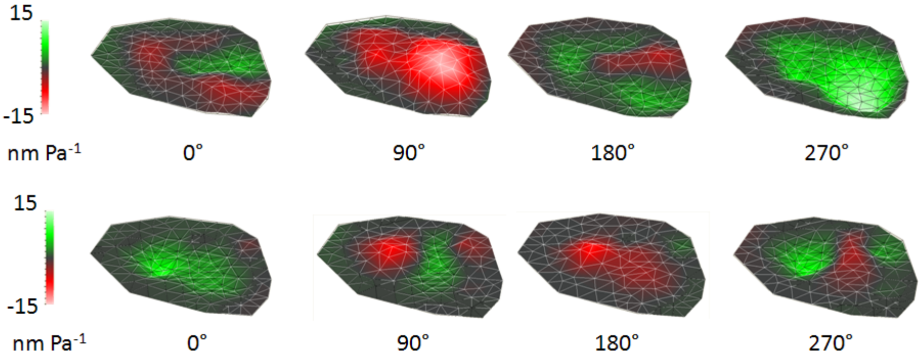

Figure 6.10: Area map and deflection shape of the right tympana motion in response to a sound source at 0° (top) and at 60° (bottom). The deflections are shown each time for four difference phases along the oscillation cycle.

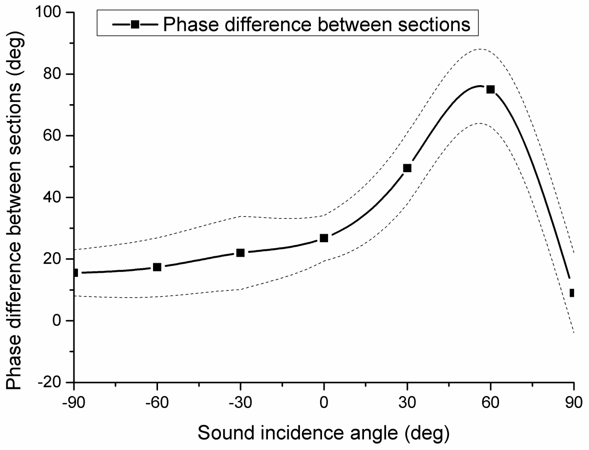

Figure 6.11: Phase difference between anterior and posterior sections of the tympana. The phase at the lower section is measured at the attachment point, which that on the conjunctivum is measured at the peak displacement.

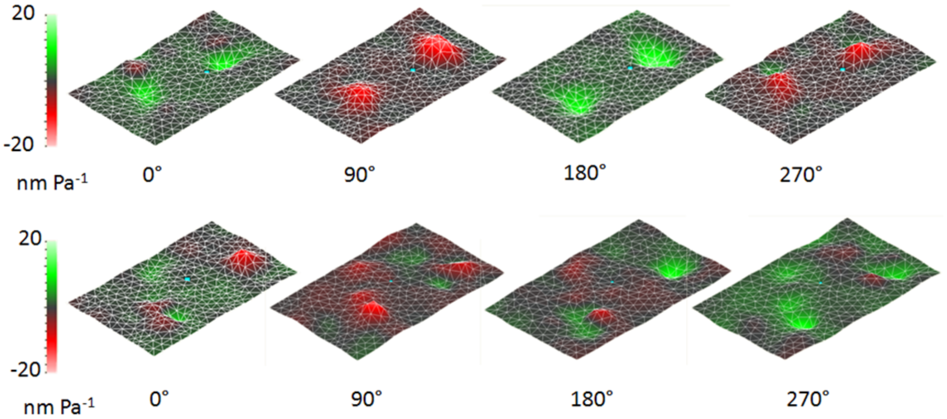

Figure 6.12: Area scan of the first abdominal segment of A. Grisella abdomen showing the motion response to a sound source at 0° (top) and 60° (bottom). The deflections are shown for four different phases along the oscillation cycle, showing both tympana moving in phase when the sound source is located at the midpoint ahead of the insect and approaching antiphase when the sound source is located at 60°.

conjunctivum. When a pressure difference is present the motion of the upper and lower sections is dominated by the pressure gradient across the membrane, remaining closely in phase with the acoustic phase difference across the membrane. When the pressure gradient modal force is reduced the anti-phase motion is still stimulated by the total pressure, counter-intuitively creating a larger phase difference across the membrane. Comparing the phase difference at the attachment points produces a similar picture (Figure 6.12). The phase difference remains low for all sound angles other than -60° and +60° where it jumps to 91.4° (±29.73° S.D.) and -86.34° (±35.07° S.D.) respectively (Figure 6.13). This phase difference, which occurs purely as a result of the absence of a pressure gradient across each membrane at a specific sound source angle, represents an increase of 1.67x the acoustic phase difference between the attachment points at that sound source angle for an effective TDOA of 2.92 μs.

6.4.2 Directional sensitivity of the tympana

On a finer scale the pattern of vibration across the membrane was characterised by a sharp spike in displacement amplitude near the scoloparium attachment point which was frequently found surrounded by a series of smaller peaks in a ring for-

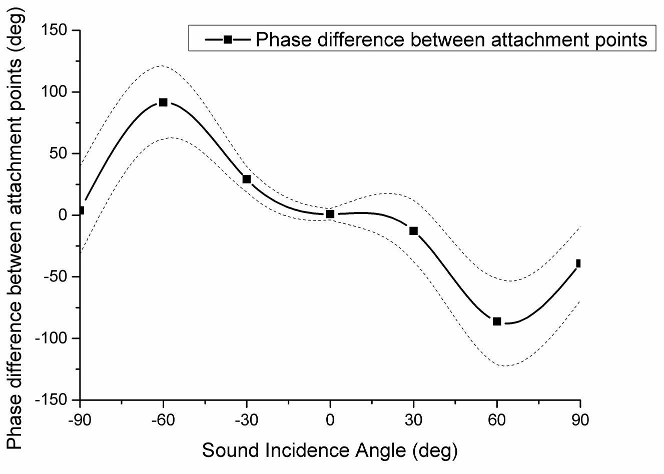

Figure 6.13: Phase difference as measured between the attachment points in the right and left tympana. A sharp increase in phase difference occurs where the acoustic pressure gradient would be smallest.

mation around the primary peak, which also showed a significant phase difference to the primary peak. The conjunctivum displaced no such spike, and a uniform phase, but instead a smaller, broader oscillation characteristic of a 1st order drum mode (Figure 6.14). The amplitude of the dominant peak did not vary significantly with sound source angle, with a typical displacement of 1.5 μm per Pascal, however detailed scans of the area surrounding the scoloparium revealed that the location of the dominant peak is not well matched with the scoloparium attachment point. The location of the dominant peak moves across the tympana with sound source angle. When the sound source is located at +30° or -150° to the midline of *Achroia grisella* (i.e. along the vector normal to the interface between the upper and lower sections of the ear) the dominant peak appears to be closer to the attachment point when the measurement points are overlaid on video image of the tympanum. As the sound field moved around the body the primary peak moves away from the scoloparium and a series of secondary peak form in a ring around the dominant peak (Figure 6.15). Comparing the displacement at the attachment points, rather than the maximum displacement, shows that the amplitude of displacement approximately doubles when the sound source is along the long axis of the membrane. The primary peak averages 1.6x the deflection magnitude of the secondary peak and 2.2x the deflection magnitude for all other loudspeaker angles tested. Signifi-

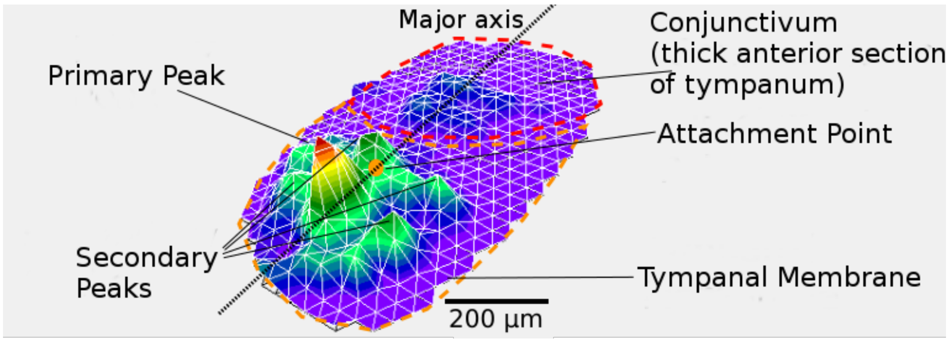

Figure 6.14: Laser vibrometry measurement of deflection magnitude measured at 390 points in a representative tympanum (the tympanum presented is the insect's right). The deflections are characterized by a sharp, primary peak and sever smaller secondary peaks nearby. The sharp primary peak was found in the centre of the posterior, membranous segment of the tympanum (region surrounded by the dashed orange line).

cantly a comparable study of the tympanum responses in a closes related species, *Galleria mellonella* (greater waxmoth; Pyralidae: Galleriinae) that perceived high frequency sound but has neither a male calling song nor female phonotaxis [162] did not reveal pronounced deflection peaks for any azimuth (Figure 6.16).

6.5 Finite Element Modelling

The sound field around the insect body was simulated using COMSOL Multiphysics. A floating point mesh of the moth thorax and abdomen was created from the volumetric image taken from the μCT scans and used as a template for a simple geometrical representation of the insect body. The principle feature is the cleft (Figure 6.17), which is 500 μm wide at the ventral surface and extends 1500 μm back into the insect's body. The complete model comprised the simplified thorax and abdomen resting in a spherical air domain of radius 10 mm (Figure 6.18).
Material properties of the insect body were approximated with a Young's modulus of 800 MPa and a standard Poisson's ratio of 0.3 with density set at 1300 kgm^{-3}. As with the Laser Vibrometry measurements, sound stimulus was a pure tone of 100 kHz presented perpendicular to the membrane surface with the angle of incidence varied around the axis normal to the ventral surface. The simulated sound source location was varied in steps of 10° with 0° representing a sound source directly ahead of the insect on the midline. The stimulus amplitude was set to 94 dB

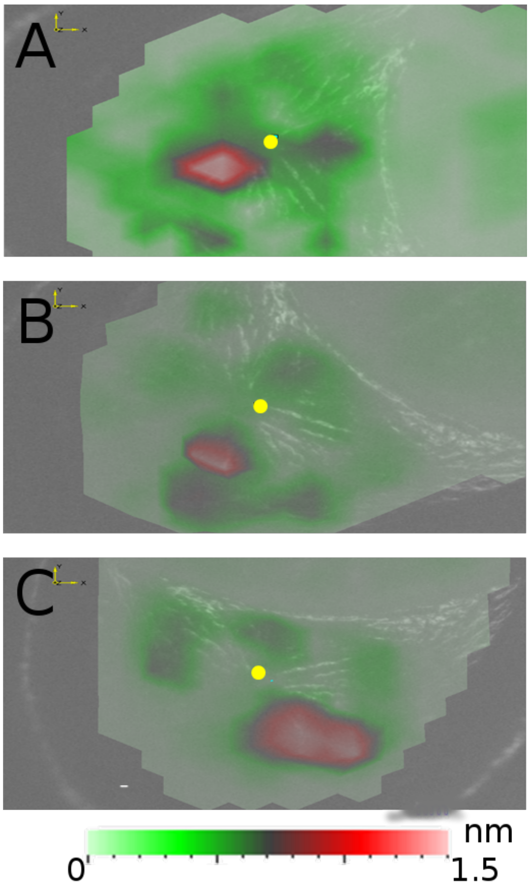

Figure 6.15: Displacement magnitude overlaid on video images of the tympanum. Yellow dot represents the approximate location of the attachment point. With sound source along the long axis of the tympanum, peak displacement occurs close to the attachment point with secondary peaks also close in or merged to a single peak (Panel A). As the sound field moves around the body the amplitude of the peak remains relatively constant at 1.3 nm, but the location of the primary and secondary peaks retreat from the scoloparium (Panel B and C at 0° and +30° to the insect midline respectively).

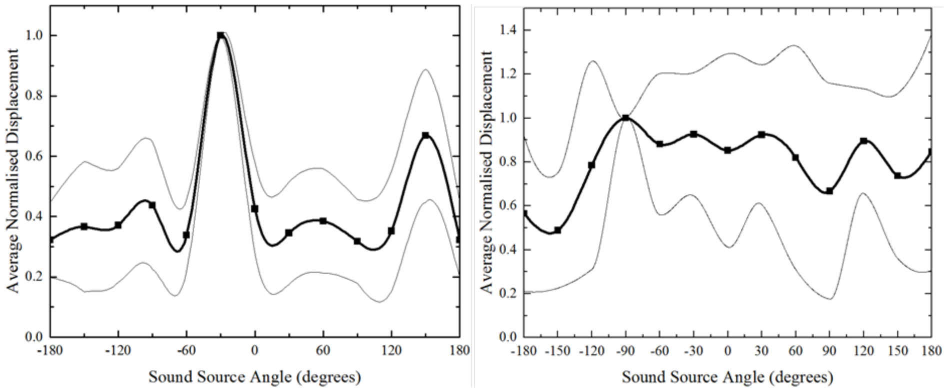

Figure 6.16: (Left) Average normalized displacement magnitude at the attachment point in the right tympanum for sound arriving from different azimuth angles. Angles are measured clockwise around the vector normal to the dorsal surface of the moth. Normalized values are determined by setting the maximum value that a tympanum exhibits among all azimuth angles to 1.0 and then adjusting the other values accordingly. The thickened curve shows the average values as measured from 10 females. Thin curves above and below show th maximum and minimum values among the 10 females. Curve smoothing was done with OriginPro's spline feature. An analogous curve was found for measurements of the left tympanum, with primary and secondary peaks occurring at +30Â° and -150Â° respectively. (Right) Similar measurements of deflection magnitude in Galleria mellonella. Displacement here is normalized at the highest point (-120Â°) however there is no significant directionality evident.

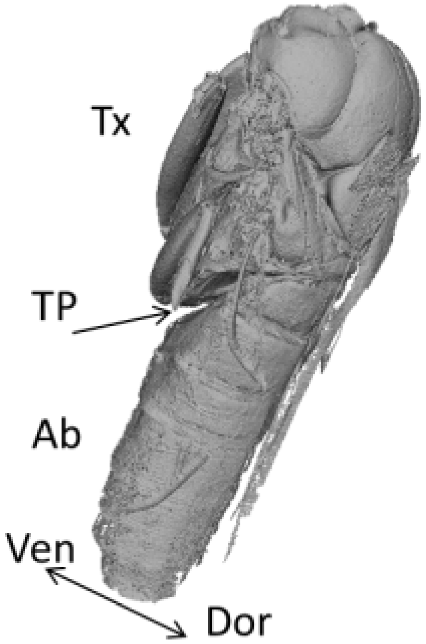

Figure 6.17: Floating point mesh of insect thorax (Tx) and abdomen (Ab), side view. The auditory system rests in the cleft in the ventral (Ven) side of the insect body formed by the overlap of the thorax and the abdomen.

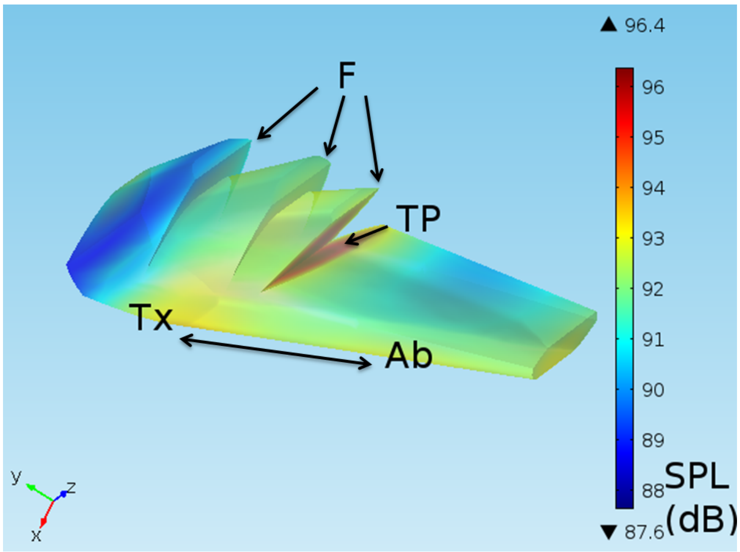

Figure 6.18: Simplified insect body simulated in COMSOL Multiphysics showing the SPL around the body. Incident pressure wave was set to 1 Pa at the air domain boundary, with the sound field incidence directly in front of the midline of the insect. Tx represents the thorax, Ab the abdomen, TP the location of the tympanal pits and F represents the base of the insect femurs. The insect is presented here with ventral side upwards, however later results use a ground plane underneath the insect and therefore do not possess the same symmetry along the y-axis of the domain.

SPL at the boundary of the air domain. With the sound source directly along the midline of the body a significant gain in sound pressure level can be seen in the cleft where the tympana sit with the largest gain occurring at the centre of the upper segment of the abdomen. Isolating the face on which the tympana rest a significant change in SPL is seen across the surface which varies with the angle of the sound source (Figure 6.19). A clearer picture of how the pressure gradient varies with angle can be obtained by looking at the gradient along the major axis of the right tympana. Measuring the absolute sound pressure along the major axis of the tympana shows that the ears will see a significant pressure gradient when the sound source is within 30° of the midline with the gradient tailing off sharply after this point (Figure 6.20).

6.6 Discussion

6.6.1 Resolution of front-rear ambiguity

The ability of *Achroia grisella* females that were not initially facing the sound source to establish an average heading within 45° of it within the first second following release demonstrates their reliable resolution of the front-rear ambiguity in directional hearing [163]. This ability cannot depend simply on the higher pressure gradient along the vector normal to the interface between the upper and lower sections of the tympana, since those gradients should be identical for sound arrival from behind the insect as well as in front. The ability also cannot depend on a sequential sampling of sound amplitude, which *A. Grisella* are capable of [164], since the amplitude to which a moth is exposed while running on the sphere remains constant. Instead, orienting in the correct direction towards the sound source depends on the fine-scale features of tympanal vibration as well as on diffraction of the sound field in the general region of the tympana. Vibrometry measurements show that the primary deflection peak in the right ear for a sound source at -30° azimuth is approximately 1.6x the secondary deflection peak for a sound source at 150° azimuth. The difference was consistently recorded over 12 insects, however there is no apparent reason why sound waves arriving along the major axis from the front should stimulate vibration more strongly that those arriving along the major axis from the rear. It is possible that, even with the thorax pinned back and the first segment of the abdomen completely exposed, that some diffraction of the

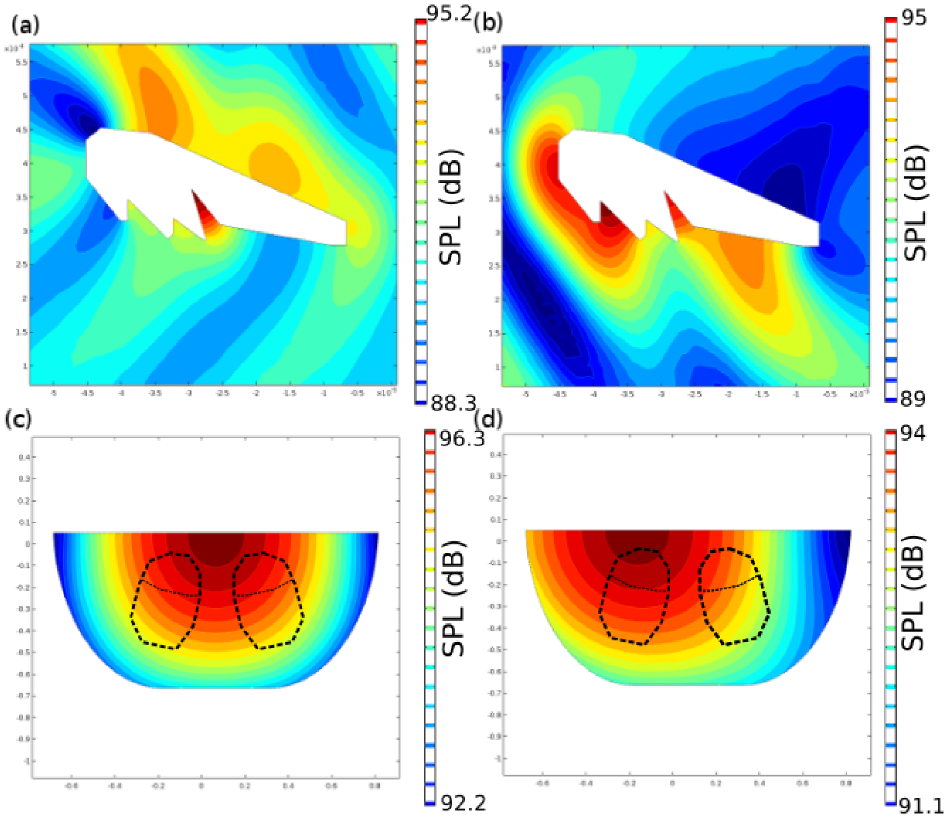

Figure 6.19: Sound pressure level (SPL) around a simple model of a female moth. (a) Predicted SPLs for a 94 dB (measured at air domain boundary 10 cm from the insect) sound source situated directly in front of the moth. SPLs are 6-7 dB higher in the cleft between the abdomen and the thorax, the location of the 2 tympana, than in the immediately surrounding sound field. (b) Predicted SPLs for the same sound source located directly behind the moth. The SPL in the cleft between the abdomen and the thorax is now 203 dB lower than when the sound source was in front of the insect. (c) Predicted SPLs across the ventral surface of the 1st abdominal segment for a sound source directly in front of the insect; approximate location of the tympana are indicated by dashed lines. SPL is equivalent across both tympana and reaches a maximum of 96.3 dB. (d) Predicted SPLs for a sound source at -30Â° azimuth with respect to the dorsal view of the insect (+30Â° in the ventral view shown). SPL is notably higher across the contralateral membrane (ranging from 93.9-94.8 dB) than across the ipsilateral one (ranging from 92.1-93.9 dB).

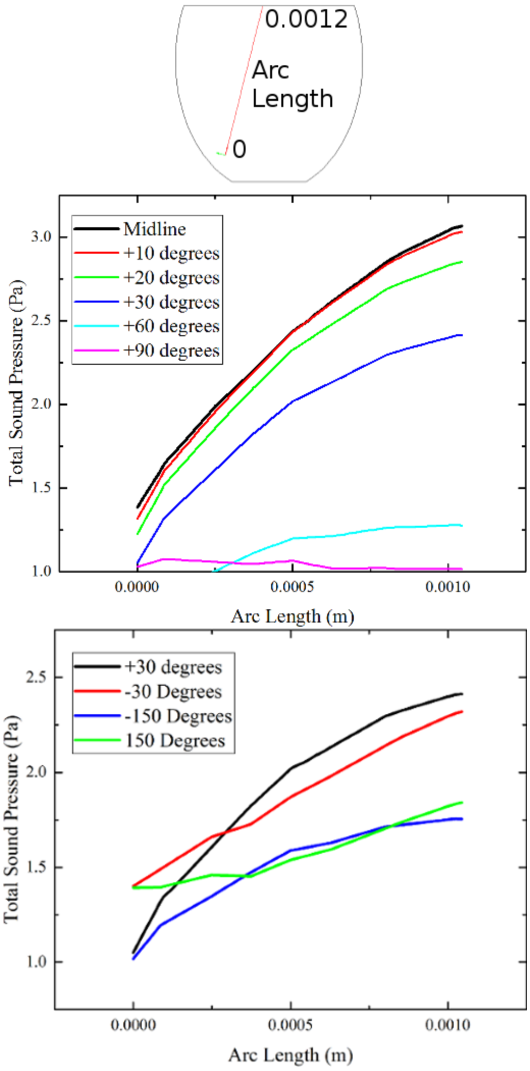

Figure 6.20: (Top) The imaginary arc line along which the pressure gradients are taken. The location of the line is approximately the location of the major axis of the right tympanum. (Middle) The gradient of the total acoustic pressure along the long axis of the tympanum is highest when the sound source is directly in front of the body and drops rapidly after 30Â°. When approaching 60Â° there is virtually no pressure gradient along the major axis. (Bottom) Comparison of the pressure gradients at 30Â° from the midline in front of the insect and 30Â° behind (-150Â°). The amplification of the pressure gradient is notably less pronounced.

sound field is occurring around the insect body. The front-rear ambiguity seems more neatly solved by the finite element analysis of the sound field around the moth, which indicated a localized elevation in sound pressure level in the vicinity of the tympana when sound waves arrive from a source within 30° of the moth's midline. The region is approximately 1 mm in diameter and features sound pressure levels 6-7 dB above the local sound field. It forms by diffraction in the ventral cleft between the thorax and the abdomen. Importantly, the pressure increase is 2 dB greater for sound arriving from the front than from directly behind the insect. Similarly, when sound arrives from one side of the midline, e.g. an azimuth of 30°, the critical region forms in the opposite side of the cleft such that the contralateral tympanum would be subject to sound pressure levels approximately 2 dB higher than the ipsilateral one. In addition sound arriving off the midline from the front elicits a larger pressure gradient in the contralateral ear, whereas sound arriving from off the midline from behind gives a lower pressure gradient but stimulus the ipsilateral ear more than the contralateral. The difference between the diffraction levels may be sufficient to attain correct orientation, albeit following some lengthy zigzags. The rapidity with which *A. grisella* females found the general directional of a playback stimulus at its onset demonstrates reliable resolution of the front-rear ambiguity in directional hearing. Unlike phonotaxis toward the stimulus, these rotational movements do appear to be initiated by binaural comparison of the two ears. At the end of the first part of the 2 speaker trials most females faced in the general direction of the sound stimulus at 0°. Consequently their right ears were normally more closely aligned than their left ears with the sound stimulus at 135°, which was broadcast from behind them in the second part of the trial. Thus their right ears would have been more strongly stimulated in the second part, and binaural comparison would have led them to rotate toward the right and eventually face in the general direction of the 135° speaker. We suggest that binaural comparison operated in this context because the secondary deflection peak at -150° or +150°, being much less pronounced than the primary deflection peak and subject to a reduced benefit from diffraction, did not invoke a high enough level of relative excitation to release the monaural tracking process.

6.6.2 Thoughts on efficiency and sound localization

Achroia grisella obviously localize sound sources, but the means by which they do so is not particularly efficient when compared with the capabilities of other acoustic insects [165, 103]. Much of their trajectory is spent in extensive zigzagging, and their arrival at the sound source is largely due to their running speed and manoeuvrability. Given the importance of efficient mate finding, one must question why the searching protocol persists in this species. A likely answer may be found in studying the timeline of evolution of acoustic communication in the Lepidoptera [166]. All but one of the 10-12 independent origins of hearing in the Lepidoptera occurred since 65 MA before the present, the currently accepted date for the appearance of echolocation in bats [167]. This timing, taken in conjunction with ecological patterns, had led to the inference that tympanal organs and hearing ability in Lepidoptera evolved as a response to hunting by insectivorous bats. In three major moth clades, Noctuoidea, Geometridae, and Pyraloidea, each including over 20,000 species, hearing is ubiquitous except in species found in geographical regions lacking bats or that are active during seasons or times of day when bats are not [167]. In these latter moth species tympanal organs and hearing ability are reduced or absent, presumably as a secondary loss. The hearing that had evolved in moths is simple but highly effective for avoiding and escaping predatory bats. Moths have 1-4 neurons per tympanum, minimum tuning over a broad frequency range which extends well above 100 kHz in some pyraloid moths [102, 18], and their directional ability remains unexplored. In the context of evading and escaping bats, the ability to localize a sound source may be relatively unimportant, as time for evaluating directional information would seldom be available. As expected, moth exposed to bat echolocation signals exhibit random evasive movement, general negative phonotaxis, or diving toward the ground if in flight [168], and become immobile if running on the substrate [30, 169, 170], thus giving no hint of an accurate directional response. In contrast to hearing, acoustic communication in moths is rare and only occurs among isolated species and genera in the three major clades, a pattern that reflects an origin of sound signalling via sensory bias mechanism [171]. In many cases the acoustic communication is restricted to close-range courtship [172] wherein directional hearing would not be critical, but in species such as *Achroia grisella* that transmit sound signals over longer distances the evolution of accurate directional ability would be expected. Conceivably, this development could have been achieved via evolution of an entirely new, highly efficient mechanism; e.g. the rocker-arm device in parasitoid *Ormia ochracea*. Unlike *O. Ochracea*, whose acoustic perception of host crickets had probably evolved *de novo*, *A. Grisella* already had an ancient system for perceiving sound. Thus it apparently followed a different evolutionary trajectory and refitted old equipment - a bat detector - for a new task, localizing a mate. Despite the overall similarity between *Achroia grisella* ears and those of related moth species wherein the ears still serve primary as bat detectors, some aspect of the directional hearing mechanism in *Achroia grisella* may be highly derived characteristics. The differential deflection of the neural attachment point in response to sound sources at different azimuth angles around the tympanum depends on the coupled vibration of the two segments of the tympanal membrane; however the simplicity of the basic moth ear can be a constraint. For example, the primary deflection peak of tympanal vibration is rather sharp, exhibiting changes in magnitude of 0.4 dB per degree azimuth, and one might expect the females to use this information for accurate turning towards the song stimulus [165]. However with only three peripheral neurons per tympanum [158] *A. Grisella* would not be able to benefit from pooling the responses of a population of neurons, and its turn accuracy remains limited as the result of intrinsic transmission variation within individual neurons. A general premise in evolution is that when a specific trait B depends on the existence of a general trait A, and A is already present and functional, the evolution of B may be constrained to forms that are less than optimal with respect to what is known to be possible. These peaks and valleys in the adaptive landscape may restrain evolutionary trajectories to certain routes [173], thereby ruling out various possibilities for some species. Further study of communication in diverse acoustic species should reveal the extent to which this premise may be applicable to directional ability and basic hearing.

Chapter 7

Conclusions and futher work

The work presented in this thesis investigates two very different stages of bio-inspired research: the relatively mature investigation into *Ormia* inspired directional hearing in which the biological work is long established and the current work is near pure engineering research and the novel investigation of directional hearing in *Achroia grisella* where the tone shifts to a first-principles scientific investigation. The very different techniques and style of each of the main pieces of research leaves the work seeming somewhat separated, but it is the unique challenge of bio-inspired design that the two disciplines be bridged. Moving from a purely behavioural study of sound localization in insects, such as is presented in Chapter 6, to a practical engineering design is a long road: the behavioural and biological experiments that lead to the development of the *Ormia* inspired microphone are now over twenty years old and have inspired a steady stream of publications which have moved ever closer to a realisable microphone design in that time.

7.1 *Ormia* inspired sound localization

Ormia inspired directional hearing systems have been studied extensively over the last twenty years. Much of the material covered in the literature review in Chapter 3 focused on either the basic mechanical principles of such systems or on the application to hearing aids. For that purpose the directivity index of the microphone is paramount, with a cardioid or hyper-cardioid directivity being the primary desired attribute. The use of *Ormia* inspired devices for sound localization was suggested by a team from the University of Maryland working with the U.S.

Army Research Laboratory [110]. Solving the lumped parameter equations allowed parametric studies on optimal mIID and mIPD to be performed, resulting in the notion of an optimized linear measurement of directionality which may be used for sound localization and noting the coincidence of the linearity of measurement and the maximum directional sensitivity. This result, and the demonstration from a working MEMS microphone, was published by the University of Maryland team in 2012 [106] during the first year of this PhD and coined the term 'dual-optimization' which has been appropriated and used throughout this work. The review of existing *Ormia* inspired designs made clear that electrical transduction of the membrane motion is a major obstacle to a commercial realisation of this design. Traditional capacitive back-plating was excluded because of the effect of thin film damping on the system. A 2 mm x 1 mm membrane would be critically damped in the translational mode would be critically damped with an air gap of the order of 50 μm, greatly reducing electrical sensitivity, and overdamped at lower air gaps, greatly reducing the mechanical sensitivity of the system. Additionally, as the parametric studies on the lumped parameter model revealed, higher damping requires a higher bridge coupling strength to reach the point of 'dual-optimization' requiring the translational mode to be at least 5-6 times higher frequency than the rocking mode of the device (this minimum estimation being based on a critically damped system with the same dimensions as the devices described here). Such a large gap between resonance frequencies can be challenging to design in a single device layer (although Miles et al. have designed a system with a coupling strength η=10.21 by constraining the rocking mode frequency to $<$ 1 kHz and stiffening the bridge with a second, deposited boss layer [126]). Without the advantages of traditional condenser microphone design the remaining strategies for transduction can be divided into two main approaches: those which constrain sensing to a single device layer (such as the capacitive combs and deposited piezoelectric sensing used in this PhD) and stacked devices, with a second sensing layer bonded onto the diaphragm wafer - a strategy that has been adopted to include sensing via interferometry through diffraction gratings imprinted on the membrane, or by creating a Fabry-Perot cavity with the membrane deflection. Though sensing via interferometry offers the possibility of very sensitive, low noise solutions the expense of small footprint cavity lasers as well as the inherent challenge of the additional fabrication and bonding steps required for stacked devices made this unfeasible for the PhD and likely too expensive and too large to be commercially viable for a final system. Using the cheap and readily available single layer multi-user processes from MEMSCAP presented its own set of challenges. The first, and perhaps most difficult to overcome, was that the membranes could no longer be fixed periphery devices - no second layer was available to create a bridging structure between the two membranes and, with a minimum 10 μm thick device layer resonance frequencies for the membranes and bridge would fall well into the ultrasonic range. For both capacitive comb sensing and piezoelectric sensing then an air gap around the device was unavoidable. This greatly impacts the mechanical sensitivity from the device, since at any frequency in the audio range the diffraction around the membrane would be expected to be so large that the sound shadow from the membrane would be extremely small. Indeed, in simulations where the back side of the wafer was closed the resulting deflection from a 94 dB incoming plane wave at resonance was of the order of tens of picometers, and the net force on the membrane less than 1% of the pressure amplitude of the acoustic wave. Counter-intuitively the mechanical response of the membrane was increased by having it open backed, suggesting that the main source of pressure difference on the membrane in most experiments was the path difference around the wafer. The wafer and mounting itself therefore contributed a directional sensitivity which would be difficult to distinguish from the directional sensitivity caused by the interference of modal forces on the membrane. The experience of the previous PhD student who performed experiments on an earlier iteration of these devices was that the path difference around the membrane cause a large spike in mIID at around $\pm 8-^\circ$ [89]. This was with the membrane in a full 11 mm x 11 mm die, the standard returned die from MEMSCAP. The devices returned during this PhD were further sub-diced into 4.5 mm x 4.5 mm dies where the spike appeared to occur closer to 45°-50° at the frequencies of interest. These spikes in mIID appeared in simulation as a drop in net-pressure on the ipsilateral side of the membrane, effectively where the phase difference from the path around the membrane itself and around the handle wafer dropped to zero. Below that critical point the directionality due to the path difference around the wafer was extremely small, particularly in after the second iteration of the device where the working range was constrained to within 10° of the midline. While we could be reasonably certain in this case that the directionality of the membrane was attributable to the effect of the coupling between the wings, the effect of the housing of any completed device would be pronounced in a design with a potential path difference, and operation with a closed back would reduce the sensitivity of transduction from acoustic wave to mechanical motion to below the point where any hope of making an electrical measurement would be lost. The second problem with a single layer design is the sensitivity of either capacitive or piezoelectric sensing. An ideal capacitive comb measurement would be expected to produce a change in capacitance of the order of femtoFarads for ranges of motion of 1 μm, in practice meaning any putative measurement scheme would have to be able to distinguish delta C's of tens or hundreds of attoFarads for even the most basic resolution of motion. Compared to this the parasitic capacitance from the wire bonding to the chip would be expected to be in the range of 0.1 pF, swamping the signal from the capacitive combs before the pre-amplifier stage is reached. Similarly with the Aluminium Nitride an expected current in the nA range could only realistically be resolved with heavy averaging and, in the final result, the use of a lock-in amplifier. The principle contributions of this section were the expansion to the concept of dual-optimization, increasing the coupling strength between the wings of the membrane to increase the directional sensitivity at the expense of angular range of operation, which was intended at least in part as a solution to the previously undescribed problem of the Cauchy like (or Hinckley) noise that is inherent to the mIID and mIPD measures. The large noise and errors inherent to the mIID and mIPD measures appears to have been well known (from correspondence with other researchers in the field), but has not been described in the literature nor identified as being the result of taking a ratio of two noisy sources. The use of over-coupling to combat this problem, while perhaps a brute force solution, was successfully accomplished and found to be reproducible up to the point where the error that was purely attributable to the mechanical noise within the membrane was less than 1° in the azimuthal measurement. The modelling of the predicted interquartile range of mIID measurement revealed a further problem with electrical transduction: small reductions in the SNR performance of the sensor produce large increases in the measurement error. With the deflections being measured under the laser vibrometer, where the principle source of noise would be the mechanical-thermal noise of the sensor itself (the contribution of noise from the laser vibrometry measurement would be expected to be minimal and was found, from the measurements of H1 and H2 to be less than 1% of the noise signal), the interquartile range could be reduced to around 0.5 dB in the mIID measure. However with the introduction of electrical noise, from parasitic coupling in the wire bonding stage as well as the pre-amplifier noise, the SNR degraded to a point where any meaningful measure of azimuth would be impossible without the extensive filtering and averaging employed in the final iteration of the device. The mIPD measure, which was less sensitive to the coherent noise pollution of electromagnetic interference, gave a sensitivity of 9.24° phase change per degree change in sound incidence angle and an average error of 1.82°. Unfortunately the difficulty in reducing the measurement error placed some severe constraints on the effectiveness of these devices, and the results given here are heavily reliant on brute force-techniques: mechanically increasing the directional sensitivity around the midline at the expense of range of measurement, and electrically filtering and processing the signal. This section also showed the development of computational models for parametric study of *Ormia* inspired microphones, as well as successful application of finite element modelling that correctly anticipated the damping conditions and coupled operation of the membranes. Agreement between modelling and the final measured device was consistently good, with the exception of the first iteration of the device. While manufacturing tolerances and under-estimation of Eigenfrequency both contributed to differences in resonance frequencies, the resulting change in coupling strength and damping conditions was relatively small so the results for the final iteration device modelled with a rocking mode resonance frequency of 8080 Hz were very close to the physical measurements taken on the device with a rocking mode resonance of 8120 Hz. The methodology behind the mechanical design of *Ormia* inspired sound localization devices was successful, with an overview of the techniques published in *Optimization of a bio-inspired sound localization sensor for high directional sensitivity* (2015).

7.2 Sound localization in *Achroia grisella*

The lesser wax moth, *Achroia grisella*, has presented an attractive target for researchers due to its unusual (among Pyralids) courtship employing male song and female phonotaxis. The reliability of virgin females to begin phonotactic walking in response to a simulated signal has allowed researchers to investigate sexual selection, with females showing marked preferences for asynchronicity of the pulse pattern and higher pulse rates. However the mechanics of the phonotaxis have not been well studied. At first look, *A. grisella* faces a similar problem to *Ormia ochracea*, with the size and location of its auditory system constrained by its small size the directional cues between the ipsilateral and contralateral ear would be extremely small. *A. grisella* has a less overwhelming task, being required to track a

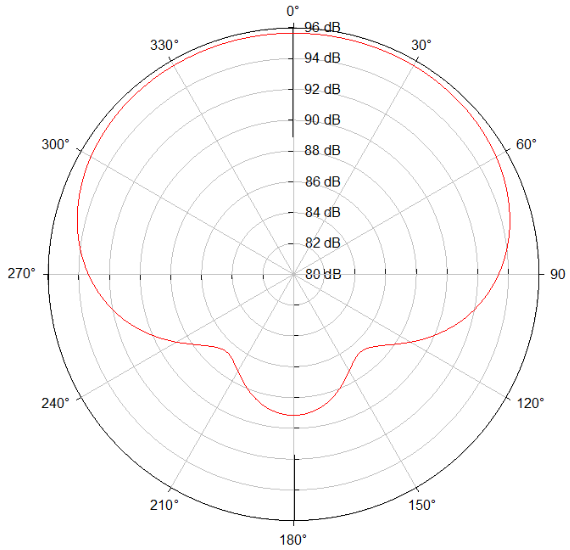

Figure 7.1: Simulation of the sound field around the circumference of a cylinder of 600 μm radius in response to a stimulus at 100 kHz at 94 dB (re 20 μPa). The sound shadow between the ipsilateral and contralateral side represents a change of 6 dB, which may have been sufficient to trigger a binaural sound localization in the insect, however the actual ear locations would be co-located on the ventral surface of the insect so with the sound source on the insects left the ears would be located at 75° and 105° where there is a SPL difference of only 3.1 dB.

signal at 100 kHz rather than the 5 kHz of *Ormia ochracea* and might be expected to benefit from some sound shadowing around the body. Indeed, if the wax moths ears had been located on the side of the thorax as with noctuid moths the sound showing may well have been sufficient to preclude the need for any additional mechanisms. In a simple simulation of the sound field around the circumference of a 600 μm cylinder, the approximate size of *A. grisella*s abdomen there is a notable sound shadow between the ipsilateral and contralateral sides (Figure 7.1). The co-location of the ears on the first segment of the abdomen, where they are almost completely covered by the last segment of the thorax and the hind legs, would therefore appear to be extremely unhelpful to the insect. This observation flows naturally from the suggestion in Chapter 6 that the relative inefficiency of the hearing system is due to the ears principally being evolved from a simple bat detector hearing system, with a simple 'panic' behaviour in response. Like the example of the mammalian laryngeal nerve which loops around the aorta and ligaments in the chest before returning back upwards to the larynx, natural selection could not simply disconnect and reform the ears in a better location since that would have been a step that reduces fitness. So the ears in their existing location needed to be retro-fitted to accomplish the new task of phonotaxis. The unusual segmented tympana are common in Pyralid moths where there is no evidence of phonotactic behaviour (although some Noctuids have been known to employ some negative phonotaxis as part of predator avoidance the Noctuid ears lie on opposite sides of the much larger thorax where sound shadowing would be sufficient to localize the sound source). Laser vibrometry measurements were taken of the similarly segmented tympana of the Greater Wax Moth *Galleria mellonella*, this time to the biologically relevant frequencies of 40 - 60 kHz (the range of bat echolocation calls). Despite the similar structure of the tympana, no similar directionality was found in *Galleria* either at the attachment point or at the point of maximum deflection. Given the lack of correlation between the segmented structure of the tympanum and phonotaxis it is reasonable to conclude that the contribution of the segmented structure to Pyralid hearing serves some other primary purpose (or no purpose) before being adapted to the task of sound localization. Previous work on *Achroia grisella* had noted their remarkable phonotactic ability, but there had been no effort to quantify their capabilities as there had with *Ormia ochracea* [103]. Behavioural studies of the insect therefore had the original goal of determining the accuracy with which a sound source could be located. While the observations of previous researchers were that *Achroia* would run directly towards the source, measurements on the servosphere revealed that the path taken was marked by a near constant counterturning pattern. The rapidity of this behaviour is difficult to see from direct observation since *Achroia* can complete a movement from the left to right extreme as quickly as twice a second giving the impression that it is moving directly towards the source. Additionally it seemed that *Achroia*'s phonotactic accuracy was not as good as previously thought, with most insects veering 20-30° to the left or the right of the target. Concurrently with these experiments Laser Doppler Vibrometry measurements of the mechanical motion of the tympana was conducted in response to a 100 kHz stimulus source from various sound angles. The aim was to determine some response pattern which would allow the insect to distinguish azimuthal heading. Here there was some guidance from a previous Laser Doppler Vibrometry experiment conducted by Rafael Rodriguez [161], albeit performed with a single point system and solely from one sound incidence angle - plane to the ventral surface of the abdomen. Rodriguez experiment suggested that the segmented structure of the tympanum would play a role - with the thicker upper segment of the tympanum oscillating in anti-phase with the lower segment on which the neuronal attachment points were located. This suggested the possibility that each ear may operate similarly to *Ormia*'s connected tympana, with the upper and lower sections responding to a combination of pressure gradient and total pressure resulting in an amplified phase difference. The laser Doppler vibrometry experiments did indeed reveal a phase difference both within each individual tympanum and between the attachment points (See section 6.3), however the phase difference recorded reached a maximum at 60° to the insect midline of 90° phase difference - an effective time difference at 100 kHz of only 2.3 μs. This was scarcely an improvement on the equivalent of 2 μs time difference that would be expected for a sound source arriving at 90°, and would likely be too small for the insect to distinguish with a mere four neurons per tympana and a likely timing jitter of 80 - 100 μs. Initial measurements of the amplitude difference between tympana were similarly disappointing, recording little difference in the peak of displacement in the lower membrane with sound source angle. During the course of the experiments an unusual pattern of membrane displacement was noted: the primary deflection peak did not appear at the attachment point as expected, but shifted position on the tympana with sound source angle. The experiments were repeated with the microscope laser Doppler vibrometer - a 3D system, but the primary advantage that this system allowed was a much smaller spot size and greater accuracy of placement. Using this system the measurements were performed with care to record the vibration at the point of attachment, and it was only here that the amplitude was found to vary in response to sound incidence angle. The pronounced spike in amplitude when the sound incidence angle was at 30° to the insect midline, along the major axis of the tympanum not only offered a good signal for the wax moth to distinguish but also suggested a closer look at the insect's phonotactic behaviour would be merited: the paths recorded were consistently $\pm 20 - 30°$ away from the sound source, rarely if ever did *Achroia* walk directly towards the source. The congruence of the insect's path with the angle of the tympana, and the discovery of the peak in displacement when the sound incidence angle was along the major axis of those tympana gave the impression that *Achroia* was following the peak in displacement of a single ear. Given the comparison with *Ormia ochracea* it was deemed necessary to exclude the possibility that some connecting mechanism was responsible for this displacement pattern. No bridging or connecting structures between the tympana could be observed externally, and the X-Ray μCT scans did not reveal anything internally down to a resolution of 2 μm. Additionally no spiracles or acoustic ducts connecting the tympana could be observed at this resolution, nor were any seen linking the apparently closed tympanal pits to the air outside. It seems unlikely that such spiracles do not exist: as with pressure release vents in microphones and the Eustachian tubes in human ears some compensation for changes in barometric pressure must be available to prevent damage to the ears. As this pressure regulation must occur over extremely long time scales (compared to the pressure variation of an acoustic wave) it may be extremely small, and still provide this function even it is below the resolution of our measurements. For any significant transfer of energy during stimulation from an acoustic wave, below 2 μm is simply too small for any linking spiracle or cuticular structure to have any effect. Further behavioural tests then followed with the goal of distinguishing phonotactic tracking with other related behaviours such as searching or evaluation. To these ends trials incorporating a 3 second silence, and dual speaker trials in which the location of the sound source was changed midway through the experiment were conducted. Notably all these experiments were open loop, which is the insect's location on the servosphere was constant, as was the stimulus broadcast. In an arena trial, where *A. grisella* could close the distance to its mate, moving in a direction $\pm 30^\circ$ from the sound source would produce a path that curved inwards towards the goal. The interrupted trials showed the insects behaviour when losing the signal: the insects would often circle, and then come to a complete stop frequently facing the opposite direction to the stimulus location before coming to a rest. When the sound stimulus restarted the searching behaviour would recommence, again with the insect settling on a path $\pm 20-30^\circ$ away from the sound source. On suggestion from colleagues and reviewers a further trial was attempted to confirm the monaural phonotaxis hypothesis in which one of the eardrums was punctured, however despite many attempts the insects did not engage in any form of phonotaxis after the surgery. Whether some binaural comparison remained necessary or the insects were simply too traumatised to engage in mating behaviour is not known. A more complete effort to evaluate the diffraction of the sound field around the insect body and thorax was completed using model data generated from the X-Ray μCT system. These simulations revealed that the apparently disadvantageous cleft in which the auditory system sat in fact acted as an acoustic hotspot, creating an increase in sound pressure level of 4-6 dB when the sound stimulus was broadcast from the front of the insect. The hotspot continued when sound incidence angle reached 30° of the midline, at which point the pressure gradient along the contralateral ear - the one which would now have its major axis normal to the plane of the incident wave - would be at a maximum. Thereafter the pressure gain decreased rapidly, falling to no gain with the sound source at 90° to the insect midline. The effect of the sound shadow was estimated at this point at a little over 2 dB between the ipsilateral and contralateral membranes, lower than the estimates from the simple cylinder above due to the flattening of the insect body on the ventral surface of the abdomen. In this way the combination of diffraction around the thorax and the segmented tympanal structure may be seen to reinforce to create a significant difference in displacement between an ear with the major axis normal to the plane of the incident wave and its pair. Whether this is a 'true' monaural phonotaxis is unclear. It may yet be true that a comparison must be made to the ear which is not so hyper-stimulated in order to track the source. Nevertheless the system is a novel one, and poses particular interest due to the evolutionary constraints under which it is assumed to have developed.

7.3 Future Work

The primary intention of studying the mechanisms of phonotaxis in *Achroia grisella* was in hope of recreating those principles in a micro-scale microphone system. With current MEMS technology implementing a thickness change across a membrane is not possible; however we may yet achieve the same effect by altering the shape and size of a single thickness membrane. During the course of this work some attempts were made to recreate the phase and amplitude behaviour of *Achroia grisella* in a simulated thickness gradient membrane, however several barriers to creating a satisfactory model exist. Firstly recreating the ear of the Lesser Wax Moth stumbles upon estimating the unknown Young's Modulus, Poisson's ratio and damping of the membrane itself, as well as the precise change in thickness across the membrane. Measurement of these quantities is complicated by the need to perform the measurements in vivo, since the material properties of cuticle are highly dependent on the water content and the thin membrane dried rapidly post mortem. Secondly the peculiar pattern of displacement peaks around the attachment point suggests that the scolopale rod is acting as a spring attached to the membrane, which has its own unmeasured stiffness and damping properties. Finally there remains the

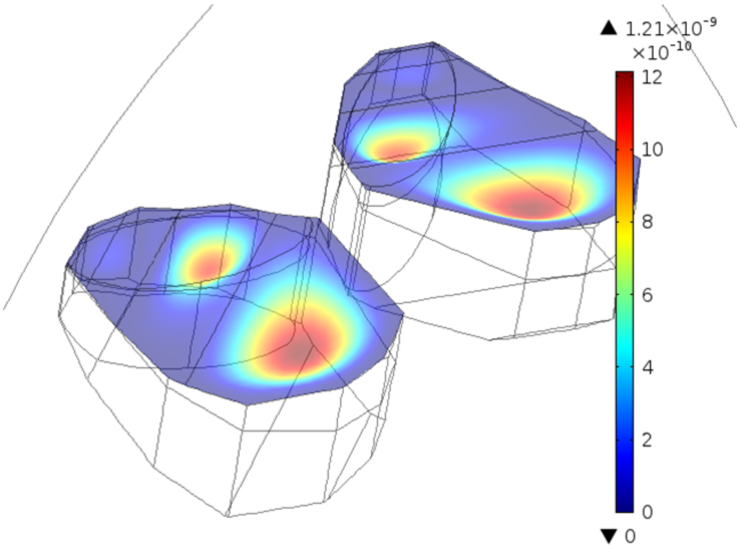

Figure 7.2: COMSOL model of Achroia grisella hearing system based on μCT measurements of the tympanal pits. The thicknesses of the upper and lower sections are 1 μm and 1.5μm respectively with the membrane material given a Young's modulus of 1 GPa and a Poisson's ratio of 0.3.

possibility of some active hearing processes, known to exist in related moth species [102], which may further deviate simulation from measurement. Reconstructing the geometry of the ear and parametrically altering the relative thickness of the upper and lower segments, as well as the Young's modulus of the membrane material some reasonable guesses into the mechanics of Achroia's membrane were made (Figure 7.2 and Figure 7.3). Of more interest was whether this pattern could be replicated in a MEMS device, which would likely therefore be an asymmetric model with one wing of the membrane notably larger than the other. Similar membranes have been shown before with the goal of giving an amplification of directional cues at two or more distinct frequency bands [174, 175, 123], but operating similarly to the *Ormia* inspired microphones by comparing the displacement at each of the wings of a single membrane. Early simulations suggest it is possible to use a measurement from a single side of an angled pair of devices produce an amplification of directional cues at a single frequency, or, similarly to the microphone operation of *Ormia* inspired sensors, to produce a much lower amplification of directional cues across a broader frequency range (Figures 7.4 and 7.5). Employing these sensors in pairs in this manner draws inspiration from the asymmetric nature of *Achroia*'s tympana and dovetails into the next logical progression for *Ormia* inspired sound localization

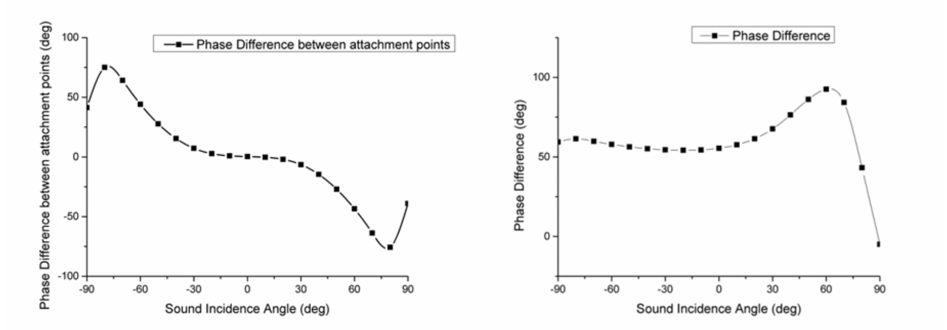

Figure 7.3: (Left) Phase difference between peak displacement for COMSOL model shown above. The peaks in phase difference seen in the measurement of Achroia itself can be reproduced in this model, however they occur slightly beyond the 60Â° from the laser Doppler vibrometry experiments. (Right) phase difference between peak displacement in upper and lower segments of a single ear. Again there is good agreement in the phase difference spike, however the phase difference at other angles is larger than that recorded from Achroia. The model here represents best guesses into material properties and thickness dimensions of the membrane, and was the closest approximation to the actual insect behaviour that was able to be achieved.

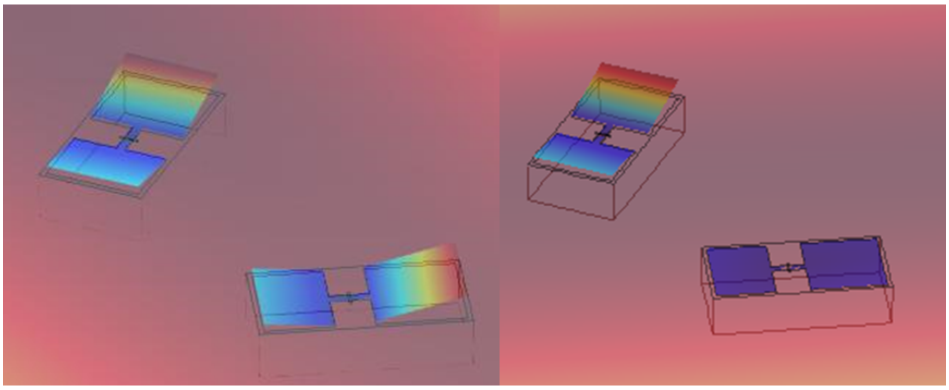

Figure 7.4: An angled pair of Ormia / Achroia inspired sensors with a sound source at the midline between the pair (left) and at 60° to that midline.

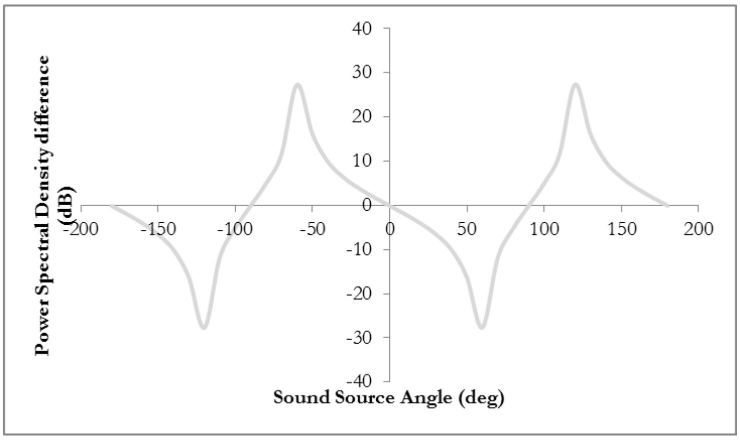

Figure 7.5: Power Spectral Density difference between angled pair of asymmetric membranes measured on a single side (equivalent to mIID). The measurement here is not the linear directional sensitivity that would be ideal for a sound localization device, but may be more useful for its cardioid directivity pattern.

devices - the implementation of arrays of sensors. As with the sensors described in this work, fundamental problems exist with the mechanical and electrical sensitivity of such sensors. Research into alternative configurations which may permit a fixed periphery membrane in conjunction with a coupling mechanism would aid the mechanical sensitivity of such devices. In terms of electrical sensitivity the integration of piezoelectrics with MEMS technology continues to develop, holding out the possibility of more sensitive and stable sensing layers (for example, by integrating the sputtering of PZT onto a device layer). Arrays of membranes introduce a further noise problem, since the noise on two diaphragms will be uncorrelated (compared to the mechanical noise on a single coupled pair of membranes, where the noise would be expected to be highly correlated or anti-correlated) further increasing the measurement error. Despite these drawbacks, arrays of sound localization sensors are a necessity for any putative sound localization system since a single sensor is unable to resolve the ambiguity between sound incidences in the azimuth and pitch angles. Additionally, the solution to the problem of noise presented here involved severely restricting the linear range of operation of the *Ormia* inspired devices to $\pm 10°$, requiring an array of 18-36 such devices to make a full estimate of angle in one plane. In *Achroia* itself several interesting opportunities for further research present themselves. The first, concerned purely with the evolution of hearing systems, takes as its principle that the location of the ears on *Achroia grisella* in a cleft between the abdomen and thorax was caused by the acoustic hotspot generated by the diffraction around the thorax. This diffraction is still present at lower ultrasonic frequencies (between 40 kHz and 60 kHz), so that region of the abdomen would be particularly susceptible to acoustic stimulation. It has been postulated that a precursor to tympanic hearing systems would be vibrational sensing of susceptible tracheal systems [167], and insect tympanal hearing systems are found in a variety of places around the body. As well as *Achroia grisella* a similar acoustic hotspot has been discovered co-located with the tympanal hearing system of the desert locust [89]. Investigation of related pyralid species may reveal the diffraction around the insect body to be a significant driver of the location of the development of tympanal hearing systems. On the mechanics of the membrane itself the so-far under-utilized 3D vibrational measurement of the attachment point would be of interest. The location of the primary deflection peak away from the attachment point seems counter-intuitive. The creation of an impulse in the scoloparium seems to depend on a strain induced in the scolopale rod, yet compared to the membrane deflection the attachment point moves far less. Detailed measurements of the attachment points' in-plane vibrations may give some insight into the sensitivity of the scoloparium. Often described as a 'stretch sensor' could the scoloparium respond more to bending stresses than tensile or compressive stresses? Beyond this question, analysis of the membrane's in-plane motion would be hoped to give additional information on the material properties of the membrane, including some guidance on the question of whether the stiffness of the membrane is attributable to simple Kirchoff-Love plate mechanics, or whether it is more properly treated as a flexible membrane under tension. Answers to these questions could inform better models of the mechanics of tympana with variable thicknesses, and lead to the generation of microphone diaphragms capable of tonotopy or sound localization purely from the mechano-acoustic interaction on the membrane itself.

Appendix A - MATLAB code

MATLAB function calculating mIID, mIPD and directional sensitivity arrays from Chapter 3 as well as measurement of non-linearity used in optimisation of devices in Chapter 4.

Lumped parameter model

```
% Provides waterfall graphs of mIID and mIPD swept over both frequency and
% sound incidence angle in nested parametric study
clear all;
close all;

eta = 1.2; % Bridge coupling strength
fRocking = 7120; % Rocking mode frequency
fTranslational = eta*fRocking; % Translational mode frequency

dampingTranslational = 1.23; % Translational mode damping coefficient
dampingRocking = 0.89; % Rocking mode damping coefficient

fArray= 5000:1:10000; % Sweep range of frequency
deg = -90:1:90; % Sweep range of sound angle (deg)
thetaArray = -pi/2:pi/180:pi/2; % Sweep range of sound angle (rad)
iTheta = length(thetaArray); % Counters for length of frequency and angle arrays
iFreq = length(fArray);
```

```
% Blank arrays for results

mIIDArray=zeros(iTheta,1);
mIPDArray=zeros(iTheta,1);
mIIDfArray=zeros(iFreq,1);
mIPDfArray=zeros(iFreq,1);

for m=1:length(fArray)
f=fArray(m);
fNormalized=f/fRocking; % Parameter Omega from Chapter 3

% Parameter lambda is constant with frequncy (Capital Lambda parameter
% in Chapter 3 (Equation 3.29)
lambda = (1-fNormalizedˆ2+j*2*fNormalized*dampingRocking)...
/(etaˆ2-fNormalizedˆ
2+j*2*fNormalized*eta*dampingTranslational);

% Calculate directional sensitivity at midline with limit h-¿0 (Equation 3.35)
DSmIPDLimit(m)=angle((lambda+j*tan(pi*plateLength*f*sin(h)/343))/...
(lambda-j*tan(pi*plateLength*f*sin(h)/343)))/h;
DSmIIDLimit(m)=20*log10(abs((lambda+j*tan(pi*plateLength*f*sin(h)/343))/...
(lambda-j*tan(pi*plateLength*f*sin(h)/343))))/h;

for i=1:iTheta
theta=thetaArray(i);
phi = 2*pi*plateLength*f*sin(theta)/343;

% Calculate and store mIID (Equation 3.30)
mIIDArray(i)=20*log10(abs((lambda+j*tan(phi/2))/(lambda-j*tan(phi/2))));

% Calculate and store mIPD (Equation 3.31)
mIPDArray(i)=180/pi*(angle((lambda+j*tan(phi/2))/(lambda-j*tan(phi/2))));

% Numerical calculation of directional sensitivity for mIID and mIPD
```

```
DSmIID=diff(mIIDArray);
DSmIPD=diff(mIPDArray);

% Calculates average error across angular range from directional sensitivity
around the midline
errorMIPD(i)=(DSmIPDLimit(m)*theta-(pi/180)*mIPDArray(i))^2;
errorMIID(i)=(DSmIIDLimit(m)*theta-mIIDArray(i))^2;

% Stores mIID, mIPD, DSmIID and DSmIPD arrays in 2D matrices
mIIDwaterfall(m,:)=mIIDArray;
mIPDwaterfall(m,:)=mIPDArray;
DSmIIDwaterfall(m,:)=DSmIID;
DSmIPDwaterfall(m,:)=DSmIPD;

% Calculation of non-linearity of measurement over the angular range
NLmIPD(m)=1/abs(DSmIPDLimit(m))*sqrt((1/iTheta)*sum(errorMIPD));
NLmIID(m)=1/abs(DSmIIDLimit(m))*sqrt((1/iTheta)*sum(errorMIID));

figure(1)
[ax,h1,h2]=plotyy(fArray,DSmIPDLimit,fArray,NLmIPD);
xlabel(’Frequency (Hz)’);
title(’mIPD’);
set(get(ax(1), ’Ylabel’), ’String’, ’mIPD (Â°)’);
set(get(ax(2), ’Ylabel’), ’String’, ’NL (Â°)’);

figure(2)
[ax,h1,h2]=plotyy(fArray,pi/180*DSmIIDLimit,fArray,NLmIID);
xlabel(’Frequency (Hz)’);
title(’mIID’);
set(get(ax(1), ’Ylabel’), ’String’, ’mIID (dB)’);
set(get(ax(2), ’Ylabel’), ’String’, ’NL (dB)’);
```

7.4 Hinckley distribution

```
% Provides graphs of Hinckley distribution and cumulative function X/Y given
% parameters of mean, standard deviation and correlation of two Guassian
% distributions X and Y.

clear all;
close all;

u=0.5:0.001:2; % Range over which distribution will be calculated. The
% expected range (if the means are much larger than the
% standard deviations) will be the ratio of the means

mux=6e-4; % Mean for Guassian distribution X
muy=6e-4; % Mean for Guassian distribution Y
sigmax=6e-6; % Std. Deviation for Guassian distrubution X
sigmay=6e-6; % Std. Deviation for Guassian distrubution Y
rho=0; % Correlation coefficient between X and Y (-1¡rho¡1)

% Parameters a, b, c, d are constants from the five parameters above

a=sqrt(u.^2/sigmax^2-2*rho.*u/(sigmax*sigmay)+1/(sigmay^2)); % Equation
4.13
b=mux.*u/sigmax^2-rho*(mux+muy.*u)/(sigmax*sigmay)+muy/sigmay^2;% Equa-
tion 4.14
c=mux^2/sigmax^2-2*rho*mux*muy/(sigmax*sigmay)+muy^2/sigmay^2;% Equa-
tion 4.15
d=exp((b.^2-c.*a.^2)./(2*(1-rho^2).*a.^2));% Equation 4.16

phi = @(x) 1/(sqrt(2*pi))*exp(-0.5*x.^2); % Setting up function for
% calculation of definite
% integral in f(x) and F(x)

for k=1:length(u);
```

```
% Distribution function (Equation 4.12)
f(k)=(b(k)*d(k)/(sqrt(2*pi)*sigmax*sigmay*a(k)^3)+...
(integral(phi,-Inf,(b(k)/(sqrt(1-rho^2)*a(k))))-...
integral(phi,-Inf,(-b(k)/(sqrt(1-rho^2)*a(k)))))+...
sqrt(1-rho^2)/(pi*sigmax*sigmay*a(k)^2)*exp(-0.5*c/(1-rho^2)))/length(u);

% Cumulative function
F(k)=integral(phi,-Inf,((muy*u(k)-mux)/(sigmax*sigmay*a(k))));
end;

figure(1)
% Expected ratios expressed in dB scale to match mIID
plot(20*log10(u),f);

figure(2);
plot(20*log10(u),F);
```

Appendix B - COMSOL reports

Electrostatic field capacative combs

Global Definitions

Date	Sept 18, 2013
Name	Electrostatic Field Capacitive Combs.mph
Path	D:\Users\isb12210\Downloads\Electrostatic Field Capacitive Combs.mph
Build	COMSOL 4.3b (Build: 189)
Used Products	COMSOL Multiphysics CAD Import Module MEMS Module

Parameters

Name	Expression	Description
Cw	6[um]	Comb width
Cl	100[um]	Comb length
Ct	10[um]	Comb thickness
g	6[um]	Separation between combs
sep	10[um]	Separation between comb and substrate
disp	0	Initial out of plane displacement

Materials

Single crystal silicon

Air

Electrostatics

Equations:

$$\nabla \cdot \boldsymbol{D} = \rho_v \tag{7.1}$$

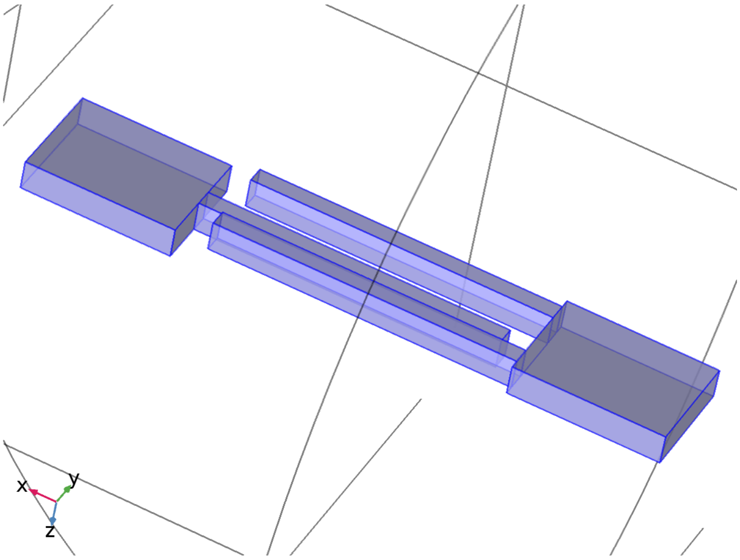

Figure 7.6: Silicon (Domains 2-6)

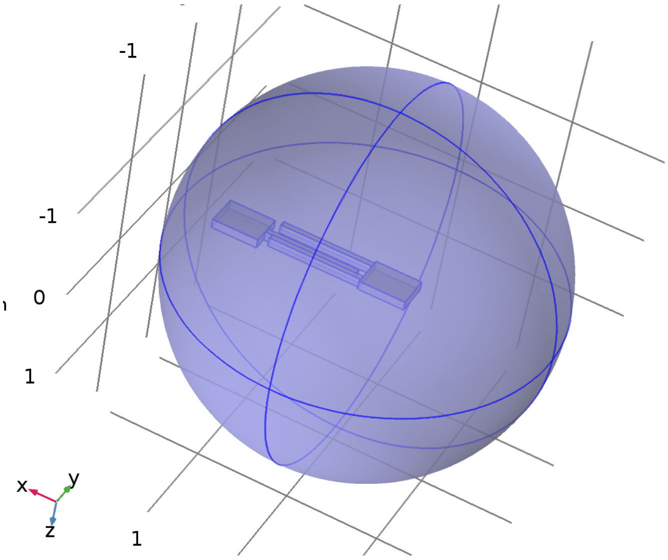

Figure 7.7: Air (Domain 1)

$$\boldsymbol{E} = -\nabla V \tag{7.2}$$

$$\boldsymbol{n} \cdot \boldsymbol{D} = 0 \tag{7.3}$$

7.4.1 Study

Stationary

Parameter name	Parameter value list
dist	range(0,1e-9,1e-6)

Description	Value
Sweep type	Specified combinations
Parameter name	dist
Parameter value list	range(0,1e-9,1e-6)
Include geometric nonlinearity	Off

First iteration silicon on insulator device

Global Definitions

Date	Jun 30, 2016
Name	1stDevice1stRun-FineFrequencySweep.mph
Path	D:\Users\isb12210\Downloads\1stDevice1stRun-FineFrequencySweep.mph
Build	COMSOL 5.2a (Build: 152)
Used Products	COMSOL MultiphysicsAcoustics ModuleCAD ModuleStructural Mechanics

Materials

Single crystal silicon

Air

Pressure Acoustics - Frequency Domain

Equations:

$$\nabla \cdot \left(-\frac{1}{\rho_c}(\nabla p_t - q_d)\right) - \frac{k_{eq}^2 p_t}{\rho_c} = Q_m \tag{7.4}$$

$$p_t = p + p_b \tag{7.5}$$

$$k_{eq}^2 = \left(\frac{\omega}{c_c}\right)^2 \tag{7.6}$$

Sound Hard Boundary 1

$$-\boldsymbol{n} \cdot \left(-\frac{1}{\rho_c}(\nabla p_t - q_d)\right) = 0 \tag{7.7}$$

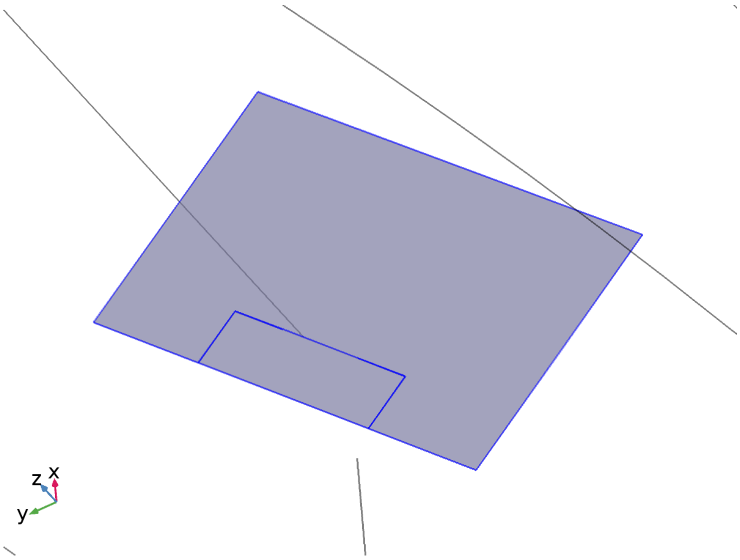

Figure 7.8: Single Crystal Silicon (Boundaries 4-9)

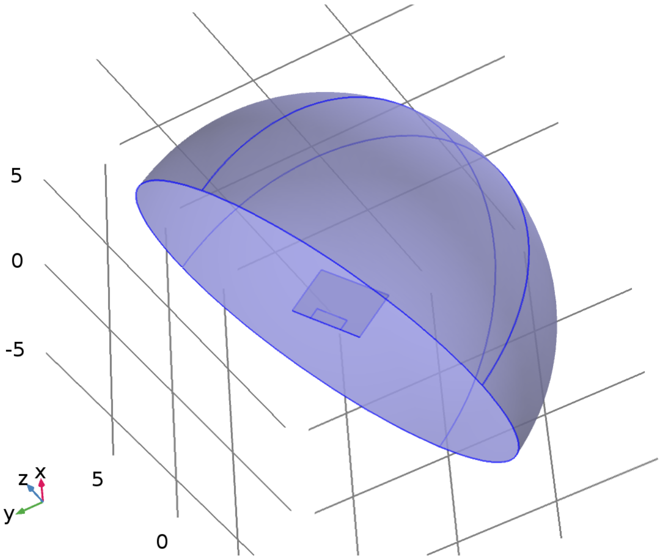

Figure 7.9: Air (Domain 1)

Spherical Wave Radiation 1

$$-\boldsymbol{n}\cdot\left(-\frac{1}{\rho_c}(\nabla p_t-q_d)\right)+\left(\imath k_{eq}+\frac{1}{r_{rf}}\right)\frac{p}{\rho_c}-\frac{r_{rf}\delta_{||}p}{2\rho_c(1+k_{eq}r_{rf})}=Q_i \tag{7.8}$$

Incident Pressure Field

$$r_{rf}=|(\boldsymbol{x_0}-\boldsymbol{r_0})| \tag{7.9}$$

$$Q_i = \left(\imath k_{eq} + \frac{1}{r_{rf}}\right)\frac{p}{\rho_c} - \frac{r_{rf}\delta_{||}p_i}{2\rho_c(1 + k_{eq}r_{rf})} + \boldsymbol{n} \cdot \frac{1}{\rho_c}\nabla p_i \tag{7.10}$$

$$p_i = p_0 e^{-\imath k_s \frac{\boldsymbol{x}\cdot\boldsymbol{e_k}}{|\boldsymbol{e_k}|}} \tag{7.11}$$

$$k_s^2 = \left(\frac{\omega}{c}\right)^2 \tag{7.12}$$

Symmetry 1

$$-\boldsymbol{n} \cdot \left(\frac{1}{\rho_c}(\nabla p_t - \boldsymbol{q_d})\right) = 0 \tag{7.13}$$

Linear Elastic Material

General Equations:

$$-\rho\omega^2\boldsymbol{u} = \nabla \cdot \sigma + \boldsymbol{F}_v e^{\imath\phi} + 6(\boldsymbol{M_v} \times \boldsymbol{n})\frac{z}{d}e^{\imath M_{ph}} \tag{7.14}$$

$$-\imath k_z = \lambda \tag{7.15}$$

$$\sigma_m = \sigma_{ad} + \boldsymbol{C}(\gamma - \gamma_{inel}), \gamma_{inel} = \gamma_0 + \gamma_{th} + \gamma_{hs} \tag{7.16}$$

$$\chi_b = \chi_{ad} + \frac{\boldsymbol{C}d}{2}(\chi - \chi_{inel}) \tag{7.17}$$

$$\sigma_s = \sigma_{ad} + \frac{5}{6}2G(\xi - \xi_0) \tag{7.18}$$

$$\sigma_{inplane} = \sigma_m + z\sigma_b \tag{7.19}$$

$$\sigma_{ad} = \sigma_0 + \sigma_{ext} + \sigma_d \tag{7.20}$$

$$\boldsymbol{C} = \boldsymbol{C(D)} \tag{7.21}$$

Shell Local System

$$\boldsymbol{n}_| = \boldsymbol{n} \tag{7.22}$$

$$\boldsymbol{t_{ll}} = \frac{e_{x1} - e_{x1} \cdot n_1)n_1}{|e_{x1} - e_{x1} \cdot n_1)n_1|} \tag{7.23}$$

$$\boldsymbol{t_{l2}} = n_1 \times t_{l1} \tag{7.24}$$

Acoustic structure boundary

$$-\boldsymbol{n} \cdot \left(-\frac{1}{\rho_c}(\nabla p_t - q_d)\right) = -\boldsymbol{n \cdot u_{tt}} \tag{7.25}$$

$$F_A = p_t\boldsymbol{n} \tag{7.26}$$

7.4.2 Study

Parametric Sweep

Parameter name	Parameter value list
theta	range(-3.1415926, 0.174532925, 3.1415926)

Description	Value
Sweep type	Specified combinations
Parameter name	theta
Parameter value list	range(-3.1415926, 0.174532925, 3.1415926)
Frequencies (Hz)	range(1000,500,10000)
Include geometric nonlinearity	Off

Bow Tie Model Simulations

Global Definitions

Date	Sep 4, 2015
Name	PolygonalModelThetaSweep 20150904.mph
Path	D:\Users\isb12210\Downloads\PolygonalModelThetaSweep 20150904.mph
Build	COMSOL 5.1 (Build: 180)
Used Products	COMSOL MultiphysicsAcoustics ModuleCAD ModuleStructural Mechanics

Parameters

Name	Expression	Description
theta	pi/4[rad]	Sound Azimuth Angle
pi	pi/4[rad]	Sound Pitch Angle
k1	sin(theta)*cos(phi)	Wave Vector x-axis
k2	sin(theta)*sin(phi)	Wave Vector y-axis
k3	cos(theta)	Wave Vector z-axis

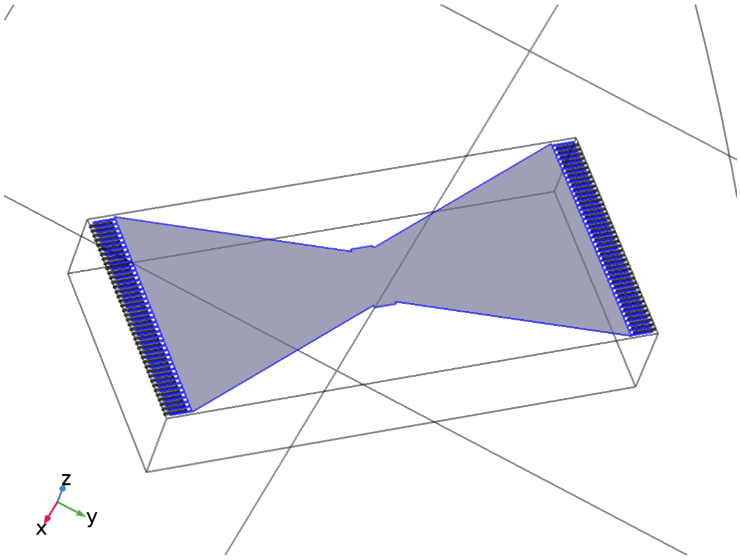

Figure 7.10: Single crystal silicon (Boundary 12)

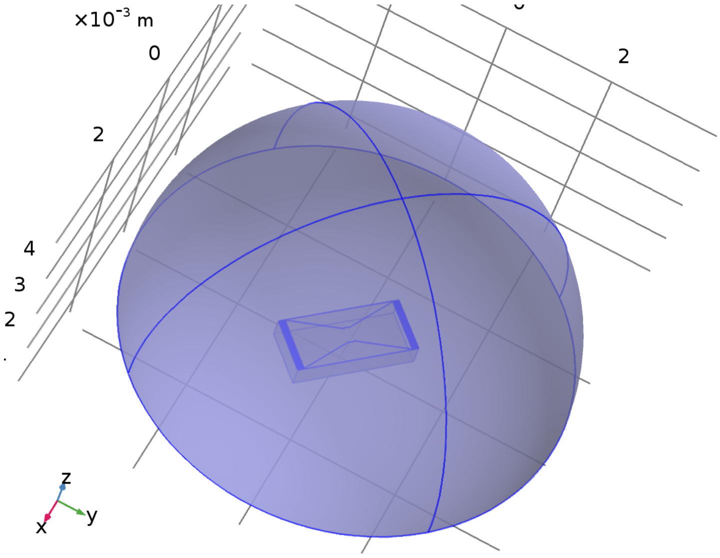

Figure 7.11: Air (Domains 1-2)

Materials

Single crystal silicon

Air

Pressure Acoustics - Frequency Domain

Equations:

$$\nabla \cdot \left(-\frac{1}{\rho_c} (\nabla p_t - q_d) \right) - \frac{k_{eq}^2 p_t}{\rho_c} = Q_m \tag{7.27}$$

$$p_t = p + p_b \tag{7.28}$$

$$k_{eq}^2 = \left(\frac{\omega}{c_c}\right)^2 \tag{7.29}$$

Sound Hard Boundary 1

$$-\boldsymbol{n} \cdot \left(-\frac{1}{\rho_c}(\nabla p_t - q_d)\right) = 0 \tag{7.30}$$

Spherical Wave Radiation 1

$$-\boldsymbol{n} \cdot \left(-\frac{1}{\rho_c}(\nabla p_t - q_d)\right) + \left(\imath k_{eq} + \frac{1}{r_{rf}}\right)\frac{p}{\rho_c} - \frac{r_{rf}\delta_{||}p}{2\rho_c(1 + k_{eq}r_{rf})} = Q_i \tag{7.31}$$

Incident Pressure Field

$$r_{rf} = |(\boldsymbol{x_0} - \boldsymbol{r_0})| \tag{7.32}$$

$$Q_i = \left(\imath k_{eq} + \frac{1}{r_{rf}}\right)\frac{p}{\rho_c} - \frac{r_{rf}\delta_{||}p_i}{2\rho_c(1 + k_{eq}r_{rf})} + \boldsymbol{n} \cdot \frac{1}{\rho_c}\nabla p_i \tag{7.33}$$

$$p_i = p_0 e^{-\imath k_s \frac{\boldsymbol{x}\cdot\boldsymbol{e_k}}{|\boldsymbol{e_k}|}} \tag{7.34}$$

$$k_s^2 = \left(\frac{\omega}{c}\right)^2 \tag{7.35}$$

Symmetry 1

$$-\boldsymbol{n} \cdot \left(\frac{1}{\rho_c}(\nabla p_t - \boldsymbol{q_d})\right) = 0 \tag{7.36}$$

Linear Elastic Material

General Equations:

$$-\rho\omega^2\boldsymbol{u} = \nabla \cdot \sigma + \boldsymbol{F}_v e^{\imath\phi} + 6(\boldsymbol{M_v} \times \boldsymbol{n})\frac{z}{d}e^{\imath M_{ph}} \tag{7.37}$$

$$-\imath k_z = \lambda \tag{7.38}$$

$$\sigma_m = \sigma_{ad} + \boldsymbol{C}(\gamma - \gamma_{inel}), \gamma_{inel} = \gamma_0 + \gamma_{th} + \gamma_{hs} \tag{7.39}$$

$$\chi_b = \chi_{ad} + \frac{\boldsymbol{C}d}{2}(\chi - \chi_{inel}) \tag{7.40}$$

$$\sigma_s = \sigma_{ad} + \frac{5}{6}2G(\xi - \xi_0) \tag{7.41}$$

$$\sigma_{inplane} = \sigma_m + z\sigma_b \tag{7.42}$$

$$\sigma_{ad} = \sigma_0 + \sigma_{ext} + \sigma_d \tag{7.43}$$

$$\boldsymbol{C} = \boldsymbol{C}(\boldsymbol{D}) \tag{7.44}$$

Shell Local System

$$\boldsymbol{n}_{|} = \boldsymbol{n} \tag{7.45}$$

$$\boldsymbol{t_{ll}} = \frac{e_{x1} - e_{x1} \cdot n_1)n_1}{|e_{x1} - e_{x1} \cdot n_1)n_1|} \tag{7.46}$$

$$\boldsymbol{t_{l2}} = n_1 \times t_{l1} \tag{7.47}$$

Acoustic structure boundary

$$-\boldsymbol{n} \cdot \left(-\frac{1}{\rho_c} (\nabla p_t - q_d) \right) = -\boldsymbol{n} \cdot \boldsymbol{u_{tt}} \tag{7.48}$$

$$F_A = p_t \boldsymbol{n} \tag{7.49}$$

Study

Parametric Sweep

Parameter name	Parameter value list
theta	range(-3.1415926, 0.174532925, 3.1415926)

Description	Value
Sweep type	Specified combinations
Parameter name	theta
Parameter value list	range(-3.1415926, 0.174532925, 3.1415926)
Frequencies (Hz)	range(1000,500,10000)
Include geometric nonlinearity	Off

7.5 Sound field around body of *Achroia grisella*

Global Definitions

Date	Jun 8, 2015
Name	2015Jun08 AchroiaBodyModelv2.mph
Path	D:\Users\isb12210\Downloads\2015Jun08 AchroiaBodyModelv2.mph
Build	COMSOL 5.1 (Build: 180)
Used Products	COMSOL Multiphysics Acoustics Module CAD Module

Parameters

Name	Expression	Description
theta	pi/4[rad]	Sound Azimuth Angle
pi	pi/4[rad]	Sound Pitch Angle
k1	sin(theta)*cos(phi)	Wave Vector x-axis
k2	sin(theta)*sin(phi)	Wave Vector y-axis
k3	cos(theta)	Wave Vector z-axis

Materials

Insect Cuticle

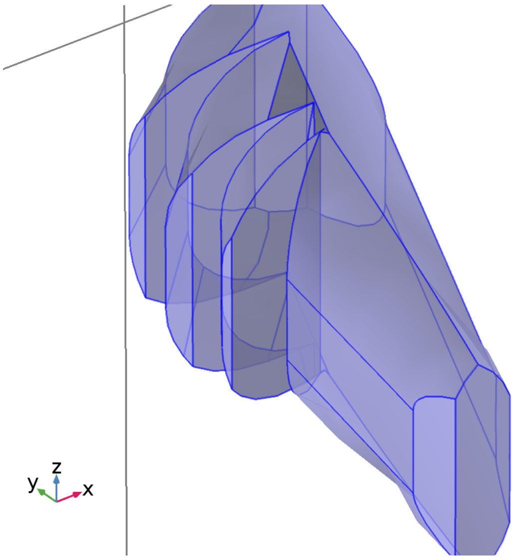

Figure 7.12: Insect cuticle (Domain 2)

Air

Pressure Acoustics - Frequency Domain

Equations:

$$\nabla \cdot \left(-\frac{1}{\rho_c} (\nabla p_t - q_d) \right) - \frac{k_{eq}^2 p_t}{\rho_c} = Q_m \tag{7.50}$$

$$p_t = p + p_b \tag{7.51}$$

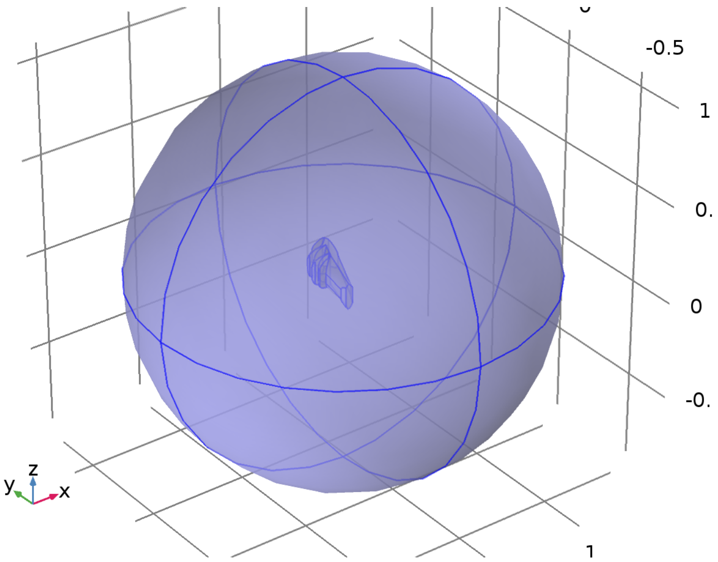

Figure 7.13: Air (Domain 1)

$$k_{eq}^2 = \left(\frac{\omega}{c_c}\right)^2 \tag{7.52}$$

Sound Hard Boundary 1

$$-\boldsymbol{n} \cdot \left(-\frac{1}{\rho_c}(\nabla p_t - q_d)\right) = 0 \tag{7.53}$$

Spherical Wave Radiation 1

$$-\boldsymbol{n} \cdot \left(-\frac{1}{\rho_c}(\nabla p_t - q_d)\right) + \left(\imath k_{eq} + \frac{1}{r_{rf}}\right)\frac{p}{\rho_c} - \frac{r_{rf}\delta_{||}p}{2\rho_c(1 + k_{eq}r_{rf})} = Q_i \tag{7.54}$$

Incident Pressure Field

$$r_{rf} = |(\boldsymbol{x_0} - \boldsymbol{r_0})| \tag{7.55}$$

$$Q_i = \left(\imath k_{eq} + \frac{1}{r_{rf}}\right)\frac{p}{\rho_c} - \frac{r_{rf}\delta_{||}p_i}{2\rho_c(1 + k_{eq}r_{rf})} + \boldsymbol{n} \cdot \frac{1}{\rho_c}\nabla p_i \tag{7.56}$$

$$p_i = p_0 e^{-\imath k_s \frac{\boldsymbol{x}\cdot\boldsymbol{e_k}}{|\boldsymbol{e_k}|}} \tag{7.57}$$

$$k_s^2 = \left(\frac{\omega}{c}\right)^2 \tag{7.58}$$

Symmetry 1

$$-\boldsymbol{n} \cdot \left(\frac{1}{\rho_c}(\nabla p_t - \boldsymbol{q_d})\right) = 0 \tag{7.59}$$

Solid mechanics

General Equations:

$$\rho\omega^2\boldsymbol{u} = \nabla\cdot S + \boldsymbol{F}_v e^{\imath\phi}, ik_x = \lambda \tag{7.60}$$

Linear Elastic Material

$$0 = \nabla\cdot S + \boldsymbol{F}_v \tag{7.61}$$

$$S = S_{ad} + \boldsymbol{C} : \epsilon_{el} \tag{7.62}$$

$$S_{ad} = S_0 + S_{ext} + S_q \tag{7.63}$$

$$\epsilon_{inel} = \epsilon_0 + \epsilon_{ext} + \epsilon_{th} + \epsilon_{hs} + \epsilon_{pl} + \epsilon_{cr} + \epsilon_{vp} \tag{7.64}$$

$$\epsilon = \frac{1}{2}\left[(\nabla\boldsymbol{u})^T + \nabla\boldsymbol{u}\right] \tag{7.65}$$

$$\boldsymbol{C} = \boldsymbol{C}(E, \upsilon) \tag{7.66}$$

Acoustic structure boundary

$$-\boldsymbol{n}\cdot\left(-\frac{1}{\rho_c}(\nabla p_t - q_d)\right) = -\boldsymbol{n}\cdot\boldsymbol{u_{tt}} \tag{7.67}$$

$$F_A = p_t\boldsymbol{n} \tag{7.68}$$

Study

Parametric Sweep

Parameter name	Parameter value list
theta	range(-3.141592653589793,0.17453292519943295,3.141592653589793)

Description	Value
Sweep type	Specified combinations
Parameter name	theta
Parameter value list	range(-3.141592653589793, 0.17453292519943295, 3.1415926535897
Frequencies (Hz)	range(1000,500,10000)
Include geometric nonlinearity	Off

Bibliography

[1] M. L. Kuntzman, J. Gloria Lee, N. N. Hewa-Kasakarage, D. Kim, and N. A. Hall, "Micromachined piezoelectric microphones with in-plane directivity," *Applied Physics Letters*, vol. 102, feb 2013.

[2] C. Gibbons, "Design of a biomimetic directional microphone diaphragm," in *Proceedings of IMECE*, (Orlando), 2000.

[3] R. N. Miles, W. Cui, Q. T. Su, and D. Homentcovschi, "A MEMS Low-Noise Sound Pressure Gradient Microphone With Capacitive Sensing," *Journal of Microelectromechanical Systems*, vol. 24, pp. 241–248, feb 2015.

[4] R. Miles, "High-order directional microphone diaphragm," nov 2005.

[5] R. S. Muller and Etc, eds., *Microsensors*. New York: IEEE Publications,U.S., may 1994.

[6] M. Esashi, "Revolution of Sensors in Micro-Electromechanical Systems," *Japanese Journal of Applied Physics*, vol. 51, p. 080001, jul 2012.

[7] L. Baumgartel, A. Vafanejad, S. J. Chen, and E. S. Kim, "Resonance-Enhanced Piezoelectric Microphone Array for Broadband or Prefiltered Acoustic Sensing," *Journal of Microelectromechanical Systems*, vol. 22, pp. 107–114, feb 2013.

[8] J. C. Eloy and E. Mounier, "Status of the MEMS industry," vol. 5717, pp. 43–49, 2005.

[9] E. Times, "MEMS Microphone Market to Hit 13% CAGR." Available: http://www.eetimes.com/document.asp?doc_id=1328892. Accessed: 24 Aug 2016, 2012.

[10] R. Bogue, “Recent developments in MEMS sensors: a review of applications, markets and technologies,” *Sensors Review.*

[11] S. S. Je, F. Rivas, R. E. Diaz, J. Kwon, J. Kim, B. Bakkaloglu, S. Kiaei, and J. Chae, “A Compact and Low-Cost MEMS Loudspeaker for Digital Hearing Aids,” *IEEE Transactions on Biomedical Circuits and Systems*, vol. 3, pp. 348–358, oct 2009.

[12] G. Bhargava, R. Bhasin, and S. V. Kumar, “System and methodology for voice activated access to multiple data sources and voice repositories in a single session,” may 2005.

[13] G. Valenzise, L. Gerosa, M. Tagliasacchi, F. Antonacci, and A. Sarti, “Scream and gunshot detection and localization for audio-surveillance systems,” in *IEEE Conference on Advanced Video and Signal Based Surveillance, 2007. AVSS 2007*, pp. 21–26, sep 2007.

[14] J. Huang, T. Supaongprapa, I. Terakura, F. Wang, N. Ohnishi, and N. Sugie, “A model-based sound localization system and its application to robot navigation,” *Robotics and Autonomous Systems*, vol. 27, pp. 199–209, jun 1999.

[15] E. J. Addeo, J. D. Robbins, and G. Shtirmer, “Sound localization system for teleconferencing using self-steering microphone arrays,” aug 1994.

[16] D. D. Yager, “Structure, development, and evolution of insect auditory systems,” *Microscopy Research and Technique*, vol. 47, pp. 380–400, dec 1999.

[17] A. N. Clements, *The Physiology of Mosquitoes: International Series of Monographs on Pure and Applied Biology: Zoology.* Elsevier, sep 2013.

[18] H. M. Moir, J. C. Jackson, and J. F. C. Windmill, “Extremely high frequency sensitivity in a ’simple’ ear,” *Biology Letters*, vol. 9, p. 20130241, aug 2013.

[19] G. Boyan, “Another look at insect audition: The tympanic receptors as an evolutionary specialization of the chordotonal system,” *Journal of Insect Physiology*, vol. 39, pp. 187–200, mar 1993.

[20] T. M. Laurence H. Field, “Chordotonal Organs of Insects,” *Advances in Insect Physiology*, vol. 27, 1998.

[21] J. Strauß and R. Lakes-Harlan, “Sensory neuroanatomy of stick insects highlights the evolutionary diversity of the orthopteroid subgenual organ complex,” *The Journal of Comparative Neurology*, vol. 521, pp. 3791–3803, nov 2013.

[22] M. J. Van Staaden, M. Rieser, S. R. Ott, M. A. Pabst, and H. Römer, “Serial hearing organs in the atympanate grasshopper Bullacris membracioides (Orthoptera, Pneumoridae),” *The Journal of Comparative Neurology*, vol. 465, pp. 579–592, oct 2003.

[23] L. A. Miller, “Structure of the green lacewing tympanal organ (Chrysopa carnea, neuroptera),” *Journal of Morphology*, vol. 131, pp. 359–382, aug 1970.

[24] L. A. Miller, “Physiological responses of green lacewings (Chrysopa, Neuroptera) to ultrasound,” *Journal of Insect Physiology*, vol. 17, pp. 491–506, Mar 1971.

[25] K. Lomas, F. Montealegre-Z, S. Parsons, L. H. Field, and D. Robert, “Mechanical filtering for narrow-band hearing in the weta,” *Journal of Experimental Biology*, vol. 214, pp. 778–785, mar 2011.

[26] A. Michelsen, “The physiology of the locust ear,” *Zeitschrift für vergleichende Physiologie*, vol. 71, pp. 49–62, mar 1971.

[27] J. E. Yack, “The structure and function of auditory chordotonal organs in insects,” *Microscopy Research and Technique*, vol. 63, pp. 315–337, Apr 2004.

[28] N. Mhatre, “Active amplification in insect ears: mechanics, models and molecules,” *Journal of Comparative Physiology A*, vol. 201, pp. 19–37, Dec 2014.

[29] W. A. Yost and G. Gourevitch, eds., *Directional Hearing.* Proceedings in Life Sciences, New York: Springer US, 1987.

[30] M. D. Greenfield, *Signalers and receivers: mechanisms and evolution of arthropod communication.* Oxford University Press, 2002.

[31] A. Michelsen, “Hearing and Sound Communication in Small Animals: Evolutionary Adaptations to the Laws of Physics,” in *The Evolutionary Biology*

of Hearing (D. B. Webster, A. N. Popper, and R. R. Fay, eds.), pp. 61–77, Springer New York, 1992.

[32] A. Michelsen, A. V. Popov, and B. Lewis, “Physics of directional hearing in the cricket Gryllus bimaculatus,” *Journal of Comparative Physiology A*, vol. 175, pp. 153–164, aug 1994.

[33] D. Robert, R. N. Miles, and R. R. Hoy, “Tympanal mechanics in the parasitoid fly Ormia ochracea : intertympanal coupling during mechanical vibration,” *Journal of Comparative Physiology A*, vol. 183, pp. 443–452, oct 1998.

[34] A. C. Mason, N. Lee, and M. L. Oshinsky, “The start of phonotactic walking in the fly Ormia ochracea: a kinematic study,” *The Journal of Experimental Biology*, vol. 208, pp. 4699–4708, dec 2005.

[35] T. D. Rossing, ed., *Springer Handbook of Acoustics*. New York: Springer New York, 2014.

[36] D. A. Russell, J. P. Titlow, and Y.-J. Bemmen, “Acoustic monopoles, dipoles, and quadrupoles: An experiment revisited,” *American Journal of Physics*, vol. 67, pp. 660–664, aug 1999.

[37] J. W. Judy, “Microelectromechanical systems (MEMS): Fabrication, design and applications,” *Smart Materials and Structures*, vol. 10, no. 6, pp. 1115–1134, 2001.

[38] J. M. Bustillo, R. T. Howe, and R. S. Muller, “Surface micromachining for microelectromechanical systems,” *Proceedings of the IEEE*, vol. 86, pp. 1552–1574, aug 1998.

[39] A. Cowen, G. Hames, D. Monk, S. Wilcenski, and B. Hardy, “SOIMUMPs Design Handbook,” *ResearchGate*, vol. 6, jan 2011.

[40] E. J. Boyd and D. Uttamchandani, “Measurement of the Anisotropy of Young’s Modulus in Single-Crystal Silicon,” *Journal of Microelectromechanical Systems*, vol. 21, pp. 243–249, feb 2012.

[41] D. C. Miller, B. L. Boyce, M. T. Dugger, T. E. Buchheit, and K. Gall, “Characteristics of a commercially available silicon-on-insulator MEMS material,” *Sensors and Actuators A: Physical*, vol. 138, pp. 130–144, jul 2007.

[42] L. Li, *MEMS micromirrors for imaging applications.* PhD thesis, 2013.

[43] R. Bauer, *Applications of programmable MEMS micromirrors in laser systems.* PhD thesis, 2013.

[44] A. Cowen, G. Hames, K. Glukh, and B. Hardy, *PiezoMUMPs Design Handbook Revision 1.0.* MEMSCAP Inc, 2012.

[45] D. Hohm and G. Sessler, "An integrated silicon-electret condenser microphone," *Proc. 11th Int. Congr. Acoustics*, vol. 6, pp. 29–32, 1983.

[46] D. Hohm and G. Hess, "A subminiature condenser microphone with silicon nitride membrane and silicon back plate," *The Journal of the Acoustical Society of America*, vol. 85, pp. 476–480, jan 1989.

[47] G. Sessler and J. West, "Self-Biased Condenser Microphone with High Capacitance," *The Journal of the Acoustical Society of America*, vol. 34, no. 11, pp. 1787–1788, 1962.

[48] M. Bao and H. Yang, "Squeeze film air damping in MEMS," *Sensors and Actuators A: Physical*, vol. 136, pp. 3–27, may 2007.

[49] F. Goericke and M. Chan, "High temperature compatible aluminum nitride resonating strain sensor," *Solid-State Sensors, . . .*, pp. 1994–1997, 2011.

[50] T. Roszhart, "The effect of thermoelastic internal friction on the Q of micromachined silicon resonators," *Solid-State Sensor and Actuator Workshop, . . .*, pp. 13–16, 1990.

[51] C. Zener, "Internal friction in solids. I. Theory of internal friction in reeds," *Physical review*, vol. 206, no. 1932, 1937.

[52] R. Lifshitz and M. Roukes, "Thermoelastic damping in micro- and nanomechanical systems," *Physical Review B*, vol. 61, pp. 5600–5609, feb 2000.

[53] D. Photiadis, B. Houston, X. Liu, J. Bucaro, and M. Marcus, "Thermoelastic loss observed in a high Q mechanical oscillator," *Physica B: Condensed Matter*, vol. 316-317, pp. 408–410, may 2002.

[54] T. Klose, H. Conrad, T. Sandner, and H. Schenk, "Fluidmechanical Damping Analysis of Resonant Micromirrors with Out-of-plane Comb Drive," *ResearchGate*, nov 2008.

[55] T. Sandner, T. Klose, A. Wolter, H. Schenk, H. K. Lakner, and W. Davis, "Damping analysis and measurement for a comb-drive scanning mirror," 2004.

[56] T. Klose, H. Conrad, T. Sandner, and H. Schenk, "Fluidmechanical damping analysis of resonant micromirrors with out-of-plane comb drive," *Proc. COMSOL Conf.(. . .* , 2008.

[57] U. S. Lindholm, D. D. Kana, W.-H. Chu, and H. N. Abramson, "Elastic Vibration Characteristics of Cantilever Plates in Water.," tech. rep., aug 1962.

[58] R. Sandberg, W. Svendsen, K. Mølhave, and A. Boisen, "Temperature and pressure dependence of resonance in multi-layer microcantilevers," *Journal of Micromechanics and Microengineering*, vol. 15, pp. 1454–1458, aug 2005.

[59] M. Yu, "Fly Ear Inspired Miniature Acoustic Sensors for Detection and Localization," tech. rep., 2011.

[60] D. J. Bell, T. J. Lu, N. a. Fleck, and S. M. Spearing, "MEMS actuators and sensors: observations on their performance and selection for purpose," *Journal of Micromechanics and Microengineering*, vol. 15, pp. S153–S164, jul 2005.

[61] B. Bicen, C. Garcia, N. A. Hall, M. Okandan, W. Cui, Q. T. Su, R. N. Miles, and L. Degertekin, "Diffraction based optical MEMS microphones and accelerometers with active electrostatic force feedback," *The Journal of the Acoustical Society of America*, vol. 123, pp. 3230–3230, may 2008.

[62] B. Bicen, S. Jolly, and K. Jeelani, "Integrated optical displacement detection and electrostatic actuation for directional optical microphones with micromachined biomimetic diaphragms," *Sensors Journal, . . .* , vol. 9, no. 12, pp. 1933–1941, 2009.

[63] M. Jeelani, *Integration and characterization of micromachined optical microphones*. PhD thesis, 2009.

[64] W. Cui, B. Bicen, N. Hall, S. A. Jones, F. L. Degertekin, and R. N. Miles, "Optical Sensing Inadirectional Memsmicrophone Inspired by the Ears of the Parasitoid Fly, Ormia Ochracea," in *19th IEEE International Conference on Micro Electro Mechanical Systems*, pp. 614–617, 2006.

[65] H. J. Liu, M. Yu, and X. M. Zhang, "Biomimetic optical directional microphone with structurally coupled diaphragms," *Applied Physics Letters*, vol. 93, p. 243902, dec 2008.

[66] H. Liu, Z. Chen, and M. Yu, "Biology-inspired acoustic sensors for sound source localization," vol. 6932, pp. 69322Y–69322Y–8, 2008.

[67] W. Cui, R. N. Miles, Q. Su, and D. Homentcovsci, "A Bio-Inspired Miniature Comb Sense Differential Microphone Diaphragm," pp. 143–148, jan 2010.

[68] A. Dehe and M. Nawaz, "Mems device," Jan. 22 2015. US Patent App. 13/947,823.

[69] G. L. Smith, J. S. Pulskamp, L. M. Sanchez, D. M. Potrepka, R. M. Proie, T. G. Ivanov, R. Q. Rudy, W. D. Nothwang, S. S. Bedair, C. D. Meyer, and R. G. Polcawich, "PZT-Based Piezoelectric MEMS Technology," *Journal of the American Ceramic Society*, vol. 95, pp. 1777–1792, jun 2012.

[70] R. Przybyla and S. Shelton, "In-air rangefinding with an aln piezoelectric micromachined ultrasound transducer," *Sensors Journal, . . .*, vol. 11, no. 11, pp. 2690–2697, 2011.

[71] S. Shelton, M.-L. Chan, H. Park, D. Horsley, B. Boser, I. Izyumin, R. Przybyla, T. Frey, M. Judy, K. Nunan, F. Sammoura, and K. Yang, "CMOS-compatible AlN piezoelectric micromachined ultrasonic transducers," *2009 IEEE International Ultrasonics Symposium*, pp. 402–405, sep 2009.

[72] M. D. Williams, B. a. Griffin, T. N. Reagan, J. R. Underbrink, and M. Sheplak, "An AlN MEMS Piezoelectric Microphone for Aeroacoustic Applications," *Journal of Microelectromechanical Systems*, vol. 21, pp. 270–283, apr 2012.

[73] N. A. Hall, M. Okandan, R. Littrell, B. Bicen, and F. L. Degertekin, "Micromachined optical microphone structures with low thermal-mechanical noise levels," *The Journal of the Acoustical Society of America*, vol. 122, pp. 2031–2037, oct 2007.

[74] R. Littrell and K. Grosh, "Modeling and characterization of cantilever-based MEMS piezoelectric sensors and actuators," *Microelectromechanical Systems, Journal of*, vol. 21, no. 2, pp. 406–413, 2012.

[75] A. Cowen, G. Hames, K. Glukh, and B. Hardy, "PiezoMUMPs Design Handbook a MUMPs ® process," 2013.

[76] A. American and N. Standard, "An American National Standard IEEE Standard on Piezoelectricity," 1988.

[77] J. Smits and W. Choi, "The constituent equations of piezoelectric heterogeneous bimorphs," *Ultrasonics, Ferroelectrics and Frequency . . .*, no. 7, pp. 1275–1278, 1991.

[78] P. Castellini, G. M. Revel, and E. P. Tomasini, "Laser Doppler Vibrometry," in *An Introduction to Optoelectronic Sensors*, vol. 7, pp. 216–229, World Scientific, jan 2009.

[79] D. Malacara-Hernández and Z. Malacara-Hernández, *Handbook of Optical Design, Second Edition.* New York: CRC Press, 2 edition ed., sep 2003.

[80] "Polytec Scanning Vibrometer Software Theory and Hardware Manuals," 2004.

[81] M. H. McKetty, "The AAPM/RSNA physics tutorial for residents. X-ray attenuation.," *RadioGraphics*, vol. 18, pp. 151–163, jan 1998.

[82] J. L. Nation, "A New Method Using Hexamethyldisilazane for Preparation of Soft Insect Tissues for Scanning Electron Microscopy," *Stain Technology*, vol. 58, pp. 347–351, jan 1983.

[83] D. F. Bray, J. Bagu, and P. Koegler, "Comparison of hexamethyldisilazane (HMDS), Peldri II, and critical-point drying methods for scanning electron microscopy of biological specimens," *Microscopy Research and Technique*, vol. 26, pp. 489–495, dec 1993.

[84] Faulwetter, "Investigation of contrast-enhancing techniques for the application of Micro-CT in marine biodiversity studies," in *SkyScan MicroCT User Meeting*, (Brussels), pp. 12–20, 2012.

[85] J. Beutel, H. L. Kundel, and R. L. V. Metter, *Handbook of Medical Imaging: Physics and psychophysics.* SPIE Press, 2000.

[86] W. Ritz, “Über eine neue Methode zur Lösung gewisser Variationsprobleme der mathematischen Physik.,” *Journal für die reine und angewandte Mathematik*, vol. 135, pp. 1–61, 1909.

[87] M. Krizek, P. Neittaanmaki, and R. Stenberg, *finite element methods: fifty years of the Courant element.* CRC Press, aug 1994.

[88] K. Nam-Ho and B. V. Sankar.

[89] D. J. Mackie, *Biologically inspired acoustic systems : from insect ears to MEMS microphone structures.* PhD thesis, 2015.

[90] *COMSOL Reference Manual.* 2007.

[91] “How to Implement a Mesh Refinement Study,” aug 2013.

[92] Y. Jang and M. D. Greenfield, “Ultrasonic communication and sexual selection in wax moths: female choice based on energy and asynchrony of male signals,” *Animal Behaviour*, vol. 51, pp. 1095–1106, may 1996.

[93] S. M. Whiteley, D. A. Waters, G. Hayward, S. G. Pierce, and I. Farr, “Wireless recording of the calls of Rousettus aegyptiacus and their reproduction using electrostatic transducers,” *Bioinspiration & Biomimetics*, vol. 5, p. 026001, jun 2010.

[94] S. A. Adamo, D. Robert, J. Perez, and R. R. Hoy, “The response of an insect parasitoid, Ormia ochracea (Tachinidae), to the uncertainty of larval success during infestation,” *Behavioral Ecology and Sociobiology*, vol. 36, pp. 111–118, feb 1995.

[95] W. H. Cade, M. Ciceran, and A.-M. Murray, “Temporal patterns of parasitoid fly (Ormia ochracea) attraction to field cricket song (Gryllus integer),” *Canadian Journal of Zoology*, vol. 74, pp. 393–395, feb 1996.

[96] S. Adamo, D. Robert, and R. Hoy, “Effects of a tachinid parasitoid, Ormia ochracea, on the behaviour and reproduction of its male and female field cricket hosts (Gryllus spp),” *Journal of Insect Physiology*, vol. 41, pp. 269–277, mar 1995.

[97] N. Ramsauer and D. Robert, “Free-flight phonotaxis in a parasitoid fly: behavioural thresholds, relative attraction and susceptibility to noise,” *Naturwissenschaften*, vol. 87, pp. 315–319, aug 2000.

[98] D. Robert, M. P. Read, and R. R. Hoy, “The tympanal hearing organ of the parasitoid fly Ormia ochracea (Diptera, Tachinidae, Ormiini),” *Cell and Tissue Research*, vol. 275, pp. 63–78, jan 1994.

[99] R. S. Edgecomb, D. Robert, M. P. Read, and R. R. Hoy, “The tympanal hearing organ of a fly: phylogenetic analysis of its morphological origins,” *Cell and Tissue Research*, vol. 282, pp. 251–268, nov 1995.

[100] D. Robert, R. N. Miles, and R. R. Hoy, “Directional hearing by mechanical coupling in the parasitoid fly Ormia ochracea,” *Journal of Comparative Physiology. A, Sensory, Neural, and Behavioral Physiology*, vol. 179, no. 1, pp. 29–44, 1996.

[101] R. N. Miles, D. Robert, and R. R. Hoy, “Mechanically coupled ears for directional hearing in the parasitoid fly Ormia ochracea,” *The Journal of the Acoustical Society of America*, vol. 98, pp. 3059–3070, dec 1995.

[102] J. F. C. Windmill, J. H. Fullard, and D. Robert, “Mechanics of a ’simple’ ear: tympanal vibrations in noctuid moths,” *The Journal of Experimental Biology*, vol. 210, pp. 2637–2648, aug 2007.

[103] A. C. Mason, M. L. Oshinsky, and R. R. Hoy, “Hyperacute directional hearing in a microscale auditory system,” *Nature*, vol. 410, pp. 686–690, apr 2001.

[104] T. J. Walker, “Phonotaxis in female *Ormia ochracea* (Diptera: Tachinidae), a parasitoid of field crickets,” *Journal of Insect Behavior*, vol. 6, pp. 389–410, may 1993.

[105] S. S. Rao, *Mechanical vibrations.* Addison-Wesley Longman, Incorporated, 1986.

[106] H. Liu, L. Currano, D. Gee, T. Helms, and M. Yu, “Understanding and mimicking the dual optimality of the fly ear,” *Scientific Reports*, vol. 3, aug 2013.

[107] R. N. Miles and R. R. Hoy, “The development of a biologically-inspired directional microphone for hearing aids,” *Audiology & Neuro-Otology*, vol. 11, no. 2, pp. 86–94, 2006.

[108] J. Chang, W. Mendyk, L. Thier, P. Yun, A. LaRow, S. Shaw, and W. Schoenborn, “Early attack reaction sensor (EARS), a man-wearable gunshot detection system,” vol. 6201, pp. 62011T–62011T–8, 2006.

[109] T. Damarla, L. M. Kaplan, and G. T. Whipps, “Sniper Localization Using Acoustic Asynchronous Sensors,” *IEEE Sensors Journal*, vol. 10, pp. 1469–1478, sep 2010.

[110] H. Liu, L. Currano, D. Gee, B. Yang, and M. Yu, “Fly-ear inspired acoustic sensors for gunshot localization,” vol. 7321, pp. 73210A–73210A–10, 2009.

[111] A. P. Lisiewski, H. J. Liu, M. Yu, L. Currano, and D. Gee, “Fly-ear inspired micro-sensor for sound source localization in two dimensions,” *The Journal of the Acoustical Society of America*, vol. 129, pp. EL166–EL171, may 2011.

[112] T. Pham and N. Srour, “TTCP AG-6: acoustic detection and tracking of UAVs,” vol. 5417, pp. 24–30, 2004.

[113] G. L. Duckworth, D. C. Gilbert, and J. E. Barger, “Acoustic counter-sniper system,” vol. 2938, pp. 262–275, 1997.

[114] G. L. Duckworth, J. E. Barger, and D. C. Gilbert, “Acoustic counter-sniper system,” jul 1999.

[115] R. B. Stoughton, “SAIC SENTINEL acoustic counter-sniper system,” vol. 2938, pp. 276–284, 1997.

[116] R. Maboudian, “Surface processes in MEMS technology,” *Surface Science Reports*, vol. 30, pp. 207–269, jan 1998.

[117] H. Liu, X. Zhang, and M. Yu, “Understanding fly-ear inspired directional microphones,” vol. 7292, pp. 72922M–72922M–11, 2009.

[118] L. J. Currano, H. Liu, D. Gee, B. Yang, and M. Yu, “Microscale implementation of a bio-inspired acoustic localization device,” p. 73210B, may 2009.

[119] H. Liu, M. Yu, L. Currano, and D. Gee, “Fly-Ear Inspired Miniature Directional Microphones: Modeling and Experimental Study,” *JASA*, vol. 129, no. 5, pp. 1–7, 2009.

[120] M. Yu and B. Balachandran, “Acoustic Measurements Using a Fiber Optic Sensor System,” *Journal of Intelligent Material Systems and Structures*, vol. 14, pp. 409–414, jul 2003.

[121] X. Ding, “Behavior and application of silicon diaphragms with a boss and corrugations,” in *, IEEE Solid-State Sensor and Actuator Workshop, 1992. 5th Technical Digest*, pp. 166–169, jun 1992.

[122] D. Gnewikow, T. Ricketts, G. W. Bratt, and L. C. Mutchler, “Real-world benefit from directional microphone hearing aids,” *Journal of Rehabilitation Research and Development*, vol. 46, no. 5, pp. 603–618, 2009.

[123] Y. Zhang, R. Bauer, J. Windmill, and D. Uttamchandani

[124] T. J. Shivok, *MEMS PolyMUMPS-Based Miniature Microphone for Directional Sound Sensing.*

[125] M. L. Kuntzman and N. A. Hall, “Sound source localization inspired by the ears of the Ormia ochracea,” *Applied Physics Letters*, vol. 105, p. 033701, jul 2014.

[126] R. N. Miles, Q. Su, W. Cui, M. Shetye, F. L. Degertekin, B. Bicen, C. Garcia, S. Jones, and N. Hall, “A low-noise differential microphone inspired by the ears of the parasitoid fly Ormia ochracea,” *The Journal of the Acoustical Society of America*, vol. 125, pp. 2013–2026, apr 2009.

[127] R. N. Miles, F. L. Degertekin, W. Cui, Q. Su, D. Homentcovschi, and F. Banser, “A biologically inspired silicon differential microphone with active Q control and optical sensing,” *Proceedings of Meetings on Acoustics*, vol. 19, p. 030031, jun 2013.

[128] R. J. Baken and R. F. Orlikoff, *Clinical Measurement of Speech and Voice.* Cengage Learning, 2000.

[129] M. Yang, X. Zhu, Y. Zhang, N. Ta, and Z. Rao, “Design and parameter study of a biologically inspired sound source locator,” *ResearchGate*, vol. 2, pp. 1107–1114, jan 2014.

[130] S. Ando, T. Kurihara, K. Watanabe, Y. Yamanishi, and T. Ooasa, "Novel theoretical design and fabrication test of biomimicry directional microphone," in *TRANSDUCERS 2009 - 2009 International Solid-State Sensors, Actuators and Microsystems Conference*, pp. 1932–1935, jun 2009.

[131] N. Ono, A. Saito, and S. Ando, "Design and experiments of bio-mimicry sound source localization sensor with gimbal-supported circular diaphragm," in *TRANSDUCERS, Solid-State Sensors, Actuators and Microsystems, 12th International Conference on, 2003*, vol. 1, pp. 935–938 vol.1, jun 2003.

[132] C. C. Chen and Y. T. Cheng, "Physical Analysis of a Biomimetic Microphone With a Central-Supported (C-S) Circular Diaphragm for Sound Source Localization," *IEEE Sensors Journal*, vol. 12, pp. 1504–1512, may 2012.

[133] R. Miles and Yang, Liu, "A silicon directional microphone with second-order directivity," in *Proceedings of Internation congress on Acoustics*, (Madrid), 2007.

[134] X. Huo, *Design, analysis and characterization of a miniature second-order directional microphone.* PhD thesis, 2009.

[135] J. George and L. M. Kaplan, "Shooter localization using soldier-worn gunfire detection systems," in *2011 Proceedings of the 14th International Conference on Information Fusion (FUSION)*, pp. 1–8, jul 2011.

[136] R. C. Maher, "Acoustical Characterization of Gunshots," in *IEEE Workshop on Signal Processing Applications for Public Security and Forensics, 2007. SAFE '07*, pp. 1–5, apr 2007.

[137] B. M. Brustad and J. C. Freytag, "A Survey of Audio Forensic Gunshot Investigations," Audio Engineering Society, jul 2005.

[138] B. M. Sadler, T. Pham, and L. C. Sadler, "Optimal and wavelet-based shock wave detection and estimation," *The Journal of the Acoustical Society of America*, vol. 104, pp. 955–963, aug 1998.

[139] S. D. Beck, H. Nakasone, and K. W. Marr, "Variations in recorded acoustic gunshot waveforms generated by small firearms," *The Journal of the Acoustical Society of America*, vol. 129, pp. 1748–1759, apr 2011.

[140] J. A. Mazurek, J. E. Barger, M. Brinn, R. J. Mullen, D. Price, S. E. Ritter, and D. Schmitt, “Boomerang mobile counter shooter detection system,” vol. 5778, pp. 264–282, 2005.

[141] G. Simon, M. Maróti, Á. Lédeczi, G. Balogh, B. Kusy, A. Nádas, G. Pap, J. Sallai, and K. Frampton, “Sensor Network-based Countersniper System,” in *Proceedings of the 2Nd International Conference on Embedded Networked Sensor Systems*, SenSys ’04, (New York), pp. 1–12, ACM, 2004.

[142] R. Mirzazadeh, S. Mariani, and M. De Fazio, “Modeling of Fluid Damping in Resonant Micromirrors with Out-of-Plane Comb-Drive Actuation,” p. e007, MDPI, jun 2014.

[143] D. Homentcovschi, M. J. Aubrey, and R. N. Miles, “A two-dimensional model of a directional microphone: calculation of the normal force and moment on the diaphragm,” *The Journal of the Acoustical Society of America*, vol. 119, pp. 756–768, feb 2006.

[144] F. H. Fletcher and N. H. Fletcher, *Acoustic Systems in Biology.* New York: Oxford University Press, jul 1992.

[145] R. H. Downey and G. Karunasiri, “Reduced Residual Stress Curvature and Branched Comb Fingers Increase Sensitivity of MEMS Acoustic Sensor,” *Journal of Microelectromechanical Systems*, vol. 23, pp. 417–423, apr 2014.

[146] D. V. Hinkley, “On the Ratio of Two Correlated Normal Random Variables,” *Biometrika*, vol. 56, no. 3, pp. 635–639, 1969.

[147] A. Cedilnik, K. Košmelj, and A. Blejec, “The distribution of the ratio of jointly normal variables,” *ResearchGate*, vol. 1, pp. 99–108, jan 2004.

[148] K. Joudrey, G. G. Adams, and N. E. McGruer, “Design, modeling, fabrication and testing of a high aspect ratio electrostatic torsional MEMS micromirror,” *Journal of Micromechanics and Microengineering*, vol. 16, no. 10, p. 2147, 2006.

[149] R. N. Miles, Q. T. Su, W. Cui, S. A. Jones, F. L. Degertekin, B. Bicen, C. Garcia, and N. A. Hall, “A low-noise biomimetic differential microphone,” *The Journal of the Acoustical Society of America*, vol. 123, pp. 3228–3228, may 2008.

[150] G. Kunike, "Zur Biologie der kleinen Wachsmotte, Achroea grisella Fabr," *Zeitschrift für Angewandte Entomologie*, vol. 16, pp. 304–356, aug 1930.

[151] M. D. Greenfield and J. A. Coffelt, "Reproductive Behaviour of the Lesser Waxmoth, Achroia grisella (Pyralidae: Galleriinae): Signalling, Pair Formation, Male Interactions, and Mate Guarding," *Behaviour*, vol. 84, no. 3/4, pp. 287–315, 1983.

[152] K. H. Dahm, D. Meyer, W. E. Finn, V. Reinhold, and H. Röller, "The olfactory and auditory mediated sex attraction in Achroia grisella (Fabr.)," *Die Naturwissenschaften*, vol. 58, pp. 265–266, may 1971.

[153] H. G. Spangler, M. D. Greenfield, and A. Takessian, "Ultrasonic mate calling in the lesser wax moth," *Physiological Entomology*, vol. 9, pp. 87–95, mar 1984.

[154] null Conner, "'Un chant d'appel amoureux': acoustic communication in moths," *The Journal of Experimental Biology*, vol. 202 (Pt 13), pp. 1711–1723, jul 1999.

[155] M. D. G. YW Jang, "Ultrasonic communication and sexual selection in wax moths: female choice based on energy and asynchrony of male signals.," *Animal Behaviour*, vol. 51, no. 5, pp. 1095–1106, 1996.

[156] R. L. Rodríguez and M. D. Greenfield, "Behavioural context regulates dual function of ultrasonic hearing in lesser waxmoths: bat avoidance and pair formation," *Physiological Entomology*, vol. 29, pp. 159–168, jun 2004.

[157] L. S. Brandt, B. C. Ludwar, and M. D. Greenfield, "Co-Occurrence of Preference Functions and Acceptance Thresholds in Female Choice: Mate Discrimination in the Lesser Wax Moth," *Ethology*, vol. 111, pp. 609–625, jun 2005.

[158] H.-P. Knopek, L, "Uber den Bau der abdominalen Tympanalorgane der Kleinen Wachsmotte Achroia grisella (Fbr.).," *Zoologische Jahrbuecher Abteilung fuer Anatomie und Ontogenie der Tiere*, no. 1141, pp. 83–93, 1986.

[159] V. M. Hintze-Podufal, Christel, "Die Entwicklung der Tympanalorgane und ihrer invers gerichteten Skolopidien bei Wachsmotten (Lepidoptera: Pyralidae: Galleriinae)," *Entomologia Generalis*, vol. 20, pp. 195–201, jan 1996.

[160] M. A. Cook and M. J. Scoble, "Tympanal organs of geometrid moths: a review of their morphology, function, and systematic importance," *Systematic Entomology*, vol. 17, pp. 219–232, jul 1992.

[161] R. L. Rodríguez, J. Schul, R. B. Cocroft, and M. D. Greenfield, "The contribution of tympanic transmission to fine temporal signal evaluation in an ultrasonic moth," *Journal of Experimental Biology*, vol. 208, pp. 4159–4165, nov 2005.

[162] M. D. Greenfield, "Acoustic Communication in the NocturnalLepidoptera," pp. 81–100, 2013.

[163] F. L. Wightman and D. J. Kistler, "Resolution of front-back ambiguity in spatial hearing by listener and source movement," *The Journal of the Acoustical Society of America*, vol. 105, pp. 2841–2853, may 1999.

[164] M. D. Greenfield, M. K. Tourtellot, C. Tillberg, W. J. Bell, and N. Prins, "Acoustic orientation via sequential comparison in an ultrasonic moth," *Die Naturwissenschaften*, vol. 89, pp. 376–380, aug 2002.

[165] S. Schöneich and B. Hedwig, "Hyperacute Directional Hearing and Phonotactic Steering in the Cricket (Gryllus bimaculatus deGeer)," *PLOS ONE*, vol. 5, p. e15141, dec 2010.

[166] W. E. Conner and A. J. Corcoran, "Sound strategies: the 65-million-year-old battle between bats and insects," *Annual Review of Entomology*, vol. 57, pp. 21–39, 2012.

[167] R. R. Hoy, "The Evolution of Hearing in Insects as an Adaptation to Predation from Bats," in *The Evolutionary Biology of Hearing* (D. B. Webster, A. N. Popper, and R. R. Fay, eds.), pp. 115–129, Springer New York, 1992.

[168] K. Roeder, "The behaviour of free flying moths in the presence of artificial ultrasonic pulses," *Animal Behaviour*, vol. 10, pp. 300–304, jul 1962.

[169] M. D. Greenfield and H. Hohendorf, "Independence of Sexual and Anti-Predator Perceptual Functions in an Acoustic Moth: Implications for the Receiver Bias Mechanism in Signal Evolution," *Ethology*, vol. 115, pp. 1137–1149, dec 2009.

[170] M. D. G. E. I. Greig, "Sexual selection and predator avoidance in an acoustic moth: Discriminating females take fewer risks," *Behaviour*, vol. 141, no. 7, pp. 799–815, 2004.

[171] S. Alem and M. D. Greenfield, "Economics of mate choice at leks: do female waxmoths pay costs for indirect genetic benefits?," *Behavioral Ecology*, vol. 21, pp. 615–625, may 2010.

[172] R. Nakano, Y. Ishikawa, S. Tatsuki, N. Skals, A. Surlykke, and T. Takanashi, "Private ultrasonic whispering in moths," *Communicative & Integrative Biology*, vol. 2, pp. 123–126, mar 2009.

[173] S. Wright, "The Roles of Mutation, Inbreeding, Crossbreeding and Selection in Evolution," *Proceedings of the Sixth International Congress of Genetics*, vol. 1, pp. 356–366, 1932.

[174] M. Touse, J. Sinibaldi, and G. Karunasiri, "MEMS directional sound sensor with simultaneous detection of two frequency bands," in *2010 IEEE Sensors*, pp. 2422–2425, nov 2010.

[175] Y. Zhang, J. F. C. Windmill, and D. Uttamchandani, "Biomimetic MEMS directional microphone structures for multi-band operation," in *IEEE SENSORS 2014 Proceedings*, pp. 440–443, nov 2014.